

Optical cavities, coherent emitters, and protocols for diamond-based quantum networks

van Dam, Suzanne

DOI

[10.4233/uuid:225ba0ab-22d7-4d1e-a12c-85e0ed55c51d](https://doi.org/10.4233/uuid:225ba0ab-22d7-4d1e-a12c-85e0ed55c51d)

Publication date

2019

Document Version

Final published version

Citation (APA)

van Dam, S. (2019). *Optical cavities, coherent emitters, and protocols for diamond-based quantum networks*. [Dissertation (TU Delft), Delft University of Technology]. <https://doi.org/10.4233/uuid:225ba0ab-22d7-4d1e-a12c-85e0ed55c51d>

Important note

To cite this publication, please use the final published version (if applicable). Please check the document version above.

Copyright

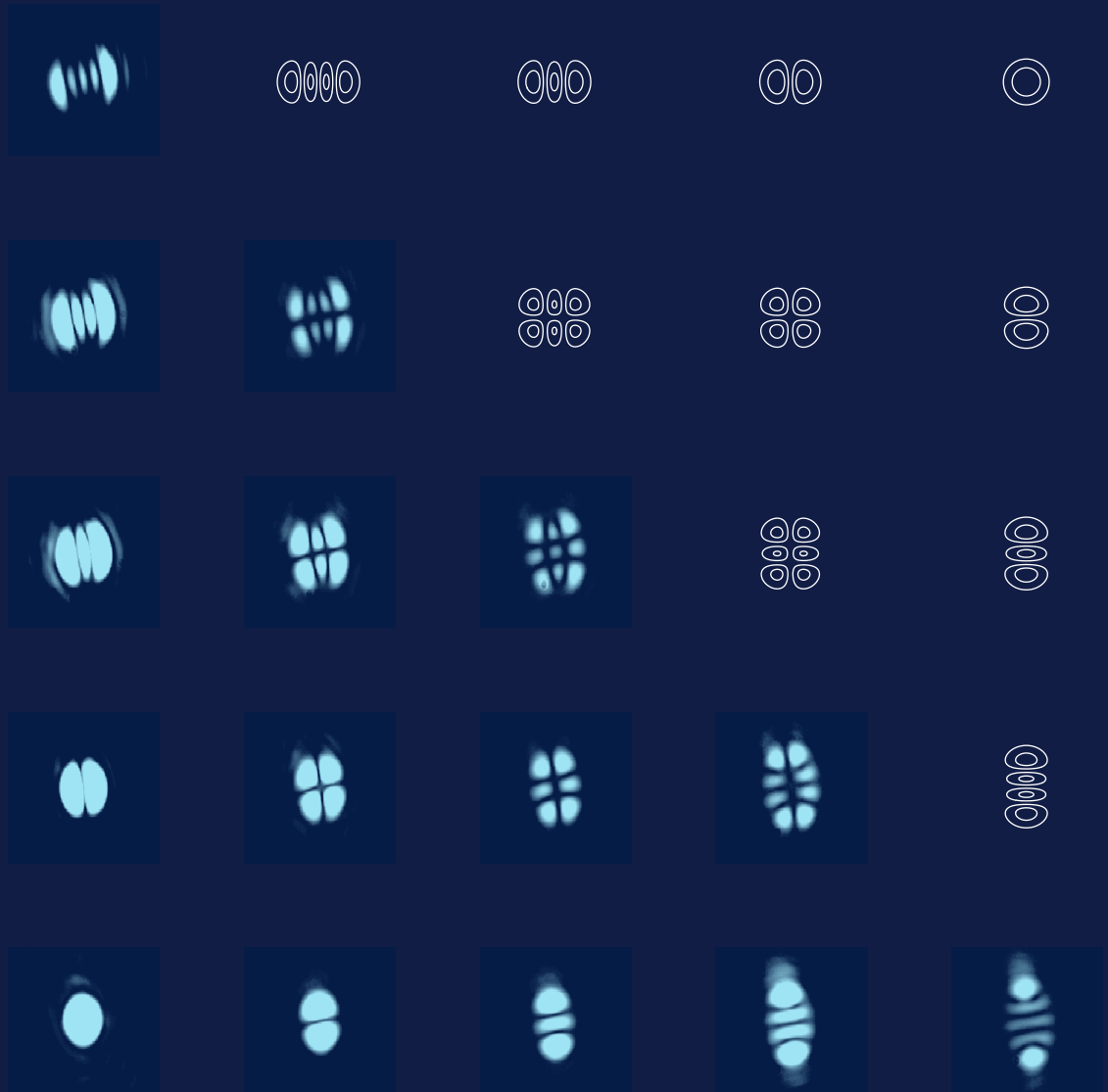
Other than for strictly personal use, it is not permitted to download, forward or distribute the text or part of it, without the consent of the author(s) and/or copyright holder(s), unless the work is under an open content license such as Creative Commons.

Takedown policy

Please contact us and provide details if you believe this document breaches copyrights. We will remove access to the work immediately and investigate your claim.

Optical cavities, coherent emitters, and protocols for diamond-based quantum networks

Suzanne van Dam



**OPTICAL CAVITIES, COHERENT EMITTERS, AND
PROTOCOLS FOR DIAMOND-BASED QUANTUM
NETWORKS**



OPTICAL CAVITIES, COHERENT EMITTERS, AND PROTOCOLS FOR DIAMOND-BASED QUANTUM NETWORKS

Proefschrift

ter verkrijging van de graad van doctor
aan de Technische Universiteit Delft,
op gezag van de Rector Magnificus prof. dr. ir. T. H. J. J. van der Hagen,
voorzitter van het College voor Promoties,
in het openbaar te verdedigen op vrijdag 1 februari 2019 om 10:00 uur

door

Suzanne Barbera VAN DAM

Master of Science in Applied Physics,
Technische Universiteit Delft, Nederland

Master of Advanced Study in Mathematics,
University of Cambridge, Verenigd Koninkrijk

geboren te Rotterdam, Nederland.

Dit proefschrift is goedgekeurd door de promotor.

Samenstelling promotiecommissie:

Rector Magnificus, Prof. dr. ir. R. Hanson,	voorzitter Technische Universiteit Delft, promotor
--	---

Onafhankelijke leden:

Prof. dr. C. Becher,	Universität des Saarlandes
Prof. dr. L. DiCarlo,	Technische Universiteit Delft
Prof. dr. ir. P. Kruit,	Technische Universiteit Delft
Prof. dr. G.A. Steele,	Technische Universiteit Delft
Prof. dr. ir. C.H. van der Wal,	Rijksuniversiteit Groningen

Overige leden:

Prof. dr. S.D.C. Wehner,	Technische Universiteit Delft
--------------------------	-------------------------------



Copyright © 2018 by Suzanne Barbera van Dam

Casimir PhD Series, Delft-Leiden 2018-52

ISBN 978-90-8593-383-0

Cover design by Peter Humphreys, Suzanne van Dam, and Sophie Hermans

Printed by Gildeprint – Enschede

An electronic version of this dissertation is available at

<http://repository.tudelft.nl/>.

CONTENTS

1	Introduction	1
1.1	Quantum foundations and quantum technology	2
1.2	The nitrogen-vacancy centre in diamond	2
1.3	Entangling nitrogen-vacancy centres	3
1.4	Thesis overview	4
	References	5
2	The nitrogen-vacancy centre as a quantum network node	9
2.1	The nitrogen-vacancy centre in diamond	10
2.2	The nitrogen-vacancy centre as optical interface	10
2.3	Ground state spin structure of the nitrogen-vacancy centre.	14
2.4	Controlling weakly coupled nuclear spin states	16
	References	18
3	Multipartite entanglement generation and contextuality tests using non-destructive three-qubit parity measurements	23
3.1	Introduction	24
3.2	Three-qubit parity measurements on nuclear spins in diamond	24
3.3	Generation of genuine multipartite entanglement	25
3.4	Quantum contextuality experiments	26
3.5	Conclusions.	31
	References	31
4	Purcell enhancement in diamond-air Fabry-Pérot microcavities	35
4.1	An efficient optical interface through Purcell enhancement.	36
4.2	Experimental optical cavities	42
4.3	Diamond-air Fabry-Pérot microcavities.	43
4.4	Conclusions.	60
	References	60
5	Optimal design of diamond-air microcavities for quantum networks using an analytical approach	65
5.1	Introduction	66
5.2	The one-dimensional structure of a hybrid cavity.	67
5.3	Transverse extent of Gaussian beams in a hybrid cavity	75
5.4	Including real-world imperfections	78
5.5	Conclusions.	80
5.6	Methods	82
	References	85

6 Nitrogen-vacancy centres in diamond membranes: requirements, creation and characterisation	89
6.1 Introduction	90
6.2 Required optical properties	91
6.3 Nitrogen ion implantation and electron irradiation	92
6.4 Measurement methods	94
6.5 Characterisation of optical properties.	98
References	99
7 Optical coherence of diamond NV centres formed by ion implantation and annealing	103
7.1 Introduction	104
7.2 Nitrogen ion implantation	104
7.3 NV densities and host isotopes	106
7.4 Linewidth of optical transitions.	107
7.5 Local strain fields	109
7.6 Conclusions.	110
References	116
8 Measurement methods for Fabry-Pérot microcavities	121
8.1 Cavity characterisation	122
8.2 NV-cavity coupling	132
References	136
9 Robust nano-fabrication of an integrated platform for spin control in a tunable microcavity	137
9.1 Introduction	138
9.2 Fiber dimple and mirror coatings	138
9.3 Fabrication of striplines and marker field	139
9.4 Cavity finesse	139
9.5 Diamond membrane preparation and van der Waals bonding	140
9.6 Electron spin resonance	141
9.7 Conclusions.	141
References	143
10 Design and low-temperature characterization of a tunable microcavity for diamond-based quantum networks	147
10.1 Introduction	148
10.2 A fiber Fabry-Pérot cavity	148
10.3 Cavity mode structure	148
10.4 Finesse measurements	150
10.5 Cavity stability characterisation.	152
10.6 Conclusions.	154
10.7 Methods	154
References	155

11 Coupling nitrogen-vacancy centres to a microcavity	159
11.1 Introduction	160
11.2 Sample characterisation	160
11.3 Bare cavity characterisation.	161
11.4 Diamond-air cavity characterisation	162
11.5 NV-cavity coupling	163
11.6 Probing the Purcell effect	166
11.7 Conclusions.	166
11.8 Acknowledgments	168
11.9 Methods	168
References	169
12 Multiplexed entanglement generation over quantum networks using multi-qubit nodes	173
12.1 Introduction	174
12.2 Modelling.	179
12.3 Conclusions.	183
12.4 acknowledgments.	183
References	183
13 Conclusions and outlook	187
13.1 Summary	188
13.2 Towards an efficient optical interface in a quantum network	189
13.3 Quantum network sequences in optical cavities	190
13.4 Towards a quantum repeater	192
13.5 Foundational questions in quantum mechanics	193
13.6 Device-independent quantum key distribution.	193
References	200
A Appendix	207
A.1 Resonance condition of the diamond-air cavity.	208
A.2 Analytic solution to a coupled Gaussian modes model for a curved diamond surface	209
A.3 Optical characterisation of NV centres in diamond membranes	211
References	214
Summary	215
Samenvatting	217
Acknowledgements	219
List of Publications	223
Curriculum Vitæ	225



1

INTRODUCTION

Quantum mechanics differs deeply from classical intuition and knowledge, sparking fundamental questions and radically new technology. Generating large entangled states between distant nodes of a quantum network will advance both domains. The nitrogen-vacancy (NV) centre in diamond is a promising building block for such a network, since it has a coherent optical interface as well as access to local quantum memories (section 1.2). Extending quantum networks to more nodes and larger distances however relies upon improving the entangling efficiency of these defect centres (section 1.3). In this thesis we approach this challenge by embedding NV centres in an optical cavity, taking care to preserve coherence of the NV optical transition, and we develop protocols for efficient quantum communication over an NV-based quantum network (outlined in section 1.4).

1.1. QUANTUM FOUNDATIONS AND QUANTUM TECHNOLOGY

Quantum mechanics is rooted in experiments. The theory was created to explain experimental phenomena and since then its predictions have been verified experimentally with remarkable accuracy. But quantum mechanics has elements that go strongly against classical intuition. The nonclassicality of elements in quantum theory such as quantum superposition and quantum entanglement have been subject of debate since their introduction [1–3].

It took half a century of technological progress to be able to scrutinize these concepts in a pure form experimentally [4, 5]. The technological ability to create and control quantum states has since then expanded, and enabled scientists working with quantum theory to develop a ‘quantum intuition’ to understand experimental outcomes. Quantum intuition often goes against classical intuition, helping us to better understand fundamentally quantum concepts such as superposition and entanglement. Importantly, this intuition also guides an understanding of how these quantum phenomena translate into classical measurement outcomes. An intuition is here not only handy, but necessary: there is no clear description in quantum mechanics on how to treat or where to pose a quantum-to-classical boundary.

With these tools in hand, scientists and engineers are able to create new technology by itself: quantum technology. Among quantum technologies are quantum sensing [6], quantum simulation [7], quantum computing [8] and a quantum internet [9]. Quantum intuition works astonishingly well to explain experimental and technological achievements in these fields. It works so well, that the lack of clear description of the quantum-to-classical boundary is veiled. Nevertheless, almost a century since the first descriptions of quantum theory, these fundamental questions still need to be answered.

In quantum mechanics, progress on foundational questions and technological achievements proceed hand-in-hand. This is showcased by the realization of a loophole-free test of Bell’s inequalities [3, 10–13]. These tests mark an important step in the foundations of quantum mechanics by refuting with high certainty local-realistic theories. At the same time they show the progress of quantum network technologies, demonstrating how entangled links that allow for e.g. device-independent quantum key distribution [14] can be extended to truly distant links.

The exciting idea of progress towards entangling more and more nodes over longer and longer distances underpins the creation of quantum networks. It pushes the quantum boundary closer to the classical macroscopic realm, and enables a quantum internet [9].

1.2. THE NITROGEN-VACANCY CENTRE IN DIAMOND

First building blocks of quantum networks have been established on several different platforms, including all-photonic networks [15–20], trapped ions or neutral atoms [21], and in solid-state platforms, such as superconducting qubits [22–24], quantum dots [25], and defects in solids [26].

In this thesis we focus on the nitrogen-vacancy (NV) centre in diamond as a quantum network node. Embedded in the solid state structure of diamond, it has a long-lived spin ground state that can be used as a quantum bit (qubit). Furthermore, at cyrogenic

temperatures (below 10 K) it has a coherent spin-photon interface [27, 28], that provides optical initialisation and readout [29], and can be used to generate entanglement between distant spins [30]. The NV centre as a quantum network node strongly benefits from the presence of surrounding nuclear spins that can be coherently controlled [31–33]. These nuclear spins can serve as quantum memories [34, 35], or can be used to perform local quantum computations [36–38].

With all these facets the NV centre is a workhorse for foundational and technological progress, both by exploiting and improving control over many spins within one node, and for the prospect of creating large entangled states over macroscopic distances. To create these large entangled states with NV centres an important technological challenge needs to be addressed: improving the entangling efficiency. We discuss this in more detail below, and suggest a potential solution.

1.3. ENTANGLING NITROGEN-VACANCY CENTRES

The origin of a low entangling efficiency between distant NV centres can be understood by studying the entangling scheme [39] schematically represented in Fig. 1.1. This scheme consists of three consecutive steps: (1) Entanglement is generated at each diamond between the NV centre's spin state and a photon number state through excitation of a spin-dependent optical transition. (2) The two photon modes are made to interfere using a beam splitter. (3) Detection of two photons heralds entanglement generation through entanglement swapping.

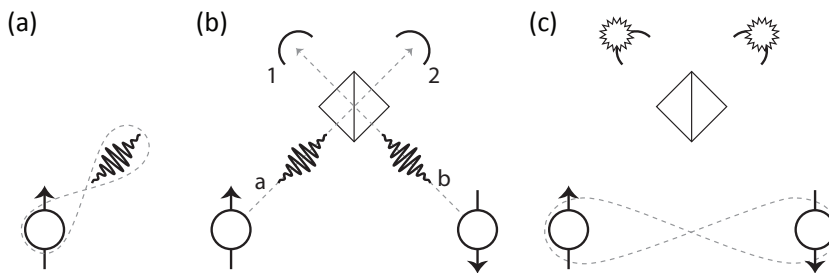


Figure 1.1: Entangling scheme following the Barrett-Kok scheme [39]. (a) Local entanglement is generated between the NV spin and a photon mode. (b) The photon modes interfere on a beam splitter at a central station. (c) Detection of two photons heralds entanglement generation. Figure adapted from [40].

The heralded nature of this entanglement scheme makes it very appealing: photon losses do not influence the fidelity of the entangled state. This has underpinned the generation of high fidelity entanglement between NV centres [30], enabling unconditional quantum teleportation [41], and extension to a distance of > 1 km [10].

However, photon losses do influence the entangling rate. Since two photons have to be detected within one round of entanglement generation, the rate of the protocol is proportional to the square of the photon losses. For the NV-NV distance of more than a kilometer in Ref. [10], the total emission and detection efficiency per photon is $\approx 10^{-4}$, leading to a total success probability of $\approx 10^{-8}$. With a repetition rate of less than $(10 \mu\text{s})^{-1}$,

the entangling rate in this experiment was around one per hour. To create a network over larger distances, and with many more nodes, connected by quantum repeaters [42], this low entangling rate has to be addressed.

There are two complementary approaches to increasing the entangling rate between distant NV centres.

First, this could be achieved by adapting the entanglement generation protocol. A linear dependency of the rate on photon losses can be achieved by employing an extreme-photon-loss protocol [43] or single-photon protocol [44]. Demonstrated implementations of these protocols with NV centres indeed provide a speed-up in entanglement rate of three orders of magnitude [34, 45]. Further improvements to the implementations of these protocols are needed to improve the entangled state fidelities to the level of those achieved with the Barrett-Kok scheme [10].

Second, an increase in the entanglement rate can be achieved by a reduction of the photon losses per round. These losses consist of three parts: fiber attenuation, a low coherent-photon emission probability, and a non-unit collection efficiency.

The photon attenuation during transmission over fibers is ≈ 8 dB for the NV emission wavelength (637 nm). To maintain high entangling rates for distant setups, photon losses due to fiber attenuation can be reduced by frequency down-conversion of NV photons to telecom wavelengths [46, 47].

The low coherent-photon emission probability is the result of a low branching ratio of photon emission into the zero phonon line (ZPL); only about 3% for the NV centre. The collection efficiency is limited by direction of dipole emission and the high diamond refractive index, to approximately 10% in conventional setups [30]. Low emission- and collection efficiency can be addressed simultaneously by embedding the NV centre in an optical cavity. When the optical cavity is on-resonance with the NV ZPL, Purcell enhancement [48] leads to an enhanced emission of coherent photons [49]. Since these photons are emitted in the approximately Gaussian cavity mode, the collection efficiency is also enhanced. This approach to enhancement of entanglement generation is pursued in this thesis.

1.4. THESIS OVERVIEW

This thesis is structured as follows.

In **chapter 2** we describe the NV centre in diamond as a quantum network node.

We realize sequential three-qubit parity measurements on nuclear spins within a single NV centre node in **chapter 3**, and use these to generate GHZ state and for quantum contextuality experiments.

In **chapter 4** we describe embedding the NV centre in an optical cavity can increase the efficiency of the NV optical interface through Purcell enhancement. In the same chapter, we give an overview of various experimental approaches to realize such a cavity, and describe in detail the platform that we believe is most suited: a diamond-air Fabry-Pérot microcavity.

In **chapter 5** we develop analytical descriptions of these microcavities that guide the focus for design improvements. We take into account the realistic conditions under which these cavities operate, including the effect of vibrations.

A key requirement for applications in quantum networks is that the cavities can support optically coherent NV centres. We describe the creation and optical characterisation of NV centres in thin diamond membranes in **chapter 6**. In **chapter 7** we study the optical stability of NV centres that are created via nitrogen ion implantation. We correlate optical linewidth of the NV centres after implantation to the source of nitrogen (native or implanted).

The next chapters focus on experimental realisation of diamond Fabry-Pérot microcavities. First, the measurement techniques developed for the characterisation of Fabry-Pérot cavities with diamond, and for measuring NV-cavity coupling are presented in **chapter 8**. We then present a method for microwave addressing of the NV spin in diamond membranes in **chapter 9**. We characterise a Fabry-Pérot cavity with a diamond membrane at cryogenic temperatures in **chapter 10**: we measure the finesse of the cavity, and characterise the impact of vibrations.

In **chapter 11** we observe coupling of an ensemble of NV centres to the cavity mode, although low cavity finesse hinders observation of ZPL enhancement. We use a diamond membrane with NV centres with a narrow optical linewidth, formed by high-energy electron irradiation and annealing.

We look ahead to quantum networks employing optical cavities in **chapter 12**, analyzing protocols with multiplexing in multi-qubit quantum nodes to overcome limits on entangling rate imposed by classical communication time.

Finally we present the conclusions of this thesis and provide an outlook for future research in **chapter 13**.

REFERENCES

- [1] Einstein, A., Podolsky, B. & Rosen, N., *Can Quantum-Mechanical Description of Physical Reality Be Considered Complete?* Phys. Rev. **47**, 777 (1935).
- [2] Bohr, N., *Can Quantum-Mechanical Description of Physical Reality be Considered Complete?* Phys. Rev. **48**, 696 (1935).
- [3] Bell, J., *On the Einstein Podolsky Rosen Paradox*, Physics **1**, 195 (1964).
- [4] Freedman, S. J. & Clauser, J. F., *Experimental test of local hidden-variable theories*, Phys. Rev. Lett. **28**, 938 (1972).
- [5] Aspect, A., Dalibard, J. & Roger, G., *Experimental test of bell's inequalities using time-varying analyzers*, Phys. Rev. Lett. **49**, 1804 (1982).
- [6] Degen, C. L., Reinhard, F. & Cappellaro, P., *Quantum sensing*, Rev. Mod. Phys. **89**, 1 (2017).
- [7] Georgescu, I. M., Ashhab, S. & Nori, F., *Quantum simulation*, Rev. Mod. Phys. **86**, 153 (2014).
- [8] Nielsen, M. A. & Chuang, I. L., *Quantum Computation and Quantum Information* (Cambridge University Press, Cambridge, UK, 2010).

- [9] Wehner, S., Elkouss, D. & Hanson, R., *Quantum Internet: a vision for the road ahead*, Science **362**, 303 (2018).
- [10] Hensen, B. *et al.*, *Loophole-free Bell inequality violation using electron spins separated by 1.3 kilometres*, Nature **526**, 682 (2015).
- [11] Shalm, L. K. *et al.*, *Strong Loophole-Free Test of Local Realism*, Phys. Rev. Lett. **115**, 250402 (2015).
- [12] Giustina, M. *et al.*, *Significant-Loophole-Free Test of Bell's Theorem with Entangled Photons*, Phys. Rev. Lett. **115**, 250401 (2015).
- [13] Rosenfeld, W. *et al.*, *Event-Ready Bell Test Using Entangled Atoms Simultaneously Closing Detection and Locality Loopholes*, Phys. Rev. Lett. **119**, 010402 (2017).
- [14] Pironio, S. *et al.*, *Device-independent quantum key distribution secure against collective attacks*, New J. Phys. **11**, 045021 (2009).
- [15] Peev, M. *et al.*, *The SECOQC quantum key distribution network in Vienna*, New J. Phys. **11**, 075001 (2009).
- [16] Sasaki, M. *et al.*, *Field test of quantum key distribution in the tokyo qkd network*, Opt. Express **19**, 10387 (2011).
- [17] Stucki, D. *et al.*, *Long-term performance of the SwissQuantum quantum key distribution network in a field environment*, New J. Phys. **13**, 123001 (2011).
- [18] Wang, S. *et al.*, *Field and long-term demonstration of a wide area quantum key distribution network*, Opt. Express **22**, 21739 (2014).
- [19] Vallone, G. *et al.*, *Experimental Satellite Quantum Communications*, Phys. Rev. Lett. **115**, 040502 (2015).
- [20] Liao, S. K. *et al.*, *Satellite-to-ground quantum key distribution*, Nature **549**, 43 (2017).
- [21] Reiserer, A. & Rempe, G., *Cavity-based quantum networks with single atoms and optical photons*, Rev. Mod. Phys. **87**, 1379 (2014).
- [22] Dickel, C. *et al.*, *Chip-to-chip entanglement of transmon qubits using engineered measurement fields*, Phys. Rev. B **97**, 064508 (2018).
- [23] Axline, C. J. *et al.*, *On-demand quantum state transfer and entanglement between remote microwave cavity memories*, Nat. Phys. **14**, 705 (2018).
- [24] Campagne-Ibarcq, P. *et al.*, *Deterministic Remote Entanglement of Superconducting Circuits through Microwave Two-Photon Transitions*, Phys. Rev. Lett. **120**, 200501 (2018).
- [25] Delteil, A., Sun, Z., Gao, W.-b., Togan, E. & Faelt, S., *Generation of heralded entanglement between distant hole spins*, Nat. Phys. **12**, 218 (2016).

- [26] Awschalom, D. D., Hanson, R., Wrachtrup, J. & Zhou, B. B., *Quantum technologies with optically interfaced solid-state spins*, Nat. Photon. **12**, 516 (2018).
- [27] Batalov, A. *et al.*, *Temporal coherence of photons emitted by single nitrogen-vacancy defect centers in diamond using optical rabi-oscillations*, Phys. Rev. Lett. **100**, 077401 (2008).
- [28] Robledo, L., Bernien, H., Van Weperen, I. & Hanson, R., *Control and coherence of the optical transition of single nitrogen vacancy centers in diamond*, Phys. Rev. Lett. **105**, 177403 (2010).
- [29] Robledo, L. *et al.*, *High-fidelity projective read-out of a solid-state spin quantum register*, Nature **477**, 574 (2011).
- [30] Bernien, H. *et al.*, *Heralded entanglement between solid-state qubits separated by three metres*. Nature **497**, 86 (2013).
- [31] Kolkowitz, S., Unterreithmeier, Q. P., Bennett, S. D. & Lukin, M. D., *Sensing distant nuclear spins with a single electron spin*, Phys. Rev. Lett. **109**, 137601 (2012).
- [32] Taminiau, T. H. *et al.*, *Detection and control of individual nuclear spins using a weakly coupled electron spin*, Phys. Rev. Lett. **109**, 137602 (2012).
- [33] Zhao, N. *et al.*, *Sensing single remote nuclear spins*, Nat. Nanotechnol. **7**, 657 (2012).
- [34] Kalb, N. *et al.*, *Entanglement Distillation between Solid-State Quantum Network Nodes*, Science **356**, 928 (2017).
- [35] Kalb, N., Humphreys, P. C., Slim, J. J. & Hanson, R., *Dephasing mechanisms of diamond-based nuclear-spin memories for quantum networks*, Phys. Rev. A **97**, 062330 (2018).
- [36] Waldherr, G. *et al.*, *Quantum error correction in a solid-state hybrid spin register*, Nature **506**, 204 (2014).
- [37] Taminiau, T. H., Cramer, J., van der Sar, T., Dobrovitski, V. V. & Hanson, R., *Universal control and error correction in multi-qubit spin registers in diamond*. Nat. Nanotechnol. **9**, 171 (2014).
- [38] Cramer, J. *et al.*, *Repeated quantum error correction on a continuously encoded qubit by real-time feedback*, Nat. Commun. **7**, 11526 (2016).
- [39] Barrett, S. D. & Kok, P., *Efficient high-fidelity quantum computation using matter qubits and linear optics*, Phys. Rev. A **71**, 060310 (2005).
- [40] Pfaff, W., *Quantum Measurement and Entanglement of Spin Quantum Bits in Diamond*, Ph.D. thesis, Delft University of Technology (2013).
- [41] Pfaff, W. *et al.*, *Unconditional quantum teleportation between distant solid-state quantum bits*, Science **345**, 532 (2014).

- [42] Childress, L., Taylor, J., Sørensen, A. & Lukin, M., *Fault-Tolerant Quantum Communication Based on Solid-State Photon Emitters*, Phys. Rev. Lett. **96**, 070504 (2006).
- [43] Campbell, E. T. & Benjamin, S. C., *Measurement-based entanglement under conditions of extreme photon loss*, Phys. Rev. Lett. **101**, 16 (2008).
- [44] Cabrillo, C., Cirac, J. I., García-Fernández, P. & Zoller, P., *Creation of entangled states of distant atoms by interference*, Phys. Rev. A **59**, 1025 (1999).
- [45] Humphreys, P. C. *et al.*, *Deterministic delivery of remote entanglement on a quantum network*, Nature **558**, 268 (2018).
- [46] Bock, M. *et al.*, *High-fidelity entanglement between a trapped ion and a telecom photon via quantum frequency conversion*, Nat. Commun. **9**, 1 (2018).
- [47] Dréau, A., Tchekhovateva, A., Mahdaoui, A. E., Bonato, C. & Hanson, R., *Quantum frequency conversion to telecom of single photons from a nitrogen-vacancy center in diamond*, Phys. Rev. Appl. **9**, 064031 (2018).
- [48] Purcell, E., *Spontaneous Emission Probabilities at Radio Frequencies*, in *Proc. Am. Physical Soc.*, Vol. 69 (1946).
- [49] Faraon, A., Barclay, P. E., Santori, C., Fu, K.-M. C. & Beausoleil, R. G., *Resonant enhancement of the zero-phonon emission from a colour centre in a diamond cavity*, Nat. Photon. **5**, 301 (2011).

2

THE NITROGEN-VACANCY CENTRE AS A QUANTUM NETWORK NODE

This chapter describes the NV centre as the node of a quantum network. In section 2.2 we describe the optical interface of the NV centre, describing the transitions between the NV ground and excited states, effects of strain and temperature, and vibrational levels on the optical transitions. Then we give an overview of the ground state spin properties of the NV centre and the coherent coupling to a nuclear spin register in section 2.3 and section 2.4.

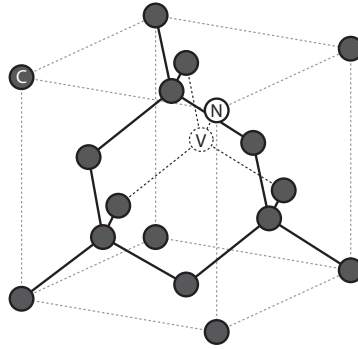


Figure 2.1: Crystal structure of the NV centre in diamond. Figure taken from Pfaff, Bernien [22, 23]. The nitrogen-vacancy centre consists of a substitutional nitrogen and adjacent vacant lattice site, forming a point defect with C_{3v} symmetry. In the diamond lattice there are four possible orientations of the N-V axis. Six electrons occupy the vacancy in the negative charge state (NV^-).

2.1. THE NITROGEN-VACANCY CENTRE IN DIAMOND

The nitrogen-vacancy (NV) centre is a defect centre in diamond, consisting of a substitutional nitrogen impurity and an adjacent vacant lattice site (see Fig. 2.1). NV centres can be as-grown in the diamond lattice, grown in doped δ -layers [1] or created through (nitrogen) ion implantation [2–5], electron irradiation [6–8] or laser writing techniques [9, 10]. Dangling bonds from the carbon and nitrogen atoms give rise to an electronic state in the vacancy. A negative charge state NV centre, NV^- , is formed when the defect receives an additional electron from a nearby donor. The negative charge state is widely used in quantum experiments, and is therefore the one we will consider here. This section will focus on the aspects of the NV centre relevant for the experiments described in this thesis. For a detailed overview of the NV centre and its applications we refer to the many available reviews [11–21].

2.2. THE NITROGEN-VACANCY CENTRE AS OPTICAL INTERFACE

The nitrogen and carbon atomic orbitals linearly combine to form molecular orbitals, as indicated in Fig. 2.2a. In the ground state the two levels lowest in energy (a'_1 and a_1) are doubly occupied, while two unpaired electrons are distributed over the degenerate molecular orbitals $e_{x,y}$. The excited state is formed when one electron from the orbital a_1 is promoted to the $e_{x,y}$ orbital. Both in the ground and excited state two unpaired electron spins can combine into triplet or singlet states. The triplet states are lowest in energy as a result of Coulomb repulsion. The lowest energy ground state of the NV centre is thus the ground molecular orbital with $S = 1$. It forms the basis of the NV centre as a spin qubit. The ground state (fine) structure is discussed in more detail in section 2.3.

Fig. 2.2b shows the ground and excited spin triplet states and the ground state singlets. Transitions between the ground and excited states can occur with the absorption

or emission of photons. The transition between the ground state $m_s = 0$, and the excited states $E_{x,y}$ is mostly spin conserving, with only a small spin-mixing component originating from coupling to the $E_{1,2}$ states. This provides a cycling transition that can be used to read out the spin state using resonant optical excitation [29].

The A_1 and $E_{1,2}$ levels couple to the singlet states through a spin-orbit coupling [27, 28], leading to an inter system crossing (ISC) between the triplet and singlet states. The singlet state 1A_1 is believed to decay very rapidly to the 1E state, that is metastable and determines the total singlet state lifetime measured to be ≈ 370 ns for single NV centres at cryogenic temperatures [30, 31]. From the singlet state, the decay is primarily to the $m_s = 0$ ground state, providing an efficient spin initialisation mechanism, that is effective even at ambient temperatures.

2.2.1. STRAIN AND TEMPERATURE EFFECTS

The ground and excited state spin triplets consists of respectively three and six states, that are further split in energy by spin-spin and spin-orbit interactions. In the case of no strain, the excited state levels E_x and E_y , and E_1 and E_2 are doubly degenerate. Lateral strain in the diamond lattice (ξ_{\perp}), perpendicular to the N-V axis, lifts this degeneracy (Fig. 2.3a), and changes the relative energy of the excited state levels [24, 32]. Longitudinal strain shifts all levels simultaneously up or down in energy. In high purity type IIa diamond the resulting inhomogeneous distribution of the excited state transitions is around 30 GHz, as we conclude from observations of NVs in around 7 different diamonds in our lab. In nanodiamonds, or diamond containing a high concentration of impurities or damage, the inhomogeneous distribution can be on the order of THz.

At cryogenic temperatures (around 4 K) and low lateral strain the transitions between ground and excited state are individually discernible (see Fig. 2.3b). In a high purity diamond low in defects, the direct excited state transitions are coherent, showing homogeneous linewidths close to the lifetime-limited value of 13 MHz [33]. For higher temperatures (> 10 K) the excited states become subject to phonon-induced mixing. A two-phonon Raman process mixes the excited state pairs E_x/E_y , A_1/A_2 , and E_1/E_2 . The rate of these processes has a temperature-dependency of T^5 [34]. The effect is therefore strongly suppressed at temperatures below 10 K, while at room temperature it leads to averaging of the excited states resulting in a strongly broadened homogeneous linewidth of 15 THz [35].

Although at low strain the two-phonon process is dominant, at high strain a one-phonon emission process can play a role. This one-phonon process induces spontaneous emission processes from E_x to E_y , and from A_1 and A_2 to E_1 and E_2 [28]. The transition rate increases with an increased energy splitting, as present at high lateral strain ($\xi_{\perp} \gtrsim 20$ GHz). In these conditions a depopulation of the E_x excited state to the E_y state, and depopulation from A_1 and A_2 to E_1 and E_2 is predicted [36].

2.2.2. OPTICAL TRANSITIONS VIA VIBRATIONAL LEVELS

When the electronic state occupies an NV orbital it influences the equilibrium position of the surrounding nuclei. Different NV orbitals correspond to different lowest-energy nuclear configurations, as depicted in Fig. 2.4a. Electronic transitions are instantaneous compared to the timescale of nuclear movement, such that the transitions are with high

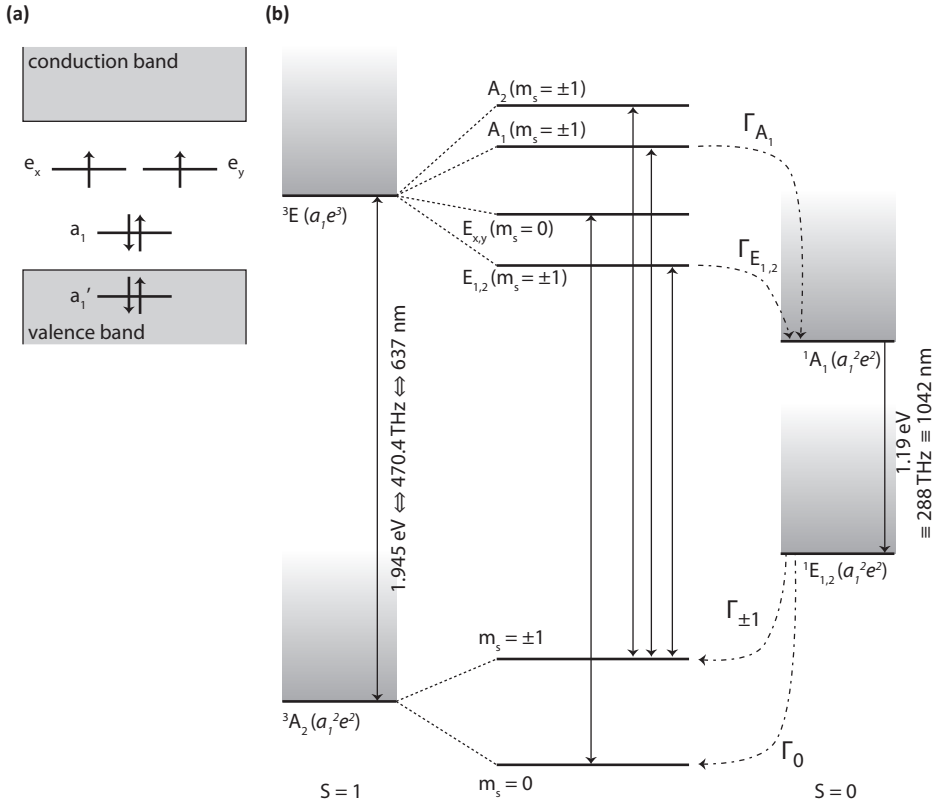


Figure 2.2: Energy levels of the NV centre. Figure adapted from Pfaff, Bernien [22, 23]. **(a)** The available electron molecular orbitals, linear combinations of the nitrogen and carbon atomic orbitals, are situated in the diamond bandgap (5.5 eV). In the orbital ground state, the lowest levels (a_1' , a_1) are doubly occupied, while the degenerate levels e_x and e_y have an unpaired electron. The level is indicated as $a_1^2e^2$. In the orbital excited state, an electron is promoted from a_1 to $e_{x,y}$, resulting in the level $a_1^2e^3$ [24]. The situation of the orbitals in the diamond bandgap isolates the NV centre from its solid-state environment, creating an ion-like system. **(b)** The orbital ground state triplet and singlet states split in energy through Coulomb interactions. The triplet states 3A_2 are lower in energy than the singlet states. The singlet states $^1E_{1,2}$ are believed to have lower energy than the singlet state 1A_1 , separated by a zero-phonon line in the infrared (1042 nm) [25, 26]. Recent measurements and analysis indicate that the energy separation between 1A_1 and the excited state 3E is in the range 344 meV - 430 meV [27, 28]. The ground and excited state triplets are made up of three and six states respectively, that are split in energy through spin-spin and spin-orbit interactions. At zero strain and magnetic field, four of the excited states, E_x and E_y and E_1 and E_2 , are doubly degenerate. The excited states $E_{x,y}$ have $m_s = 0$ character, whereas the other four states are equal mixtures of $m_s = -1$ and $m_s = +1$. These follow optical selection rules: linear polarisation is required to excite the spin-conserving $m_s = 0$ transition, whereas the other transitions are excited by circularly polarised light. First-order transitions from the excited states A_1 and $E_{1,2}$ to the singlet states can take place. The decay from the singlet state is mainly to $m_s = 0$, providing an effective polarising channel, even at ambient temperatures.

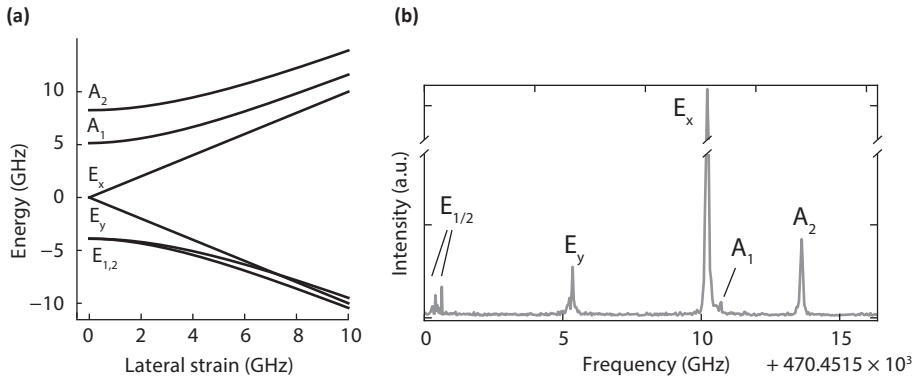


Figure 2.3: Strain-splitting of the excited state energy levels and transitions. Figure adapted from Pfaff, Bernien [22, 23]. (a) The excited state energy levels shift with lateral strain. The lateral strain value is defined with respect to the frequency of the E_x and E_y transition as the half splitting: $(f_{E_x} - f_{E_y})/2$, while the longitudinal strain is their average: $(f_{E_x} + f_{E_y})/2$. (b) The excited state transitions can be accessed by scanning a tunable red laser across the resonance, while monitoring the off-resonantly emitted photons. At low temperatures (here 4.2 K), the individual transitions can be discerned.

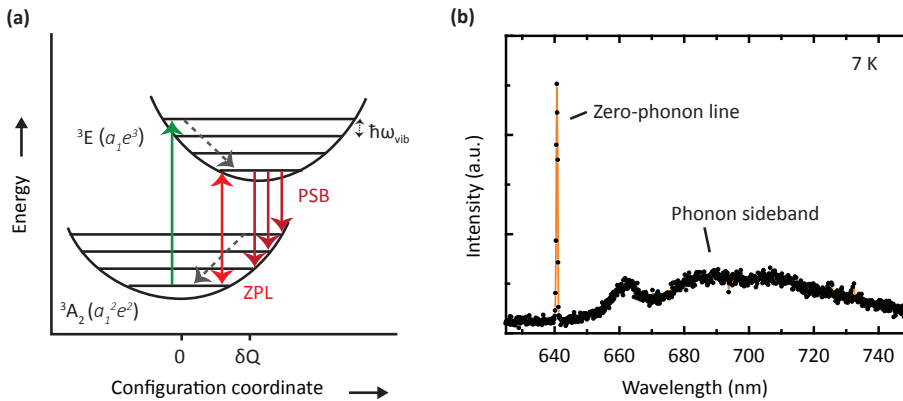


Figure 2.4: Optical transitions via vibrational states. (a) A schematic of the configuration coordinate diagram as in the Huang-Rhys model [12, 37, 38], showing the dependency of energy of the ground and excited state levels 3A_2 and 3E on the effective nuclear coordinates. Electronic transitions are instantaneous compared to the timescale of nuclear movement (the Franck-Condon approximation), corresponding to vertical arrows in the diagram. A transition to an excited vibrational state is accompanied by a rapid decay to the ground state (dashed lines). The main vibronic mode has an energy of $\hbar\omega_{\text{vib}} = 65$ meV [12, 26, 38]. (b) Figure adapted from Van der Sar [39]. The NV emission spectrum at cryogenic temperatures is measured using a spectrometer. At these temperatures the zero-phonon line is narrow, while the phonon sideband is broadened as a result of the short lifetime of the vibrational states it decays to.

probability to excited vibrational levels. The state subsequently non-radiatively decays to the ground vibrational state, corresponding to a displacement of the nuclei to the new equilibrium [12, 37, 38]. The vibronic structure of the orbital states is quantified by the Huang-Rhys factor, that is a measure for the emission into the ZPL. For the NV centre the Huang-Rhys factor is 3.49 at cryogenic temperatures [26], corresponding to a small contribution ($\approx 3\%$) of emission into the ZPL. This branching ratio is known as the Debye-Waller factor.

In the NV spectrum (Fig. 2.4b) this gives rise to a phonon sideband (PSB) next to the direct zero-phonon line (ZPL). The presence of the PSB has several advantages for NV manipulation. It enables off-resonant excitation of the NV centre, commonly used for NV initialization and readout at ambient temperatures. The PSB also enables spectral separation of excitation and detection light during resonant spin-state readout. However, the frequency of the photons emitted into the PSB is not well-defined, making them unsuitable for distant entanglement generation that relies on interference of indistinguishable photons [40]. Instead, for these protocols the ZPL photons are spectrally frequency filtered, at the expense of entangling efficiency [41, 42].

2.3. GROUND STATE SPIN STRUCTURE OF THE NITROGEN-VACANCY CENTRE

The triplet ground state forms the basis of the NV centre as a spin qubit. The Hamiltonian in the presence of a magnetic field is given by:

$$H_{gs} = D_{gs}\sigma_z^2 + \gamma_e \vec{B} \cdot \vec{S}, \quad (2.1)$$

where S_i is i -th the electronic spin-1 Pauli operator, $D_{gs} = 2.88$ GHz is responsible for the zero-field splitting, and \vec{B} is the magnetic field. $\gamma_e = 2\pi \times 2.802$ MHz/G is the electron gyromagnetic ratio. The resulting energy levels as a function of magnetic field are shown in Fig. 2.5a.

Hyperfine coupling to the nitrogen nucleus gives rise to an additional level splitting. This level splitting is dependent on the nitrogen isotope. The ^{14}N isotope has the largest natural abundance (99.6%), and therefore makes up almost all of naturally formed NVs. The ^{15}N isotope has a low natural abundance (the remaining 0.4%), but can be implanted in diamond to form NV centres. The Hamiltonian for the NV with an ^{14}N isotope is described by:

$$H_{N14} = H_{gs} - QI_{N,z}^2 + \gamma_{N14}B_zI_{N,z} - A_{\parallel,N14}S_zI_{N,z} - A_{\perp,N14}(S_xI_{N,x} + S_yI_{N,y}), \quad (2.2)$$

with $I_{N,i}$ the i -components of the nuclear spin-1 Pauli operator, A_{N14} parametrizes the hyperfine coupling, that is separated in a parallel and perpendicular part, and Q is the quadrupole splitting. The nuclear gyromagnetic ratio ($\approx 10^{-4}$ MHz/G) is negligible compared to the quadrupole splitting and hyperfine interactions. In a secular approximation the last terms (proportional to S_x and S_y) are neglected, valid at low magnetic fields where the energy splitting D_{gs} is the dominant energy scale. This range is relevant for the conditions explored in this thesis.

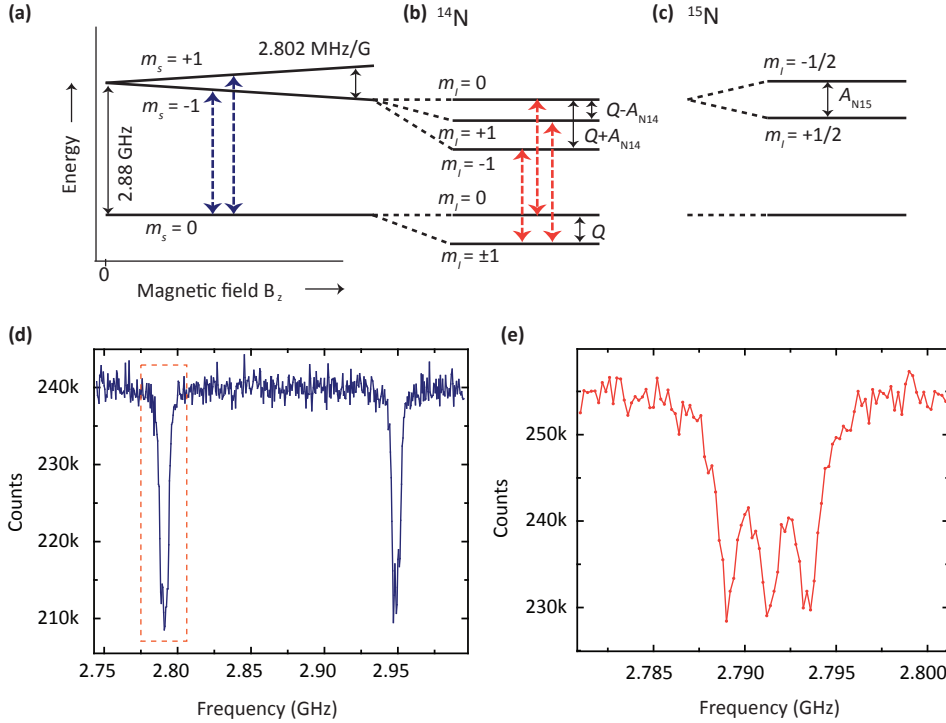


Figure 2.5: Fine structure of the NV spin ground state. Figure adapted from Van der Sar [39]. (a) The electronic $m_s = 0$ and $m_s = \pm 1$ states are split by a zero-field splitting of 2.88 GHz, and subject to further Zeeman splitting under the influence of a magnetic field. (b) The nuclear spin states $m_I = \pm 1$ of the ^{14}N host ($I=1$) are lower in energy compared to the $m_I = 0$ states due to a nuclear quadrupole splitting ($Q = 2\pi \times 4.946$ MHz). For $m_s = -1$ and $m_s = +1$ (not shown) the $m_I = \pm 1$ states are further split by the hyperfine interaction parametrized by $2A_{\parallel, N14} = 2\pi \times 2.1$ MHz. (c) The ^{15}N nuclear spin ($I=1/2$) hyperfine interaction splits the $m_I = \pm 1/2$ state further with a coupling constant $A_{\parallel, N15} = 3.1$ MHz. (d-e) An ODMR measurement using off-resonant excitation shows (d) the splitting of the $m_s = \pm 1$ states as a resulting of an externally applied magnetic field, and (e) the hyperfine structure resulting from coupling to the nitrogen nucleus, in this case a ^{14}N isotope.

In the case of a ^{15}N NV centre (with total nuclear spin $I = 1/2$) the hyperfine coupling is described by:

$$H_{N15} = H_{gs} + \gamma_{N15} B_z \sigma_{N,z} + A_{\parallel,N15} S_z I_{N,z} + A_{\perp,N15} (S_x I_{N,x} + S_y I_{N,y}), \quad (2.3)$$

with \vec{I}_N the spin-1/2 nuclear spin operator. The spin-1/2 ^{15}N does not have a quadrupole splitting, and the gyromagnetic ratio is again small compared to the other effects.

The resulting level structure for ^{14}N and ^{15}N are shown in Fig. 2.5b,c. The distinct hyperfine coupling allows one to distinguish ^{14}N NV centres from ^{15}N NV centres in an optically detected magnetic resonance (ODMR) measurement. The ^{14}N structure shows three hyperfine lines, separated by $A_{\parallel,N14} = 2.1$ MHz (Fig. 2.5e), whereas the ^{15}N shows two dips, separated by $A_{\parallel,N15} = 3.1$ MHz.

The electron spin ground state coherence (T_2^* is several μs at cryogenic temperatures) can be extended through dynamical decoupling sequences to coherence times of one second [43]. The NV can be operated with Rabi frequencies of tens of MHz, allowing for many gate operations within the spin coherence time. Furthermore, hyperfine coupling to the nitrogen and weakly coupled ^{13}C nuclear spins [44–47] unlocks the environment in a function as a quantum processor or for quantum memories [48–52].

2.4. CONTROLLING WEAKLY COUPLED NUCLEAR SPIN STATES

We here present a brief summary of how weakly coupled nuclear spins can be coherently controlled and read out via the electron spin. For a detailed overview we refer to Ref. [53].

The hyperfine interaction of the electron with ^{13}C spins (total spin $I=1/2$) in the environment of the NV centre, creates a dependency of the carbon spin Hamiltonian on the electron spin state. If the electron spin is in the state $m_s = 0$ the nuclear Hamiltonian only depends on an external magnetic field. If the electron spin state is $m_s = \pm 1$ however, the carbon spin state additionally feels the parallel and perpendicular electron hyperfine interaction (see Fig. 2.6). By flipping the electron spin between the $m_s = 0$ and $m_s = -1$ state, the carbon spin can be rotated. The direction of rotation depends on the initial state of the electron spin, which allows - for an appropriately chosen electron spin flipping frequency - to perform controlled rotations on the carbon spin over the full Bloch sphere. An important element of this method is that by flipping the electron spin it is at the same time decoupled from the rest of the spin bath, allowing to preserve coherence during the measurement [44, 46].

These electron-controlled carbon spin rotations can be used to map the carbon spin state onto the electron spin state. The carbon can thus be read out via the electron spin state. Moreover, by concatenating controlled rotations of different carbon spins, it is possible to construct parity measurements that probe a collective observable on the nuclear spins, without revealing information about the individual spin states [50]. These parity measurements are an indispensable tool in for example quantum error correction [50, 51]. In the next chapter we use nuclear spin parity measurements for tests of quantum contextuality.

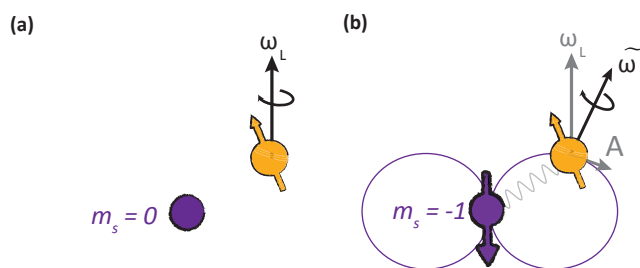


Figure 2.6: Dynamics of a weakly coupled ^{13}C spin. Figure from Cramer [53]. **(a)** When the electron (purple) has spin state $m_s = 0$, the carbon (orange) precesses with the Larmor frequency ω_L determined by an external magnetic field. **(b)** When the electron has spin state $m_s = -1$, the hyperfine interaction components A change the frequency and angle of carbon spin precession. By interleaving situation **(a)** and **(b)** the nuclear spin can be coherently rotated.

REFERENCES

- [1] Ohno, K. *et al.*, *Engineering shallow spins in diamond with nitrogen delta-doping*, Appl. Phys. Lett. **101**, 082413 (2012).
- [2] Pezzagna, S., Naydenov, B., Jelezko, F., Wrachtrup, J. & Meijer, J., *Creation efficiency of nitrogen-vacancy centres in diamond*, New J. Phys. **12**, 065017 (2010).
- [3] Naydenov, B. *et al.*, *Enhanced generation of single optically active spins in diamond by ion implantation*, Appl. Phys. Lett. **96**, 163108 (2010).
- [4] Antonov, D. *et al.*, *Statistical investigations on nitrogen-vacancy center creation*, Appl. Phys. Lett. **104**, 012105 (2014).
- [5] De Oliveira, F. F. *et al.*, *Tailoring spin defects in diamond by lattice charging*, Nat. Commun. **8**, 15409 (2017).
- [6] Davies, G., Lawson, S. C., Collins, A. T., Mainwood, A. & Sharp, S. J., *Vacancy-related centers in diamond*, Phys. Rev. B **46**, 13157 (1992).
- [7] Gruber, A., *Scanning Confocal Optical Microscopy and Magnetic Resonance on Single Defect Centers*, Science **276**, 2012 (1997).
- [8] Twitchen, D. J. *et al.*, *Electron paramagnetic resonance (EPR) and optical absorption studies of defects created in diamond by electron irradiation damage at 100 and 350K*, Phys. B Condens. Matter **273-274**, 628 (1999).
- [9] Chen, Y. C. *et al.*, *Laser writing of coherent colour centres in diamond*, Nat. Photon. **11**, 77 (2017).
- [10] Chen, Y.-C. *et al.*, *Laser writing of individual atomic defects in a crystal with near-unity yield*, arXiv:1807.04028 (2018).
- [11] Jelezko, F. & Wrachtrup, J., *Single defect centres in diamond: A review*, Phys. Status Solidi Appl. Mater. Sci. **203**, 3207 (2006).
- [12] Doherty, M. W. *et al.*, *The nitrogen-vacancy colour centre in diamond*, Phys. Rep. **528**, 1 (2013).
- [13] Acosta, V. & Hemmer, P., *Nitrogen-vacancy centers: Physics and applications*, MRS Bull. **38**, 127 (2013).
- [14] Childress, L. & Hanson, R., *Diamond NV centers for quantum computing and quantum networks*, MRS Bull. **38**, 134 (2013).
- [15] Toyli, D. M., Bassett, L. C., Buckley, B. B., Calusine, G. & Awschalom, D. D., *Engineering and quantum control of single spins in semiconductors*, MRS Bull. **38**, 139 (2013).
- [16] Loncar, M. & Faraon, A., *Quantum photonic networks in diamond*, MRS Bull. **38**, 144 (2013).

- [17] Wrachtrup, J., Jelezko, F., Grotz, B. & McGuinness, L., *Nitrogen-vacancy centers close to surfaces*, MRS Bull. **38**, 149 (2013).
- [18] Hong, S. *et al.*, *Nanoscale magnetometry with NV centers in diamond*, MRS Bull. **38**, 155 (2013).
- [19] Hall, L., Simpson, D. & Hollenberg, L., *Nanoscale sensing and imaging in biology using the nitrogen-vacancy center in diamond*, MRS Bull. **38**, 162 (2013).
- [20] Gao, W. B., Imamoglu, A., Bernien, H. & Hanson, R., *Coherent manipulation, measurement and entanglement of individual solid-state spins using optical fields*, Nat. Photon. **9**, 363 (2015).
- [21] Casola, F., Van Der Sar, T. & Yacoby, A., *Probing condensed matter physics with magnetometry based on nitrogen-vacancy centres in diamond*, Nat. Rev. Mat. **3**, 17088 (2018).
- [22] Pfaff, W., *Quantum Measurement and Entanglement of Spin Quantum Bits in Diamond*, Ph.D. thesis, Delft University of Technology (2013).
- [23] Bernien, H., *Control, measurement and entanglement of remote quantum spin registers in diamond*, Ph.D. thesis, Delft University of Technology (2014).
- [24] Doherty, M. W., Manson, N. B., Delaney, P. & Hollenberg, L. C. L., *The negatively charged nitrogen-vacancy centre in diamond: the electronic solution*, New J. Phys. **13**, 025019 (2011).
- [25] Rogers, L. J., Armstrong, S., Sellars, M. J. & Manson, N. B., *Infrared emission of the NV centre in diamond: Zeeman and uniaxial stress studies*, New J. Phys. **10**, 103024 (2008).
- [26] Kehayias, P. *et al.*, *Infrared absorption band and vibronic structure of the nitrogen-vacancy center in diamond*, Phys. Rev. B **88**, 165202 (2013).
- [27] Goldman, M. L. *et al.*, *Phonon-induced population dynamics and intersystem crossing in nitrogen-vacancy centers*, Phys. Rev. Lett. **114**, 145502 (2015).
- [28] Goldman, M. L. *et al.*, *State-selective intersystem crossing in nitrogen-vacancy centers*, Phys. Rev. B **91**, 165201 (2015).
- [29] Robledo, L. *et al.*, *High-fidelity projective read-out of a solid-state spin quantum register*, Nature **477**, 574 (2011).
- [30] Robledo, L., Bernien, H., van der Sar, T. & Hanson, R., *Spin dynamics in the optical cycle of single nitrogen-vacancy centres in diamond*, New J. Phys. **13**, 025013 (2011).
- [31] Kalb, N., Humphreys, P. C., Slim, J. J. & Hanson, R., *Dephasing mechanisms of diamond-based nuclear-spin memories for quantum networks*, Phys. Rev. A **97**, 062330 (2018).

- [32] Maze, J. R. *et al.*, *Properties of nitrogen-vacancy centers in diamond: The group theoretic approach*, New J. Phys. **13**, 025025 (2011).
- [33] Tamarat, P. *et al.*, *Stark shift control of single optical centers in diamond*, Phys. Rev. Lett. **97**, 083002 (2006).
- [34] Fu, K.-M. C. *et al.*, *Observation of the Dynamic Jahn-Teller Effect in the Excited States of Nitrogen-Vacancy Centers in Diamond*, Phys. Rev. Lett. **103**, 256404 (2009).
- [35] Albrecht, R., Bommer, A., Deutsch, C., Reichel, J. & Becher, C., *Coupling of a single N-V center in diamond to a fiber-based microcavity*, Phys. Rev. Lett. **110**, 243602 (2013).
- [36] Fronik, T., *Homogeneous broadening of the zero-phonon line in the nitrogen-vacancy centre in diamond for all strain regimes*, (2018), B.Sc. thesis.
- [37] Davies, G., *The Jahn-Teller effect and vibronic coupling at deep levels in diamond*, Reports Prog. Phys. **44**, 787 (1981).
- [38] Alkauskas, A., Buckley, B. B., Awschalom, D. D. & Van De Walle, C. G., *First-principles theory of the luminescence lineshape for the triplet transition in diamond NV centres*, New J. Phys. **16**, 073026 (2014).
- [39] van der Sar, T., *Quantum control of single spins and single photons in diamond*, Ph.D. thesis, Delft University of Technology (2012).
- [40] Legero, T., Wilk, T., Kuhn, A. & Rempe, G., *Time-resolved two-photon quantum interference*, Appl. Phys. B **77**, 797 (2003).
- [41] Bernien, H. *et al.*, *Two-photon quantum interference from separate nitrogen vacancy centers in diamond*, Phys. Rev. Lett. **108**, 043604 (2012).
- [42] Sipahigil, A. *et al.*, *Quantum Interference of Single Photons from Remote Nitrogen-Vacancy Centers in Diamond*, Phys. Rev. Lett. **108**, 143601 (2012).
- [43] Abobeih, M. H. *et al.*, *One-second coherence for a single electron spin coupled to a multi-qubit nuclear-spin environment*, Nat. Commun. **9**, 2552 (2018).
- [44] van der Sar, T. *et al.*, *Decoherence-protected quantum gates for a hybrid solid-state spin register*, Nature **484**, 82 (2012).
- [45] Kolkowitz, S., Unterreithmeier, Q. P., Bennett, S. D. & Lukin, M. D., *Sensing distant nuclear spins with a single electron spin*, Phys. Rev. Lett. **109**, 137601 (2012).
- [46] Taminiau, T. H. *et al.*, *Detection and control of individual nuclear spins using a weakly coupled electron spin*, Phys. Rev. Lett. **109**, 137602 (2012).
- [47] Zhao, N. *et al.*, *Sensing single remote nuclear spins*, Nat. Nanotechnol. **7**, 657 (2012).
- [48] Pfaff, W. *et al.*, *Unconditional quantum teleportation between distant solid-state quantum bits*, Science **345**, 532 (2014).

- [49] Waldherr, G. *et al.*, *Quantum error correction in a solid-state hybrid spin register*, *Nature* **506**, 204 (2014).
- [50] Taminiau, T. H., Cramer, J., van der Sar, T., Dobrovitski, V. V. & Hanson, R., *Universal control and error correction in multi-qubit spin registers in diamond*. *Nat. Nanotechnol.* **9**, 171 (2014).
- [51] Cramer, J. *et al.*, *Repeated quantum error correction on a continuously encoded qubit by real-time feedback*, *Nat. Commun.* **7**, 11526 (2016).
- [52] Kalb, N. *et al.*, *Entanglement Distillation between Solid-State Quantum Network Nodes*, *Science* **356**, 928 (2017).
- [53] Cramer, J., *Quantum error correction with spins in diamond*, Ph.D. thesis, Delft University of Technology (2016).



3

MULTIPARTITE ENTANGLEMENT GENERATION AND CONTEXTUALITY TESTS USING NON-DESTRUCTIVE THREE-QUBIT PARITY MEASUREMENTS

**Suzanne van Dam, Julia Cramer, Tim Taminiau, and
Ronald Hanson**

We report on the realization and application of non-destructive three-qubit parity measurements on nuclear spin qubits in diamond. We use high-fidelity quantum logic to map the parity of the joint state of three nuclear spin qubits onto an electronic spin qubit that acts as an ancilla, followed by single-shot non-destructive readout of the ancilla combined with a spin echo on the nuclear spins to ensure outcome-independent evolution. Through the sequential application of three such parity measurements, we demonstrate the generation of genuine multipartite entangled states out of fully mixed states. Furthermore, we implement a single-shot version of the GHZ experiment that can generate a quantum versus classical contradiction in each run. Finally, we test a state-independent non-contextuality inequality in eight dimensions. The techniques and insights developed here are relevant for fundamental tests as well as for quantum information protocols such as quantum error correction.

The results in this chapter are in preparation for submission

3.1. INTRODUCTION

Parity measurements - measurements that reveal whether the sum of a (quantum) bit string is even or odd - are a prime example of the radically different roles of measurement in quantum physics and classical physics. In contrast to classical parity measurements, a quantum parity measurement is able to extract only the parity information from the system without revealing any information about the individual qubit states. Therefore, the coherences within the parity subspace into which the system is projected remain unaffected. Thanks to these unique quantum properties parity measurements are at the heart of quantum information protocols protocols, for example as stabilizer measurements in quantum error correction [1, 2] or to generate entangled states. In addition, their strikingly non-classical behavior features in tests of the foundations of quantum mechanics [3, 4].

Experimentally, realizing parity measurements that project a system on a parity subspace but are otherwise non-destructive is challenging as uncontrolled interactions with the environment as well as crosstalk between system and measurement device lead to leakage of information out of the measured system. Several types of parity measurements have been implemented in circuit quantum electrodynamics, trapped ions and nuclear spins. Two-qubit parity measurements were realised non-destructively and repeatedly [5–8], and were used for pioneering demonstrations of multiple-round quantum error correction [6, 7], to test quantum contextuality [9], and for the preparation and stabilisation of entangled states [5–8, 10–13]. Multi-qubit parity measurements have so far been limited to destructive 4-qubit measurements, which were used as a benchmark for quantum processors [14], or to single non-destructive parity measurements that were used to generate 3-qubit [6], and 4-qubit entangled state [15] out of an initially pure state. However, to generate an entangled state directly out of an initially mixed state requires the repeated application of highly non-destructive multi-qubit parity measurements. Furthermore, the ability to sequentially apply multi-qubit parity measurements would open up new opportunities for quantum error detection and -correction codes and fundamental tests of contextuality.

In this chapter, we realize repeated three-qubit parity measurements on nuclear spin qubits in diamond while minimizing the disturbance of the state of the qubits. We exploit their non-destructive nature to deterministically generate a three-qubit Greenberger-Horne-Zeilinger (GHZ) state from an initially mixed state with three consecutive parity measurements. Finally, we demonstrate the usefulness of these measurements for fundamental tests by performing two quantum contextuality experiments.

3.2. THREE-QUBIT PARITY MEASUREMENTS ON NUCLEAR SPINS IN DIAMOND

We implement the parity measurements on ^{13}C nuclear spins in diamond that are weakly coupled via hyperfine interaction to the electron spin of a nitrogen-vacancy (NV) centre. These nuclear spins are an excellent workhorse for multi-qubit protocols [6, 16, 17] thanks to their long coherence times and their insensitivity to the optical and microwave fields that are used to control the NV centre electron. We use conditional quantum logic to map the parity of multiple nuclear spin onto the electron spin that acts as an ancilla

qubit. The electron is then read out in a single shot [18, 19]. In this way only the parity of the nuclear spin is projected and no information about the individual state of the nuclei is extracted, ensuring the non-destructive nature of the measurement.

The measurement of the spin state is performed by optical excitation of a spin-dependent transition (see Fig. 3.1a). The cycling nature of the transition [20, 21] allows for a high readout fidelity, even for a finite photon detection efficiency. The readout fidelity and the non-destructive nature of the readout are limited by spin-flips during the readout. To maximize non-destructiveness we stop the optical excitation as soon as a photon is detected [6, 19]. The resulting characterisation of assignment fidelity (the probability that the readout yields the correct outcome) and projectiveness (the probability that the state after the measurements corresponds to the assigned state) [22, 23] is shown in Fig. 3.1a.

The nuclear spin state is mapped onto the electron spin using electron-controlled nuclear spin rotations [16] (Fig. 3.1b). We apply sequences of electron π -pulses with the inter-pulse delay tuned to the hyperfine coupling of one of the weakly coupled nuclear spins to induce a rotation, while dynamically decoupling the electron state from the rest of the nuclear spin bath [16]. Because the precession frequency of the nuclei depends on the electron spin state, the nuclear phase needs to be carefully tracked throughout the experiment based on knowledge of the electron spin state. An electron spin flip at an unknown time during the readout consequently dephases the nuclear state [24–26]. We find that this is one of the main sources of disturbance for the nuclear spin state during the parity measurement (see Fig. 3.1b). Additional disturbances are due to imperfections of the electron-controlled gate.

After the electron readout the nuclear spins have undergone extra $\pi/2$ rotations as a result of the electron-controlled gate (that deviate from a standard controlled-NOT gate). To enable consecutive measurements along well-defined axes, we reverse the unitary operations that were used to map the nuclear spin parity onto the ancilla (see Fig. 3.1c). This also resets the electron spin state to the initial state $m_s = 0$, independent of the measurement outcome. The sequence is compiled where possible: we remove unnecessary gates to reduce measurement disturbances and adapt the gates based on the phase accumulated by the nuclear spins.

The phase evolution of the nuclear spins depends on the electron spin readout outcome. This can be accounted for by branching the measurement sequence after each readout, to track the phase acquired for readout outcomes $m_s = 0$ and $m_s = -1$ separately [6] (Fig. 3.1d). However, if each branch is pre-programmed, this leads to memory requirements exponential in the number of measurements. To avoid branching, we implement a spin echo [27] after the readout, such that the phase evolution of each nuclear spin is independent electron readout outcome (see Fig. 3.1e). This removes any measurement outcome-dependence of the remainder of the sequence and is an important step towards more complex protocols with more subsequent readouts, as it reduces the memory required to store measurement sequences from exponential to linear in the number of readouts.

3.3. GENERATION OF GENUINE MULTIPARTITE ENTANGLEMENT

We now use these three-qubit parity measurements for the creation of a maximally entangled three-qubit GHZ state [28] out of an initial mixed state. We consecutively apply

the following three parity measurements:

$$\begin{aligned} M_1 &= \sigma_{x,1} \otimes \sigma_{y,2} \otimes \sigma_{y,3}; \\ M_2 &= \sigma_{y,1} \otimes \sigma_{x,2} \otimes \sigma_{y,3}; \\ M_3 &= \sigma_{y,1} \otimes \sigma_{y,2} \otimes \sigma_{x,3}, \end{aligned} \tag{3.1}$$

where $\sigma_{i,k}$ represents the i -th Pauli matrix on the k -th qubit. These measurements project the three nuclei into one of the eight GHZ states (e.g. $1/\sqrt{2}(|000\rangle + |111\rangle)$), depending on the measurement outcomes. We ensure that the nuclei are in a mixed state before each measurement round by using resonant lasers that induce electron spin-flips and thereby dephase the nuclear spin states.

Each parity measurement contains four or five electron-controlled nuclear spin rotations, that consist of around 40 electron π -pulses per controlled rotation. The total measurement sequence for GHZ state generation and verification spans a total time of approximately 10 ms. The dephasing times of the nuclear spin states are of the same order (t_2^* is 9.9(2) ms, 11.2(3) ms and 17.3(6) ms for Carbon 1, 2, and 3 respectively). However, dephasing is suppressed by the quantum Zeno effect [29, 30]: repeated measurements project the state, restricting its evolution.

Measurements of the non-zero components of the resulting GHZ states on three nuclear spins is shown in Fig. 3.2, for phase-branched measurements. As expected from the readout characterisation, we find that the best fidelity with a GHZ state ($F_{\text{GHZ}} = 0.68 \pm 0.01$) is obtained when positive parity (corresponding to the electron spin state $m_s = 0$) is found three times in a row. Also when obtaining negative parity three times, the nuclear state has a fidelity $F = 0.57 \pm 0.01$, demonstrating genuine multipartite entanglement [31, 32]. The average fidelity for all eight states is 0.634(3). The protocol can thus deterministically generate a multipartite entangled state, as the long coherence times enable the application of feedback based on the measurement outcomes [6].

Phase echoed measurements (data not shown) give an average fidelity of 0.600(3). We attribute the slight decrease in fidelity for the phase echoed protocol to imperfect calibration of the nuclear precession frequency and imperfections in the electron echo pulse. We note that the good performance of the phase echoed implementation is promising as it enables extending to more complex protocols with more subsequent measurements, as required for e.g. quantum error correction.

3.4. QUANTUM CONTEXTUALITY EXPERIMENTS

We next use the sequential non-destructive parity measurement for a quantum contextuality experiment. Quantum contextuality goes against the classical notion of noncontextuality: that a measurement outcome should not depend on which other compatible measurements are done jointly. Measurements are compatible if they can be measured jointly without disturbing each other's measurement outcome, i.e. observables A and B are compatible if measuring consecutively A-B-A gives twice the same outcome for A.

These classical versus quantum contradictions can be probed experimentally in a GHZ test [28]. In the original version of this test a system is prepared in a GHZ state and four sets of observables are measured: the three observables described in Eq. (3.1), and

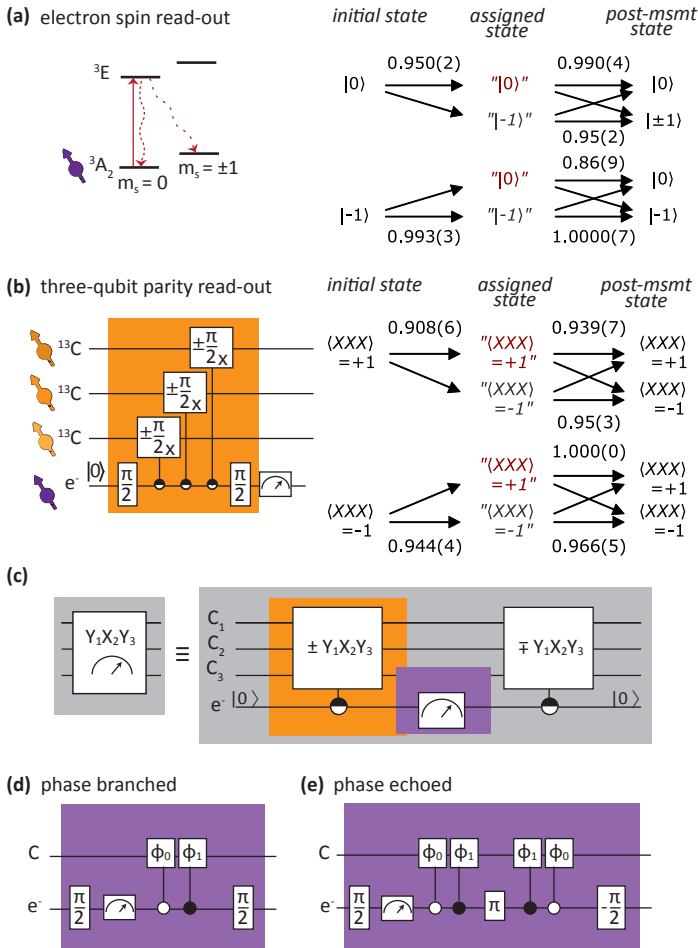


Figure 3.1: Three-qubit quantum parity measurements. (a) The NV electron spin is read out in a single shot using spin-selective optical excitation. The readout fidelity and projectiveness are obtained with a maximum-likelihood estimation on raw data from two repeated readouts. The data is analyzed assuming an electron spin initialisation of 0.998 ± 0.002 and 0.995 ± 0.005 for the $m_s = 0$ and $m_s = -1$ spin states respectively. (b) ^{13}C nuclear spins are initialized and read out using the electron as ancilla. Here, the positive (negative) parity subspace $\langle XXX \rangle$ ($-\langle XXX \rangle$) is mapped onto electron state $|m_s = 0\rangle$ ($|m_s = -1\rangle$). The readout fidelity and projectiveness are obtained with a maximum-likelihood estimation on raw data from three repeated readouts on an initially mixed state. Coherent errors are not tracked. (c) After the parity readout an inverse unitary operation undoes remaining rotations on the nuclear spins, needed to perform the next parity measurement. (d) In the conventional parity measurement [6], nuclear phases acquired when reading out $m_s = 0$ ($\phi_C = \phi_0$) or $m_s = -1$ ($\phi_C = \phi_1$) are separately tracked (nuclear phase accumulation is explicitly shown as conditional-phase gates). (e) Using an echo on the electron spin state, the nuclear states acquire a phase $\phi_C = \phi_0 + \phi_1$, that is independent of the measurement outcome.

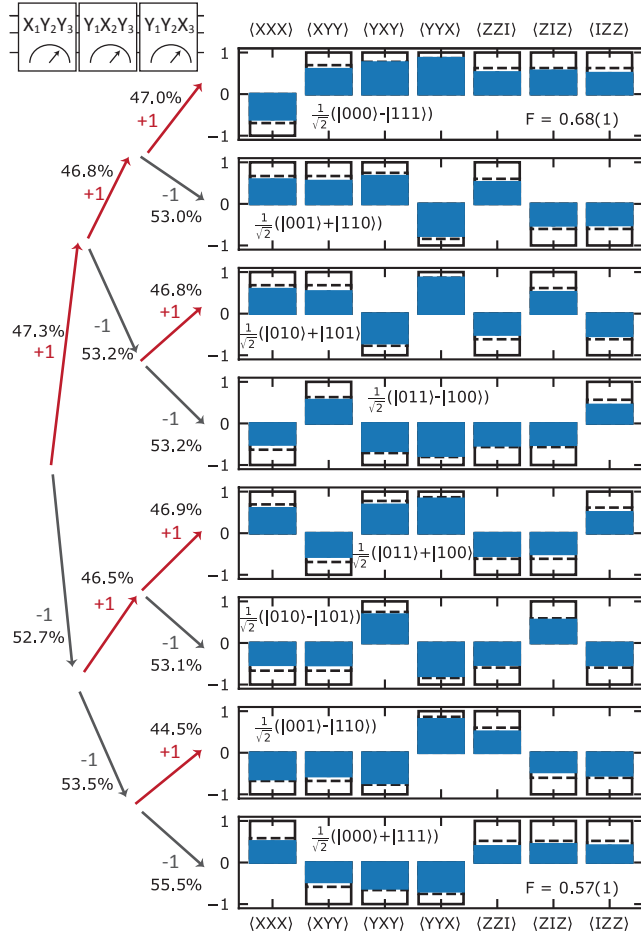


Figure 3.2: Creating a GHZ state out of an initially mixed state. Conditional on the outcomes of three consecutive parity measurements one out of eight maximally entangled GHZ states is created out of an initially mixed state. To obtain the best estimate for the nuclear state the final readout is corrected for electron spin readout infidelity. Positive parity is mapped onto the $m_s = 0$ electron state during the measurements, such that the electron readout asymmetry results in the highest state fidelity for $\frac{1}{\sqrt{2}}(|000\rangle - |111\rangle)$. The data shown here (blue bars) is obtained using phase-branched measurements. Black lines indicate the ideal outcome for a GHZ state, and black dashed lines are the outcome of a simulation with independently characterised parameters.

a fourth observable,

$$M_4 = \sigma_{x,1} \otimes \sigma_{x,2} \otimes \sigma_{x,3}. \quad (3.2)$$

If we measure the first three sets of observables on the GHZ state $\sqrt{1/2}(|000\rangle + |111\rangle)$, we would, for ideal measurements, get the outcomes $(M_1, M_2, M_3) = (+1, +1, +1)$. Given these three outcomes, a noncontextual theory predicts $M_4 = +1$. But quantum theory predicts $M_4 = -1$, thus showing a maximal contradiction with noncontextual models [28].

In previous experiments the observables M_j ($j = 1, \dots, 4$) were implemented as classical parity measurements: each qubit is measured individually and the parity calculated. Because these measurements do not preserve coherences between the individual qubit and therefore do not preserve the quantum state, each measurement M_j is performed separately on newly prepared GHZ states. In that case the result can be formalized into an inequality as done by Mermin [33]. This GHZ experiment can probe quantum nonlocality, and has been implemented in local [34–37] and distant setups [38, 39].

An interesting variation of the GHZ experiment has been proposed in which the measurements M_j are performed as sequential quantum parity measurements [40, 41] (see Fig. 3.3a). In such an implementation, a maximal quantum versus classical contradiction is obtained in every single measurement run, since a non-contextual theory predicts $\langle M_1 \times M_2 \times M_3 \times M_4 \rangle = 1$, while quantum theory gives $\langle M_1 \times M_2 \times M_3 \times M_4 \rangle = -1$. This single-shot form of the GHZ experiment is state-independent: the input of the measurement sequence does not have to be a maximally entangled GHZ state, but can be any state, even a mixed state. State-independence can be distinctly present in quantum contextuality tests [9, 42–50] while tests of quantum nonlocality require the preparation of a specific (entangled) state.

We realize the single-shot GHZ experiment using parity measurements on nuclear spins both with the conventional phase-branched and new phase-echoed readout methods. We find non-classical results with both readout methods: $\langle M_1 \times M_2 \times M_3 \times M_4 \rangle = -0.58(6)$ and $-0.55(7)$, as shown in Fig. 3.3b-c. The similar performance of the phase-echoed and phase-branched methods underlines the suitability of the phase-echoed method.

With the implementation of the GHZ experiment we assume that the parity measurements probe the individual underlying observables, e.g. that $\sigma_{x,1} \otimes \sigma_{y,2} \otimes \sigma_{y,3}$ probes $\sigma_{x,1}$, $\sigma_{y,2}$, and $\sigma_{y,3}$. The experiment can be extended to explicitly measure this. This is done by measuring four additional contexts (Fig. 3.4a), testing a noncontextuality inequality (NCI) as proposed by Cabello [51]:

$$\begin{aligned} C &= \langle C_1 \rangle + \langle C_2 \rangle + \langle C_3 \rangle + \langle C_4 \rangle - \langle C_5 \rangle \leq 3; \\ C_1 &= \sigma_{x,1} \times \sigma_{y,2} \times \sigma_{y,3} \times M_1; \\ C_2 &= \sigma_{y,1} \times \sigma_{x,2} \times \sigma_{y,3} \times M_2; \\ C_3 &= \sigma_{y,1} \times \sigma_{y,2} \times \sigma_{x,3} \times M_3; \\ C_4 &= \sigma_{x,1} \times \sigma_{x,2} \times \sigma_{x,3} \times M_4; \\ C_5 &= M_1 \times M_2 \times M_3 \times M_4. \end{aligned} \quad (3.3)$$

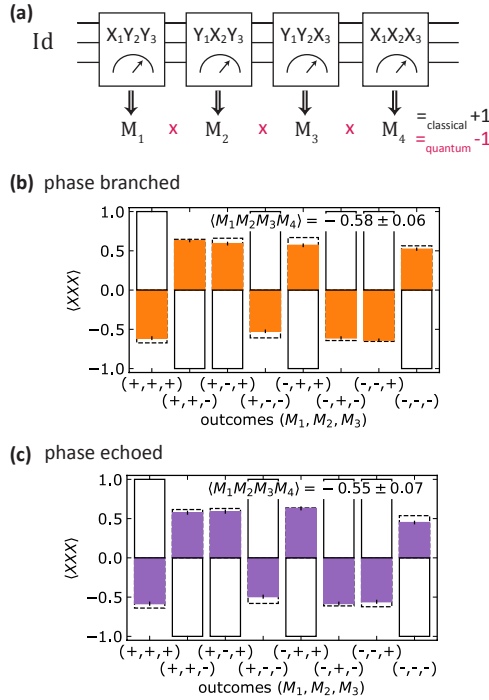


Figure 3.3: A single-shot GHZ experiment. (a) For the consecutive application of four parity measurements a quantum versus classical contradiction is predicted in each measurement run. (b-c) Both the phase branched (orange bars) and phase echoed implementations (purple bars) of the protocol lead to a non-classical result. Black lines indicate the classically expected outcomes, black dashed lines are the expected result from simulations with independently characterised parameters.

The bound of 3 is dictated by noncontextual models, while for an ideal quantum system, with perfectly non-destructive quantum parity measurements, $C = 5$ is predicted. Like the single-shot GHZ experiment, this NCI is state-independent. To test it requires the application of four consecutive three-qubit parity measurements in an eight-dimensional system. So far, the highest-dimensional state-independent NCI that has been tested features three sequential two-qubit parity measurements in a four-dimensional system [9].

We implement the noncontextuality inequality using the phase-echoed nuclear spin parity measurements (see Fig. 3.4b) and observe a violation of the noncontextual bound: $C = 3.14 \pm 0.02$, rejecting the hypothesis that nature is governed by a non-contextual model with a p-value of 1.58×10^{-11} [52]. We note that to reach this result we assume measurement compatibility [53]. Since we efficiently detect the observables, no fair sampling assumption is necessary. With improved experimental parameters, e.g. using refocusing pulses on the nuclear spin states, decoherence-protected subspaces [54] or isotopic purification of the nuclear environment [55], an experiment may be designed in which measurement compatibility can be addressed [53].

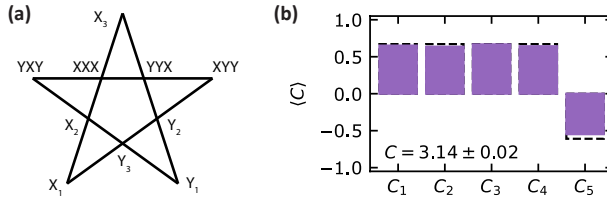


Figure 3.4: A noncontextuality test in 8 dimensions. (a) A schematic representation of the five contexts in the non-contextuality inequality as described in Eq. (3.3). (b) Implementation of the noncontextuality inequality on nuclear spins in diamond, showing a violation of the inequality bound ($C \leq 3$).

3.5. CONCLUSIONS

In conclusion, we realized non-destructive three-qubit parity measurements on nuclear spins in diamond. We use a readout echo pulse to prevent nuclear phase branching, enabling memory-efficiency implementation of sequential measurements. We apply three-qubit parity measurements on an initially mixed state to generate genuine multipartite entanglement, and we realize a test of quantum contextuality in a single-shot. Furthermore, we show the implementation of noncontextuality tests in a higher-dimensional system than previously reported. The techniques and insights developed here can be directly applied to parity-measurement-based quantum computing protocols such as quantum error correction [1, 2, 6].

ACKNOWLEDGEMENTS

We thank M. Abobeih, C. Bradley, N. Bultink, A. Cabello, K. Goodenough, P. Humphreys, N. Kalb, and M.A. Rol for helpful discussions. We acknowledge support from the Netherlands Organisation for Scientific Research (NWO) through a VICI grant, the European Research Council through a Synergy Grant, and the Royal Netherlands Academy of Arts and Sciences and Ammodo through an Ammodo KNAW Award.

REFERENCES

- [1] Bravyi, S. B. & Kitaev, A. Y., *Quantum codes on a lattice with boundary*, arXiv:quant-ph/9811052 (1998).
- [2] Raussendorf, R. & Harrington, J., *Fault-tolerant quantum computation with high threshold in two dimensions*, Phys. Rev. Lett. **98**, 1 (2007).
- [3] Bell, J. S., *On the problem of hidden variables in quantum mechanics*, Rev. Mod. Phys. **38**, 447 (1966).
- [4] Kochen, S. & Specker, E., *The problem of hidden variables in quantum mechanics*, J. Math. Mech. **17**, 59 (1967).
- [5] Sun, L. *et al.*, *Tracking photon jumps with repeated quantum non-demolition parity measurements*, Nature **511**, 444 (2014).

- [6] Cramer, J. *et al.*, *Repeated quantum error correction on a continuously encoded qubit by real-time feedback*, Nat. Commun. **7**, 11526 (2016).
- [7] Kelly, J. *et al.*, *State preservation by repetitive error detection in a superconducting quantum circuit*, Nature **519**, 66 (2015).
- [8] Negnevitsky, V. *et al.*, *Repeated multi-qubit readout and feedback with a mixed-species trapped-ion register*, Nature **563**, 527 (2018).
- [9] Kirchmair, G. *et al.*, *State-independent experimental test of quantum contextuality*, Nature **460**, 494 (2009).
- [10] Risté, D. *et al.*, *Deterministic entanglement of superconducting qubits by parity measurement and feedback*, Nature **502**, 350 (2013).
- [11] Pfaff, W. *et al.*, *Demonstration of entanglement-by-measurement of solid-state qubits*, Nat. Phys. **9**, 29 (2013).
- [12] Saira, O. *et al.*, *Entanglement Genesis by Ancilla-Based Parity Measurement in 2D Circuit QED*, Phys. Rev. Lett. **112**, 070502 (2014).
- [13] Chow, J. M. *et al.*, *quantum computing fabric*, Nat. Commun. **5**, 4015 (2014).
- [14] Takita, M. *et al.*, *Demonstration of weight-four parity measurements in the surface code architecture*, Phys. Rev. Lett. **117**, 210505 (2016).
- [15] Barreiro, J. T. *et al.*, *An open-system quantum simulator with trapped ions*. Nature **470**, 486 (2011).
- [16] Taminiau, T. H., Cramer, J., van der Sar, T., Dobrovitski, V. V. & Hanson, R., *Universal control and error correction in multi-qubit spin registers in diamond*. Nat. Nanotechnol. **9**, 171 (2014).
- [17] Waldherr, G. *et al.*, *Quantum error correction in a solid-state hybrid spin register*, Nature **506**, 204 (2014).
- [18] Robledo, L. *et al.*, *High-fidelity projective read-out of a solid-state spin quantum register*, Nature **477**, 574 (2011).
- [19] Blok, M. S. *et al.*, *Manipulating a qubit through the backaction of sequential partial measurements and real-time feedback*, Nat. Phys. **10**, 189 (2014).
- [20] Tamarat, P. *et al.*, *Spin-flip and spin-conserving optical transitions of the nitrogen-vacancy centre in diamond*, New J. Phys. **10**, 045004 (2008).
- [21] Robledo, L., Bernien, H., van der Sar, T. & Hanson, R., *Spin dynamics in the optical cycle of single nitrogen-vacancy centres in diamond*, New J. Phys. **13**, 025013 (2011).
- [22] Lupaşcu, A. *et al.*, *Quantum non-demolition measurement of a superconducting qubit*, AIP Conf. Proc. **1074**, 26 (2008).

- [23] Ristè, D., van Leeuwen, J. G., Ku, H. S., Lehnert, K. W. & Dicarlo, L., *Initialization by measurement of a superconducting quantum bit circuit*, Phys. Rev. Lett. **109**, 050507 (2012).
- [24] Blok, M. S., Kalb, N., Reiserer, A., Taminiou, T. H. & Hanson, R., *Towards quantum networks of single spins: Analysis of a quantum memory with an optical interface in diamond*, Faraday Discuss. **184**, 173 (2015).
- [25] Reiserer, A., *Robust Quantum-Network Memory Using Decoherence-Protected Subspaces of Nuclear Spins*, Phys. Rev. X **6**, 021040 (2016).
- [26] Kalb, N., Humphreys, P. C., Slim, J. J. & Hanson, R., *Dephasing mechanisms of diamond-based nuclear-spin memories for quantum networks*, Phys. Rev. A **97**, 062330 (2018).
- [27] Hahn, E., *Spin Echoes*, Physical Review **80**, 580 (1950).
- [28] Greenberger, D. M., Horne, M. A., Shimony, A. & Zeilinger, A., *Bell's theorem without inequalities*, Am. J. Phys. **58**, 1131 (1990).
- [29] Misra, B. & Sudarshan, E. C. G., *The Zeno's paradox in quantum theory*, J. Math. Phys. **18**, 756 (1977).
- [30] Kalb, N. *et al.*, *Experimental creation of quantum Zeno subspaces by repeated multi-spin projections in diamond*, Nat. Commun. **7**, 1 (2016), arXiv:1603.03368 .
- [31] Acín, A., Bruß, D., Lewenstein, M. & Sanpera, A., *Classification of mixed three-qubit states*, Phys. Rev. Lett. **87**, 040401 (2001).
- [32] Bourennane, M. *et al.*, *Experimental Detection of Multipartite Entanglement using Witness Operators*, Phys. Rev. Lett. **92**, 087902 (2004).
- [33] Mermin, N. D., *Extreme quantum entanglement in a superposition of macroscopically distinct states*, Phys. Rev. Lett. **65**, 1838 (1990).
- [34] Laflamme, R., Knill, E., Zurek, W., Catasti, P. & Mariappan, S. V. S., *NMR Greenberger-Horne-Zeilinger states*, Phil. Trans. R. Soc. Lond. A **356**, 1941 (1998).
- [35] Dicarlo, L. *et al.*, *Preparation and measurement of three-qubit entanglement in a superconducting circuit*. Nature **467**, 574 (2010).
- [36] Neeley, M. *et al.*, *Generation of three-qubit entangled states using superconducting phase qubits*. Nature **467**, 570 (2010).
- [37] Lanyon, B. P. *et al.*, *Experimental violation of multipartite bell inequalities with trapped ions*, Phys. Rev. Lett. **112**, 1 (2014).
- [38] Pan, J.-W., Bouwmeester, D., Daniell, M., Weinfurter, H. & Zeilinger, A., *Experimental test of quantum nonlocality in three-photon Greenberger-Horne-Zeilinger entanglement*, Nature **9**, 515 (2000).

- [39] Erven, C. *et al.*, *Experimental three-photon quantum nonlocality under strict locality conditions*, Nat. Photon. **8**, 292 (2014).
- [40] Lloyd, S., *Microscopic analogs of the Greenberger-Horne-Zeilinger experiment*, Phys. Rev. A **57**, R1473 (1998).
- [41] Laloe, F., *Do we really understand quantum mechanics?* (Cambridge University Press, 2012).
- [42] Amselem, E., Rådmark, M., Bourennane, M. & Cabello, A., *State-Independent Quantum Contextuality with Single Photons*, Phys. Rev. Lett. **103**, 160405 (2009).
- [43] Moussa, O., Ryan, C. A., Cory, D. G. & Laflamme, R., *Testing Contextuality on Quantum Ensembles with One Clean Qubit*, Phys. Rev. Lett. **104**, 160501 (2010).
- [44] Zu, C. *et al.*, *State-independent experimental test of Quantum contextuality in an indivisible system*, Phys. Rev. Lett. **109**, 150401 (2012).
- [45] Huang, Y. F. *et al.*, *Experimental test of state-independent quantum contextuality of an indivisible quantum system*, Phys. Rev. A **87**, 1 (2013).
- [46] D'Ambrosio, V. *et al.*, *Experimental Implementation of a Kochen-Specker Set of Quantum Tests*, Phys. Rev. X **3**, 011012 (2013).
- [47] Zhang, X. *et al.*, *State-independent experimental test of quantum contextuality with a single trapped ion*, Phys. Rev. Lett. **110**, 070401 (2013).
- [48] Cañas, G. *et al.*, *Experimental implementation of an eight-dimensional Kochen-Specker set and observation of its connection with the Greenberger-Horne-Zeilinger theorem*, Phys. Rev. A **90**, 012119 (2014).
- [49] Cañas, G. *et al.*, *Applying the simplest kochen-specker set for quantum information processing*, Phys. Rev. Lett. **113**, 090404 (2014).
- [50] Leupold, F. M. *et al.*, *Sustained state-independent quantum contextual correlations from a single ion*, Phys. Rev. Lett. **120**, 180401 (2018).
- [51] Cabello, A., *Experimentally Testable State-Independent Quantum Contextuality*, Phys. Rev. Lett. **101**, 210401 (2008).
- [52] Elkouss, D. & Wehner, S., *(Nearly) optimal P values for all Bell inequalities*, npj Quantum Inf. **2**, 16026 (2016).
- [53] Gühne, O. *et al.*, *Compatibility and noncontextuality for sequential measurements*, Phys. Rev. A **81**, 022121 (2010).
- [54] Reiserer, A. *et al.*, *Robust quantum-network memory using decoherence-protected subspaces of nuclear spins*, Phys. Rev. X **6**, 1 (2016).
- [55] Bar-Gill, N., Pham, L. M., Jarmola, A., Budker, D. & Walsworth, R. L., *Solid-state electronic spin coherence time approaching one second*, Nat. Commun. **4**, 1743 (2013).

4

PURCELL ENHANCEMENT IN DIAMOND-AIR FABRY-PÉROT MICROCAVITIES

The probability that an NV centre emits a coherent photon after optical excitation can be enhanced by embedding the NV in an optical cavity, benefiting from Purcell enhancement. In this chapter we first describe the enhancement of the spontaneous emission rate via the Purcell effect in section 4.1. Next, we give an overview of the possible experimental cavity platforms in which Purcell enhancement of the NV can be established in section 4.2. We then describe in section 4.3 the cavities that we believe are very well suited for Purcell enhancement of the NV in a quantum network: a Fabry-Pérot microcavity with an embedded diamond membrane.

4.1. AN EFFICIENT OPTICAL INTERFACE THROUGH PURCELL ENHANCEMENT

For application in quantum networks we desire to enhance the relative emission of photons from the NV excited state into the zero-phonon line (ZPL), compared to the phonon sideband (PSB). In this section we discuss which factors determine this emission rate, and how the desired enhancement can be achieved by embedding the NV in an optical cavity.

4.1.1. TRANSITION RATES FOR A GENERAL EMITTER

In a general quantum mechanical system, following the basic rules of quantum mechanics [1], the transition rate between two of the system's eigenstates $|\phi_n\rangle$ is zero. A transition in such a system is only possible if there is an external disturbance that modifies the Hamiltonian such that $|\phi_n\rangle$ are no longer good eigenstates. For a system like the NV centre, or more general an emitter, the vacuum electric field takes up this role to enable spontaneous transitions from the excited state to the ground state. In the electric dipole approximation, the coupling between vacuum electric field and an emitter can be described by [2, 3]:

$$\hat{H}_{int} = -\vec{d} \cdot \vec{E}, \quad (4.1)$$

with \vec{d} the electric dipole moment of the electronic transition, and \vec{E} the electric field.

The transition rate for the disturbance can be determined using time-dependent perturbation theory. We will not go into the details of the derivation, but refer to the many accounts that can be found in literature, for example [1, 3]. The result is Fermi's golden rule, that is given by:

$$\Gamma_{e \rightarrow g} = \frac{2\pi}{\hbar^2} |\langle f | \hat{H}_{int} | i \rangle|^2 D(\omega), \quad (4.2)$$

where $|i\rangle$ is the initial state in which the emitter is in the excited state and there is an electric field vacuum ($|e\rangle \otimes |0\rangle$) and $|f\rangle$ is the final state, containing the emitter in the ground state and a single photon of energy $\hbar\omega$: $|g\rangle \otimes |1_{\hbar\omega}\rangle$. $D(\omega)$ is the photon density of states at the transition frequency ω . Analysing the operation of the quantized electric field on the electric field vacuum state and the transition matrix element of the electric dipole [3], one can find that the rate is given by:

$$\Gamma_{e \rightarrow g} = \frac{\pi\omega}{\hbar\epsilon_0 V_0} \mu_{ge}^2 |\hat{d} \cdot \hat{e}|^2 D(\omega) \equiv 2\pi g^2 D(\omega) |\hat{d} \cdot \hat{e}|^2, \quad (4.3)$$

where \hat{e} is the electric field polarisation. A factor $\frac{\hbar\omega}{2V_0\epsilon_0}$ originates from the electric field quantization, where V_0 is the quantization volume and ϵ_0 the vacuum permittivity. We further have $\mu_{ge}\hat{d} = \langle g | \vec{d} | e \rangle$, the transition matrix element. In Eq. (4.3) we have defined g to quantify the emitter-field coupling [4]:

$$g \equiv \sqrt{\frac{\omega \mu_{ge}^2}{2\hbar\epsilon_0 V_0}}. \quad (4.4)$$

In free space the average over all relative orientations of dipole \hat{d} and electric field polarization \hat{e} is $|\hat{d} \cdot \hat{e}|^2 = 1/3$. Further the photon density of states in free space is given

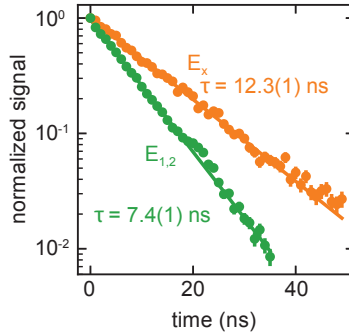


Figure 4.1: NV excited state lifetime. Figure from Kalb et al. [6]. The spontaneous emission rate from the NV triplet excited ground state can be found from the lifetime of the E_x state. The lifetime of the $E_{1,2}$ is reduced as the result of an additional decay channel to the singlet states.

by [5]:

$$D(\omega) = \frac{\omega^2 V_0 n^3}{\pi^2 c^3}, \quad (4.5)$$

where we again use a quantization volume V_0 , c is the speed of light and n is the refractive index of the material in which the emitter is embedded. When we use this in Eq. (4.3) we find the spontaneous emission rate for an emitter in free space:

$$\Gamma_{\text{free space}} = \frac{n^3 \omega^3}{c^3} \frac{\mu_{eg}^2}{3\pi \hbar \epsilon_0}. \quad (4.6)$$

4.1.2. TRANSITION RATES FOR THE NV CENTRE

As described in section 2.2.2 the NV centre can decay not only directly, in the zero-phonon line (ZPL) but also via vibrational states in the phonon sideband (PSB). The transition rate for each of these transitions can be described by Eq. (4.3), where the transition dipole moment includes the overlap between the vibrational states. For each transition the density of states has to be evaluated at the frequency of the emitted photon in that specific transition. The total rate is the sum of all individual transition rates. Separating the ZPL and PSB explicitly, the total decay rate is given by $\Gamma_{tot} = \Gamma_{ZPL} + \Gamma_{PSB}$.

Experimentally, this total rate can be found from the inverse of the lifetime of the E_x (or E_y) excited state (Fig. 4.1): $\Gamma_{tot}^{-1} = 12.3(1)$ ns. Using the Debye-Waller factor for the NV (Fig. 2.4) we further know that $\Gamma_{ZPL}/\Gamma_{tot} = 0.03$. From this we can determine that $\Gamma_{ZPL} = (410 \text{ ns})^{-1}$ and $\Gamma_{PSB} = (12.7 \text{ ns})^{-1}$.

For the A_1 and $E_{1,2}$ excited states there are additional transitions via the singlet states. For these transitions the total decay rate is given by $\Gamma_{ZPL} + \Gamma_{PSB} + \Gamma_{ISC}$. The resulting difference in excited state lifetime between the E_x state whose decay is effectively only directly to the ground triplet state, and $E_{1,2}$ that also decays via the singlet state is found experimentally (see Fig. 4.1).

4.1.3. MODIFICATION OF THE TRANSITION RATE THROUGH THE PURCELL EFFECT

We want to make the NV centre a more efficient coherent emitter by enhancing the branching ratio (β) into the ZPL:

$$\beta = \frac{\Gamma_{ZPL}}{\Gamma_{ZPL} + \Gamma_{PSB}}. \quad (4.7)$$

This can be achieved by increasing Γ_{ZPL} . Fermi's golden rule indicates that we can do this by modifying the density of states at the transition frequency ω_{ZPL} . This can be achieved with an optical cavity. We here provide the key aspects of optical cavities that are required to understand the interaction of a cavity and an embedded emitter. In section 4.3 a more detailed analysis of optical cavities is provided.

An elementary optical cavity consists of two reflecting surfaces separated by a distance L_{cav} . In the direction of the cavity, the electromagnetic field only interferes constructively if the cavity length is a multiple of the half wavelength of the mode, i.e. if

$$L_{cav} = m \frac{\lambda}{2} = m \frac{c}{2n\nu}. \quad (4.8)$$

Here we use $\lambda = c/n\nu$, with λ the wavelength and ν the frequency of the mode, and n the refractive index of the material in the cavity. m is the mode number: the number of times the half wavelength fits in the cavity. The frequency separation of the modes m and $m + 1$ for a fixed cavity length can be found from Eq. (4.8). It is referred to as the free spectral range (ν_{FSR}):

$$\nu_{FSR} = \frac{c}{2nL_{cav}}. \quad (4.9)$$

The resonant modes form a repeating pattern in frequency space. The density of states of an optical cavity follows this same repeating pattern. For an ideal cavity the modes consist of a single frequency. However, in reality, the mode has a finite lifetime as a result of losses in the optical cavity such as a finite mirror reflectivity. The decay of the cavity mode is parametrized by a decay rate κ . A finite decay rate manifests as a frequency broadening of the cavity mode. The Fourier transform of the exponential decay gives a Lorentzian shaped spectral line around the resonance frequency ν_0 with a full width at half maximum (FWHM) $\delta\nu$ of:

$$\delta\nu = \frac{\kappa}{2\pi}. \quad (4.10)$$

The density of states in an optical cavity is thus given by equally spaced Lorentzians with a finite linewidth $\delta\nu$, as shown in Fig. 4.2. Each resonance contains a single mode so we normalise each Lorentzian, finding for a mode around $\nu_0 = \omega_0/(2\pi)$ that the density of state is [5]:

$$D_{cav}(\omega) = \frac{1}{2} \frac{\delta\omega_0/2}{(\omega - \omega_0)^2 + (\delta\omega_0/2)^2}. \quad (4.11)$$

The maximum spontaneous emission rate (Eq. (4.3)) of an emitter in a cavity, is found when the cavity and emitter frequency are on resonance ($\omega = \omega_0$), such that $D_{cav}(\omega_0) = 2/(\pi\delta\omega) = 1/(\pi^2\delta\nu)$.

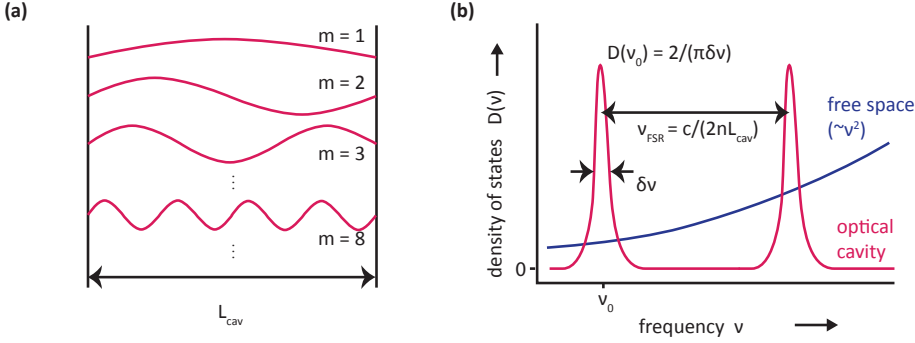


Figure 4.2: Resonant modes of an optical cavity. (a) The resonant modes of an optical cavity satisfy Eq. (4.8), as consistent with having field antinodes at the interfaces of ideal mirrors. (b) The density of states of an optical cavity shows resonances at the frequencies set by Eq. (4.8). The linewidth is determined by the finite decay rate of the cavity mode as a result of intracavity losses ($\delta\nu = \kappa/(2\pi)$). The density of states at a resonance can be larger than the density of states in free space, resulting in enhanced spontaneous emission rate of an emitter that emits at this frequency: the Purcell effect (Eq. (4.12)).

We can compare the emission rate of an emitter in free space to an emitter in the cavity by comparing Eq. (4.11) to Eq. (4.5). To get the full effect we should also take into account that in the cavity the field mode has a specific polarisation \hat{e} such that overlap between dipole and field is $\xi^2 = |\hat{e} \cdot \hat{d}|^2$, while in free space it averaged out to $1/3$. The enhancement of the emission rate through an altered density of states is known as the Purcell effect [7], and described by the Purcell factor [5, 8]:

$$F_p = \frac{\Gamma_{\text{cav}}}{\Gamma_{\text{free space}}} = \frac{\xi^2}{1/3} \frac{D_{\text{cav}}(\omega_0)}{D(\omega_0)} = 3\xi^2 \frac{1}{\pi^2 \delta\nu} \frac{4V_0 c^3}{n^3 \nu^2} = \xi^2 \frac{3Q}{4\pi^2 V_0} \frac{c^3}{n^3 \nu^3}, \quad (4.12)$$

where for V_0 we should now take the cavity mode volume. In the last step we have used

$$Q = \frac{\nu}{\delta\nu} \quad (4.13)$$

to show the Purcell factor in the form in which it is commonly presented. Q is the quality factor of the optical cavity, representing the number of optical cycles in the cavity before the field mode energy decays to $1/e$ of the initial value. If the Purcell factor is larger than unity the embedding of the emitter in the cavity increases the transition rate. Eq. (4.12) shows that the Purcell enhancement is largest for high quality factors and small mode volumes.

4.1.4. THE PURCELL EFFECT FOR THE NV CENTRE

The previous section described the Purcell effect for an emitter with a single transition with a linewidth that is much narrower than the cavity linewidth. For isolated atoms in a cavity this condition is often satisfied. However, the NV centre, that is embedded in a solid state environment, can have significant broadened linewidths. How does this influence the Purcell enhancement of the ZPL and PSB transitions?

At cryogenic temperatures and in a low-defect environment, the NV ZPL transitions can have narrow linewidths. For the ZPL the assumption that the emitter linewidth (near the lifetime-limited value of ≈ 13 MHz) is much narrower than the cavity linewidth (on the order of a GHz for the cavities in this thesis) thus holds. We can describe the Purcell effect of an optical cavity on the NV ZPL by Eq. (4.12).

However, the optical lines of the PSB transitions are broadened as a result of the short lifetime of the vibrational states (section 2.2.2). The resulting linewidths in this case are ≈ 80 THz [9]. To account for this in the Purcell factor, the cavity quality factor Q should be replaced by an effective quality factor [10]:

$$\frac{1}{Q_{\text{eff}}} = \frac{1}{Q_{\text{cav}}} + \frac{1}{Q_{\text{em}}}, \quad (4.14)$$

where $Q_{\text{em}} = \nu/\delta\nu_{\text{em}}$, with ν the transition frequency, and $\delta\nu_{\text{em}}$ the broadened emitter linewidth. As the effective quality factor is low ($Q_{\text{em}} \approx 6$), Purcell enhancement of the PSB transitions only occurs for a cavity with a very low mode volume. The mode volume required to achieve a Purcell factor $F_p > 1$ for the PSB is $V_0 < 7\lambda^3$ [11]. The regime of mode volumes considered in this thesis is much larger, such that the PSB transitions are not enhanced by the cavity.

4.1.5. BRANCHING RATIO INTO THE ZPL

We here analyze how the enhancement of the branching ratio of emission into the ZPL is influenced by Purcell enhancement of the NV ZPL.

The Purcell-enhanced ZPL emission rate into the cavity is $F_p\Gamma_{\text{ZPL}}$. The broad-linewidth PSB is not Purcell enhanced. Since the cavity mode extends only in the longitudinal spatial direction, the NV ZPL and PSB dipoles couple to free space modes in the lateral direction. We approximate this decay rate into the lateral free space modes as the free space rate $\Gamma_{\text{tot}} = \Gamma_{\text{ZPL}} + \Gamma_{\text{PSB}}$. The total branching ratio into the ZPL is thus $(F_p + 1)\Gamma_{\text{ZPL}}/(F_p\Gamma_{\text{ZPL}} + \Gamma_{\text{tot}})$. However, since we are interested in photons emitted into the cavity mode that we can efficiently collect, the factor of interest is the branching ratio into the ZPL into the cavity mode only, given by:

$$\beta_{\text{cav}} = \frac{F_p\Gamma_{\text{ZPL}}}{F_p\Gamma_{\text{ZPL}} + \Gamma_{\text{tot}}} = \frac{F_p\beta_0}{F_p\beta_0 + 1}, \quad (4.15)$$

where $\beta_0 = \Gamma_{\text{ZPL}}/\Gamma_{\text{tot}} \approx 0.03$ is the Debye-Waller factor of the NV in bulk diamond as described in section 2.2.2. It is important to notice that increasing the Purcell effect increases the branching ratio, but after $F_p \approx 1/\beta_0 \approx 33$ the relative benefit from increasing the Purcell factor is moderate (Fig. 4.3).

4.1.6. SYSTEM DYNAMICS IN THE STRONG AND WEAK COUPLING REGIMES

In this section we discuss Purcell enhancement in different parameter regimes. To explore the dynamics of the system, we study the rates that are involved. We have already encountered these: the relevant rates are κ , the cavity decay rate (Eq. (4.10)), Γ , the free space emitter decay rate (Eq. (4.6)), and g , the atom-cavity coupling (Eq. (4.4)). Express-

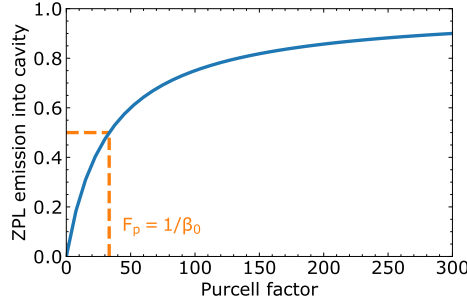


Figure 4.3: NV branching ratio into the zero-phonon line. The relative emission into the ZPL into the cavity depends on the Purcell enhancement of the ZPL transition as described in Eq. (4.15). While initially the branching ratio grows rapidly with increasing Purcell factor, when $F_p > 1/\beta_0 \approx 33$ the growth rate of the emission into the ZPL begins to decrease. This behaviour plays an important role in the design optimization of optical cavities as described in chapter 5.

ing the Purcell factor in terms of these rates we find:

$$F_p = \frac{4g^2}{\kappa\Gamma}. \quad (4.16)$$

Written in this way, F_p is known as the cooperativity. If it is larger than unity the spontaneous emission rate is enhanced. But this condition can be fulfilled with different relations between the three rates. Specifically, we distinguish two different regimes [5]:

$$g \gg \Gamma, \kappa, \quad \text{strong coupling regime}; \quad (4.17)$$

$$\kappa \gg g \gg \Gamma, \quad \text{weak coupling regime}. \quad (4.18)$$

In the first regime of strong coupling the photon is reabsorbed by the atom before it is lost from the cavity. In the weak coupling regime the photon is lost from the cavity before it is reabsorbed. For the enhancement of the branching ratio of photons emitted into the ZPL, we are interested in the second regime. The strong coupling regime has many interesting applications, but we will not go into the details here. An overview can be found, for example, in Refs. [4, 12].

We next explore in which range the rates κ , Γ and g should be to be in the weak coupling regime, and to achieve an enhanced branching ratio of NV emission into the ZPL. We first focus on the condition for the weak coupling regime: $\kappa \gg g \gg \Gamma$. The spontaneous emission rate of the NV E_x excited state is $\Gamma = (12.3 \text{ ns})^{-1} = 81.7 \text{ MHz}$ section 4.1.2. In the weak coupling regime we require that the atom-cavity coupling g is much greater than this. Using Eq. (4.3) we can express g as:

$$g = \sqrt{\frac{3}{8\pi} \frac{\lambda^3}{V_0} \nu \Gamma}. \quad (4.19)$$

In the case of the NV centre, we should separately consider the coupling to the individual transitions [9]. Specifically, since we are interested in coupling the ZPL to the cavity, we

should use $\Gamma = \Gamma_{\text{ZPL}}$ (see section 4.1.2). Doing this, we find $g = \sqrt{\lambda^3/V_0} \times 11.7$ GHz. Thus as long as the mode volume satisfies $V_0 \ll 10^6 \lambda^3$ we satisfy $g \gg \Gamma$. These mode volumes are easily achieved in microcavities.

The requirement that the cavity decay rate is larger than the coupling ($\kappa \gg g$) is straightforward to satisfy: making a bad cavity is easy. However, we do not want to make κ too large, since to have $F_p > 1$ a small κ is essential as clear from Eq. (4.16). The achievable and desired κ depends on the cavity design that determines the amount of unwanted cavity losses as well as the achievable cavity mode volume. Finally, the selected cavity decay rate may depend on real-world imperfections such as vibrations. In chapter 5 of this thesis we discuss these trade-offs in detail.

4.2. EXPERIMENTAL OPTICAL CAVITIES

4

In this section we describe cavity designs that can be employed for the enhancement of the NV centre ZPL. We classify the existing designs in three categories: (1) Monolithic diamond cavities; (2) Optical cavities with evanescently coupled NV centres; (3) Fabry-Pérot cavities with embedded diamond. Below we describe each of these designs and weigh their advantages and disadvantages for quantum network applications.

Monolithic diamond cavities In monolithic diamond cavities, the optical cavity is integrated in the diamond that contains the NV centre (see Fig. 4.4a). Designs include ring resonators [13], photonic crystal cavities [14–18]. Advantages of monolithic design is that they are robust e.g. against vibrations, and the mode volumes can be small (order λ^3). However, the monolithic design prevents straightforward tunability of the cavity resonance. Furthermore, intrinsic to the design of a photonic crystal cavity is the presence of nearby surfaces; the nearest surface will typically be less than half a wavelength (≈ 130 nm) away. Surface proximity, and the requirement of intensive diamond processing threaten the NV centre optical stability in these structures [13].

Optical cavities with evanescently coupled NV centres Instead of integrating the cavity in the diamond, the cavity may be fabricated in a different material, coupling the NV centre to the evanescent cavity mode. Architectures that exploit this include photonic crystal cavities coupled to NVs in nanodiamonds (see Fig. 4.4b) [19–21], and whispering gallery resonators coupled to shallow implanted NVs in bulk diamond [22, 23]. Other hybrid-system implementations can lead to direct rather than evanescent coupling, e.g. in Ref. [24] where NVs in nanodiamonds are embedded within polymer disks. The advantage of evanescently coupling NV centres to an optical cavity is that no or little diamond processing is required. Instead, cavities can be fabricated in easier to fabricate materials such as gallium phosphide (GaP). Moreover, the cavities can be robust against vibrations. However, for the evanescent field, the electric field strength decays exponentially with the distance of the NV from the cavity. For an NV embedded in diamond, this distance is given by the NV depth. The coupling strength thus highly benefits from shallow NV centres. Shallow NV centres however suffer from spin decoherence and optical instability induced by surface charges [25, 26], leading to a fundamental trade-off for this type of cavity.

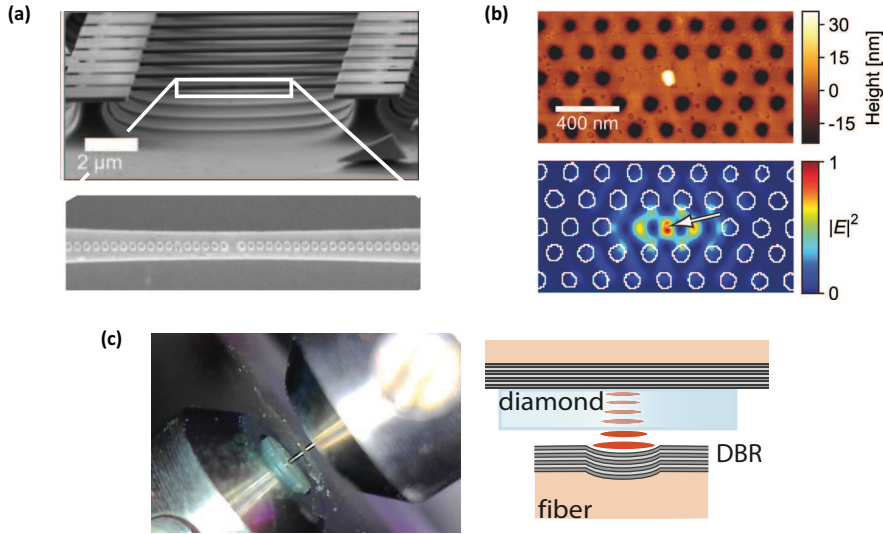


Figure 4.4: Optical cavities for resonant enhancement of the NV centre ZPL. (a) Figure adapted from [15]. SEM image of a one-dimensional diamond photonic crystal cavity. NV centres contained within the diamond nanobeam couple to the cavity. (b) Figure adapted from [19]. AFM image and simulated electric field profile of a GaP photonic crystal cavity, with a nanodiamond on top. The NV centres in the nanodiamond evanescently couple to the cavity mode. (c) Figure adapted from [31, 33]. Camera image and schematic of a Fabry-Pérot microcavity formed from a plane mirror and a fiber tip. A diamond membrane can be embedded through Van der Waals bonding to the plane mirror. A reflection of the fiber tip and housing is visible in the plane mirror (left).

Fabry-Pérot cavities with embedded diamond In an open Fabry-Pérot microcavity a diamond with NV centres can be embedded within the cavity, enabling direct coupling of the NV to the cavity mode. The NV centre can reside in a nanodiamond [9, 11, 27–29] or diamond membrane (Fig. 4.4c) [30–32], the latter enabling the NV centre to be far away ($> 1 \mu\text{m}$) from the diamond surface. Such NV centres can have stable optical transitions, as required for applications in quantum networks. Another advantage of this cavity type is its spatial and spectral tunability: no 3D positioning accuracy of NV centres is needed and the cavity can be easily tuned on resonance with the NV ZPL. However, the tunability makes the design inherently susceptible to vibrations, which requires careful passive and active cavity stabilisation. We believe these systems provide the most promising design for ZPL enhancement of optically stable NV centres as required for quantum network applications. We therefore work in this thesis towards the realization of ZPL enhancement in this type of optical cavity.

4.3. DIAMOND-AIR FABRY-PÉROT MICROCAVITIES

The physics of resonators is well-established and has been thoroughly described in texts such as Refs. [5, 34]. This chapter focuses on the theory specific to open Fabry-Pérot cavities with a diamond membrane ('diamond-air cavities'). First we describe bare cavities consisting of only a single material with refractive index n : in section 4.3.1 we introduce

the key parameters of a bare cavity using a one-dimensional model, and we discuss the transverse extent of Gaussian beams in plane-concave cavities in section 4.3.2. Next, we extend the description to diamond-air cavities, finding altered resonance conditions and the electric field distribution in section 4.3.3. In section 4.3.4 we adapt the Gaussian beam model for diamond-air cavities. We briefly discuss possible sources of unwanted cavity losses in section 4.3.5 and frequency splitting of the polarisation modes (section 4.3.6). We finish with a description of the coupling efficiency of the cavity mode to the detection path in section 4.3.7.

4.3.1. KEY PARAMETERS OF A BARE CAVITY FROM A ONE-DIMENSIONAL MODEL

In this section we describe the bare optical cavity using a one-dimensional model describing the reflection and transmission on the cavity mirrors. We find the key parameters needed to describe the cavity.

The one-dimensional model is based on a ‘transfer matrix’ approach [35, Chapter 5]. In this approach the electric field in the z -direction is split into a forward and backward propagating mode, $E_+(z)$ and $E_-(z)$. The propagation of the field and behaviour at dielectric interfaces is described by matrices relating the electric field E at an initial position to the field E' at a position further along the propagation direction. The propagation along distance t in material with refractive index n is described by:

$$\begin{pmatrix} E_+ \\ E_- \end{pmatrix} = \begin{pmatrix} e^{ikt} & 0 \\ 0 & e^{-ikt} \end{pmatrix} \begin{pmatrix} E'_+ \\ E'_- \end{pmatrix}; \quad k = 2\pi n / \lambda_0; \quad (4.20)$$

and the matching matrix for propagation along a boundary between a material with index n_1 to a material with index n_2 is given by:

$$\begin{pmatrix} E_+ \\ E_- \end{pmatrix} = \frac{1}{\tau_{12}} \begin{pmatrix} 1 & \rho_{12} \\ \rho_{12} & 1 \end{pmatrix} \begin{pmatrix} E'_+ \\ E'_- \end{pmatrix}; \quad \rho_{12} = \frac{n_1 - n_2}{n_1 + n_2}; \quad \tau_{12} = \frac{2n_1}{n_1 + n_2}. \quad (4.21)$$

A model of a system can be constructed by multiplication of these matrices. In this way any one-dimensional system can be described. For example, the matrix model for a Distributed Bragg Reflector (DBR) can in principle be constructed from the transfer matrices for alternating layers of high and low refractive index. To enable a simple derivation of the cavity resonance condition we will here instead use a single transfer matrix to represent a mirror:

$$M = \frac{1}{t} \begin{pmatrix} 1 & r \\ r & 1 \end{pmatrix}, \quad (4.22)$$

with reflection and transmission coefficients r and t .

A bare cavity of length L_{cav} (Fig. 4.5) can then be described by the following matrix model:

$$M_b = M_r P_a M_l = \frac{1}{t_r} \begin{pmatrix} 1 & r_r \\ r_r & 1 \end{pmatrix} \begin{pmatrix} e^{ikL_{\text{cav}}} & 0 \\ 0 & e^{-ikL_{\text{cav}}} \end{pmatrix} \frac{1}{t_l} \begin{pmatrix} 1 & -r_l \\ -r_l & 1 \end{pmatrix}, \quad (4.23)$$

where $M_{r(l)}$ is the transfer matrix representing the right (left) mirror, and P_a is the transfer matrix describing propagation through air. $r_{r(l)}$ and $t_{r(l)}$ are the reflection and trans-

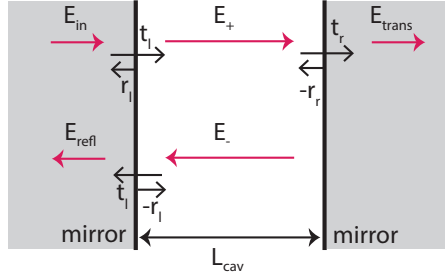


Figure 4.5: One-dimensional model of a bare cavity. A one-dimensional cavity model can be used to create a transfer matrix model of the cavity (Eq. (4.23)). The electric field is split into forward (E_{in} , E_+ , and E_{trans}) and backward (E_{refl} and E_-) propagating modes. There is no field incident on the cavity from the right-hand side.

mission coefficients of the left and right mirror stacks. Assuming that there is no incoming light from the right side we find that the transmission of the cavity is given by:

$$\begin{aligned}
 T &= |1/M_{b[1,1]}|^2 = \frac{|t_r|^2 |t_l|^2}{|e^{ikL_{cav}} - r_r r_l e^{-ikL_{cav}}|^2} \\
 &= \frac{|t_r|^2 |t_l|^2 / (1 - r_r r_l)^2}{1 + (2\mathcal{F}/\pi)^2 \sin^2(kL_{cav})}, \tag{4.24}
 \end{aligned}$$

where in the last step we have written out the denominator and defined the finesse \mathcal{F} as:

$$\mathcal{F} \equiv \frac{\pi\sqrt{r_r r_l}}{(1 - r_r r_l)} \approx \frac{2\pi}{\mathcal{L}_r + \mathcal{L}_l}, \tag{4.25}$$

where the approximation is valid for high-reflectivity mirrors ($r_{r(l)} = \sqrt{1 - \mathcal{L}_{r(l)}}$, with losses $\mathcal{L}_r, \mathcal{L}_l \ll 1$ ¹). The finesse is the number of round-trips of the light in the cavity before the energy in the cavity mode decays to $1/e$ of its initial value. In the following we describe several cavity properties that can be inferred from Eq. (4.24): the resonance condition, the linewidth and finesse, and the maximum transmission and reflection of a bare cavity.

Resonance condition of a bare cavity In the expression for the cavity transmission we can recognize the resonance condition of the cavity. The transmission of a cavity is maximised if $\sin^2(kL_{cav}) = 0$; i.e. if $kL_{cav} = m\pi$, for all integer m . Using $k = 2\pi n/\lambda_0$, we thus find that the resonance condition is:

$$L_{cav} = \frac{m\lambda_0}{2n} = \frac{mc}{2nv}, \tag{4.26}$$

in agreement with the resonance condition defined in Eq. (4.8).

¹We approximate the square-root using a Taylor series such that $r \sim 1 - \frac{1}{2}\mathcal{L}$ neglecting terms of $O(L_{cav}^2)$.

Linewidth and finesse of a bare cavity Using Eq. (4.24) the width of the resonance peak can be determined. The full width at half maximum (the cavity linewidth $\delta\nu$) is given by²:

$$\delta\nu = \frac{c}{2nL_{\text{cav}}\mathcal{F}} = \frac{\nu_{FSR}}{\mathcal{F}}. \quad (4.27)$$

This expression shows the relationship between the decay rate of the cavity and the finesse. Earlier in this chapter we described that the cavity linewidth is proportional to the decay rate of the cavity (Eq. (4.10)). Indeed combining this with Eq. (4.27) the finesse can be described as the number of round-trips light makes in the cavity before the energy in the mode decays to 1/e of its initial value.

The quality factor Q (Eq. (4.13)) can also be used to describe a cavity. It is defined as the ratio of total energy stored in the cavity to the energy loss per optical cycle. Since the number of optical cycles per round trip is given by $m = 2\nu/(cnL_{\text{cav}}) = \nu/\nu_{FSR}$, it is related to the finesse as

$$Q = \nu/\nu_{FSR}\mathcal{F}. \quad (4.28)$$

When the dominant cavity losses are at the surfaces of the cavity, the finesse is independent of L_{cav} . However, Q will be proportional to the cavity length. Therefore we prefer throughout this thesis to specify cavity properties using the finesse.

Maximum transmission and reflection The maximum transmission of the full cavity stack described by Eq. (4.24) is given by:

$$T_{\text{max}} = |t_r|^2 |t_l|^2 / (1 - r_r r_l)^2. \quad (4.29)$$

It can reach unity for a symmetric ($r_r = r_l = r$) and lossless ($r^2 + t^2 = 1$) cavity. Similarly, the on-resonance reflectivity that is described by [36]

$$R = |M_{b[2,1]}/m_{b[1,1]}|^2 = |(r_r - r_l)/(1 - r_r r_l)|^2, \quad (4.30)$$

reaches its minimum $R = 0$ only when the cavity is symmetric. For an asymmetric cavity the transmission is reduced, and the reflection increased. The on-resonance transmission and reflection are plotted in Fig. 4.6.

4.3.2. GAUSSIAN BEAM OPTICS IN A BARE CAVITY

To describe the transverse extent of the light in a cavity we can use wave optics. The time-independent part of the wavefunction (the complex amplitude $U(\mathbf{r})$) satisfies the time-independent wave equation:

$$\nabla^2 U + k^2 U = 0, \quad (4.31)$$

with $k = 2\pi\nu/c$ the wavenumber. We assume that the wavefront normals make a small angle with the z-axis, such that we can use the paraxial approximation:

$$U(\mathbf{r}) = A(\mathbf{r}) \exp(-ikz), \quad (4.32)$$

where A is the complex envelope of the wave that varies slowly in z .

²We find the frequency $\nu_{\text{res}} + \delta\nu/2$ for which $T = T_{\text{max}}/2$, giving $(2\mathcal{F}/\pi)^2 \sin^2\left(\frac{2\pi(\nu_{\text{res}} + \delta\nu/2)nL_{\text{cav}}}{c}\right) = 1$ where we evaluate the sine near resonance: $\sin(\pi m + \pi\delta\nu nL_{\text{cav}}/c) \approx (\pi\delta\nu nL_{\text{cav}}/c)$.

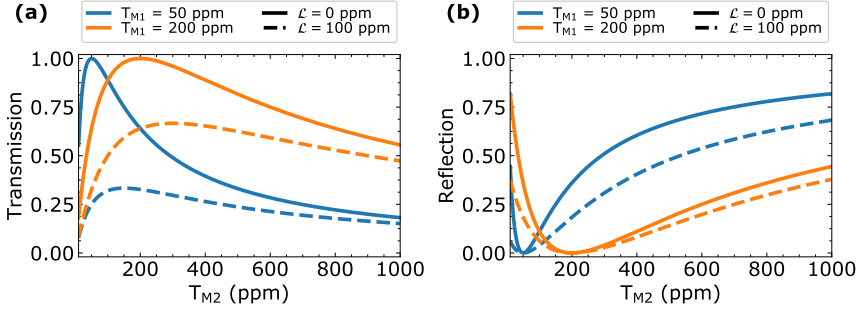


Figure 4.6: Transmission and reflection of an asymmetric optical cavity. (a) The maximum on-resonance transmission of a bare cavity (T_{\max} as defined in Eq. (4.29)) can reach a maximal value of unity when the mirrors are symmetric ($T_{M1} = T_{M2}$). When the mirror transmissions are asymmetric, or when other types of losses are present in the cavity (dashed lines) the maximum transmission is reduced. (b) The minimum on-resonance reflectivity of the cavity reaches a minimum for a symmetric cavity. Losses do not influence the reflectivity of the cavity.

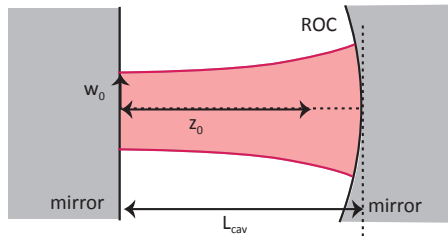


Figure 4.7: Gaussian beam in a plane-concave cavity. The beam front matches the radius of curvature (ROC) of the concave mirror. The beam waist with $W = w_0$ is located at the plane mirror. The Rayleigh length z_0 is the distance between the beam waist and the position where the beam width is $W(z_0) = \sqrt{2}w_0$.

A solution to the corresponding paraxial Helmholtz equation should satisfy the boundary conditions set by the interfaces of a plane-concave cavity (Fig. 4.7). The wavefronts should follow the plane and concave mirrors. The Gaussian beam is a solution to these conditions. We use the standard notation [34]:

$$\begin{aligned} U(\mathbf{r}) &= \frac{A_1}{q(z)} \exp\left(-ik \frac{\rho^2}{2q(z)}\right) \exp(-ikz) \\ &= A_0 \frac{w_0}{W(z)} \exp\left(-\frac{\rho^2}{W^2(z)}\right) \exp\left(-ikz - ik \frac{\rho^2}{2R(z)} + i\zeta(z)\right); \end{aligned} \quad (4.33)$$

$$W(z) = w_0 \sqrt{1 + \left(\frac{z}{z_0}\right)^2}; \quad (4.34)$$

$$R(z) = z \left(1 + \left(\frac{z_0}{z}\right)^2\right); \quad (4.35)$$

$$\zeta(z) = \arctan \frac{z}{z_0}; \quad (4.36)$$

$$w_0 = \sqrt{\frac{\lambda_0 z_0}{n\pi}}, \quad (4.37)$$

where the complex beam parameter $q(z) = z + iz_0$ has been written as

$$\frac{1}{q(z)} = \frac{1}{R(z)} - i \frac{\lambda_0}{\pi n W^2(z)}, \quad (4.38)$$

to make the beam width $W(z)$ and the wave front curvature $R(z)$ explicit in the formulation. $\zeta(z)$ is the Gouy phase shift that occurs as a result of the deviation of the Gaussian beam from a planar wave, and we use $A_0 = A_1/(iz_0)$ for the wave amplitude. Further, ρ is the radial coordination, z is the coordinate along the beam and $k = \frac{2\pi}{\lambda_0}$ is the wavenumber.

A schematic of a Gaussian beam in a plane-concave cavity is shown in Fig. 4.7. The beam waist w_0 is the narrowest beam width, where the beam curvature is infinite. The Rayleigh length z_0 is the distance from the beam waist position at which the beam front curvature is minimal. The beam waist and Rayleigh length are not independent: the Gaussian beam is fully specified by either of them. To satisfy the boundary conditions for a plane-concave cavity, the beam waist (with infinite beam front curvature) is located at the plane mirror ($W(0) = w_0$), and the beam front curvature at the concave mirror (positioned at $z = L$) equals the mirror's radius of curvature (ROC): $R(L) = \text{ROC}$. These conditions fix the beam waist for a bare plane-concave cavity to:

$$w_0 = \sqrt{\lambda_0/\pi(L(\text{ROC} - L))^{1/4}}. \quad (4.39)$$

Hermite-Gauss modes The lateral intensity profile of a cavity mode does not have to be the fundamental Gaussian profile of the Gaussian beam. Rather, the Gaussian beam is the simplest form of a class of mutually orthogonal solutions: the Hermite-Gauss modes.

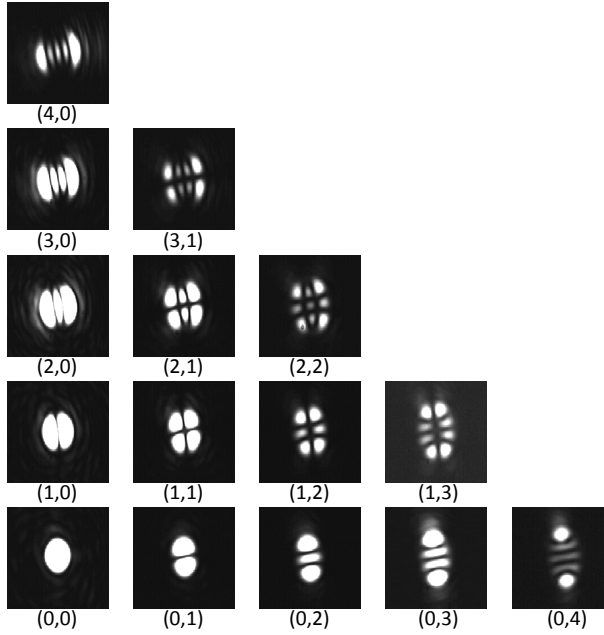


Figure 4.8: Hermite-Gauss modes in an optical cavity. Figure from Hermans [37]. The characteristic spatial structure of the fundamental Gaussian mode ($m = 0, n = 0$) and higher order Hermite-Gauss modes (the order is indicated by (m, n)) are excited by resonant excitation and observed in a CCD camera.

They are described by:

$$\begin{aligned}
 U_{m,n}(\mathbf{r}) = & A_0 \frac{w_0}{W(z)} H_m \left(\frac{\sqrt{2}x}{W(z)} \right) \exp \left(-\frac{x^2}{W^2(z)} \right) H_n \left(\frac{\sqrt{2}y}{W(z)} \right) \times \\
 & \exp \left(-\frac{y^2}{W^2(z)} \right) \exp \left(-ikz - ik \frac{x^2 + y^2}{2R(z)} + i\zeta(z) \right); \\
 \zeta(z) = & (1 + m + n) \arctan \left(\frac{z}{z_0} \right),
 \end{aligned} \tag{4.40}$$

where $H_n(x)$ is the Hermite polynomial of degree n , and the order of the Hermite-Gauss mode is indicated by (m,n) . The dependence of R and W on z is the same as for the Gaussian beam (Eqs. (4.34) and (4.35)), However, the Gouy phase (Eq. (4.36)) is extended to include the additional phase shift for the higher order Hermite-Gauss mode. The higher order Hermite-Gauss modes have a characteristic spatial structure as shown in Fig. 4.8.

Since the Gouy phase depends on the order of the mode, the resonance frequency of each Hermite-Gauss mode is shifted by a different amount. The frequency of a mode in

a bare cavity³ is given by [38]:

$$v = \frac{c}{4\pi L} \left(2\pi k + (2m + 1) \arccos \left(\sqrt{1 - L_{\text{cav}}/ROC_x} \right) + (2n + 1) \arccos \left(\sqrt{1 - L_{\text{cav}}/ROC_y} \right) \right), \quad (4.41)$$

where a potential ellipticity of the fiber dimple is accounted for by separately specifying the radius of curvature for the x and y direction as ROC_x and ROC_y . Since the splitting depends on the ROC of the fiber, a measurement of the higher order mode frequencies for a known cavity length provides a method to measure the ROC .

4

4.3.3. KEY PARAMETERS OF A DIAMOND-AIR CAVITY FROM A ONE-DIMENSIONAL MODEL

The open Fabry-Pérot cavity that is central to this thesis has a diamond membrane embedded in it. The diamond membrane is Van der Waals bonded to the plane mirror. The cavity thus does not consist of a single refractive index, but is made up of two parts, a diamond part where the refractive index is high ($n_d = 2.41$), and an air part where the refractive index is unity. In this section we find how this interface changes several key elements in the one-dimensional (longitudinal) description of the cavity. We first find the resonance condition for the full system. Then we find the electric field distribution over the air gap and the diamond membrane, and we discuss how we can use this to find the appropriate cavity mode volume and an effective cavity length. Finally we describe how these properties are influenced when an anti-reflection (AR) coating is applied to the diamond.

Resonance condition of a diamond-air cavity To understand how the partially reflective diamond-air interface influences the cavity system, we first look at the boundary conditions in diamond and air separately. For the air gap the diamond-air interface with a transition from a low ($n_a = 1$) to a high ($n_d = 2.41$) refractive index results in a field with an antinode at the interface. From the diamond membrane the reflection coefficient is opposite: the field in diamond has a node at this interface. Naturally, when these cavities are coupled, the electric field at the diamond-air interface has to be continuous. It is thus impossible to satisfy the resonance conditions of the two individual cavities at the same time. We therefore expect that in the combined system the individual resonances hybridize.

Below it is outlined how the resonance conditions can be found quantitatively from a transfer-matrix model described in section 4.3.1. The detailed derivations can be found in appendix A.1.

To find the resonance conditions in a diamond-air cavity we follow the same procedure as for the bare cavity, following the approach outlined in Ref. [30]. The matrix to

³We here use the expression $z_0 = \sqrt{L_{\text{cav}}(ROC - L_{\text{cav}})}$ (Eq. (4.39)) that follows from the boundary conditions of a bare plane-concave cavity. In the case of a diamond-air cavity we will see in section 4.3.4 that the appropriate substitution for the cavity length is $L_{\text{cav}} \rightarrow t_a + t_d/n_d^2$, with t_a the air gap width, t_d the diamond membrane thickness and $n_d = 2.41$ the diamond refractive index.

describe the system includes the transitions on the boundary from diamond to air and a propagation matrix in the diamond:

$$\begin{aligned}
 M &= M_r P_a I_{da} P_d I_{ad} M_l \\
 &= \frac{1}{t} \begin{pmatrix} 1 & r \\ r & 1 \end{pmatrix} \begin{pmatrix} e^{ik_a t_a} & 0 \\ 0 & e^{-ik_a t_a} \end{pmatrix} \frac{1}{(1+r_d)} \begin{pmatrix} 1 & r_d \\ r_d & 1 \end{pmatrix} \times \\
 &\quad \begin{pmatrix} e^{ik_d t_d} & 0 \\ 0 & e^{-ik_d t_d} \end{pmatrix} \frac{1}{(1-r_d)} \begin{pmatrix} 1 & -r_d \\ -r_d & 1 \end{pmatrix} \frac{1}{t} \begin{pmatrix} 1 & -r \\ -r & 1 \end{pmatrix},
 \end{aligned} \tag{4.42}$$

where $M_{r(l)}$ describe the cavity mirrors on the right (left) side (Eq. (4.22)). We assume both mirrors to have the same reflection and transmission coefficients r and t , that are specified for the mirror terminating in air. $P_{a(d)}$ are propagation matrices in air (diamond) (see Eq. (4.20)), and $I_{da(ad)}$ describe the matching matrices for transition from diamond to air (air to diamond) (see Eq. (5.26)). We distinguish between $k_a = 2\pi n_a \nu / c$ and $k_d = 2\pi n_d \nu / c$, with $n_a(n_d)$ the refractive index of air (diamond). Furthermore, t_a is the air gap width and t_d the diamond thickness. We have defined $r_d = (n_a - n_d) / (n_a + n_d)$.

To find the resonance condition of this system we determine the transmission ($T = |1/M_{1,1}|^2$), and assuming ideal mirrors (lossless, and $r = 1$) we write it as:

$$T = \frac{|(r_d - n_a)t^2|^2}{|1 - e^{2ik_a(n_a t_a + n_d t_d)} + r_d(e^{-2ik_a n_a t_a} - e^{-2ik_a n_d t_d})|^2} \tag{4.43}$$

The condition that maximizes the transmission is:

$$(n_a + n_d) \sin\left(\frac{2\pi\nu}{c}(n_a t_a + n_d t_d)\right) = (n_a - n_d) \sin\left(\frac{2\pi\nu}{c}(n_a t_a - n_d t_d)\right) \tag{4.44}$$

We approximate ν by writing it as a deviation $\Delta\nu_{da}$ from the resonance frequency of the equivalent bare cavity ($\nu = \frac{mc}{2(n_a t_a + n_d t_d)} + \Delta\nu_{da}$). The equation can be solved by neglect $\Delta\nu_{da}$ in the RHS of Eq. (4.44) [30]:

$$\nu = \frac{c}{2\pi(n_a t_a + n_d t_d)} \left(m\pi - (-1)^m \arcsin\left(\frac{n_d - n_a}{n_d + n_a} \sin\left(\pi m \frac{n_a t_a - n_d t_d}{n_a t_a + n_d t_d}\right)\right) \right). \tag{4.45}$$

The resulting spectrum is shown in Fig. 4.9a.

Two special cases for these resonant modes are distinguished: the ‘air-like mode’, in which the hybridized mode has an antinode at the diamond-air interface, and the ‘diamond-like mode’ in which there is a node at the interface. They correspond to the values for which the sine term on the right-hand side of the resonant condition vanishes:

$$t_d = m_d \frac{\lambda_0}{2n_d} \quad \text{and} \quad t_a = m_a \frac{\lambda_0}{2n_a}; \quad (\text{air-like mode}) \tag{4.46}$$

$$t_d = (2m_d + 1) \frac{\lambda_0}{4n_d} \quad \text{and} \quad t_a = (2m_a - 1) \frac{\lambda_0}{4n_a}; \quad (\text{diamond-like mode}) \tag{4.47}$$

for any integer (m_a, m_d), and $m = m_a + m_d$. $\lambda_0 = \nu / c$ is the free space wavelength.

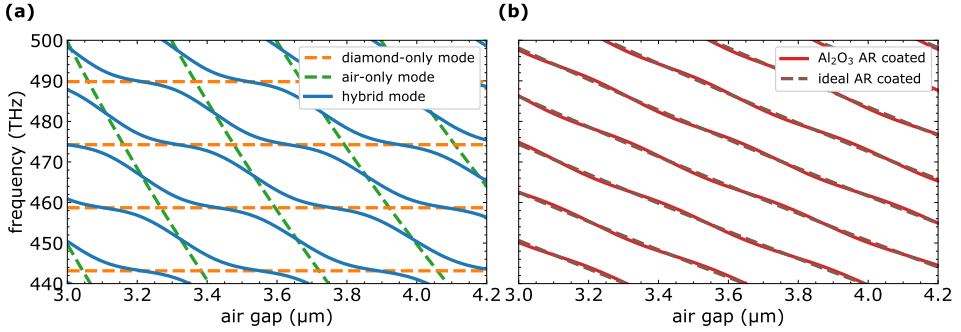


Figure 4.9: Resonance frequencies in a diamond-air cavity. (a) The diamond-only (orange) and air-only resonances (green) follow resonance conditions given by $\nu_d = (2m_d - 1)c/(4n_d t_d)$, and $\nu_a = m_a c/(2n_a t_a)$ with integer m_d and m_a respectively. The frequencies of the resonances of the diamond-air cavity (blue) are given by Eq. (4.45). (b) When an ideal anti-reflection (AR) coating is deposited on the diamond (dashed lines) with $n_{AR} = \sqrt{n_d}$ the hybrid mode behaviour disappears. A realistic AR coating with Al₂O₃ with refractive index $n_{\text{Al}_2\text{O}_3} = 1.77$ leads to resonance frequencies given by Eq. (4.54) (red solid lines).

4

Electric field distribution in a diamond-air cavity The electric field distribution in the diamond-air cavity can be found from a numeric evaluation of the transfer matrix model. To that end we replace the matrices describing the mirrors in Eq. (4.42) by layers of alternating refractive index. Starting on the right-hand side of the cavity, assuming there is no backward propagating electric field ($E_{r,-} = 0$), we then apply the propagation and matching matrices one by one to determine the electric field at each point in the cavity. Using this we can find the electric field strength $|E_+ + E_-|$ throughout the cavity.

An example of the resulting electric field distribution in a diamond-air cavity is shown in Fig. 4.10. The electric field distribution over the air gap and diamond membrane is strongly dependent on whether the cavity supports a ‘diamond-like’ or an ‘air-like’ mode. An analysis of this dependency and its influence on the ZPL emission of an NV centre are presented in chapter 5 of this thesis.

Mode volume and effective cavity length In its general form the mode volume of a cavity can be described by [10, 39]:

$$V = \frac{\int_{cav} \epsilon(\vec{r}) |E(\vec{r})|^2 d^3\vec{r}}{\epsilon(\vec{r}_{\text{NV}}) |E(\vec{r}_{\text{NV}})|^2}, \quad (4.48)$$

with $\epsilon(\vec{r}) = n(\vec{r})^2 \epsilon_0$ the permittivity at position \vec{r} where the refractive index is n . The integral is over the whole cavity volume, including the DBR mirrors, such that the penetration depth of the field into the mirrors is automatically included in the mode volume. \vec{r}_{NV} is the position of the NV centre, that we assume to be optimally positioned in an antinode of the cavity field in diamond. This assumption dictates that we choose to explicitly include effects from sub-optimal positioning in the Purcell factor in ξ^2 (see Eq. (4.12)) rather than including them here. Evaluation of the integral in the radial direc-

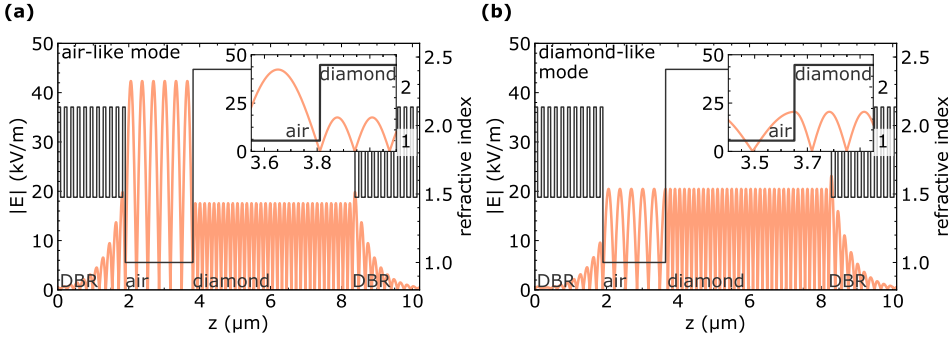


Figure 4.10: Diamond-like and air-like modes in a diamond-air cavity. The electric field distribution in a diamond-air cavity strongly depends on whether the cavity supports (a) an air-like mode or (b) a diamond-like mode. Both are shown here for a diamond thickness of $t_d \approx 4 \mu\text{m}$ and an air gap of $t_a \approx 2 \mu\text{m}$. The value of the electric field strength is further dependent on the cavity losses and dimple radius of curvature. The only source of losses implemented here are due to finite mirror transmission. The mirrors are simulated as 21 layers of alternatingly Ta_2O_5 ($n = 2.14$) and SiO_2 ($n = 1.48$). The resulting mirror transmission (taking into account the termination on diamond for the right-hand-side mirror) is $T_l = 260$ ppm and $T_r = 630$ ppm. The radius of curvature that is used to determine the mode volume and the resulting electric field density is $\text{ROC} = 25 \mu\text{m}$.

tion, assuming a Gaussian beam structure, gives:

$$V = \frac{\pi w_0^2}{2} \frac{\int_{cav} \epsilon(z) |E(z)|^2 dz}{\epsilon(z_{NV}) |E(z_{NV})|^2}, \quad (4.49)$$

where the integral is over the cavity in the longitudinal (z) direction. The expression that describes the cavity length is [40]:

$$L_{\text{eff}} = 2 \frac{\int_{cav} \epsilon(z) |E(z)|^2 dz}{\epsilon(z_{NV}) |E(z_{NV})|^2}. \quad (4.50)$$

Eq. (4.50) reduces to the standard cavity length in the case of a bare cavity with a constant refractive index n^4 . The cavity mode volume that we find from this thus is:

$$V = \frac{\pi w_0^2}{4} L_{\text{cav}}, \quad (4.51)$$

which, as it should be, is the commonly defined cavity volume for a bare cavity [41].

Effect of AR coating of the diamond membrane We have seen how the partially reflecting interface of the diamond membrane and air gap gives an unequal distribution of the electric field over the diamond membrane and air gap. The effect of the partially reflecting diamond membrane interface can in principle be removed by applying an anti-reflection (AR) coating to the diamond membrane. We here explore the effect that the

⁴In that case $\epsilon(z)$ is independent of position ($\epsilon(z) = \epsilon_0 n^2$), so that we can take it out of the integral over the cavity field. The integral over the cavity thus reduces to $\int_{cav} E(z)^2 dz = \int_{cav} (E(z_{NV}) \sin^2(2\pi z/\lambda))^2$. We ignore the contribution from penetration of the field mode into the DBR mirrors, and assume the cavity is on-resonance, so the limits of the integral are $z = 0$ and $z = L_{\text{cav}} = m\lambda/2$. The integral evaluates to $E(z_{NV})^2 L_{\text{cav}}/2$, so that for the full expression we indeed recover the standard cavity length L_{cav} .

application of such a membrane has on the resonance conditions and the electric field distribution.

An ideal AR coating has a layer of refractive index $n_{AR} = \sqrt{n_a n_d} \approx 1.55$ (with $n_a = 1$ and $n_d = 2.41$) and thickness $t_{AR} = \lambda_0 / (4n_{AR})$. We add such an AR coating to the numeric evaluation of the transfer matrix model to find the electric field distribution in the cavity. Indeed, with an AR coating, the field intensity $n(z)E_{\max}^2$ has equal value in the diamond membrane and in the air gap (Fig. 4.11).

However, a practical AR coating has to be fabricated from available materials, that will have a refractive index that is at best close to the ideal value. Suitable materials are for example SiO_2 ($n_{\text{SiO}_2} \approx 1.46$) or Al_2O_3 ($n_{\text{Al}_2\text{O}_3} \approx 1.77$) [42, 43]. With these AR coatings the electric field distribution will not be fully balanced.

The resonance condition for a cavity with a non-ideal AR coating with refractive index n_{AR} and a thickness $\lambda_0 / (4n_{AR})$ is given by:

$$v_{AR} = \frac{c}{2\pi(n_a t_a + n_d t_d)} \times \left((m + 1/2)\pi - (-1)^m \arcsin \left(\frac{n_{AR}^2 - n_a n_d}{n_{AR}^2 + n_a n_d} \cos \left(\pi(m + 1/2) \frac{n_a t_a - n_d t_d}{n_a t_a + n_d t_d} \right) \right) \right). \quad (4.52)$$

Compared to the resonance condition without AR coating, the optical cavity length increased by $\lambda_0/4$, and the reflectivity of the diamond-air transition is altered from $r_d = (n_a - n_d)/(n_a + n_d)$, to $(n_{AR}^2 - n_a n_d)/(n_{AR}^2 + n_a n_d)$, as expected for the reflection coefficient of a $\lambda/4$ thick film with refractive index n_{AR} [44]. For an ideal AR coating with $n_{AR} = \sqrt{n_a n_d}$ the second term on the right-hand-side of Eq. (4.52) vanishes, so that the full expression reduces to the resonance condition expected for a bare cavity with $L_{\text{cav}} = n_a t_a + n_d t_d + \lambda_0/4$:

$$v_{\text{ideal},AR} = \frac{(m + 1/2)c}{2(n_a t_a + t_d n_d)}. \quad (4.54)$$

The resonance spectra for the ideal and a realistic Al_2O_3 AR coated diamond-air cavities are shown in Fig. 4.9b.

4.3.4. COUPLED GAUSSIAN BEAMS IN A HYBRID CAVITY

The previous section described how the introduction of a diamond membrane changes several of the key parameters of the one-dimensional structure of a cavity. In this section we analyse the effect on the transverse extent of the cavity mode.

In section 4.3.2 the transverse extent of the cavity mode was described by a Gaussian beam. The relation between the Gaussian beam parameters w_0 and z_0 depends on the refractive index in which the Gaussian beam lives (see Eq. (4.37)). We thus cannot use a single Gaussian beam to describe the field in a diamond-air cavity with two different refractive-index regions. Instead, we require two separate Gaussian beams, of which one lives in air and the other in diamond (Fig. 4.12a). We define their beam waist as $w_{0,a}$ and $w_{0,d}$ for the beam in diamond and air respectively. They are related to the Rayleigh

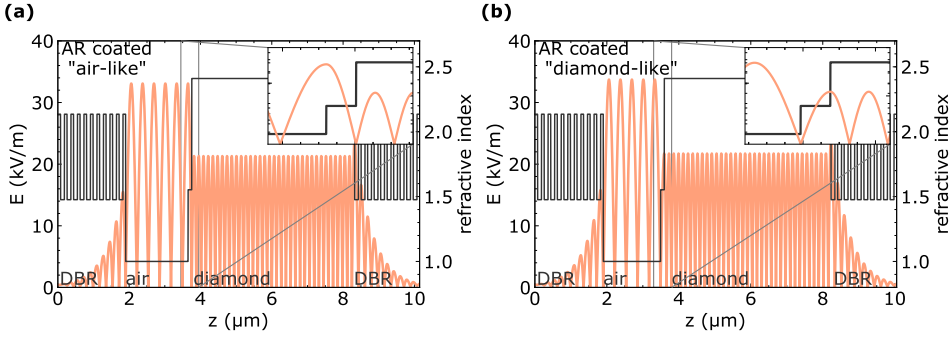


Figure 4.11: Electric field distribution in a diamond-air cavity with an AR coating. (a-b) The electric field distribution for a hybrid cavity with an AR-coated diamond membrane for what would have been (a) an air-like mode, or (b) a diamond-like mode if there were no AR coating. With the AR coating, the electric field intensity in the diamond and air parts is equal: $E_{max,a}^2 = n_d E_{max,d}^2$.

lengths $z_{0,a}$ and $z_{0,d}$ as:

$$w_{0,a} = \sqrt{\frac{\lambda_0 z_{0,a}}{n_a \pi}} \quad (4.55)$$

$$w_{0,d} = \sqrt{\frac{\lambda_0 z_{0,d}}{n_d \pi}} \quad (4.56)$$

We further require that the beam waist of the diamond beam is fixed on the plane mirror (at $z = 0$). The air beam waist is free to be at distance Δz_a from the plane mirror. The wave front curvature and beam widths of these two beams are then described as:

$$R_d(z) = z \left(1 + \left(\frac{z_{0,d}}{z} \right)^2 \right); \quad (4.57)$$

$$R_a(z) = (z - \Delta z_a) \left(1 + \left(\frac{z_{0,a}}{z - \Delta z_a} \right)^2 \right), \quad (4.58)$$

$$W_d(z) = w_{0,d} \sqrt{1 + \left(\frac{z}{z_{0,d}} \right)^2} \quad (4.59)$$

$$W_a(z) = w_{0,a} \sqrt{1 + \left(\frac{z - \Delta z_a}{z_{0,a}} \right)^2} \quad (4.60)$$

where subscript a (d) is used for the Gaussian beam in air (diamond). The beam waists of the two Gaussian beams, $w_{0,a}$ and $w_{0,d}$, and the distance of the air beam waist to the plane mirror Δz_a , follow from the additional boundary conditions imposed by the cavity dimensions. The boundary conditions at the diamond-air interface can be found from the 'ABCD-matrix' that transforms the Gaussian beam parameters going from air (with $n = n_a$) to diamond (with $n = n_d$) [34]:

$$\begin{pmatrix} A & B \\ C & D \end{pmatrix} = \begin{pmatrix} 1 & 0 \\ 0 & n_a/n_d \end{pmatrix}. \quad (4.61)$$

Following the corresponding ABCD law for Gaussian beams we find that the complex beam parameters in diamond and air (q_d and q_a , Eq. (4.38)) are related by:

$$q_d = \frac{Aq_a + B}{Cq_a + D} = \frac{q_a}{n_a/n_d}. \quad (4.62)$$

This leads to the following conditions on the beam curvature and beam width at the interface:

$$n_d R_a(t_d) = n_a R_d(t_d); \quad (4.63)$$

$$W_a(t_d) = W_d(t_d), \quad (4.64)$$

that can be solved analytically to give [45]:

$$w_{0,a} = w_{0,d}, \quad (\rightarrow z_{0,a}/n_a = z_{0,d}/n_d). \quad (4.65)$$

$$\Delta z_a = t_d \left(1 - \frac{n_a}{n_d}\right). \quad (4.66)$$

Together with the boundary condition that the beam front curvature follows the radius of curvature of the fiber dimple:

$$R_a(t_a + t_d) = ROC, \quad (4.67)$$

this gives an expression for the beam waist of the Gaussian beam:

$$w_{0,d} = w_{0,a} = \sqrt{\frac{\lambda_0}{\pi n_a} \left(\left(t_a + \frac{n_a t_d}{n_d} \right) \left(ROC - \left(t_a + \frac{n_a t_d}{n_d} \right) \right) \right)^{1/4}}. \quad (4.68)$$

In this expression we recognize the standard expression for the beam waist [41], with the cavity length replaced by:

$$L' \equiv t_a + \frac{n_a t_d}{n_d} (= t_a + t_d - \Delta z_a). \quad (4.69)$$

The numerically and analytically obtained results to the model are both shown in Fig. 4.12. These results are obtained assuming that the diamond-air interface is planar. If this interface would be curved, a different solution to the Gaussian beams model follows. The details of the solution in that situation are described in appendix A.2.

We conclude this section by discussing the stability range of the diamond-air cavity that follows from the analytical model.

Cavity stability range The stability condition of a cavity gives the ranges of cavity lengths for which a cavity mode can exist. In general, the stability condition of a cavity is found by requiring that the Rayleigh length satisfies $z_0^2 > 0$. For a bare cavity of length L this gives, in combination with the boundary condition $R(L) = ROC$, the requirement $L < ROC$. The maximum cavity length is thus given by the radius of curvature of the concave mirror.

However, for a hybrid cavity the stability range changes. In the numeric and analytic solutions in Fig. 4.12 the cavity is stable beyond $t_d + t_a = ROC$, as there are cavity modes for $t_a > 16 \mu\text{m}$ despite that $t_d = 4 \mu\text{m}$ and $ROC = 20 \mu\text{m}$. For the hybrid cavity the beam waist of the air mode can be disconnected from the plane mirror such that we expect the cavity stability region to be extended by Δz_a . Indeed, requiring $z_{0,a}^2 > 0$ in Eq. (4.68) we find that the stability condition is:

$$t_a + \frac{n_a t_d}{n_d} \lesssim ROC. \quad (4.70)$$

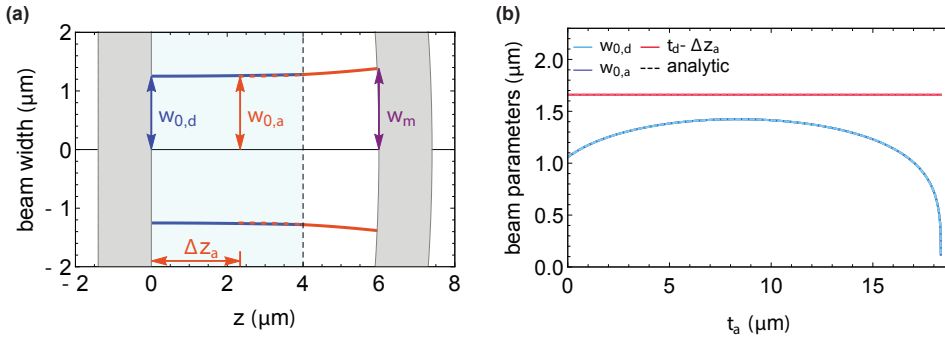


Figure 4.12: Coupled Gaussian beams in a diamond-air cavity. (a) The beam width of the Gaussian beams in a diamond-air cavity follows from the boundary conditions in Eqs. (4.63), (4.64) and (4.67). The position of the diamond beam waist is on the mirror, while the position of the air beam waist is at a distance Δz_a from the mirror. Here the solution for $t_d = 4 \mu\text{m}$, $t_a = 2 \mu\text{m}$, and $ROC = 25 \mu\text{m}$ is shown. (b) Numerically calculated beam parameters (solid lines) are shown as a function of the air gap width of a diamond-air cavity with $t_d = 4 \mu\text{m}$ and $ROC = 20 \mu\text{m}$. Analytically obtained results (Eqs. (4.65), (4.66) and (4.68)) are shown as dashed lines. The values for $w_{0,a}$ and $w_{0,d}$ overlap.

4.3.5. UNWANTED CAVITY LOSSES

Most losses in the cavity are unwanted. The only desired source of losses is mirror transmission to increase the outcoupling efficiency of photons from the cavity. The outcoupling efficiency is given by $T_o / (\mathcal{L}_{\text{tot}})$, with T_o the transmission through the outcoupling mirror and \mathcal{L}_{tot} the total cavity losses. The unwanted losses are thus $\mathcal{L}_{\text{tot}} - T_o$.

In a diamond-air cavity there are several possible sources of unwanted losses, that we shortly list here. The main source of loss in a diamond-air cavity is scattering, that predominantly occurs at the diamond-air interface. Further, there are clipping losses when the cavity beam width extends outside the dimple diameter, as well as losses from absorption in the mirrors and in the diamond. A detailed review considering the losses and their impact on the achievable ZPL enhancement is presented in chapter 5 of this thesis.

4.3.6. FREQUENCY SPLITTING OF POLARISATION MODES

Polarisation modes in fiber Fabry-Pérot cavities can become non-degenerate as a result of two effects [46–48]: ellipticity of the fiber mirrors and birefringence. For cavities with

a radius of curvature approaching the wavelength in the cavity, fiber ellipticity is the dominant source of polarization splitting over birefringence of the mirror materials [48]. However for the cavity described here, birefringence not only occurs in the mirrors, but also in the diamond. To determine the polarization splitting in our cavity, we thus both have to look at fiber ellipticity and diamond birefringence.

The relative shift of the two polarization modes as a result of the fiber ellipticity is given by [48]:

$$\frac{\Delta\nu_E}{\delta\nu} = \frac{\mathcal{F}\lambda}{4\pi^2} \frac{ROC_x - ROC_y}{ROC_x ROC_y}, \quad (4.71)$$

with ROC_x and ROC_y the radius of curvature in the x and y directions. For example, a fiber with a substantial fiber ellipticity of $(ROC_x - ROC_y)/ROC_x = 0.05$ and $ROC_y = 20 \mu\text{m}$, and a cavity Finesse of 3000 result in $\Delta\nu_E/\delta\nu = 0.08$.

Birefringence in diamond can be induced by stress originating from defects. For the CVD grown diamond that we use (Element 6) the birefringence is specified [49] to be less than $\Delta n_D < 2 \times 10^{-5}$. The resulting splitting is [51]:

$$\frac{\Delta\nu_D}{\delta\nu} = \frac{2\Delta n_D t_d \mathcal{F}}{\lambda_0}. \quad (4.72)$$

For example, for a diamond thickness of $4 \mu\text{m}$ and $F = 3000$ the polarisation splitting can be up to $\Delta\nu_D/\delta\nu = 0.8$. From these estimations we expect the birefringence in diamond to have a dominant contribution to the polarisation splitting in the cavity.

For maximal Purcell enhancement the atomic dipole and a cavity polarisation mode overlap. If the main source of polarisation splitting is fiber ellipticity, this can be achieved by rotating the fiber. If diamond birefringence is the main source of polarisation splitting, control can be exerted by electric field tuning of the NV dipole orientation within the diamond crystal.

4.3.7. COUPLING EFFICIENCY

In this section we describe the collection efficiency of the cavity mode for a fiber-based microcavity. We focus on how well the cavity mode can be matched to the detection mode.

The setup of a plane-concave fiber cavity provides two possible detection routes: directly into the laser-machined fiber, or via the free-space path. On the side of the free space path the cavity mode can be overlapped with the mode of the collection path using free space elements. By optimal positioning of the optical elements the coupling can in principle have unit efficiency.

However, on the fiber-side of the cavity path such flexibility is not present. The mode-matching efficiency is determined by the power transmittivity τ given by the overlap between the Gaussian beams in the fiber and the cavity mode [41, 52]:

$$\tau = \int U_f^*(\vec{r}) U_c(\vec{r}) d\vec{r}. \quad (4.73)$$

⁵The birefringence depends on whether the propagation direction of light is parallel to or perpendicular to the growth direction, with the lower birefringence for the second case [50]. After growth, the diamond is furthermore spliced and polished, and Van der Waals bonded to the mirror, potentially introducing extra stress in the material.

The Gaussian beams $U(\vec{r})$ are given by Eq. (4.33) in the fiber and cavity, at $z = t_a + t_d$. The integral is over the radial direction. The relevant parameters are thus the beam widths and curvatures at the dimple interface in the fiber (w_f, R_f) and cavity (w_m, R_m), as well as the spatial overlap of the beams given by the potential misalignment of the fiber due to an off-centred dimple and fiber tilt. The beam curvature of the cavity mode is given by the radius of curvature of the mirror $R_m = -ROC$. The fiber mode that has a beam curvature $R \rightarrow \infty$ in the fiber undergoes a lensing effect at the concave fiber tip (given by a focal length $f = (n_f - 1)/ROC$, such that $R_f = ROC/(n_f - 1)$ [41]. The beam width of the fiber mode is set by the radius of the fiber core, and the beam width on the cavity side can be calculated using the coupled Gaussian beams model section 4.3.4.

We decouple the x and y dimension to determine the overlap between the Gaussian beams. We consider a case where $ROC_x = ROC_y$, and we assume the fiber tilt influences both axes equally such that $\tau_x = \tau_y$ [53]. The coupling efficiency is then given by $\epsilon = \tau_x^2$, with for the x -direction [41, 52]:

$$\tau_x = \int U_f^*(x) U_c(x) dx \quad (4.74)$$

$$= \frac{2}{w_f w_m} \frac{1}{\sqrt{a^2 + b^2}} \exp\left(\frac{a(c^2 - d^2)}{2(a^2 + b^2)}\right) \exp\left(\frac{bcd}{a^2 + b^2}\right) \exp(-2f); \quad (4.75)$$

$$a = \frac{1}{w_m^2} + \frac{1}{w_f^2};$$

$$b = \frac{-\pi}{\lambda_0 R_m} + \frac{\pi}{\lambda_0 R_f};$$

$$c = \frac{2\delta x}{w_m^2};$$

$$d = 2\pi \left(\frac{-\delta x}{\lambda_0 R_m} + \frac{\theta_x}{\lambda_0} \right);$$

$$f = \frac{\delta x^2}{w_m^2},$$

where δx is the deviation of the fiber dimple from the centre of the fiber core, and θ_x is the angle over which the fiber is tilted along x .

The resulting coupling efficiency (solid lines in Fig. 4.13a) approaches unity for a large dimple radius of curvature if the beam width on the fiber mirror w_m matches the beam radius in the fiber, $w_f = 2.5 \mu\text{m}$, providing the best overlap between the Gaussian beams. We use the analytic solution to the coupled Gaussian beams model (Eqs. (4.60), (4.65) and (4.68)) to find w_m for several cavity parameters, and determine the expected coupling parameter for these cavity parameters. Fig. 4.13b shows that, for $t_d = 4 \mu\text{m}$, to achieve a coupling efficiency of > 0.75 we need at least $ROC > 35 \mu\text{m}$ in combination with an air gap $> 2 \mu\text{m}$ is needed.

In addition spatial misalignment due to fiber tilt may significantly influence the coupling efficiency. If the fiber tilt is $\theta = 50 \text{ mrad}$ (Fig. 4.13, dashed lines), a coupling efficiency > 0.75 can only be achieved for $ROC > 100 \mu\text{m}$. The influence of an off-centred dimple of $d x < 0.5 \mu\text{m}$ is negligible (not shown).

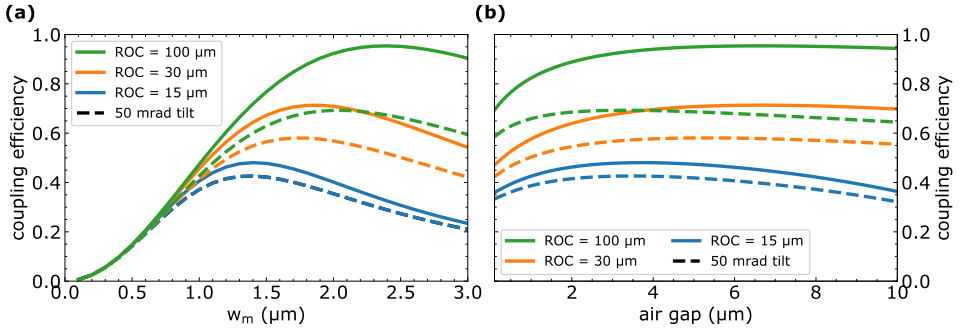


Figure 4.13: (a) The mode matching efficiency into the dimpled fiber approaches unity for an ROC of 100 μm , if the beam width of the cavity mode on the mirror approaches the beam width of the fiber mode ($w_f = 2.5 \mu\text{m}$). A fiber tilt of 50 mrad (dashed lines) decreases the maximally achievable coupling efficiency. (b) For $t_d = 4 \mu\text{m}$ the air gap width should be $> 2 \mu\text{m}$ to maximize the coupling efficiency.

The decrease of the coupling efficiency for smaller radius of curvature and a wider air gap is in direct conflict with the maximisation of the Purcell factor. To avoid having to trade-off these quantities, detection via the free space path is beneficial. A stability-argument can however be made for detection through the fiber: vibrations of the cavity as a whole with respect to the optical table, as resulting from passive vibration isolation used to minimize intra-cavity vibrations [31], might hinder free-space detection. Detection and (low-power, resonant) excitation through the fiber would remove the need to actively stabilize these vibrations.

4.4. CONCLUSIONS

In summary, in this chapter we have discussed how an optical cavity can be used for Purcell enhancement of the NV centre ZPL emission. Further, we have discussed several architectures in which such Purcell enhancement can be pursued. We have then zoomed in to the cavity design that is central to this thesis: a Fabry-Pérot cavity with an embedded diamond membrane. We have described the several theoretical handles needed for the description of these cavities. In the next chapter, we describe analytical models of these cavities that can be used to optimize the cavity design.

REFERENCES

- [1] Griffiths, D., *Introduction to Quantum Mechanics*, 2nd ed. (Pearson Prentice Hall, Upper Saddle River, NJ 07458, 2005).
- [2] Tokmakoff, A., *5.74 Introductory quantum mechanics II*, (2009), lecture notes.
- [3] Simons, B., *Advanced quantum mechanics*, (2009), lecture notes.
- [4] Reiserer, A. & Rempe, G., *Cavity-based quantum networks with single atoms and optical photons*, *Rev. Mod. Phys.* **87**, 1379 (2014).
- [5] Fox, M., *Quantum Optics* (Oxford University Press, 2016).

- [6] Kalb, N., Humphreys, P. C., Slim, J. J. & Hanson, R., *Dephasing mechanisms of diamond-based nuclear-spin memories for quantum networks*, Phys. Rev. A **97**, 062330 (2018).
- [7] Purcell, E., *Spontaneous Emission Probabilities at Radio Frequencies*, in *Proc. Am. Physical Soc.*, Vol. 69 (1946).
- [8] Haroche, S. & Raimond, J.-M., *Exploring the Quantum* (Oxford University Press, 2006).
- [9] Albrecht, R., Bommer, A., Deutsch, C., Reichel, J. & Becher, C., *Coupling of a single N-V center in diamond to a fiber-based microcavity*, Phys. Rev. Lett. **110**, 243602 (2013).
- [10] Gérard, J.-M., *Solid-state cavity-quantum electrodynamics with self-assembled quantum dots*, in *Single Quantum Dots*, edited by Michler, P. (Springer, 2003) pp. 269–314.
- [11] Kaupp, H. *et al.*, *Purcell-Enhanced Single-Photon Emission from Nitrogen-Vacancy Centers Coupled to a Tunable Microcavity*, Phys. Rev. Appl. **6**, 054010 (2016).
- [12] Miller, R. *et al.*, *Trapped atoms in cavity QED: Coupling quantized light and matter*, J. Phys. B **38**, S551 (2005).
- [13] Faraon, A., Barclay, P. E., Santori, C., Fu, K.-M. C. & Beausoleil, R. G., *Resonant enhancement of the zero-phonon emission from a colour centre in a diamond cavity*, Nat. Photon. **5**, 301 (2011).
- [14] Faraon, A., Santori, C., Huang, Z., Acosta, V. M. & Beausoleil, R. G., *Coupling of nitrogen-vacancy centers to photonic crystal cavities in monocrystalline diamond*, Phys. Rev. Lett. **109**, 033604 (2012).
- [15] Hausmann, B. J. M. *et al.*, *Coupling of NV centers to photonic crystal nanobeams in diamond*, Nano Lett. **13**, 5791 (2013).
- [16] Lee, J. C. *et al.*, *Deterministic coupling of delta-doped nitrogen vacancy centers to a nanobeam photonic crystal cavity*, Appl. Phys. Lett. **105**, 2012 (2014).
- [17] Riedrich-Möller, J. *et al.*, *Nanoimplantation and Purcell enhancement of single nitrogen-vacancy centers in photonic crystal cavities in diamond*, Appl. Phys. Lett. **106**, 221103 (2015).
- [18] Li, L. *et al.*, *Coherent spin control of a nanocavity-enhanced qubit in diamond*. Nature Comm. **6**, 6173 (2015).
- [19] Wolters, J. *et al.*, *Enhancement of the zero phonon line emission from a single nitrogen vacancy center in a nanodiamond via coupling to a photonic crystal cavity*, Appl. Phys. Lett. **97**, 141108 (2010).
- [20] Englund, D. *et al.*, *Deterministic coupling of a single nitrogen vacancy center to a photonic crystal cavity*, Nano Lett. **10**, 3922 (2010).

- [21] van der Sar, T. *et al.*, *Deterministic nanoassembly of a coupled quantum emitter-photonic crystal cavity system*, *Appl. Phys. Lett.* **98**, 193103 (2011).
- [22] Barclay, P. E., Fu, K. M. C., Santori, C., Faraon, A. & Beausoleil, R. G., *Hybrid nanocavity resonant enhancement of color center emission in diamond*, *Phys. Rev. X* **1**, 011007 (2011).
- [23] Gould, M., Schmidgall, E. R., Dadgostar, S., Hatami, F. & Fu, K. M. C., *Efficient Extraction of Zero-Phonon-Line Photons from Single Nitrogen-Vacancy Centers in an Integrated GaP-on-Diamond Platform*, *Phys. Rev. Appl.* **6**, 011001 (2016).
- [24] Ruan, Y. *et al.*, *Atom-Photon Coupling from Nitrogen-vacancy Centres Embedded in Tellurite Microspheres*. *Sci. Rep.* **5**, 11486 (2015).
- [25] Myers, B. A. *et al.*, *Probing surface noise with depth-calibrated spins in diamond*, *Phys. Rev. Lett.* **113**, 027602 (2014).
- [26] Santori, C. *et al.*, *Nanophotonics for quantum optics using nitrogen-vacancy centers in diamond*, *Nanotechnology* **21**, 274008 (2010).
- [27] Kaupp, H. *et al.*, *Scaling laws of the cavity enhancement for NV centers in diamond*, *Phys. Rev. A* **88**, 8 (2013).
- [28] Albrecht, R. *et al.*, *Narrow-band single photon emission at room temperature based on a single nitrogen-vacancy center coupled to an all-fiber-cavity*, *Appl. Phys. Lett.* **105**, 073113 (2014).
- [29] Johnson, S. *et al.*, *Tunable cavity coupling of the zero phonon line of a nitrogen-vacancy defect in diamond*, *New J. Phys.* **17**, 122003 (2015).
- [30] Janitz, E. *et al.*, *A Fabry-Perot microcavity for diamond-based photonics*, *Phys. Rev. A* **92**, 043844 (2015).
- [31] Bogdanović, S. *et al.*, *Design and low-temperature characterization of a tunable microcavity for diamond-based quantum networks*, *Appl. Phys. Lett.* **110**, 1 (2017).
- [32] Riedel, D. *et al.*, *Deterministic enhancement of coherent photon generation from a nitrogen-vacancy center in ultrapure diamond*, *Phys. Rev. X* **7**, 031040 (2017).
- [33] van Dam, S. B., Ruf, M. & Hanson, R., *Optimal design of diamond-air microcavities for quantum networks using an analytical approach*, *New J. Phys.* **20**, 115004 (2018).
- [34] Saleh, B. & Teich, M., *Fundamentals of Photonics*, Wiley Series in Pure and Applied Optics (Wiley, 2007).
- [35] Orfanidis, S. J., *Electromagnetic Waves and Antennas* (Rutgers University, Piscataway, NJ, 2016).
- [36] Bick, A. *et al.*, *The role of mode match in fiber cavities*, *Rev. Sci. Instrum.* **87** (2016), 10.1063/1.4939046.

- [37] Hermans, S., *Towards Purcell enhancement of the zero-phonon line of nitrogen-vacancy centres in diamond in an open Fabry-Pérot microcavity*, (2017), M.Sc. thesis.
- [38] Benedikter, J. *et al.*, *Transverse-mode coupling and diffraction loss in tunable Fabry-Pérot microcavities*, *New J. Phys.* **17**, 053051 (2015).
- [39] Sauvan, C., Hugonin, J. P., Maksymov, I. S. & Lalanne, P., *Theory of the Spontaneous Optical Emission of Nanosize Photonic and Plasmon Resonators*, *Phys. Rev. Lett.* **110**, 237401 (2013).
- [40] Greuter, L. *et al.*, *A small mode volume tunable microcavity: Development and characterization*, *Appl. Phys. Lett.* **105** (2014), 10.1063/1.4896415.
- [41] Hunger, D. *et al.*, *A fiber Fabry-Pérot cavity with high finesse*, *New J. Phys.* **12**, 065038 (2010).
- [42] Yeung, T. K., Le Sage, D., Pham, L. M., Stanwix, P. L. & Walsworth, R. L., *Anti-reflection coating for nitrogen-vacancy optical measurements in diamond*, *Appl. Phys. Lett.* **100**, 251111 (2012).
- [43] Pfaff, W. *et al.*, *Unconditional quantum teleportation between distant solid-state quantum bits*, *Science* **345**, 532 (2014).
- [44] Macleod, H. A., *Thin-Film Optical Filters*, 3rd ed. (Institute of Physics Publishing, Bristol and Philadelphia).
- [45] Nemoto, S., *Waist shift of a Gaussian beam by plane dielectric interfaces*. *Appl. Opt.* **27**, 1833 (1988).
- [46] Lynn, T. W.-Z., *Measurement and Control of Individual Quanta in Cavity QED*, Ph.D. thesis, California Institute of Technology (2003).
- [47] Brandstätter, B. *et al.*, *Integrated fiber-mirror ion trap for strong ion-cavity coupling*, *Rev. Sci. Instrum.* **84** (2013), 10.1063/1.4838696.
- [48] Uphoff, M., Brekenfeld, M., Rempe, G. & Ritter, S., *Frequency splitting of polarization eigenmodes in microscopic Fabry-Perot cavities*, *New J. Phys.* **17**, 013053 (2014).
- [49] Element Six, *The Element Six CVD Diamond Handbook* (2015).
- [50] Friel, I., *Control of surface and bulk crystalline quality in single crystal diamond grown by chemical vapour deposition*, *Diam. Rel. Mater.* **18**, 808.
- [51] Jensen, K. *et al.*, *Cavity-enhanced room-temperature magnetometry using absorption by nitrogen-vacancy centers in diamond*, *Phys. Rev. Lett.* **112**, 160802 (2014).
- [52] Joyce, W. B. & DeLoach, B. C., *Alignment of Gaussian beams*, *Appl. Opt.* **23**, 4187 (1984).
- [53] Ruf, M., *Fiber-based fabry-perot microcavities*, (2016), MSc. thesis.



5

OPTIMAL DESIGN OF DIAMOND-AIR MICROCAVITIES FOR QUANTUM NETWORKS USING AN ANALYTICAL APPROACH

Suzanne van Dam, Maximilian Ruf, and Ronald Hanson

Defect centres in diamond are promising building blocks for quantum networks thanks to a long-lived spin state and bright spin-photon interface. However, their low fraction of emission into a desired optical mode limits the entangling success probability. The key to overcoming this is through Purcell enhancement of the emission. Open Fabry-Pérot cavities with an embedded diamond membrane allow for such enhancement while retaining good emitter properties. To guide the focus for design improvements it is essential to understand the influence of different types of losses and geometry choices. In particular, in the design of these cavities a high Purcell factor has to be weighed against cavity stability and efficient outcoupling. To be able to make these trade-offs we develop analytic descriptions of such hybrid diamond-and-air cavities as an extension to previous numeric methods. The insights provided by this analysis yield an effective tool to find the optimal design parameters for a diamond-air cavity.

This chapter has been published in *New Journal of Physics* **20**, 115004 (2018) [1].

5.1. INTRODUCTION

Quantum networks rely on entanglement distributed among distant nodes [2]. Nitrogen-vacancy (NV) defect centers in diamond can be used as building blocks for such networks, with a coherent spin-photon interface that enables the generation of heralded distant entanglement [3, 4]. The long-lived electron spin and nearby nuclear spins provide quantum memories that are crucial for extending entanglement to multiple nodes and longer distances [5–9]. However, to fully exploit the NV centre as a quantum network building block requires increasing the entanglement success probability. One limitation to this probability is the low efficiency of the NV spin-photon interface. Specifically, entanglement protocols depend on coherent photons emitted into the zero-phonon line (ZPL), which is only around 3% of the total emission [10], and collection efficiencies are finite due to limited outcoupling efficiency out of the high-refractive index diamond. These can both be improved by embedding the NV centre in an optical microcavity at cryogenic temperatures, benefiting from Purcell enhancement [11–18]. A promising cavity design for applications in quantum networks is an open Fabry-Pérot microcavity with an embedded diamond membrane [10, 19–21]. Such a design provides spatial and spectral tunability and achieves a strong mode confinement while the NV centre can reside in the diamond membrane far away ($\approx \mu\text{m}$) from the surface to maintain bulk-like optical properties.

The overall purpose of the cavity system is to maximize the probability to detect a ZPL photon after a resonant excitation pulse. This figure of merit includes both efficient emission into the ZPL into the cavity mode, and efficient outcoupling out of the cavity. The core requirement is accordingly to resonantly enhance the emission rate into the ZPL. However this must be accompanied by vibrational stability of the system; an open cavity design is especially sensitive to mechanical vibrations that change the cavity length, bringing the cavity off-resonance with the NV centre optical transition. Furthermore the design should be such that the photons in the cavity mode are efficiently collected. We aim to optimize the cavity parameters in the face of these (often contradicting) requirements. For this task, analytic expressions allow the influence of individual parameters to be clearly identified and their interplay to be better understood. In this manuscript we take the numerical methods developed in [20] as a starting point, and find the underlying analytic descriptions of hybrid diamond-air cavities. We use these new analytic descriptions to investigate the optimal parameters for a realistic cavity design.

We define two boundary conditions for the design of the cavity, within which we operate to maximize the figure of merit: the probability to detect a ZPL photon. Firstly we require the optical transition to be little influenced by decoherence and spectral diffusion so that the emitted photons can be used for generating entanglement between remote spins [3]. Showing enhancement of the ZPL of narrow linewidth NV centres is still an outstanding challenge. The demonstration in [10] employed NV centres in a $1 \mu\text{m}$ thick membrane with optical transitions with a linewidth under the influence of spectral diffusion of $\approx 1 \text{ GHz}$, significantly broadened compared to the $\approx 13 \text{ MHz}$ lifetime-limited value. While the mechanism of broadening is not fully understood, using a thicker diamond may be desired. We therefore conservatively use a diamond membrane thickness of $4 \mu\text{m}$ in the simulations throughout this manuscript. Secondly, we consider a

design that enables long uninterrupted measurements at cryogenic temperatures, potentially at a remote location with no easy access (such as a data center), through the use of a closed-cycle cryostat. The vibrations induced by the cryostat's pulse tube can be largely mitigated passively [21]. Active stabilisation of Fabry-Pérot cavities has been demonstrated [22, 23], including at a high bandwidth [24, 25], however these results have not yet been extended to operation in a pulse-tube cryostat. In the simulations in this manuscript we therefore assume that vibrations lead to passively stabilised cavity length deviations of 0.1 nm RMS [21]. While these boundary conditions influence the simulated maximally achievable probability to detect a ZPL photon, the analytic descriptions in this manuscript are not limited to these parameter regimes.

The layout of this manuscript is the following. We start by describing the one-dimensional properties of the cavities in section 5.2. These are determined by the distribution of the electric field over the diamond and air parts of the cavity and its impact on the losses out of the cavity. In section 5.3 we extend this treatment to the transverse extent of the cavity mode, analyzing the influence of the geometrical parameters. Finally we include real-world influences of vibrations and unwanted losses to determine the optimal mirror transmittivity and resulting emission into the ZPL in section 5.4.

5.2. THE ONE-DIMENSIONAL STRUCTURE OF A HYBRID CAVITY

The resonant enhancement of the emission rate in the ZPL is determined by the Purcell factor [11, 26]:

$$F_p = \xi \frac{3c\lambda_0^2}{4\pi n_d^3} \frac{1}{\delta\nu V}, \quad (5.1)$$

where ξ describes the spatial and angular overlap between the NV centre's optical transition dipole and the electric field in the cavity; c is the speed of light, λ_0 is the free-space resonant wavelength and n_d the refractive index in diamond. $\delta\nu$ is the cavity linewidth (full width at half maximum (FWHM) of the resonance that we assume to be Lorentzian), and V is the mode volume of the cavity. While the ZPL emission rates can be enhanced through the Purcell effect, the off-resonant emission into the phonon side band (PSB) will be nearly unaffected in the parameter regimes considered. This is the result of the broad PSB transition linewidth ($\delta\nu_{PSB}$ is several tens of THz), that leads to a reduced effective quality factor, replacing $\nu/\delta\nu \rightarrow \nu/\delta\nu + \nu/\delta\nu_{PSB}$ [27]. This results in a low Purcell factor for the PSB. Selection rules for the optical transitions further prevent enhancement of the ZPL emission rate to ground states other than the desired one. The resulting branching ratio of photons into the ZPL, into the cavity mode is therefore [12, 16]:

$$\beta = \frac{\beta_0 F_p}{\beta_0 F_p + 1}, \quad (5.2)$$

where β_0 is the branching ratio into the ZPL in the absence of the cavity. Values for β_0 have been found in a range $\approx 2.4 - 5\%$ [10, 12]; we here use $\beta_0 = 3\%$. Note that to maximize the branching ratio we should maximize the Purcell factor, but that if $\beta_0 F_p \gg 1$ the gain from increasing F_p is small.

To optimize the Purcell factor through the cavity design we should consider the cavity linewidth and mode volume. In this section we focus on the linewidth of the cavity, that

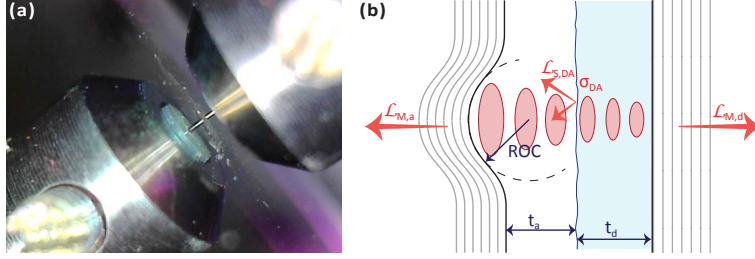


Figure 5.1: Plane-concave fiber-based microcavities. (a) Experimental plane-concave fiber-based microcavity. The cavity is formed at the fiber tip. Reflections of the fiber and holders are visible in the mirror. (b) The geometry of an open diamond-air cavity is described by the diamond thickness t_d , air gap t_a , and the dimple radius of curvature (ROC). The most important losses are through the mirror on the air-side ($\mathcal{L}_{M,a}$) and on the diamond-side ($\mathcal{L}_{M,d}$), and from scattering on the diamond-air interface ($\mathcal{L}_{S,DA}$) resulting from a rough diamond surface with surface roughness σ_{DA} .

5

is determined by the confinement of the light between the mirrors. In section 5.3 we evaluate the mode volume of the cavity.

The cavity linewidth is given by the leak rate out of the cavity: $\delta\nu = \kappa/(2\pi)$. For a general bare cavity this can be expressed as:

$$\delta\nu = \frac{1}{2\pi} \frac{\text{losses per round-trip}}{\text{round-trip duration}} = \frac{1}{2\pi} \frac{\mathcal{L}}{2nL/c} = \frac{c/(2nL)}{2\pi/\mathcal{L}} = \nu_{\text{FSR}}/F, \quad (5.3)$$

for a cavity of length L in a medium with refractive index n . \mathcal{L} are the losses per round-trip. In the last two steps we have written the expression such that one can recognize the standard definitions of free spectral range ($\nu_{\text{FSR}} = c/(2nL)$) and Finesse ($F = 2\pi/\mathcal{L}$). By using this description we assume that the losses per round trip are independent of the cavity length, which is true if losses appear at surfaces only.

For a hybrid diamond-air cavity (Fig. 5.1) this definition does not work anymore: due to the partially reflective interface between diamond and air, we cannot use the simple picture of a photon bouncing back and forth in a cavity. Instead, we should consider the electric field mode and its relative energy density in each part of the cavity. Staying close to the formulations used for a bare cavity, and choosing the speed of light in the diamond part (c/n_d) as a reference, the duration of an *effective round-trip* is $c/(2n_d L_{\text{eff}})$, where L_{eff} is an effective cavity length. This effective length should contain the diamond thickness and the width of the air gap weighted by the local energy density of the photon mode, relative to the energy density in the diamond membrane. Generalizing this, the effective length of the cavity system can be described by the ‘energy distribution length’ [28]:

$$L_{\text{eff}} \equiv \frac{\int_{\text{cav}} \epsilon(z) |E(z)|^2 dz}{\epsilon_0 n_d^2 |E_{\text{max},d}|^2 / 2}. \quad (5.4)$$

In this formulation $\epsilon = \epsilon_0 n^2$ is the permittivity of a medium with refractive index n , $E(z)$ is the electric field in the cavity and $E_{\text{max},d}$ is the maximum electric field in diamond. The integral extends over the full cavity system, such that the effective length automatically includes the penetration depth into the mirrors. The resulting formulation for the

linewidth of a hybrid cavity analogous to Eq. (5.3) is:

$$\delta\nu = \frac{c/(2n_d L_{\text{eff}})}{(2\pi/\mathcal{L}_{\text{eff}})}, \quad (5.5)$$

where \mathcal{L}_{eff} are the losses encountered during the effective round-trip. Here, like in the bare cavity case, we assume these losses to occur only at surfaces. This is a realistic assumption since the most important losses are expected to be from mirror transmission and absorption and diamond surface roughness.

In the above we have taken the field in diamond as reference for the effective round-trip. This choice is motivated by the definition of the mode volume as the integral over the electric field in the cavity relative to the electric field at the position of the NV centre - in diamond. It is given by [27, 29]:

$$V = \frac{\int_{\text{cav}} \epsilon(\vec{r}) |E(\vec{r})|^2 d^3\vec{r}}{\epsilon(\vec{r}_0) |E(\vec{r}_0)|^2}, \quad (5.6)$$

with \vec{r}_0 the position of the NV centre, that we assume to be optimally positioned in an antinode of the cavity field in diamond, such that $E(\vec{r}_0) = E_{\text{max},d}$. We choose to explicitly include effects from sub-optimal positioning in the factor ξ in the Purcell factor (Eq. (5.1)) rather than including them here. If we evaluate the integral in the radial direction we see that the remaining integral describes the effective length as defined above:

$$V = \frac{\pi w_0^2 \int_{\text{cav}} \epsilon(z) |E(z)|^2 dz}{2 \epsilon_0 n_d^2 |E_{\text{max},d}|^2} = \frac{\pi w_0^2}{4} L_{\text{eff}}, \quad (5.7)$$

where w_0 is the beam width describing the transverse extent of the cavity mode at the NV, that we will come back to in section 5.3. We notice that the effective length appears in both the linewidth and the mode volume. In the Purcell factor ($F_p \sim 1/(\delta\nu V)$), the effective length cancels out. This is the result of our assumption that the losses per round-trip occur only at surfaces in the cavity.

The parameter relevant for Purcell enhancement in Eq. (5.5) is thus \mathcal{L}_{eff} . Since these are the losses in an effective round-trip, we expect that they depend on the electric field distribution. We therefore first analyse the electric field distribution in the following section, before finding the effective losses related to the mirror losses and diamond surface scattering in sections 5.2.2 and 5.2.3.

5.2.1. ELECTRIC FIELD DISTRIBUTION OVER DIAMOND AND AIR

The electric field distribution in the cavity on resonance is dictated by the influence of the partially reflective diamond-air interface. If the two parts were separated, the resonant mode in air would have an antinode at this interface, but the mode in diamond would have a node at that position. These cannot be satisfied at the same time, such that in the total diamond-air cavity system the modes hybridize, satisfying a coupled system resonance condition [20, 21, 30]. Two special cases can be distinguished for these resonant modes: the ‘air-like mode’, in which the hybridized mode has an antinode at the diamond-air interface, and the ‘diamond-like mode’ in which there is a node at the interface. For a fixed resonance frequency matching the NV-centre’s ZPL emission frequency

(≈ 470.4 THz), the type of mode that the cavity supports is fully determined by the diamond thickness. The tunable air gap allows for tuning the cavity to satisfy the resonance condition for any frequency.

Using a transfer matrix model [20, 31] we find the electric field distribution for both the air-like and the diamond-like modes, as shown in Fig. 5.2a-b. If the cavity supports a diamond-like mode, the field intensity (proportional to nE_{max}^2 [32]) is higher in the diamond-part, and vice-versa for the air-like mode. The relative intensity of the electric field in the cavity in the diamond membrane compared to the air gap is shown in Fig. 5.2c for varying diamond thicknesses. The relation that the relative intensity satisfies can be explicitly inferred from the continuity condition of the electric field at the diamond-air interface:

$$E_{max,a} \sin\left(\frac{2\pi t_a}{\lambda_0}\right) = E_{max,d} \sin\left(\frac{2\pi t_d n_d}{\lambda_0}\right); \quad (5.8)$$

where the air gap t_a corresponds to the hybridized diamond-air resonance condition [30]:

$$t_a = \frac{\lambda_0}{2\pi} \arctan\left(-\frac{1}{n_d} \tan\left(\frac{2\pi n_d t_d}{\lambda_0}\right)\right) + \frac{m\lambda_0}{2}, \quad (5.9)$$

for an integer m . We use $n_{air} = 1$. The relative intensity in the air gap can thus be written as

$$\frac{E_{max,a}^2}{n_d E_{max,d}^2} = \frac{1}{n_d} \sin^2\left(\frac{2\pi n_d t_d}{\lambda_0}\right) + n_d \cos^2\left(\frac{2\pi n_d t_d}{\lambda_0}\right). \quad (5.10)$$

This ratio reaches its maximal value n_d for an air-like mode, while the minimal value $1/n_d$ is obtained for a diamond-like mode. This relation is shown in Fig. 5.2c as a dashed line, that overlaps with the numerically obtained result.

To remove the mixing of diamond-like and air-like modes, an anti-reflection (AR) coating can be applied on the diamond surface. This is in the ideal case a layer of refractive index $n_{AR} = \sqrt{n_d} \approx 1.55$ and thickness $t_{AR} = \lambda_0/(4n_{AR})$. The effect of a coating with refractive index n_{AR} is shown as a gray line in Fig. 5.2c. For a realistic coating with a refractive index that deviates from the ideal, a small diamond thickness-dependency remains [30].

Next we determine the diamond thickness-dependency of an NV centre's branching ratio into the ZPL [33]. For this we need to find the linewidth and mode volume: we use the transfer matrix to numerically find the cavity linewidth from the cavity reflectivity as a function of frequency, and we calculate the mode volume using Eq. (5.7). The method with which we determine the beam waist w_0 will be later outlined in section 5.3. We further assume that the NV center is optimally placed in the cavity. To include the effect of surface roughness we extend the Fresnel reflection and transmission coefficients in the matrix model as described in [20, 34–36][30]. Fig. 5.2d shows that the resulting emission into the ZPL is strongly dependent on the electric field distribution over the cavity, both for the cases with and without roughness of the diamond interface.

Since we have already seen that the effective cavity length does not appear in the final Purcell factor, the varying emission into the ZPL with diamond thickness has to originate from varying effective losses in Eq. (5.5). In the next paragraphs we develop analytic expressions for the effective losses that indeed exhibit this dependency on the

electric field distribution. We address the two most important sources of losses in our cavity: mirror losses and roughness of the diamond-air interface.

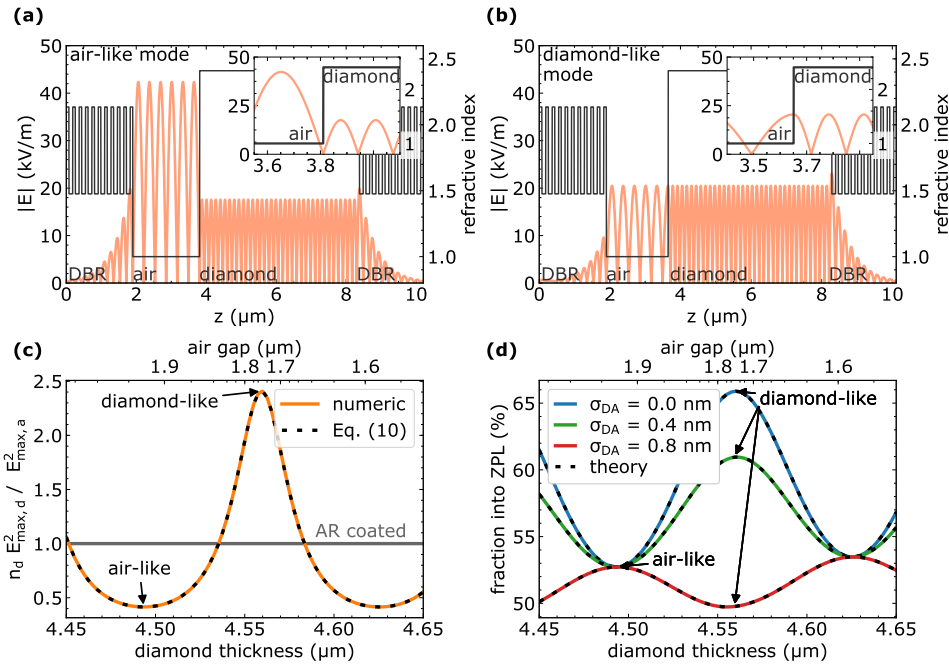


Figure 5.2: Diamond-like and air-like modes in a diamond-based microcavity. (a-b) The electric field strength (orange, left axis) in a diamond-air cavity satisfying the conditions for (a) an air-like mode and (b) a diamond-like mode is calculated using a transfer matrix model. (c) The relative intensity of light in the diamond membrane and air gap is described by Eq. (5.10). It oscillates between $n_d \approx 2.41$ for the diamond-like mode and $1/n_d \approx 0.4$ for the air-like mode. When the diamond is anti-reflection (AR) coated, the oscillations vanish. To stay on the same resonance for varying diamond thickness the air gap is tuned. The corresponding values on the top x-axis do not apply to the cavity with AR coating. (d) The fraction of photons emitted into the ZPL shows a strong dependency on the diamond thickness, presented for three values of RMS diamond roughness σ_{DA} . The emission into the ZPL is determined from Eqs. (5.1) and (5.2), with the mode volume as described in section 5.3. The linewidth is numerically found from the transfer matrix model (solid lines) or with analytic descriptions using Eq. (5.5) together with Eqs. (5.11) and (5.15) (black dashed lines). The mirror transmittivity corresponds to a distributed Bragg reflector (DBR) stack with 21 alternating layers of Ta_2O_5 ($n = 2.14$) and SiO_2 ($n = 1.48$) (giving $\mathcal{L}_{M,A} = 260$ ppm and $\mathcal{L}_{M,D} = 630$ ppm). The dimple radius of curvature used is $\text{ROC} = 25$ μm .

5.2.2. MIRROR LOSSES

As described at the start of this section the mirrors on either side of a bare cavity are encountered once per round-trip, making the total mirror losses simply the sum of the individual mirror losses. For a hybrid cavity, we have rephrased the definition of linewidth to Eq. (5.5) by introducing an effective round-trip. In this picture, the mirrors on the diamond side are encountered once per round-trip, while the losses on the air side should be weighted by the relative field intensity in the air part. The resulting effective mirror

losses are described by:

$$\mathcal{L}_{M,\text{eff}} = \frac{E_{\text{max},a}^2}{n_d E_{\text{max},d}^2} \mathcal{L}_{M,a} + \mathcal{L}_{M,d}, \quad (5.11)$$

where $\mathcal{L}_{M,a}$ are the losses of the mirror on the air side, $\mathcal{L}_{M,d}$ the losses of the diamond side mirror and the relative intensity in the air gap is given by Eq. (5.10). Since this factor fluctuates between $1/n_d$ for the diamond-like mode and n_d for the air-like mode, the effective losses are lower in the diamond-like mode than in the air-like mode. This results in the strong mode-dependency of the emission into the ZPL in Fig. 5.2d. The analytic expression for the effective mirror losses can be used to calculate the fraction of NV emission into the ZPL, resulting in the black dashed line in Fig. 5.2d. This line overlaps with the numerically obtained result. Our model using the effective round-trip thus proves to be a suitable description of the system.

In Fig. 5.3a the effective losses are plotted for a relative contribution of $\mathcal{L}_{M,a}$ to the total mirror losses, that are fixed. If this contribution is larger, the deviations between the effective mirror losses in the diamond-like and air-like mode are stronger.

For a cavity with an AR coating ($E_{\text{max},a}^2 = n_d E_{\text{max},d}^2$) the losses would reduce to the standard case $\mathcal{L}_{M,a} + \mathcal{L}_{M,d}$ as expected. From the perspective of fixed mirror losses the best cavity performance can thus be achieved in a cavity without AR coating, supporting a diamond-like mode.

5.2.3. SCATTERING AT THE DIAMOND-AIR INTERFACE

Next to mirror losses the main losses in this system are from scattering due to diamond roughness. The strength of this effect depends on the electric field intensity at the position of the interface.

The electric field intensity at the diamond-mirror interface depends on the termination of the distributed Bragg reflector (DBR). If the last DBR layer has a high index of refraction, the cavity field has a node at this interface, while if the refractive index is low the field would have a antinode there. The losses due to diamond surface roughness are thus negligible with a high index of refracted mirror. Such a mirror is therefore advantageous in a cavity design, even though a low index of refraction termination interfaced with diamond provides lower transmission in a DBR stack with the same number of layers [20]. We assume a high index of refraction mirror termination and thus negligible surface roughness losses throughout this manuscript. The mirror transmissions specified already take the interfacing with diamond into account.

At the diamond-air interface the field intensity depends on the type of the cavity mode. The air-like mode (with a node at the interface) is unaffected, while the diamond-like mode is strongly influenced (Fig. 5.2d and Fig. 5.3a, green and red lines).

From a matching matrix describing a partially reflective rough interface [20, 34–36], we can find the effective losses at the interface. To get the effective losses on one side of the interface, we find the difference between the intensity of the field travelling towards the surface and the intensity of the field travelling back. The field travelling away from the interface contains contributions both from the reflected field, as well as from the field transmitted through the other side of the interface. For one side, this is thus described

as:

$$\mathcal{L}_{S,12} = 1 - |E_{1,out}|^2 / |E_{1,in}|^2 \quad (5.12)$$

$$= 1 - |\rho'_{12} E_{1,in} + \tau'_{21} E_{2,in}|^2 / |E_{1,in}|^2, \quad (5.13)$$

where $E_{1,in}$ and $E_{2,in}$ are the incoming field from the left-hand side and right-hand side of the interface respectively. $E_{1,out}$ is the outgoing field on the left-hand side of the interface. Furthermore, ρ'_{12} and τ'_{21} are the reflection and transmission coefficients extended to include surface roughness.

We evaluate this expression for losses from the diamond-side and from the air-side, multiplying the latter by the relative intensity (Eq. (5.10)) as we did in the case for the mirror losses. The resulting losses per effective round-trip are:

$$\mathcal{L}_{S,eff} = \mathcal{L}_{S,DA} + \frac{E_{max,a}^2}{n_d E_{max,d}^2} \mathcal{L}_{S,AD} \quad (5.14)$$

$$\approx \sin^2 \left(\frac{2\pi n_d t_d}{\lambda_0} \right) \frac{(1+n_d)}{n_d} (1-n_d)^2 \left(\frac{4\pi\sigma_{DA}}{\lambda_0} \right)^2. \quad (5.15)$$

In the evaluation of this expression we use a Taylor series approximation for the exponents in the reflection and transmission coefficients, and keep terms up to $O((4\pi\sigma_{DA}/\lambda_0)^2)$. A detailed derivation can be found in the Supplementary Information [30]. This description matches well with the numerically found result, which is evidenced in Fig. 5.2d where the gray dashed lines obtained with Eq. (5.15) overlap with the numerical description (green and red lines).

In the case that the diamond would be AR coated, the coating roughness is expected to follow the diamond roughness. In this case, scattering losses are always present, with only a small modification based on the exact diamond thickness. The amount of scattering losses is however lower than in the diamond-like mode.

5.2.4. MINIMIZING THE EFFECTIVE LOSSES

Assuming that mirror losses and scattering at the air-diamond interface are the main contributors to the losses, the total effective losses are $\mathcal{L}_{eff} = \mathcal{L}_{M,eff} + \mathcal{L}_{S,eff}$. Other losses could originate from absorption in the diamond or clipping losses (see section 5.3.2), but have a relatively small contribution in the considered parameter regimes [20].

As described above, an AR coating on the diamond membrane ensures that the intensities of the electric field in diamond and air are the same, while they would otherwise fluctuate with the diamond thickness. The mirror losses are then independent of diamond thickness, and the scattering losses are close to constant. The mirror losses with an AR coating are higher than the losses in the case of no AR coating in the diamond-like mode for the same mirror parameters. The scattering losses however are lower with an AR coating than in the diamond-like mode. Whether the highest Purcell factor can be achieved with or without AR coating thus depends on the relative losses. For the parameters in Fig. 5.2 if the roughness is < 0.4 nm a higher Purcell factor can be achieved in the diamond-like mode without an AR coating than with an AR coating.

If the diamond is not AR coated, we can decide to select either a diamond-like or air-like mode. From the previous section we see that $\mathcal{L}_{M,eff}$ is lowest for the diamond-

like mode, while $\mathcal{L}_{S,\text{eff}}$ is largest in that case. Whether a system supporting an air-like or a diamond-like mode is preferential depends on their relative strength. To be able to pick this freely requires tuning of the diamond thickness on the scale $\lambda_0/(4n_d) = 66$ nm, or using the thickness gradient of a diamond membrane to select the regions with the preferred diamond thickness. Note that the diamond thickness does not have to be tuned exactly to the thickness corresponding to a diamond-like mode. From Fig. 5.2c it is clear that the effective mirror losses are reduced compared to the AR coating value in a thickness range of ≈ 40 nm around the ideal diamond-like value, corresponding to about 35% of all possible diamond thicknesses.

Using the analytic expressions for the losses (Eqs. (5.11) and (5.15)) we can decide whether being in a diamond-like and air-like is beneficial. If the total losses in the diamond-like mode are less than the total losses in the air-like mode, it is beneficial to have a cavity that supports a diamond-like mode. This is the case if:

$$\left(\frac{4\pi\sigma_{DA}}{\lambda_0}\right)^2 \frac{(n_d+1)(n_d-1)^2}{n_d} < \left(n_d - \frac{1}{n_d}\right) \mathcal{L}_{M,a}. \quad (5.16)$$

Fig. 5.3b shows the $\mathcal{L}_{M,a}$ for varying σ_{DA} for which both sides of the above expression are equal. In the region above the curve, where Eq. (5.16) holds, the best Purcell factor is achieved in the diamond-like mode. In the region below the curve, the Purcell factor is maximized for the air-like mode.

Concluding, to achieve the highest Purcell factor low losses are key. These losses are strongly influenced by whether the cavity supports diamond-like or air-like modes. Analytic descriptions of the mirror losses and losses from diamond surface roughness depending on the electric field distribution, enable to find whether a diamond-like or air-like mode performs better.

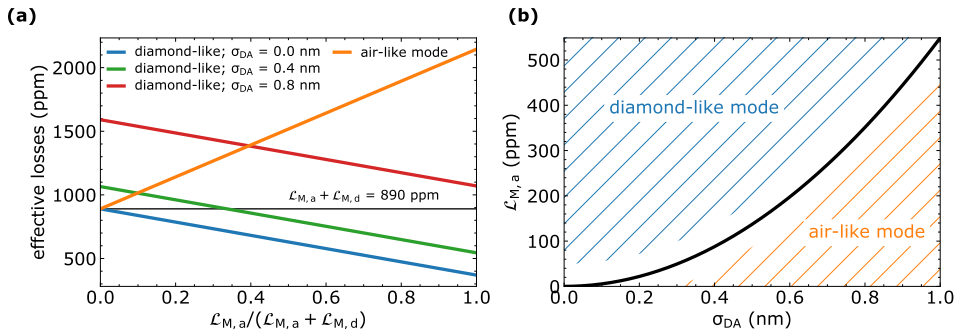


Figure 5.3: Effective losses in a diamond-based microcavity. (a) The effective losses in the cavity depend on whether the cavity supports a diamond-like or air-like mode. The difference is most pronounced if the losses on the air side are dominant. For the fixed value of $\mathcal{L}_{M,a} + \mathcal{L}_{M,d} = 890$ ppm shown, the effective losses can be up to ≈ 2150 ppm in the air-like mode (orange line), or as low as 470 ppm in the diamond-like mode (blue line). Scattering on the diamond-air interface (green and red lines) increase the losses in the diamond-like mode, but do not affect the air-like mode. (b) Depending on the bare losses on the air mirror and the amount of diamond surface roughness the total losses are lowest in the diamond-like mode (shaded region above the black curve) or the air-like mode (below the curve).

5.3. TRANSVERSE EXTENT OF GAUSSIAN BEAMS IN A HYBRID CAVITY

Having analyzed the one-dimensional structure of the cavity, we turn to the transverse electric field confinement. We have seen in Eq. (5.7) that the mode volume can be described as

$$V = \frac{\pi w_{0,d}^2}{4} L_{\text{eff}} \equiv g_0 (\lambda_0 / n_d)^2 L_{\text{eff}}, \quad (5.17)$$

where we define a geometrical factor $g_0 \equiv \frac{\pi w_{0,d}^2}{4} / (\frac{\lambda_0}{n_d})^2$, and $w_{0,d}$ is the beam waist in diamond. Since L_{eff} cancels out in the Purcell factor, g_0 captures all relevant geometrical factors in the mode volume. Note that combining Eq. (5.1) with Eqs. (5.5) and (5.17), the Purcell factor can be written as $F_p = 3\xi / (g_0 \mathcal{L}_{\text{eff}})$.

In this section we describe how to find the beam waist $w_{0,d}$, and which parameters play a role in minimizing it. Furthermore, we quantify the losses resulting if the beam extends outside of the dimple diameter.

5.3.1. BEAM WAIST

We describe the light field in our cavity using a coupled Gaussian beams model [20]. The hybrid cavity supports two Gaussian beams: one that lives in the air gap of the cavity, and one in the diamond (Fig. 5.4a, indicated in orange and blue respectively). The boundary conditions for the model are provided by the diamond thickness, width of the air gap and the radius of curvature (ROC) of the fiber dimple [30]. In the model we assume that the diamond surface is planar. We note that this deviates from the assumption in [20], where the diamond surface is assumed to follow the beam curvature at the interface. The latter assumption would introduce a lensing effect, leading to a narrower effective beam waist than for a plane surface. The planar interface causes mixing with higher-order modes, but the influence of these effects is expected to be small due to the large radius of curvature of the mode at the interface [20].

A solution to this model provides the beam waist of both beams ($w_{0,d}$ and $w_{0,a}$) and the related Rayleigh lengths ($z_{0,d}$, $z_{0,a}$) as well as the location of the beam waist of the air beam with respect to the plane mirror, Δz_a . Previously such a model has been solved numerically [20], but an analytic solution gives insight in the influence of the individual cavity parameters. The analytic solution that we find is given by [30]:

$$w_{0,a} = w_{0,d}, \quad (\rightarrow z_{0,a} \approx z_{0,d} / n_d); \quad (5.18)$$

$$\Delta z_a = t_d \left(1 - \frac{1}{n_d} \right); \quad (5.19)$$

$$w_{0,d} = \sqrt{\frac{\lambda_0}{\pi}} \left(\left(t_a + \frac{t_d}{n_d} \right) \left(\text{ROC} - \left(t_a + \frac{t_d}{n_d} \right) \right) \right)^{1/4}. \quad (5.20)$$

In the last expression for the beam waist we recognize the standard expression for the beam waist of a plane-concave cavity [19], but with a new term taking the position of cavity length:

$$L' \equiv t_a + \frac{t_d}{n_d} (= t_a + t_d - \Delta z_a). \quad (5.21)$$

As an important result, the influence of the diamond thickness is a factor $1/n_d \approx 0.42$ less than that of the width of the air gap. We indeed see in Fig. 5.4c,d that increasing the air gap from 1 to 4 μm (green line) has a larger effect on $w_{0,d}$ and g_0 than increasing the diamond thickness from 1 to 4 μm (orange line).

The minimal air gap that can be achieved is set by the dimple geometry (see Fig. 5.4b). Smooth dimples with a small ROC can be created in several ways, including with CO_2 laser ablation or focused-ion-beam milling of optical fibers or fused silica plates [19, 37–40]. The dimple depth for dimple parameters as considered here is typically $z_d \approx 0.2 - 0.5 \mu\text{m}$, while a relative tilt between the mirror of an angle θ introduces an extra distance of $z_f = D_f/2 \sin(\theta) \approx D_f \theta/2$, which is $\approx 4 \mu\text{m}$ for a fiber cavity [30]. This last effect is thus dominant over the dimple depth. To reduce the minimal air gap in fiber-based cavities, the most important approach to lowering the mode volume is thus by shaping the fiber tip [41]. For cavities employing silica plates the large extent of the plates demands careful parallel mounting of the mirror substrates.

5

5.3.2. CLIPPING LOSSES

The laser-ablated dimple has a profile that is approximately Gaussian (Fig. 5.4b). Beyond the radius $D_d/2$ the dimple significantly deviates from a spherical shape. If the beam width on the mirror (w_m) approaches this value, significant clipping losses result [19]:

$$\mathcal{L}_{clip} = \exp\left(-2\left(\frac{D_d/2}{w_m}\right)^2\right). \quad (5.22)$$

Using our coupled Gaussian beam model we find a numerical (Fig. 5.4e, solid line) and analytical (dashed line) solution to the beam width on the mirror and the resulting clipping losses (Fig. 5.4f). Like $w_{0,d}$, w_m is influenced more strongly by the air gap width than by the diamond thickness. Consequently, the clipping losses are small even when the diamond membrane is relatively thick. For a Gaussian dimple with $\text{ROC} = 25 \mu\text{m}$ and $z_d = 0.3 \mu\text{m}$, we expect that $D_d \approx 7.7 \mu\text{m}$. In this case for $t_d \approx 4 \mu\text{m}$ and $t_a < 2 \mu\text{m}$, the influence of clipping losses is negligible compared to other losses. The influence of clipping losses can be larger for cavity lengths at which transverse mode mixing appears [42].

Finally we note that the clipping losses should be treated in line with the method developed in section 5.2. The effective clipping losses are the clipping losses as found above, weighted by the relative field intensity in air (Eq. (5.10)).

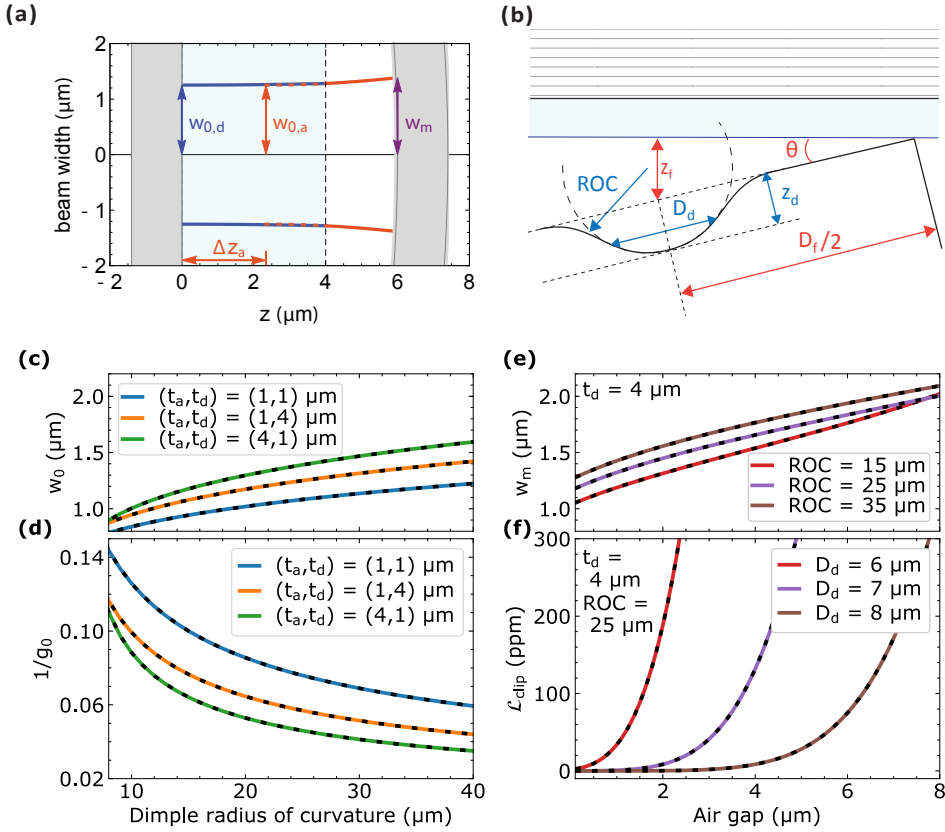


Figure 5.4: Transverse extent of Gaussian beams in a microcavity. (a) The transverse extent of the cavity mode is described using a Gaussian beams model [20], with a beam in diamond (blue) and air (orange), that are coupled at the diamond-air interface, where the beam widths match and the beam curvatures satisfy $n_d R_a = R_d$ for a planar diamond surface. The beam curvature of the air beam at the dimple follows the dimple's radius of curvature (ROC, here 25 μm). The beam waist of the diamond beam ($w_{0,d}$) is fixed at the plane mirror, whereas the position of the air beam waist ($w_{0,a}$) at $z = \Delta z_a$ is obtained as a solution to the model. (b) Schematic of the cavity geometry. The dimple has a Gaussian shape with diameter D_d (full width at $1/e$ of the Gaussian) and radius of curvature ROC , resulting in a minimum distance from fiber to mirror of z_d . The extent of the fiber (D_f) in combination with a fiber tilt θ result in an minimum extra cavity length of z_f . Figure is not to scale. (c-d) Numerical (solid lines) and analytical (dashed lines) solutions for (c) $w_{0,d}$ and (d) the corresponding factor g_0 (Eq. (5.17)) exhibit a stronger dependence on the air gap than on the diamond thickness, as described by Eq. (5.21). The exact analytic solution overlaps with the numerically obtained result. (e-f) The ratio of the beam width on the concave mirror w_m (e) and the dimple diameter D_d determine the strength of the clipping losses per round-trip (f). We here fix $t_d = 4$ μm.

5.4. INCLUDING REAL-WORLD IMPERFECTIONS

From the perspective of Purcell enhancement alone the requirements for the mirrors of our Fabry-Pérot cavity are clear: since the Purcell factor is proportional to the quality factor of the cavity, high reflectivity of the cavity mirrors will provide the largest Purcell factor.

But when including real-world imperfections, we have to revisit this conclusion. In an open cavity system, having high-reflectivity mirrors comes with a price: the resulting narrow-linewidth cavity is sensitive to vibrations. And next to that, unwanted losses in the cavity force motivate an increase of the transmission of the outcoupling mirror, to detect the ZPL photons efficiently. In this section we analyse how both these effects influence the optimal mirror parameters.

5.4.1. VIBRATION SENSITIVITY

The benefit of tunability of an open Fabry-Pérot cavity has a related disadvantage: the cavity length is sensitive to vibrations. This issue is especially relevant for systems as considered here that require operation at cryogenic temperatures. Closed-cycle cryostats allow for stable long-term operation, but also induce extra vibrations from their pulse-tube operation. In setups specifically designed to mitigate vibrations passively [21] vibrations modulate the cavity length over a range with a standard deviation of approximately 0.1 nm. Here we discuss how to make a cavity perform optimally in the presence of such vibrations.

If vibrations change the cavity length, the cavity resonance frequency is modulated around the NV center emission frequency. For a bare cavity (with $\nu_{\text{res}} = mc/(2nL)$) the resonance frequency shift $d\nu_{\text{res}}$ due to vibrations over a characteristic (small) length dL can be described by:

$$|d\nu_{\text{res}}| = \nu_{\text{res}} dL/L. \quad (5.23)$$

Comparing this to the cavity linewidth $\delta\nu = \nu_{\text{FSR}}/F = c/2nLF$ and using $\nu_{\text{res}} = c/(n\lambda_{0,\text{res}})$ we find:

$$\frac{d\nu_{\text{res}}}{\delta\nu} = 2 \frac{dL}{\lambda_{0,\text{res}}} F. \quad (5.24)$$

For the impact of the vibrations the cavity length is thus irrelevant: rather the finesse plays an important role. If we demand that $d\nu_{\text{res}} < \delta\nu$ we find that we would need to limit the finesse to $F < \lambda_{0,\text{res}}/(2dL)$.

For a hybrid cavity the frequency response is modified compared to the bare cavity situation by the influence of diamond-like and air-like modes. To find the modified response we evaluate the derivative of the resonance condition [30] at the diamond-like and air-like mode:

$$\frac{d\nu_{a,d}}{dt_a} = -\frac{c}{(t_a + n_d t_d) \lambda_{0,\text{res}}} \left(1 \pm \frac{n_d - 1}{n_d + 1} \frac{2n_d t_d}{t_a + n_d t_d} \right). \quad (5.25)$$

The plus-sign on the left hand side corresponds to the case for an air-like mode, and the minus-sign corresponds to a diamond-like mode. A diamond-like mode is therefore less sensitive to vibrations than an air-like mode. This difference can be significant. For $t_d \approx 4 \mu\text{m}$ and $t_a \approx 2 \mu\text{m}$, $\frac{d\nu_{a,d}}{dt_a} \approx 7 \text{ GHz}/\text{\AA}$ in the air-like mode, while $\frac{d\nu_{a,d}}{dt_a} \approx 1 \text{ GHz}/\text{\AA}$

in the diamond-like mode. The vibration susceptibility of a cavity with an AR coated diamond reduces to the bare cavity expression Eq. (5.23), with $L = t_a + n_d t_d + \lambda_0/2$, and thus takes an intermediate value between those for the air-like and diamond-like modes.

We include these vibrations in our model that describes the emission into the ZPL [30]. The results are shown as solid lines in Fig. 5.5a-b, for the diamond-like and air-like mode respectively. For a system with vibrations $\sigma_{\text{vib}} = 0.1$ nm, the emission into the ZPL for the diamond-like mode is $\approx 40\%$ for total losses of ≈ 800 ppm, corresponding to a finesse of $F \approx 8000$.

The optimal losses may thus be higher than the minimal value set by unwanted losses. The losses can be increased by increasing the transmission through the outcoupling mirror. In this way not only vibration stability but also an improved outcoupling efficiency is achieved, as we see below.

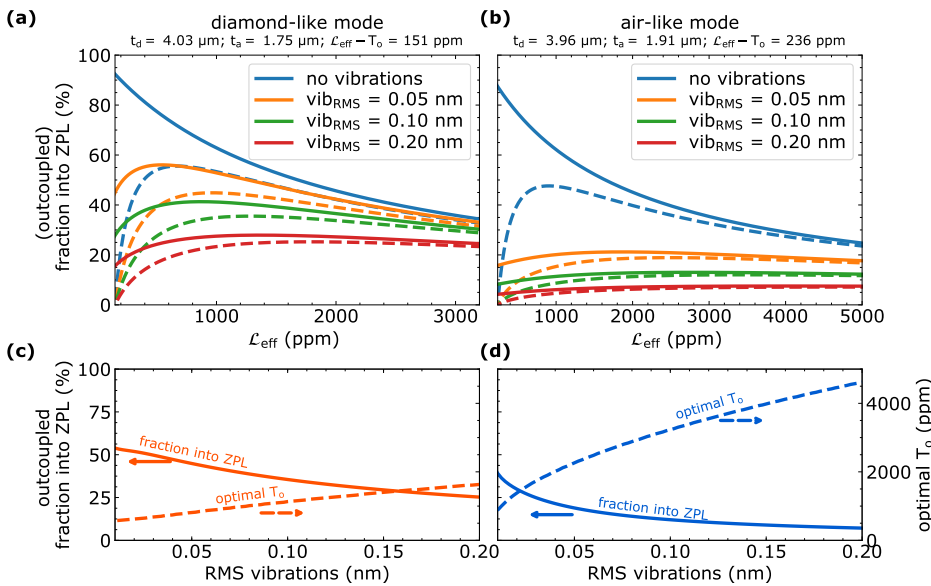


Figure 5.5: Optimal mirror parameters for a cavity under realistic conditions. (a-b) Vibrations impact the average emission into the ZPL (solid lines) for (a) the diamond-like mode and more strongly for (b) the air-like mode. A reduced vibration sensitivity can be achieved for both by increasing the total cavity losses at the expense of a lower on-resonance Purcell factor. The fraction of ZPL photons outcoupled through the desired mirror (dashed line) can be increased by increasing the total losses via the transmittivity of the outcoupling mirror T_0 . Outcoupling is assigned to be via the flat mirror, and the used parameters are $\mathcal{L}_{M,a} = 84$ ppm, $\mathcal{L}_{M,d} = T_0 + 34$ ppm, $\sigma_{\text{DA}} = 0.25$ nm RMS, and $\text{ROC} = 20 \mu\text{m}$. (c-d) By choosing an optimal T_0 (dashed line, right x-axis) the maximum outcoupled fraction into the ZPL for each level of vibrations (solid line, left x-axis) is obtained for (c) the diamond-like mode and (d) the air-like mode.

5.4.2. OUTCOUPLING EFFICIENCY

We do not only want to enhance the probability to emit a ZPL photon per excitation, but also want to couple this photon out of the cavity into the desired direction. The

outcoupling efficiency is given by $\eta_o = T_o / \mathcal{L}_{\text{eff}}$, with T_o the transmittivity of the outcoupling mirror. We choose to assign the plane mirror on the diamond side of the cavity as the outcoupling mirror. This assignment is motivated by comparison of the mode-matching efficiencies between the cavity mode and the dimpled fiber, and between the cavity mode and the free space path. For the free space path in principle perfect overlap with the Gaussian mode can be achieved, while for the fiber side this is limited to $\approx 50\%$ for a cavity with $ROC = 20 \mu\text{m}$, $t_d = 4 \mu\text{m}$, and $t_a = 2 \mu\text{m}$ [19, 30, 43]. Moreover, in this regime the mode-matching efficiency can only be improved by increasing each of these parameters, thereby compromising Purcell enhancement [30]. Since the plane mirror is interfaced with diamond, we note that in the transmission T_o this diamond termination has to be taken into account. When using a DBR stack with a high refractive index final layer, T_o is higher than the transmission of the same stack in air.

The larger the unwanted losses ($\mathcal{L}_{\text{eff}} - T_o$) in the cavity are, the higher the transmission through the output mirror has to be to achieve the same outcoupling efficiency. The contributing unwanted losses are transmission through the non-outcoupling mirror, scattering and absorption in both mirrors, and scattering at the diamond-air interface. Using values of ≈ 50 ppm, ≈ 24 ppm and ≈ 10 ppm for mirror transmission, scattering and absorption [21], and a diamond-air interface roughness of $\sigma_{\text{DA}} = 0.25$ nm [10, 44, 45], we find that the unwanted losses are 139 ppm (236 ppm) for the diamond-like (air-like) mode using the analytic expression from Eqs. (5.11) and (5.15).

An outcoupling efficiency $\eta_o > 0.5$ is then achieved for $T_o > 139$ ppm (236 ppm). The additional losses this would add to the cavity system are less than what is optimal for typical vibrations of $\sigma_{\text{vib}} \approx 0.1$ nm ($\rightarrow \mathcal{L}_{\text{eff}} \approx 800$ ppm (3000 ppm)) for both the diamond-like and air-like modes. Vibrations thus have a dominant effect. To improve the cavity performance in this regime focus should thus be on the reduction of vibrations over the reduction of unwanted losses. A possible route for vibration reduction is by extending active cavity stabilisation techniques for Fabry-Pérot cavities [22–25] to operation under pulse-tube conditions.

Including the outcoupling efficiency in our model we find the fraction of photons that upon NV excitation are emitted into the ZPL and subsequently coupled out of the cavity into the preferred mode (dashed lines in Fig. 5.5a,b). For each value of vibrations, we can maximize this fraction by picking an optimal T_o . For the diamond-like and air-like mode the results of this optimization are shown in Fig. 5.5c,d. For vibrations of 0.1 nm, the best results ($\approx 35\%$ probability of outcoupling a ZPL photon) are expected to be achieved in a diamond-like mode with $T_o \approx 1200$ ppm. We note that this corresponds to a modest Purcell factor of 40, leading to an excited state lifetime reduction to 5.2 ns, and a lifetime-limited linewidth of 31 MHz. Purcell factors higher than this lead to increased linebroadening, which should be taken into account for optical excitation, see e.g. Ref [46]. Increased Purcell factors at such levels have a small effect on the resulting emission into the ZPL (Eq. (5.2)), and thus a limited benefit for an optimal design.

5.5. CONCLUSIONS

In summary, we have developed analytical descriptions giving the influence of key parameters on the performance of a Fabry-Pérot cavity containing a diamond membrane. This analytical treatment allows us to clearly identify sometimes conflicting require-

ments and guide the optimal design choices.

We find that the effective losses in the cavity are strongly dependent on the precise diamond thickness. This thickness dictates the distribution of the electric field in the cavity, with as extreme cases the diamond-like and air-like modes in which the field lives mostly in diamond and air respectively. As a result, the losses due to the mirror on the air side are suppressed by a factor n_d in diamond-like modes while they are increased by the same factor in the air-like modes. In contrast the losses resulting from diamond surface roughness are highest in the diamond-like mode. The two types of losses can therefore be traded-off against each other. If the diamond surface roughness can be made sufficiently low (< 0.4 nm RMS for mirror losses on the air gap side of 85 ppm), the total losses are lowest in the diamond-like mode.

The transverse confinement of the cavity is captured in a geometrical factor g_0 that depends on the beam waist alone. It is determined by the radius of curvature of the dimple and an expression that captures the effect of the cavity component thicknesses: $t_a + t_d/n_d$. The width of the air gap t_a thus has a dominant influence, while the influence of the diamond thickness t_d is reduced by the diamond refractive index n_d . From a geometrical perspective, the focus in the cavity design should thus be on small radii of curvature and small air gaps.

Although the highest Purcell factors are achieved for low cavity losses, vibrational instability of the cavity length and the presence of unwanted losses suggest that lowering the cavity finesse can be advantageous. We find that a cavity supporting an air-like mode is more severely affected by vibrations than one supporting a diamond-like mode. For example, for vibrations of 0.1 nm RMS and unwanted losses of ≈ 190 ppm we find that the optimal fraction of ZPL photons reaching the detector is obtained with a diamond-like mode and an outcoupling mirror transmission of $T_o \approx 1200$ ppm.

The experimentally realistic parameter regimes considered here include a $4 \mu\text{m}$ diamond thickness to support optically coherent NV centres and vibrations of 0.1 nm RMS under pulse-tube operation with passive stabilisation. In this regime with an optimized design an emission efficiency of ZPL photons into the desired outcoupled optical mode after resonant excitation of 35% can be achieved. This constitutes a two orders of magnitude improvement compared to existing approaches, for which the branching ratio into the ZPL is $\approx 3\%$ and the collection efficiencies are typically $\approx 10\%$ [47].

Purcell enhancement with open Fabry-Pérot cavities will open the door to efficient spin-photon interfaces for diamond-based quantum networks. The analysis presented here clarifies the design criteria for these cavities. Future experimental design and investigation will determine how to combine such cavities with resonant excitation and detection for spin-state measurement [48] and long distance entanglement generation [47, 49, 50].

ACKNOWLEDGEMENTS

We thank J. Benedikter, L. Childress, A. Galiullin, E. Janitz, S. Hermans, P.C. Humphreys, and D. Hunger for helpful discussions. We acknowledge support from the Netherlands Organisation for Scientific Research (NWO) through a VICI grant, the European Research Council through a Synergy Grant, and the Royal Netherlands Academy of Arts and Sciences and Ammodo through an Ammodo KNAW Award.

5.6. METHODS

5.6.1. SCATTERING AT A PARTIALLY REFLECTIVE INTERFACE

This section describes how to find the scattering strength for a partially reflective interface.

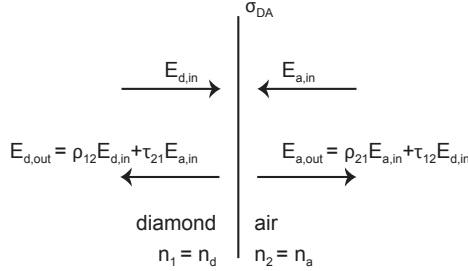


Figure 5.6: The losses for a field incident on the diamond air interface are described the difference between the incoming field and the outgoing field for each side of the interface individually, as in Eq. (5.31). The effective total losses in a diamond-air cavity are given by the losses from each side, multiplied by the relative intensity: $\mathcal{L}_{S,\text{eff}} = \mathcal{L}_{DA} + n_a E_{\text{max},a}^2 (n_d E_{\text{max},d}^2) \mathcal{L}_{AD}$

Firstly, we define the problem by drawing the schematic in Fig. 5.6. We are going to evaluate the losses upon incidence from the left-hand side and right-hand side individually. Upon incidence, the field can be reflected or transmitted. This can be described by a matching matrix, that is given by [20, 31, 34–36]:

$$\begin{pmatrix} E_{1,in} \\ E_{1,out} \end{pmatrix} = \frac{1}{\tau'_{12}} \begin{pmatrix} 1 & -\rho'_{21} \\ \rho'_{12} & \tau'_{12}\tau'_{21} - \rho'_{12}\rho'_{21} \end{pmatrix} \begin{pmatrix} E_{2,out} \\ E_{2,in} \end{pmatrix}; \quad (5.26)$$

$$\begin{aligned} \rho'_{ij} &= \rho_{ij} e^{-2\left(\frac{2\pi\sigma n_i}{\lambda_0}\right)^2} \approx \rho_{ij} \left(1 - 2\left(\frac{2\pi\sigma n_i}{\lambda_0}\right)^2\right); \\ \tau'_{ij} &= \tau_{ij} e^{-1/2\left(\frac{2\pi\sigma(n_j - n_i)}{\lambda_0}\right)^2} \approx \tau_{ij} \left(1 - 1/2\left(\frac{2\pi\sigma(n_j - n_i)}{\lambda_0}\right)^2\right); \end{aligned} \quad (5.27)$$

$$\rho_{ij} = \frac{n_i - n_j}{n_i + n_j}; \quad (5.28)$$

$$\tau_{ij} = \frac{2n_i}{n_i + n_j}.$$

Here $E_{1(2),in}$ and $E_{1(2),out}$ are the incoming and outgoing fields on the left-hand side (right-hand side) of the interface, where the refractive index is $n_1(n_2)$. For the diamond-air interface, we identify $E_{1(2)} = E_{d(a)}$ and $n_1 = n_d, n_2 = n_a$. ρ_{ij} and τ_{ij} are the Fresnel reflection and transmission coefficients, that are extended to ρ'_{ij} and τ'_{ij} to include scattering at an interface with rms roughness of σ_{ij} . We use a Taylor expansion to approximate them, keeping only terms up to $O\left(\left(\frac{2\pi\sigma}{\lambda_0}\right)^2\right)$. Using this formalism, we can write the

outgoing fields in terms of the incoming fields as:

$$E_{1,out} = \rho'_{12} E_{1,in} + \tau'_{21} E_{2,in}; \quad (5.29)$$

$$E_{2,out} = \rho'_{21} E_{2,in} + \tau'_{12} E_{1,in}. \quad (5.30)$$

The losses from the left side of the interface are described by as the normalised difference between the incoming and outgoing field:

$$\mathcal{L}_{S,12} = \frac{n_1 |E_{1,in}|^2 - n_1 |E_{1,out}|^2}{n_1 |E_{1,in}|^2} \quad (5.31)$$

$$= 1 - \frac{|\rho'_{12} E_{1,in} + \tau'_{21} E_{2,in}|^2}{|E_{1,in}|^2}, \quad (5.32)$$

and a similar formulation holds for the right hand side, replacing $1 \leftrightarrow 2$. We see that here the interference between the reflected and transmitted fields plays a role. To evaluate the interference term, we need an expression for $E_{1,in}$ and $E_{2,in}$ in the cavity. To this end we use our knowledge that the cavity field has a node at the DBR on both sides of the cavity. The fields are thus given by:

$$E_{d,in} = |E_{d,in,max}| \left(\sin \left(\frac{2\pi n_d t_d}{\lambda_0} \right) + i \cos \left(\frac{2\pi n_d t_d}{\lambda_0} \right) \right) \quad (5.33)$$

$$E_{a,in} = |E_{a,in,max}| \left(-\sin \left(\frac{2\pi n_a t_a}{\lambda_0} \right) - i \cos \left(\frac{2\pi n_a t_a}{\lambda_0} \right) \right), \quad (5.34)$$

where the field in air travelling to the left has a π phase flip compared to the field in diamond travelling to the right resulting from reflection off the mirror. $E_{d,in,max}$ and $E_{a,in,max}$ are the maxima of the incoming field in the diamond and air part respectively. They are related by Eq. (5.10):

$$|E_{a,in,max}| = \sqrt{\frac{n_d}{n_a}} \sqrt{I_{rel}} |E_{d,in,max}|; \quad (5.35)$$

$$I_{rel} \equiv \frac{n_a}{n_d} \sin^2 \left(\frac{2\pi n_d t_d}{\lambda_0} \right) + \frac{n_d}{n_a} \cos^2 \left(\frac{2\pi n_d t_d}{\lambda_0} \right)$$

where we have defined the relative intensity as I_{rel} to simplify the notation in further calculations.

Further, we know that the air gap width on-resonance is related to t_d as given by Eq. (A.5):

$$\frac{2\pi n_a t_a}{\lambda_0} = \arctan \left(-\frac{n_a}{n_d} \tan \left(\frac{2\pi n_d t_d}{\lambda_0} \right) \right), \quad (5.36)$$

where we keep $n_a = 1$ in the expression. such that:

$$\sin \left(\frac{2\pi n_a t_a}{\lambda_0} \right) = -\sqrt{\frac{1}{I_{rel}}} \sqrt{\frac{n_a}{n_d}} \sin \left(\frac{2\pi n_d t_d}{\lambda_0} \right); \quad (5.37)$$

$$\cos \left(\frac{2\pi n_a t_a}{\lambda_0} \right) = \sqrt{\frac{1}{I_{rel}}} \sqrt{\frac{n_d}{n_a}} \cos \left(\frac{2\pi n_d t_d}{\lambda_0} \right). \quad (5.38)$$

With Eqs. (5.35), (5.37) and (5.38), we can rewrite the field in the air-part in terms of $|E_{d,in,max}|$ and t_d :

$$E_{a,in} = |E_{d,in,max}| \left(\sin \left(\frac{2\pi n_d t_d}{\lambda_0} \right) - i \frac{n_d}{n_a} \cos \left(\frac{2\pi n_d t_d}{\lambda_0} \right) \right). \quad (5.39)$$

We now have all the ingredients we need to evaluate the losses per cavity round trip. For that, we add the losses from the diamond side ($n_1 = n_d$) and from the air side ($n_2 = n_a$), weighting the last one by the factor comparing the relative intensities, as we have done before for the mirror losses. Using the expressions we found above, we arrive at the resulting expression:

$$\mathcal{L}_{S,eff} = \mathcal{L}_{S,DA} + \frac{n_a E_{max,a}^2}{n_d E_{max,d}^2} \mathcal{L}_{S,AD} \quad (5.40)$$

$$= 1 - \frac{|\rho'_{12} E_{d,in} + \tau'_{21} E_{a,in}|^2}{|E_{d,in}|^2} + I_{rel} \left(1 - \frac{|\rho'_{21} E_{a,in} + \tau'_{12} E_{d,in}|^2}{|E_{a,in}|^2} \right) \quad (5.41)$$

$$= 1 + I_{rel} - \frac{|\rho'_{12} E_{d,in} + \tau'_{21} E_{a,in}|^2 + \frac{n_a}{n_d} |\rho'_{21} E_{a,in} + \tau'_{12} E_{d,in}|^2}{|E_{d,in}|^2} \quad (5.42)$$

$$= 1 + I_{rel} - \left(\rho_{12}^{\prime 2} + I_{rel} \frac{n_d}{n_a} \tau_{21}^{\prime 2} + \frac{n_a}{n_d} I_{rel} \frac{n_d}{n_a} \rho_{21}^{\prime 2} + \frac{n_a}{n_d} \tau_{12}^{\prime 2} \right) \quad (5.43)$$

$$- \left(\rho'_{12} \tau'_{21} + \frac{n_a}{n_d} \rho'_{21} \tau'_{12} \right) \frac{E_{a,in} E_{d,in}^* + E_{d,in} E_{a,in}^*}{|E_{d,in}|^2} \quad (5.44)$$

$$\approx n_1 \frac{(n_1 - n_2)^2}{n_1 + n_2} \left(\frac{4\pi\sigma_{DA}}{\lambda_0} \right)^2 + I_{rel} n_2 \frac{(n_1 - n_2)^2}{n_1 + n_2} \left(\frac{4\pi\sigma_{DA}}{\lambda_0} \right)^2 \quad (5.45)$$

$$+ n_2 \frac{(n_1 - n_2)^2}{n_1 + n_2} \left(\frac{4\pi\sigma_{DA}}{\lambda_0} \right)^2 \left(2 \sin^2 \left(\frac{2\pi n_d t_d}{\lambda_0} \right) - 2 \frac{n_1}{n_2} \cos^2 \left(\frac{2\pi n_d t_d}{\lambda_0} \right) \right) \quad (5.46)$$

$$= \sin^2 \left(\frac{2\pi n_d t_d}{\lambda_0} \right) \frac{(n_2 + n_1)}{n_1} (n_2 - n_1)^2 \left(\frac{4\pi\sigma_{DA}}{\lambda_0} \right)^2. \quad (5.47)$$

From this expression we find that the effective losses are proportional to $\sin^2(2\pi n_d t_d / \lambda_0)$, which is the field intensity at the interface. The losses will thus be 0 for an air-like mode, and maximal for a diamond-like mode.

5.6.2. QUANTITATIVE ESTIMATES OF A MINIMUM AIR GAP WIDTH

The minimum air gap in a diamond-air cavity is given by the geometry of the dimple. We here give a detailed description of the relevant parameters.

Independent of the fabrication procedure, the dimple depth z_d is fixed by the radius of curvature and the useful dimple diameter D_d as $z_d \approx D_d^2 / (8ROC)$ [19]. For dimples with radii of curvature as considered in this manuscript ($\approx 15 - 35 \mu\text{m}$) and a diameter large enough to prevent clipping losses (see section 5.3.2), $D_d \approx 8 \mu\text{m}$, the dimple depth is $z_d \approx 0.2 - 0.5 \mu\text{m}$. An extra air gap z_f is introduced when there is an angle θ between optical fiber or plate in which the dimple is created and the flat substrate. If the extent beyond the dimple centre is $D_f/2$, the extra air gap is $z_f = \frac{D_f}{2} \sin(\theta) \approx \frac{D_f}{2} \theta$. For setups

with an optical fiber on a tip-tilt stage [21], we estimate that the maximum angle the fiber tip makes with the flat substrate is $\theta_{max} \approx 70$ mrad (≈ 20 mrad from the tip-tilt stage and ≈ 50 mrad from tilt due to mounting of the fiber). In combination with a typical fiber diameter of $D_f = 125$ μm , this leads to $z_{f,max} \approx 4.4$ μm . This effect is thus dominant over the dimple depth. To reduce the minimal air gap in fiber-based cavities, the most important approach to lowering the mode volume is thus by shaping the fiber tip [41]. For cavities employing silica plates the large extent of the plates demands careful parallel mounting of the mirror substrates.

5.6.3. MODELLING THE EFFECT OF VIBRATIONS ON THE ZPL EMISSION

This section describes how the effect of vibrations is included in the model that describes the emission into the ZPL. First, we find the cavity resonance frequencies for length detuning dt_a , and use these to calculate the corresponding spectral overlap with the NV center emission frequency via

$$\xi_s(dt_a) = \frac{1}{1 + 4Q^2 \left(\frac{\lambda_{ZPL}}{\lambda_{cav}(dt_a)} - 1 \right)^2}, \quad (5.48)$$

where λ_{ZPL} is the NV emission frequency and $\lambda_{cav}(dt_a)$ the cavity frequency for length detuning dt_a . $Q = \nu/\delta\nu$ is the cavity quality factor, that is calculated using the analytic methods presented in section II of the main text. We next multiply the Purcell factor found for the on-resonance case by the spectral overlap and calculate the resulting emission into the ZPL for each length detuning. Finally an average branching ratio β_{vib} is obtained by assuming that the cavity length is normally distributed around the resonant length with a standard deviation σ_{vib} , and integrating over all air gaps around the resonance:

$$\beta_{vib} = \int \frac{\beta_0 \xi_s(dt_a) F_p}{\beta_0 \xi_s(dt_a) F_p + 1} \frac{1}{\sqrt{2\pi\sigma_{vib}^2}} e^{-\frac{dt_a^2}{2\sigma_{vib}^2}} d(dt_a) \quad (5.49)$$

This integral is integrated numerically, to obtain the average branching ratio into the ZPL.

REFERENCES

- [1] van Dam, S. B., Ruf, M. & Hanson, R., *Optimal design of diamond-air microcavities for quantum networks using an analytical approach*, New J. Phys. **20**, 115004 (2018).
- [2] Reiserer, A. & Rempe, G., *Cavity-based quantum networks with single atoms and optical photons*, Rev. Mod. Phys. **87**, 1379 (2014).
- [3] Bernien, H. *et al.*, *Heralded entanglement between solid-state qubits separated by three metres*. Nature **497**, 86 (2013).
- [4] Gao, W. B., Imamoglu, A., Bernien, H. & Hanson, R., *Coherent manipulation, measurement and entanglement of individual solid-state spins using optical fields*, Nat. Photonics **9**, 363 (2015).

- [5] Kolkowitz, S., Unterreithmeier, Q. P., Bennett, S. D. & Lukin, M. D., *Sensing distant nuclear spins with a single electron spin*, Phys. Rev. Lett. **109**, 137601 (2012).
- [6] Taminiau, T. H. *et al.*, *Detection and control of individual nuclear spins using a weakly coupled electron spin*, Phys. Rev. Lett. **109**, 137602 (2012).
- [7] Zhao, N. *et al.*, *Sensing single remote nuclear spins*, Nat. Nanotech. **7**, 657 (2012).
- [8] Kalb, N. *et al.*, *Entanglement Distillation between Solid-State Quantum Network Nodes*, Science **356**, 928 (2017).
- [9] Humphreys, P. C. *et al.*, *Deterministic delivery of remote entanglement on a quantum network*, Nature **558**, 268 (2018).
- [10] Riedel, D. *et al.*, *Deterministic enhancement of coherent photon generation from a nitrogen-vacancy center in ultrapure diamond*, Phys. Rev. X **7**, 031040 (2017).
- [11] Purcell, E. M., *Spontaneous Emission Probabilities at Radio Frequencies*, Phys. Rev. **69**, 681 (1946).
- [12] Faraon, A., Barclay, P. E., Santori, C., Fu, K.-M. C. & Beausoleil, R. G., *Resonant enhancement of the zero-phonon emission from a colour centre in a diamond cavity*, Nat. Photonics **5**, 301 (2011).
- [13] Barclay, P. E., Fu, K. M. C., Santori, C., Faraon, A. & Beausoleil, R. G., *Hybrid nanocavity resonant enhancement of color center emission in diamond*, Phys. Rev. X **1**, 011007 (2011).
- [14] Faraon, A., Santori, C., Huang, Z., Acosta, V. M. & Beausoleil, R. G., *Coupling of nitrogen-vacancy centers to photonic crystal cavities in monocrystalline diamond*, Phys. Rev. Lett. **109**, 2 (2012).
- [15] Hausmann, B. J. M. *et al.*, *Coupling of NV centers to photonic crystal nanobeams in diamond*, Nano Lett. **13**, 5791 (2013).
- [16] Li, L. *et al.*, *Coherent spin control of a nanocavity-enhanced qubit in diamond*. Nat. Commun. **6**, 6173 (2015).
- [17] Riedrich-Möller, J. *et al.*, *Nanoimplantation and Purcell enhancement of single nitrogen-vacancy centers in photonic crystal cavities in diamond*, Appl. Phys. Lett. **106**, 221103 (2015).
- [18] Johnson, S. *et al.*, *Tunable cavity coupling of the zero phonon line of a nitrogen-vacancy defect in diamond*, New J. Phys. **17**, 122003 (2015).
- [19] Hunger, D. *et al.*, *A fiber Fabry–Perot cavity with high finesse*, New J. Phys. **12**, 065038 (2010).
- [20] Janitz, E. *et al.*, *A Fabry-Perot microcavity for diamond-based photonics*, Phys. Rev. A **92**, 043844 (2015).

- [21] Bogdanović, S. *et al.*, *Design and low-temperature characterization of a tunable microcavity for diamond-based quantum networks*, Appl. Phys. Lett. **110**, 171103 (2017).
- [22] Gallego, J. *et al.*, *High-finesse fiber Fabry–Perot cavities: stabilization and mode matching analysis*, Appl. Phys. B Lasers Opt. **122**, 47 (2016).
- [23] Brachmann, J. F. S., Kaupp, H., Hänsch, T. W. & Hunger, D., *Photothermal effects in ultra-precisely stabilized tunable microcavities*, Opt. Expr. **24**, 21205 (2016).
- [24] Khudaverdyan, M. *et al.*, *Controlled insertion and retrieval of atoms coupled to a high-finesse optical resonator*, New J. Phys. **10**, 073023 (2008).
- [25] Janitz, E., Ruf, M., Fontana, Y., Sankey, J. & Childress, L., *A High-Mechanical Bandwidth Fabry-Perot Fiber Cavity*, Opt. Express **25**, 20392 (2017).
- [26] Fox, M., *Quantum Optics: an introduction* (Oxford University Press, 2006).
- [27] Gérard, J.-M., *Solid-state cavity-quantum electrodynamics with self-assembled quantum dots*, in *Single Quantum Dots*, edited by Michler, P. (Springer, 2003) pp. 269–314.
- [28] Greuter, L. *et al.*, *A small mode volume tunable microcavity: Development and characterization*, Appl. Phys. Lett. **105**, 121105 (2014).
- [29] Sauvan, C., Hugonin, J. P., Maksymov, I. S. & Lalanne, P., *Theory of the Spontaneous Optical Emission of Nanosize Photonic and Plasmon Resonators*, Phys. Rev. Lett. **110**, 237401 (2013).
- [30] See supplementary information.
- [31] Orfanidis, S. J., *Electromagnetic Waves and Antennas* (Rutgers University, Piscataway, NJ, 2002).
- [32] Dodd, J. N., *Atoms and Light: Interactions* (Springer US, Boston, MA, 1991).
- [33] We are happy to provide the code on request.
- [34] Filiński, I., *The effects of sample imperfections on optical spectra*, Phys. Status Solidi B **49**, 577 (1972).
- [35] Szczyrbowski, J. & Czapla, A., *Optical absorption in D.C. sputtered InAd Films*, Thin Solid Films **46**, 127 (1977).
- [36] Katsidis, C. C. & Siapkas, D. I., *General transfer-matrix method for optical multilayer systems with coherent, partially coherent, and incoherent interference*, Appl. Opt. **41**, 3978 (2002).
- [37] Dolan, P. R., Hughes, G. M., Grazioso, F., Patton, B. R. & Smith, J. M., *Femtoliter tunable optical cavity arrays*, Opt. Lett. **35**, 3556 (2010).
- [38] Barbour, R. J. *et al.*, *A tunable microcavity*, J. Appl. Phys. **110**, 053107 (2011).

- [39] Trichet, A. A. P., Dolan, P. R., Coles, D. M., Hughes, G. M. & Smith, J. M., *Topographic control of open-access microcavities at the nanometer scale*, Opt. Express **23**, 17205 (2015).
- [40] Najer, D., Renggli, M., Riedel, D., Starosielec, S. & Warburton, R. J., *Fabrication of mirror templates in silica with micron-sized radii of curvature*, Appl. Phys. Lett. **110**, 1 (2017).
- [41] Kaupp, H. *et al.*, *Purcell-Enhanced Single-Photon Emission from Nitrogen-Vacancy Centers Coupled to a Tunable Microcavity*, Phys. Rev. Appl. **6**, 054010 (2016).
- [42] Benedikter, J. *et al.*, *Transverse-mode coupling and diffraction loss in tunable Fabry-Pérot microcavities*, New J. Phys. **17**, 053051 (2015).
- [43] Joyce, W. B. & DeLoach, B. C., *Alignment of Gaussian beams*, Appl. Opt. **23**, 4187 (1984).
- [44] Appel, P. *et al.*, *Fabrication of all diamond scanning probes for nanoscale magnetometry*, Rev. Sci. Instrum. **87**, 063703 (2016).
- [45] Bogdanović, S. *et al.*, *Robust nano-fabrication of an integrated platform for spin control in a tunable microcavity*, APL Photonics **2**, 126101 (2017).
- [46] Hanks, M., Trupke, M., Schmiedmayer, J., Munro, W. J. & Nemoto, K., *High-fidelity spin measurement on the nitrogen-vacancy center*, New J. Phys. **19**, 103002 (2017).
- [47] Hensen, B. *et al.*, *Loophole-free Bell inequality violation using electron spins separated by 1.3 kilometres*, Nature **526**, 682 (2015).
- [48] Robledo, L. *et al.*, *High-fidelity projective read-out of a solid-state spin quantum register*, Nature **477**, 574 (2011).
- [49] Bock, M. *et al.*, *High-fidelity entanglement between a trapped ion and a telecom photon via quantum frequency conversion*, Nat. Commun. **9**, 1998 (2018).
- [50] Dréau, A., Tcheborateva, A., Mahdaoui, A. E., Bonato, C. & Hanson, R., *Quantum frequency conversion to telecom of single photons from a nitrogen-vacancy center in diamond*, Phys. Rev. Appl. **9**, 064031 (2018).

6

NITROGEN-VACANCY CENTRES IN DIAMOND MEMBRANES: REQUIREMENTS, CREATION AND CHARACTERISATION

For application of NV centres in quantum network protocols, coherent optical transitions are key. In pure bulk diamond naturally occurring NV centres can have such coherent transitions. In a thin diamond membrane that can be embedded in a microcavity, NV centres can reside far away from the surface, experiencing a bulk-like environment. However, there are several changes compared to conventional bulk diamond. First, NV centres need to be created in the diamond instead of relying on NV centres naturally occurring during CVD diamond growth. For efficient coupling of the NV to the cavity the NV centre needs to be positioned near the cavity anti-node. Creating NV centres in a well-defined location or with a high density is thus key. Second, to create thin membranes out of bulk diamonds, processing steps are necessary. Both NV creation and processing steps may create defects in the diamond that threaten the NV optical stability. In this chapter we first introduce the creation of thin diamond membranes and requirements for NV positioning in the membrane in section 6.1. Then, we discuss the optical properties required for ZPL enhancement and in entanglement protocols in section 6.2. In section 6.3 we describe NV creation via ion implantation and electron irradiation. We describe the measurement protocols to determine optical properties in section 6.4. Finally we describe the results from characterisation measurements and draw conclusions on the preferred NV creation process and boundary conditions for an etching process in section 6.5.

6.1. INTRODUCTION

We pursue a Fabry-Pérot cavity design where NV centres are embedded in a thin diamond membrane. An important advantage of this approach is that NV centres in these membranes can reside far ($\gg 100$ nm) away from the diamond surface, such that the diamond is like bulk diamond, in which naturally occurring NV centres can have narrow optical transitions [1]. However, defects in the diamond may introduce optical instability of the NV centres [2, 3]. In thin diamond membranes, defects may be introduced in the diamond membranes in two ways. First, defects can be introduced during processing steps that are needed to obtain thin membranes from bulk diamond. Second, defects in the diamond are created during NV creation processes that are needed to satisfy NV positioning constraints. We detail the diamond processing and NV positioning requirements below.

Creating thin diamond membranes The diamond membranes are obtained from bulk samples (Element 6) by laser cutting, thinning and polishing (Almax or DDK). The resulting samples are 10-50 μm thin. The thinnest of these can in principle be used in a cavity (see chapter 11), but further thinning in an etching step can serve two purposes. Firstly a higher Purcell factor can be achieved through a reduction in a mode volume, and clipping losses can be lower through a shorter cavity length. Secondly etching can remove a strained layer that resulted from polishing [4]. We note however that although the presence of polishing damage is well-studied (e.g. in Ref. [5]), no detailed study of its effect on NV centre properties has been performed to our knowledge.

Diamond can be etched by several dry etching processes [6]. Very smooth surfaces can be obtained with Ar/Cl_2 etching [4, 7], but this etch is reported to affect NV properties, potentially resulting from Cl implanted deep into the diamond [8]. An O_2 etch does not influence NV properties, but enlarges impurities and polishing marks, leading to pitches in the diamond surface [8]. For successful etching without compromising NV properties, the two etch processes should be combined in a single recipe, as reported in [4, 8–10].

NV positioning constraints There are two requirements that shape the positioning of NV centres in thin diamond membranes for optical cavities. First, the NV needs to be near an antinode of the cavity mode for maximal Purcell enhancement. The overlap with the antinode is fully determined by the ZPL emission frequency and the depth of the NV centre in the membrane. An optimally positioned NV-centre is at a distance of $(2m + 1)\lambda/(4n_d) = (2m + 1) \times 66$ nm from the diamond-mirror interface, for integer m . Second, the thickness of the diamond membrane at the position of the NV centre determines the type of cavity mode (diamond-like or air-like). This in turn sets the relative strength of loss mechanisms in the cavity and the influence of vibrations, and therefore determines the relative emission into the ZPL chapter 5. NV centres should thus be positioned in a part of the diamond with the right thickness. The diamonds after polishing typically contain a wedge of several $\mu\text{m}/\text{mm}$, such that the diamond thickness varies significantly on a lateral scale of ≈ 100 μm in the diamond.

To find an NV centre that satisfies both requirements, it is highly beneficial to increase the NV centre density compared to the concentration of naturally occurring NV

centres in high purity diamond, that we typically find to be <1 NV per $100 \mu\text{m}^2$. The NV centre density in high purity CVD-grown diamond can be increased using ion implantation or electron irradiation and subsequent annealing. Both processes crucially rely on the creation of vacancies in the diamond lattice. The related damage may impact the coherence properties of NV centres and thus has to be studied before selecting an NV creation process.

6.2. REQUIRED OPTICAL PROPERTIES

Ultimately we aim to use NV centres in diamond membranes for entanglement generation and quantum information protocols. This requires optically coherent transitions. An intermediate goal of ZPL enhancement sets less stringent requirements on the optical properties of NV centres. For ZPL enhancement the requirements are:

- The intrinsic ZPL linewidth (defined as the combined result of the transform-limited linewidth ($\delta\nu_T = 1/(2\pi\tau)$) and pure dephasing) should be less than the cavity linewidth such that the effective quality factor of the system of cavity and NV centre $Q_{\text{eff}} = \nu/(\delta\nu_{\text{NV}} + \delta\nu_{\text{cav}})$ [11] is not limited by the NV centre linewidth.
- The linewidth resulting from the influence of spectral jumps ($\delta\nu_{\text{sd}}$) should be less than the cavity linewidth, such that the NV centre stays on resonance with the cavity.

Since the cavity linewidth following from the design requirements is $\approx 1 - 5$ GHz (chapter 5), we conclude that for ZPL enhancement we need $\delta\nu_{\text{NV}}, \delta\nu_{\text{NV,sd}} \lesssim 1$ GHz.

For entanglement generation the conditions are guided by the indistinguishability of emitted photons necessary for entanglement protocols:

- The intrinsic ZPL linewidth should be close to the transform limited linewidth. This ensures good coherence of the optical transitions that is crucial for photon indistinguishability [12–14].
- The influence of spectral jumps should be not much greater than the intrinsic linewidth. While the impact of spectral jumps can be largely mitigated by performing pre-selection on an on-resonance condition [14], and using a laser resonant to the NV^0 transition for repumping into the negative NV charge state [15], this strategy is effective up to linewidths of ≈ 200 MHz. Beyond this, the preselection procedure causes significant overhead on measurement time.

The lifetime-limited linewidth of the $m_s = 0$ excited state used for entanglement generation is $\delta\nu_T \approx 13$ MHz for an NV in bulk diamond, and $\delta\nu_T \approx 22$ MHz for a Purcell-enhanced NV with a Purcell factor of $F_p = 22$ corresponding to $\beta_{\text{ZPL}} = 40\%$ and $\tau \approx 7$ ns. We thus require the intrinsic linewidth to be tens of MHz, while the requirements on $\delta\nu_{\text{sd}}$ are slightly less constrained: $\delta\nu_{\text{sd}} \lesssim 200$ MHz.

6.3. NITROGEN ION IMPLANTATION AND ELECTRON IRRADIATION

The NV centre density in high purity CVD-grown diamond can be increased using nitrogen ion implantation or electron irradiation. We describe both processes below.

6.3.1. NITROGEN ION IMPLANTATION

Nitrogen ions are implanted into the diamond lattice by accelerating them towards the diamond with high energy. They will penetrate the diamond and end up at a depth below the surface that depends on the implantation energy. By implanting ^{15}N ($\approx 0.4\%$ natural abundance) the NV centres created from implantation can be distinguished from naturally occurring NV centres that are mostly formed from ^{14}N ($\approx 99.6\%$ natural abundance). For our samples, implantation is done commercially at INNOViON. Before implantation the samples are sliced and polished. To prevent the nitrogens from ending up in a strained diamond layer resulting from polishing, a few μm thick layer of diamond can be removed in an etch step. After implantation, the diamond membranes are annealed. In this section, we analyze in detail the process of implantation and annealing.

Implantation parameters The average depth and standard deviation of the distribution in depth ('straggling') of the ions depends on the implantation energy (see Fig. 6.1a). As is clear from the figure, the resulting depth of the nitrogen-defects created during implantation has a narrow distribution, enabling the positioning of most NV centres close to the cavity antinode. For example, for an implantation energy of 330 keV, the straggling is ≈ 35 nm, such that $\approx 65\%$ of the NVs created from the implanted ^{15}N will experience an electric field strength of at least $1/\sqrt{2}$ of the maximum field strength in the field antinode. Note that in the simulations the effect of 'channeling' is not taken into account: the nitrogen ions may follow a channel in the diamond lattice that brings them deeper into the diamond such that the straggling increases.

During implantation the nitrogen ion creates damage in the diamond when it displaces carbon atoms from their lattice sites. In Fig. 6.1b the depth-distribution of implanted ^{15}N and vacancies are shown next to each other, for an implantation energy of 400 keV. While the distribution of vacancies throughout the diamond is broader than the ion-depth distribution, most vacancies reside at a distance of less than 100 nm from the nitrogen ion (Fig. 6.1c). Of ≈ 300 vacancies created upon the implantation of a single ion at this energy, on average ≈ 26 are at a distance of less than 10 nm from the nitrogen ions.

High-temperature annealing In the annealing step after the ion implantation, these vacancies become mobile and can be trapped by the nitrogen defect to form an NV centre. Typically, reported values for conversion of the implanted nitrogen density to NVs vary between 5-50% [18–21], and show a dependency on the implantation energy. In the remainder of this section we aim to estimate how probable it is that vacancies recombine not only with the ^{15}N that created them but also with another nitrogen further away, that could be naturally occurring. Therefore we estimate the diffusion distance of vacancies in diamond during annealing in the paragraph below.

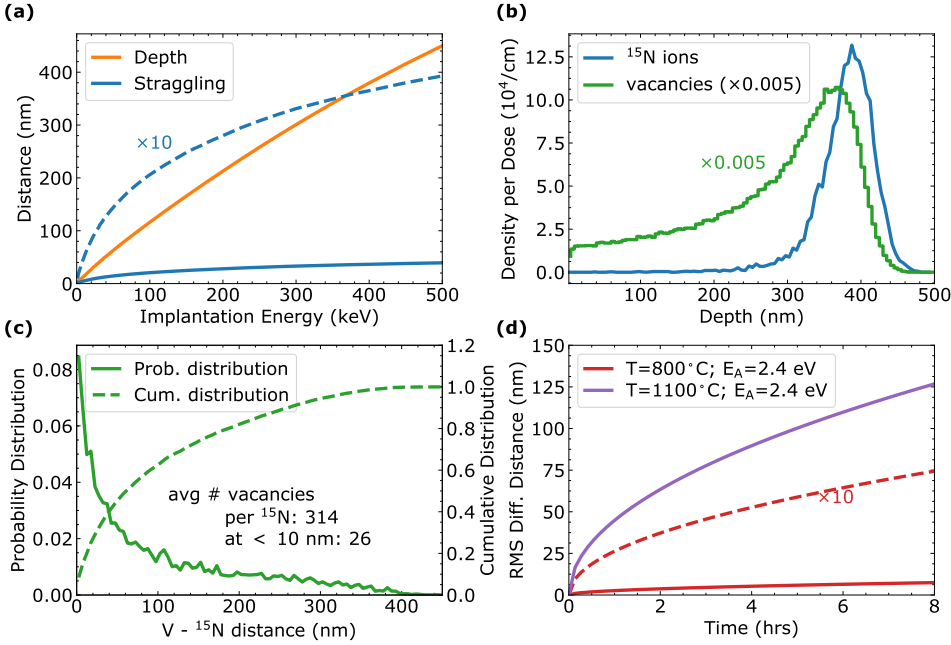


Figure 6.1: ^{15}N implantation in diamond. (a) depth (orange) and rms width of the distribution in depth (longitudinal straggling, blue) of implanted ^{15}N ions, as simulated using SRIM [16] (diamond density: 3.52 g/cm^3 , displacement energy: 37.5 eV). (b) The distribution in distance from the diamond surface of ^{15}N (blue) and vacancies created during implantation (green) shows that the implanted ion locations is peaked around a depth of $\approx 400\text{ nm}$. (c) The distribution of the distance between an implanted ^{15}N and the vacancies it created on its trajectory. The most damage is created close to the stopping point of the ion. (d) During annealing the vacancies become mobile. Their diffusion length (the root-mean-square (rms) distance traversed) is \sqrt{Dt} , with D dependent on the activation energy E_A and the temperature T (see Eq. (6.1)). The annealing protocol used for the samples described in this thesis includes several hours at 800°C and 1100°C [17].

The root-mean-square (rms) distance that the vacancies travel during annealing can be estimated using \sqrt{Dt} , where D is the diffusion coefficient. The diffusion coefficient can be found using [22, 23]

$$D = D_0 e^{-E_A/kT}, \quad (6.1)$$

in which D_0 is a constant prefactor, E_A is the activation energy, k is Boltzmann's constant and T the annealing temperature. We use the reported value of $D_0 = 3.6 \times 10^{-6}\text{ cm}^2/\text{s}$ (though measured for near-surface vacancies) [24], and $E_A = 2.4 \pm 0.3\text{ eV}$ [25]. The resulting rms diffusion distance of the vacancies through the diamond is shown in Fig. 6.1(d) versus annealing time. Evidently, the distance traveled is strongly dependent on the annealing temperature and value of the activation energy. Moreover, the diffusion is additionally influenced by other processes such as the formation of divacancies [26]. We thus use the result only as an indication.

Since the ^{15}N has many vacancies within the rms diffusion distance of the vacancies, there are many vacancies nearby enough to be available for NV creation, even for annealing at a temperature of 800°C . However, to enable recombination with the on-average

more distant naturally occurring nitrogen defects, a longer path is necessary. Assuming that the concentration n_{N14} of naturally occurring defects is < 1 ppb [27], we find that the mean separation between these ^{14}N is $(3/(4\pi n_{N14}))^{1/3} > 100$ nm. From Fig. 6.1, we see that this kind of rms diffusion distance requires annealing for several hours at temperatures $> 800^\circ\text{C}$. Since we follow an annealing recipe similar to [17] with such long annealing at high temperatures¹, we expect to also generate NV centres from naturally occurring defect centres. We do not attempt to make quantitative estimates here of the relative probabilities, given the uncertainties on D_0 , E_A and the concentration of ^{14}N .

While the vacancies created during implantation are essential to turn nitrogen atoms into NV centres, the damage can also create a fluctuating charge environment that impacts the optical coherence and spectral diffusion of the NV centre's excited state. Recently the generation of NV centres with near lifetime-limited linewidths [17] and linewidths < 100 MHz [28] have been reported, relying on a high-temperature annealing step. In these publications the origin of the narrow-line-width NV (native or implanted) has not been verified. In chapter 7 we report observations correlating NV properties after implantation and annealing to the origin of the NV centre.

6.3.2. HIGH-ENERGY ELECTRON IRRADIATION

During electron irradiation, electrons are accelerated towards the diamond at a high energy. We irradiated (bulk) samples at the Reactor Institute Delft at an energy of 2 MeV. Subsequently these samples were annealed, and only after that they were sliced and polished into thin membranes. The possibility to perform irradiation and annealing before the diamond is processed into a membrane reduces the handling steps with the membranes, which is an advantage compared to nitrogen ion implantation.

However, in contrast to ion implantation, electron irradiation does not provide control over the depth of the created vacancies. The stopping range of high-energy electrons of 2 MeV is ≈ 3 mm [29], such that they fully penetrate bulk samples with a typical thickness of 500 μm . On their way they generate a constant number of vacancies of ≈ 1.5 per electron per cm [30]. For a dose of $10^{12} - 10^{14}$ e^-/cm^2 we thus expect a vacancy density of $n_V \approx 1.5 \times 10^{18} - 10^{20}/\text{m}^3$, corresponding to an intervacancy distance of $\approx (\frac{3}{4\pi n_V})^{1/3} \approx 500 - 100$ nm (calculated using the Wigner-Seitz radius). The number of NV centres that are created during annealing through this process strongly depends on the pre-existing nitrogen concentration. Local variations in NV density may thus occur, following variations in nitrogen concentration present during growth.

6.4. MEASUREMENT METHODS

For the characterisation of the optical properties, we study the NV centres at cryogenic temperatures. The setup used for these measurements is schematically described in Fig. 6.2. Since the NV centres we study are embedded in diamond membranes, we need to take extra care to properly identify NV centres against the background fluorescence from the mirror and substrate on which the diamond is bonded. We therefore in this section first

¹During the annealing process for the nitrogen implanted samples in this chapter, the temperature was increased from room temperature to 400°C over a 4 hours period, and then the temperature was held constant for 8 hours. Subsequently, the temperature was further increased to 800°C over a 12 hours period, and held constant for 8 hrs. Finally, the temperature was further increased to 1100°C and held constant for 2 hours.

describe techniques to identify NV centres in diamond membranes, before we outline the measurement sequences used to determine the optical linewidth of these transitions.

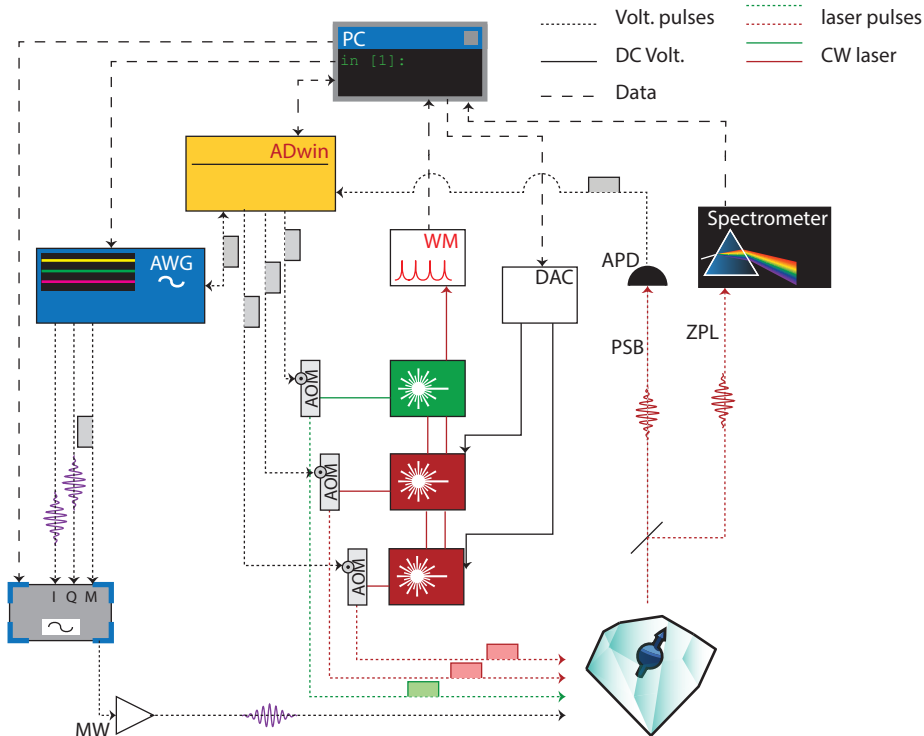


Figure 6.2: Setup for the characterisation of NV centres. Characterisation of the optical properties of NV centres has been performed in two different confocal setups with the same layout. The diamond membrane is either in a flow-cryostat (*Janis ST500*) or in a closed-cycle *Montana Instruments C2* cryostat. The microscope objective for both setups has an $NA = 0.9$. A red tunable laser (*NewFocus Velocity TLB-6300-LN*, 6700, *Toptica DLT pro*) is used for resonant excitation. Their frequencies are measured using a *HighFinesse WS/6* wavemeter, and a green laser at 532 nm is used for charge-reset. All lasers are controlled using free-space acousto-optical modulators (AOMs) in double-pass configuration. The NV emission in the ZPL is separated from the PSB and sent to a spectrometer *Princeton Instruments SP-2500i* with CCD camera *Princeton Instruments PIXIS: 100*, while the PSB is collected on a single-photon APD (*Laser Components*). Figure adapted from Pfaff [31].

6.4.1. NV DETECTION IN DIAMOND MEMBRANES

When imaging NV centres in thin diamond membranes, the diamond surface is close to the focal point. Therefore, background fluorescence from outside the diamond can make it challenging to find and identify NV centres. The background fluorescence can originate from dirt on the diamond-air or diamond-substrate interfaces or from within the substrate onto which the membrane is van-der-Waals bonded. This has two effects.

Firstly, for detecting NV centres it is essential to reduce the uniform background level to the level of NV fluorescence or lower (we typically find that the NV fluorescence gives ≈ 30 kHz detected counts at saturation power for off-resonant excitation in the setups described in Fig. 6.2). Secondly, dirt particles on the interfaces can show up as fluorescence spots that resemble NV centres. Before we describe the measurement techniques that can be used to distinguish NV centres from fluorescence spots of different origin, we describe the sources of background fluorescence.

Sources of background fluorescence We observed uniform fluorescence from the diamond-air or diamond-substrate interface. We find that this fluorescence can be reduced by cleaning the diamond or substrate. If the dirt is on the diamond-air interface this can be done with an oxygen plasma, which removes the need and risk of diamond debonding from the substrate.

Apart from this, we observed background fluorescence from the SiO_2 substrates supporting the DBR stacks on which the diamond membrane is van-der-Waals bonded. We find that the fluorescence has a spectrum that peaks around 675 nm (see Fig. 6.3), that the fluorescence intensity increases at cryogenic temperatures and that it has a long-lifetime component. These results are consistent with observations of non-bridging oxygen hole (NBOH) centres in SiO_2 [32–35]. The density of NBOH centres strongly depends on the quality of fused silica. Substrates with the lowest density of NBOH centres specified as ‘excimer grade’ can be selected.

However, even in high-quality SiO_2 , fluorescence background can be significant compared to the NV fluorescence. Since the emission wavelength overlaps with the NV centre’s emission, we cannot use spectral filtering to decrease the effect of the background. However, there are several other techniques that can be used to operate under conditions of high background fluorescence. Firstly, we use a single-mode (SM) detection fiber. Even though the NV centre’s emission is less efficiently collected into a SM fiber, this is advantageous since the fluorescence background is relatively more strongly suppressed. Secondly the NV centres for NV characterisation can be spatially selected as distant from the substrate as possible, if the membrane is more than approximately $4 \mu\text{m}$ thick. Thirdly, to prevent the excitation of NBOH centres, (high-power) green excitation can be applied as little as possible: in future protocols it can be replaced with yellow and red resonant excitation. This can be applied in a confocal scan by scanning the red laser frequency for every pixel [36]. Finally fluorescence lifetime imaging (FLIM, [37]) can be used to eliminate a fluorescence background. Dirt on the surfaces is typically short-lived (≈ 3 ns), such that the background can be suppressed by selecting the fluorescence with a longer lifetime. The NBOH lifetime is much longer than the NV centre’s, such that FLIM can in principle be performed by selecting short lifetimes. However, in practice this is challenging since the long-lived nature of the background would limit the repetition rate in such an implementation.

NV IDENTIFICATION

Dirt particles can appear in a confocal image as a fluorescence spot. To discern NV centres from such dirt requires identification mechanisms for NVs. If the diamond membrane is relatively thick ($\gtrsim 6 \mu\text{m}$), spots sufficiently far removed from the surface are with

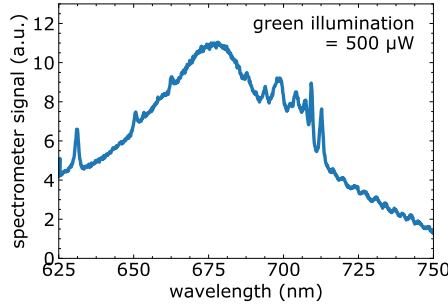


Figure 6.3: Spectrum of mirror background fluorescence at room temperature. The fluorescence spectrum measured on a bare mirror on a SiO₂ substrate around 500 μW of green illumination shows a peak at 680 nm. Since the emission frequencies largely overlap with the NV fluorescence, spectral filtering cannot be used to suppress the background.

high probability single emitters in the crystal lattice. In thinner membranes, such identification is harder, since it is more difficult to establish whether fluorescence originates from within the diamond or from the surface.

A single emitter can be discerned from a dirt particle by its Gaussian profile with a width of ≈ 300 nm, the observation of emission saturation with increasing excitation power or with an autocorrelation measurement with a Hanbury Brown-Twiss setup. To establish whether the emitter can be an NV centre we can probe the polarisation dependency of the excitation efficiency which should be present for all NV centres in a [100]-cut sample. Spots can be identified with certainty as NV centres by measuring their excited state lifetime, electron spin resonance (ESR) response, the fluorescence spectrum of ZPL and PSB or their photoluminescence upon optical excitation around 637 nm.

6.4.2. OPTICAL LINEWIDTH MEASUREMENTS

In line with the requirements outlined in section 6.2, we want to separately measure the homogeneous linewidth and the linewidth under the influence of spectral jumps. We focus our attention to measurements of the E_x and E_y transitions, since these spin-conserving transitions are typically used in entanglement generation protocols.

To measure the homogeneous linewidth, we sweep a tunable laser across the transition frequency, and record the photons emitted into the phonon side band (PSB), Fig. 6.4a. During this measurement we apply continuous microwave excitation to prevent optical pumping out of the $m_s = 0$ manifold. Ionization of the NV centre is prevented by applying low red laser power, which is effective since for powers below the saturation power the ionization rate is proportional to the square of the power. After each scan a second scan over the resonance can be performed to determine if the NV ionized during the original scan. We fit a Lorentzian to the non-ionized traces, and extract the FWHM, $\bar{\gamma}$. A homogeneous linewidth is extracted from the weighted average over many such scans:

$$\bar{\gamma} = \frac{\sum_i \gamma_i \sigma_i^{-2}}{\sum_i \sigma_i^{-2}}, \quad (6.2)$$

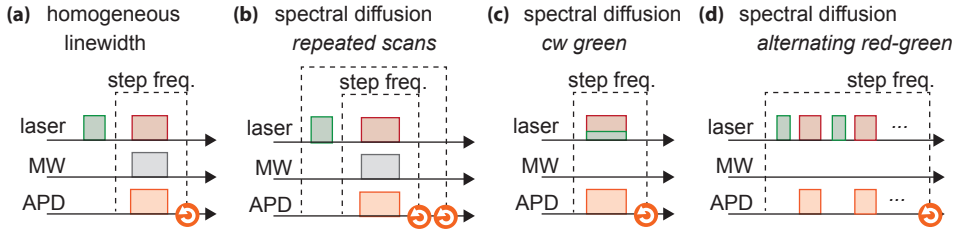


Figure 6.4: Measurement sequences for optical characterisation of the NV centre. (a) The sequence used to probe the homogeneous linewidth. (b) To probe spectral diffusion the sequence in (a) can be repeated several times. (c-d) Additionally, spectral diffusion can be probed without microwaves using continuous wave green and red excitation, or by alternating green and red excitation for an improved signal to noise ratio.

where γ_i are the fitted FWHM of the individual traces, and σ_i the corresponding standard error of the fit parameter.

For a measurement of the linewidth under the influence of spectral jumps we can use three possible measurement sequences. In the first sequence several sweeps as described above are interleaved with a green off-resonant excitation pulse that pumps the NV to the NV^- charge state (Fig. 6.4b). This off-resonance pulse also induces spectral jumps, so that adding the lines from consecutive sweeps gives the linewidth including spectral jumps. In the second sequence the green laser is on at low continuous wave (cw) power during the sweep (Fig. 6.4c). Since the green laser both resets the charge state and initializes the spin state into $m_s = 0$, the additional application of microwave driving is not necessary for this sequence. In an improved version of this sequence the green and red laser excitation are interleaved, with the detections of PSB photons only during red illumination (Fig. 6.4d).

6

6.5. CHARACTERISATION OF OPTICAL PROPERTIES

In this section we summarize the conclusions we draw from the characterisation of NV centres in diamond membranes. For the discussion we focus on two variables: the type of processing that has been performed and the NV creation method. In appendix A.3 we describe the characterisation of many individual samples in detail. The appendix also contains tables with overviews of the observed optical linewidths.

Through characterisation of NVs in membranes with naturally occurring NV centres we find that Ar/Cl₂ etching is detrimental for the optical properties of NV centres: no stable NV centres could be found after such etching. This observation is in agreement with reports in [4, 6, 8]. We therefore confirm the need for an etching recipe that removes the Cl contamination, without compromising diamond smoothness, such as can be achieved with recipes combining Ar/Cl₂ and O₂ etches [4, 8–10].

We characterised several samples with implanted NV centres. In these samples we identified several NV centres with optical properties suitable for entanglement protocols. However, in one of these samples we found that even though ¹⁵N was implanted all NV's in this small set of optically coherent NVs contained a ¹⁴N isotope. In chapter 7 we report on the detailed study that we performed following this observation, correlating

NV optical properties to the source of the nitrogen atom.

Finally we characterised samples containing NV centres created through electron irradiation. The NV centres in these samples consistently show near-lifetime limited optical linewidths. These establish the best results we have obtained with NV centres in diamond membranes. We therefore conclude that electron-irradiation is the most promising path for NV creation in diamond membranes for optical cavities. The lack in positioning accuracy will have to be compensated by an automated characterisation routine, that enables to select NVs at a suitable depth in a part of the membrane with a suitable thickness.

REFERENCES

- [1] Tamarat, P. *et al.*, *Stark shift control of single optical centers in diamond*, Phys. Rev. Lett. **97**, 083002 (2006).
- [2] Fu, K.-M. C., Santori, C., Barclay, P. E. & Beausoleil, R. G., *Conversion of neutral nitrogen-vacancy centers to negatively charged nitrogen-vacancy centers through selective oxidation*, Appl. Phys. Lett. **96**, 121907 (2010).
- [3] Orwa, J. O. *et al.*, *Engineering of nitrogen-vacancy color centers in high purity diamond by ion implantation and annealing*, J. Appl. Phys. **109**, 083530 (2011).
- [4] Appel, P. *et al.*, *Fabrication of all diamond scanning probes for nanoscale magnetometry*, Rev. Sci. Instrum. **87**, 063703 (2016).
- [5] Friel, I., *Control of surface and bulk crystalline quality in single crystal diamond grown by chemical vapour deposition*, Diam. Rel. Mater. **18**, 808.
- [6] Aharonovich, I. & Neu, E., *Diamond nanophotonics*, Adv. Opt. Mater. **2**, 911 (2014).
- [7] Bogdanović, S. *et al.*, *Robust nano-fabrication of an integrated platform for spin control in a tunable microcavity*, APL Photonics **2**, 126101 (2017).
- [8] Cui, S., *Near-surface Nitrogen Vacancy Centers in Diamond*, Ph.D. thesis, Harvard University (2014).
- [9] Johnson, S., Dolan, P. R. & Smith, J. M., *Diamond photonics for distributed quantum networks*, Prog. Quantum Electron. **55**, 129 (2017).
- [10] Challier, M. *et al.*, *Advanced fabrication of single-crystal diamond membranes for quantum technologies*, Micromachines **9**, 148 (2018).
- [11] Gérard, J.-M., *Solid-state cavity-quantum electrodynamics with self-assembled quantum dots*, in *Single Quantum Dots*, edited by Michler, P. (Springer, 2003) pp. 269–314.
- [12] Bylander, J., Robert-Philip, I. & Abram, I., *Interference and correlation of two independent photons*, Eur. Phys. J. D **22**, 295 (2003).

- [13] Batalov, A. *et al.*, *Temporal coherence of photons emitted by single nitrogen-vacancy defect centers in diamond using optical rabi-oscillations*, Phys. Rev. Lett. **100**, 077401 (2008).
- [14] Robledo, L., Bernien, H., Van Weperen, I. & Hanson, R., *Control and coherence of the optical transition of single nitrogen vacancy centers in diamond*, Phys. Rev. Lett. **105**, 177403 (2010).
- [15] Siyushev, P. *et al.*, *Optically controlled switching of the charge state of a single nitrogen-vacancy center in diamond at cryogenic temperatures*, Phys. Rev. Lett. **110**, 167402 (2013).
- [16] Ziegler, J. F., Ziegler, M. & Biersack, J., *The Stopping and Range of Ions in Matter (SRIM-2013, <http://www.srim.org/>)*.
- [17] Chu, Y. *et al.*, *Coherent optical transitions in implanted nitrogen vacancy centers*. Nano Lett. **14**, 1982 (2014).
- [18] Pezzagna, S., Naydenov, B., Jelezko, F., Wrachtrup, J. & Meijer, J., *Creation efficiency of nitrogen-vacancy centres in diamond*, New J. Phys. **12**, 065017 (2010).
- [19] Toyli, D. M., Weis, C. D., Fuchs, G. D., Schenkel, T. & Awschalom, D. D., *Chip-scale nanofabrication of single spins and spin arrays in diamond*. Nano Lett. **10**, 3168 (2010).
- [20] Sangtawesin, S., Brundage, T. O., Atkins, Z. J. & Petta, J. R., *Highly tunable formation of nitrogen-vacancy centers via ion implantation*, Appl. Phys. Lett. **105**, 063107 (2014).
- [21] Yamamoto, T. *et al.*, *Isotopic identification of engineered nitrogen-vacancy spin qubits in ultrapure diamond*, Phys. Rev. B **90**, 081117 (2014).
- [22] Antonov, D. *et al.*, *Statistical investigations on nitrogen-vacancy center creation*, Appl. Phys. Lett. **104**, 012105 (2014).
- [23] Chen, Y. C. *et al.*, *Laser writing of coherent colour centres in diamond*, Nat. Photon. **11**, 77 (2017).
- [24] Hu, X. J., Dai, Y. B., Li, R. B., Shen, H. S. & He, X. C., *The diffusion of vacancies near a diamond (001) surface*, Solid State Commun. **122**, 45 (2002).
- [25] Davies, G., Lawson, S. C., Collins, A. T., Mainwood, A. & Sharp, S. J., *Vacancy-related centers in diamond*, Phys. Rev. B **46**, 13157 (1992).
- [26] Lea-Wilson, M. A., Lomer, J. N. & Van Wyk, J. A., *Electron spin resonance of the R4/W6 defect in irradiated diamond*, Philos. Mag. B **72**, 81 (1995).
- [27] Element Six, *The Element Six CVD Diamond Handbook* (2015).
- [28] Riedel, D. *et al.*, *Deterministic enhancement of coherent photon generation from a nitrogen-vacancy center in ultrapure diamond*, Phys. Rev. X **7**, 031040 (2017).

- [29] Campbell, B. & Mainwood, A., *Radiation damage of diamond by electron and gamma irradiation*, Phys. Status Solidi A **181**, 99 (2000).
- [30] Hunt, D., Twitchen, D., Newton, M., Baker, J. & Anthony, T., *Identification of the neutral carbon $\langle 100 \rangle$ -split interstitial in diamond*, Phys. Rev. B **61**, 3863 (2000).
- [31] Pfaff, W., *Quantum Measurement and Entanglement of Spin Quantum Bits in Diamond*, Ph.D. thesis, Delft University of Technology (2013).
- [32] Skuja, L., Kajihara, K., Hirano, M. & Hosono, H., *Oxygen-excess-related point defects in glassy/amorphous SiO₂ and related materials*, Nucl. Instrum. Methods Phys. Res. Sect. B **286**, 159 (2012).
- [33] Zhang, H. *et al.*, *Laser-induced fluorescence of fused silica irradiated by ArF excimer laser*, J. Appl. Phys. **110**, 013107 (2011).
- [34] Leclerc, N., Pfeleiderer, C., Hitzler, H. & Englisch, W., *Luminescence and transient absorption bands in fused SiO₂ induced by KrF laser radiation at various temperatures*, J. Non-Cryst. Solids **149**, 115 (1992).
- [35] Vaccaro, L., Cannas, M. & Boscaino, R., *Luminescence features of nonbridging oxygen hole centres in silica probed by site-selective excitation with tunable laser*, Solid State Commun. **146**, 148 (2008).
- [36] Bersin, E. *et al.*, *Individual Control and Readout of Qubits in a Sub-Diffraction Volume*, arXiv:1805.06884 (2018).
- [37] Suhling, K. *et al.*, *Fluorescence lifetime imaging (FLIM): Basic concepts and some recent developments*, Med. Photon. **27**, 3 (2015).



7

OPTICAL COHERENCE OF DIAMOND NV CENTRES FORMED BY ION IMPLANTATION AND ANNEALING

Suzanne van Dam*, Michael Walsh*, Maarten Degen, Eric Bersin, Sarah Mouradian, Airat Galiullin, Maximilian Ruf, Mark IJspeert, Tim Taminiau, Ronald Hanson, and Dirk Englund

The advancement of quantum optical science and technology with solid-state emitters such as nitrogen-vacancy (NV) centres in diamond critically relies on the coherence of the emitters' optical transitions. A widely employed strategy to create NV centres at precisely controlled locations is nitrogen ion implantation followed by a high-temperature annealing process. We report on experimental data directly correlating the NV centre optical coherence to the origin of the nitrogen atom. These studies reveal low-strain, narrow-optical-linewidth (< 500 MHz) NV centres formed from naturally-occurring ^{14}N atoms. In contrast, NV centres formed from implanted ^{15}N atoms exhibit significantly broadened optical transitions (> 1 GHz) and higher strain. The data show that the poor optical coherence of the NV centres formed from implanted nitrogen is not due to an intrinsic effect related to the diamond or isotope. These results have immediate implications for the positioning accuracy of current NV centre creation protocols and point to the need to further investigate the influence of lattice damage on the coherence of NV centres from implanted ions.

The results in this chapter have been submitted for publication; arXiv:1812.11523 [1]

*Equally contributing authors

7.1. INTRODUCTION

Coherent optical control over solid-state quantum emitters has enabled new advances in quantum science [2–4] and may lead to technologies such as quantum networks [5]. A quantum network crucially relies on entanglement connections that can be established through a coherent spin-photon interface. The nitrogen-vacancy (NV) defect centre in diamond is a well-suited candidate owing to a spin ground state with a long coherence time [6, 7], nearby nuclear spins for quantum memories [8] or algorithms [9–11], and spin-selective optical transitions allowing for efficient optical spin initialization and readout [12]. Moreover, at low temperature (< 10 K), effects from phonon mixing in the excited state are small [13], and the optical transition can be coherent. Indeed, narrow-linewidth, coherent optical transitions [14–16] have been used for the generation of indistinguishable photons suited for two photon quantum interference [17, 18] and entanglement generation between remote NV centres [19].

To date, all experiments employing coherent photons from NV centres have been performed with NV centres that were formed during diamond growth. Key to their optical coherence is that these NV centres experience an environment with few defects, since the stability of optical transitions (as with many solid-state systems) suffers from unwanted interactions with nearby bulk and surface defects leading to changes in the strain and electric field environment [20–24]. For NV centres with a broadened linewidth below ≈ 200 MHz dominated by slow spectral diffusion, protocols using resonant charge repumping [25] and real-time monitoring of the transition frequency [26] have been used to reduce the broadened linewidth to an effective linewidth of below 50 MHz, suitable for quantum optical experiments. However, such protocols are challenging for NV centres with greater spectral diffusion.

7

7.2. NITROGEN ION IMPLANTATION

Instead of being limited to NV centres formed during diamond growth, they can be created, for example by nitrogen ion implantation [27]. Nitrogen ion implantation provides an NV positioning accuracy that enables integration with on-chip photonics [28, 29] and coupling between nearby NV centres [30–32]. Precise positioning of NV centres or accurately registering their location is also a prerequisite for optimal overlap of the dipole with the electric field mode of diamond optical cavities, for engineering and enhancing light-matter interaction [24, 33–38]. Moreover, ion implantation allows for the creation of single NV centres in high purity diamond, providing a potentially low-defect environment [22].

However, the bombardment of the diamond with nitrogen ions creates crystal damage that can deteriorate spin and optical coherence properties of NV centres [21, 22]. High-temperature annealing can mitigate some of these issues by repairing the diamond lattice [39–42]. A procedure including a low implantation dose, careful cleaning, and high-temperature annealing was reported by Chu et al. [43], leading to the creation of narrow-linewidth NV centres. These narrow-linewidth NV centres can result from implanted nitrogen atoms, or from native nitrogen atoms combined with implantation-induced vacancies (Fig. 7.1a). In principle, the source of nitrogen can be verified by implanting ^{15}N isotopes (natural abundance 0.37%) and resolving the hyperfine structure

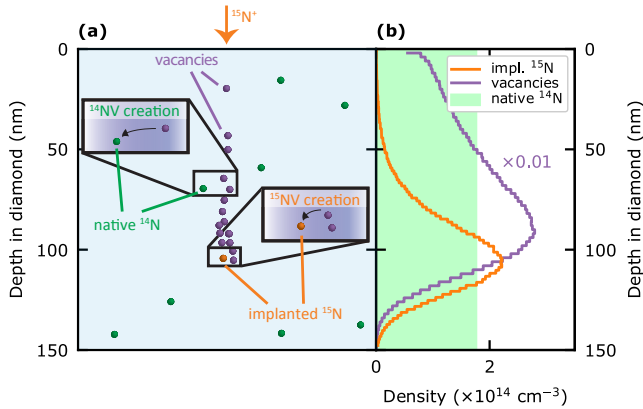


Figure 7.1: NV creation via nitrogen-ion implantation. (a) Schematic showing implanted $^{15}\text{N}^+$ ions (orange) leaving a trail of vacancies (purple) until settling into a final position. Naturally abundant ^{14}N ions (green) are shown randomly distributed throughout the diamond lattice. Vacancies mobilized by annealing can bind to a nitrogen atom (implanted or natural). (b) A SRIM simulation using the parameters in sample A show the distribution of implanted nitrogen (orange) and created vacancies (purple). The shaded green area indicates the range of estimated natural ^{14}N concentration reported by Element 6.

of the NV magnetic spectrum. However, in Chu et al. [43] the isotope of the narrowlinewidth NV centres was not investigated [44]. In a later study with similar results [38], ^{14}N isotopes were implanted, so that the origin of the NV centre's nitrogen atom could not be determined. Here we report on a study that enables us to directly correlate the optical linewidth of NV transitions to the NV formation mechanism.

To distinguish NVs formed by implanted nitrogen atoms from those formed by native nitrogen atoms, we implanted ^{15}N isotopes [45]. We then experimentally correlated the optical linewidth to the nitrogen isotope. The study was carried out on two separate samples [46]. Sample A (processed at MIT) is a bulk $\langle 100 \rangle$ CVD grown diamond (Element 6), prepared with the same implantation and annealing procedure as presented in Chu et al. [43]: it was implanted with $^{15}\text{N}^+$ at 85 keV with a fluence of 10^9 N/cm^2 and subsequently annealed at a maximum temperature of 1200 °C. Sample B (Delft) is a membrane (thickness $\approx 14 \mu\text{m}$) obtained from a bulk $\langle 100 \rangle$ CVD grown diamond (Element 6), implanted with $^{15}\text{N}^+$ at 400 keV (fluence 10^8 N/cm^2), and subsequently annealed at a maximum temperature of 1100 °C.

During implantation, nitrogen ions penetrate the diamond to a depth determined by the implantation energy (Fig. 7.1). As implanted nitrogen atoms track through the crystal, they displace carbon atoms from their lattice sites creating vacancies. The nitrogen atoms create damage along the entire trajectory, but the damage is greatest near the stopping point [47]. We performed SRIM [48] simulations to predict the stopping point of implanted ^{15}N atoms, in addition to the locations of vacancies created along the trajectory (see Fig. 7.1b). At temperatures $> 600 \text{ °C}$, vacancies become mobile [49]. These vacancies can form an NV centre, recombining with the implanted ^{15}N that created the damage or with a native ^{14}N in the lattice. The resulting ^{15}NV and ^{14}NV for-

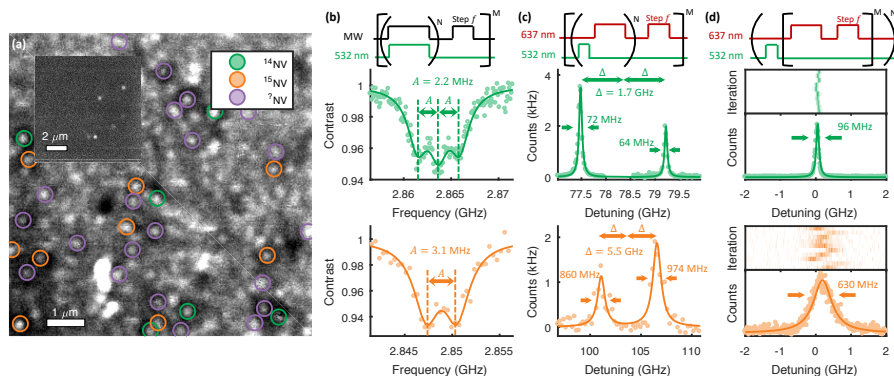


Figure 7.2: Isotope characterization and optical measurements of NV centres from ^{14}N and ^{15}N . (a) A fluorescent confocal scan of sample A taken at 4 K, with labels indicating NV centres characterized as ^{14}NV , ^{15}NV , and a set with unresolvable hyperfine lines, labeled as ^2N . A scan a few microns below the implanted layer (inset) shows a lower NV density. (b–d) Pulse sequences (top row) used for isotope characterisation and optical measurements, and representative measurement results for each isotope (green, middle row: ^{14}NV , orange, bottom row: ^{15}NV). (b) Continuous wave (CW) ODMR measurement reveal the NV isotope. The ^{14}NV is characterized by $S = 1$ hyperfine transitions; the ^{15}NV by $S = 1/2$ hyperfine transitions. (c) Interleaved red and green excitation probe the combined effect of short-timescale fluctuations and laser-induced spectral diffusion. The E_x and E_y ZPL transitions are visible for both isotopes; the ^{14}NV linewidths are narrower and show a smaller strain splitting than the ^{15}NV . (d) Individual line scans of the ZPL in sample B reveal the linewidth free from laser-induced spectral diffusion. The summation of many repeated scans is broadened as a result of repump-laser-induced spectral diffusion.

mation yields can vary significantly [30, 50–53] depending on several factors, including the initial nitrogen concentration, the implantation fluence and energy, the number of vacancies created during the implantation process, and the duration and temperature of annealing.

7.3. NV DENSITIES AND HOST ISOTOPES

A representative confocal fluorescence map at the implantation depth in sample A is shown in Fig. 7.2a. Confocal fluorescence scans at foci deeper into the diamond show a significantly lower density of fluorescent spots (Fig. 7.2a, inset), indicating that the emitters near the surface were predominantly created by the implantation and annealing process [46]. We identified emitters using different protocols in the two samples. In sample A, automated spot-recognition was performed on a fluorescence scan. For each detected spot we identified an NV centre based on its characteristic zero-phonon line (ZPL) emission around 637 nm using a spectrograph from a photoluminescence measurement at 4 K under 532 nm excitation. This protocol identified 120 fluorescent spots as NV centres in a $\approx 400 \mu\text{m}^2$ area. In sample B, spots in a fluorescence scan were detected visually, after which an automated protocol identified NV centres based on the presence of a resonance in an optically detected magnetic resonance (ODMR) spectrum around the characteristic NV centre zero-field splitting of 2.88 GHz. In this way, 52 out of a total 57 inspected spots in a $\approx 75 \mu\text{m}^2$ area in the implantation layer were identified as NV centres.

We next determined each NV centres' nitrogen isotope by observing the hyperfine structure of the ODMR spectra. A weak external magnetic field ($B_{\parallel} \approx 5\text{-}10\text{ G}$) was applied to separate the $m_s = -1$ and $m_s = +1$ electron spin transitions. We found NV centres with the characteristic triplet splitting of the ^{14}NV (with hyperfine splitting, $A = 2.2\text{ MHz}$) as well as with the ^{15}NV doublet ($A = 3.1\text{ MHz}$) [54], as indicated in Fig. 7.2b. Of the 120 NVs identified on sample A, an ODMR signal was detected in 50, out of which 18 were ^{15}NV , 18 ^{14}NV , and there were 14 in which the isotope could not be reliably determined from the ODMR spectra. Similarly, of the 52 NVs identified on sample B, 34 were ^{15}NV , 3 were ^{14}NV , and the isotope could not be determined in 15 NVs. We attribute the different isotope occurrence ratios in sample A and B to different native ^{14}N content and different implantation fluence.

7.4. LINEWIDTH OF OPTICAL TRANSITIONS

Subsequently, we measured the linewidth of optical transitions of identified NV centres, recording photoluminescence excitation (PLE) spectra at low temperature ($\approx 4\text{ K}$). A tunable laser with a wavelength near 637 nm was scanned over the optical transition while detecting emitted photons in the phonon-sideband. We performed two types of measurements. First, a scan was made in which resonant excitation (637 nm) and green illumination (532 nm) were rapidly interleaved at each data point. The red excitation causes rapid optical pumping and ionization of the NV centre. The green excitation provides repumping into the negative charge state and the $m_s = 0$ spin state. This measurement reveals the combined effect of short-time scale fluctuations and repump-laser-induced spectral diffusion in broadening the transition linewidth. Examples of the resulting traces are seen in Fig. 7.2c.

Second, in sample B, an additional scan was performed to isolate the effect of short timescale fluctuations from repump-laser-induced diffusion. A single off-resonant repump was applied before sweeping the resonant laser at low power, as seen in Fig. 7.2d. We applied microwaves on the spin resonances to prevent optical pumping into a dark spin state during the sweeps [55]. Remaining traces in which the NV centre ionized were excluded by applying a second scan over the resonance to check the charge state. If no resonance was observed, the preceding trace was disregarded. This scanning protocol was repeated many times to probe spectral diffusion through the resulting spread of the observed lines [13]. To extract the linewidth free from repump-laser-induced spectral diffusion, we performed a weighted average of linewidth values found from Lorentzian fits to each individual scan.

Fig. 7.2c and d display representative resonant optical scans for the ^{14}NV and ^{15}NV centres, each showing two resonances corresponding to the two $m_s = 0$ orbital transitions E_x and E_y . Notably, while the ^{14}NV centre (green, top row) exhibits a narrow optical linewidth with a full-width-at-half-maximum (FWHM) of $64 \pm 4\text{ MHz}$, the ^{15}NV linewidth (orange, bottom row) is broad, with a FWHM of $860 \pm 236\text{ MHz}$. The dynamics in the second scan type (Fig. 7.2d) indicate that both repump-induced fluctuations and a short-timescale mechanism broaden the ^{15}NV linewidth, but that repump-induced fluctuations are dominant in broadening beyond 200 MHz [46].

To correlate the occurrence of narrow optical linewidths with the N isotope of the NV centres, we acquired an extensive data set using the data accumulation procedures de-

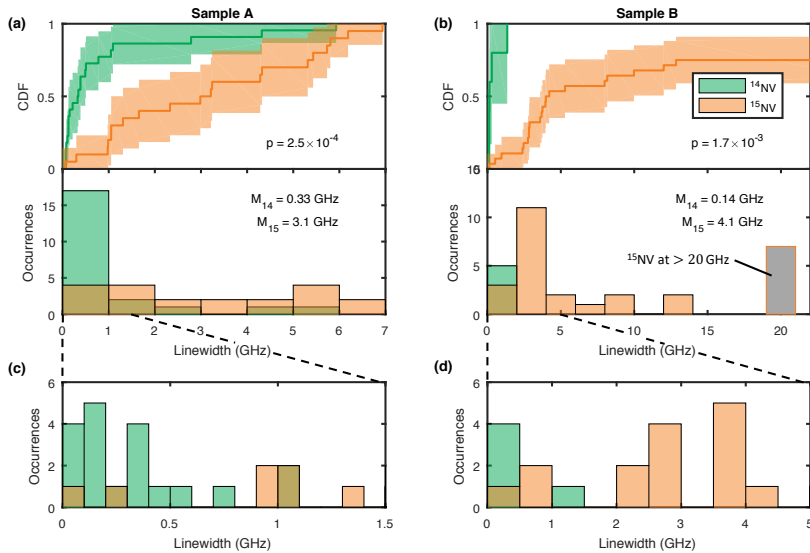


Figure 7.3: Optical linewidths per isotope. (a-b) A summary of the optical linewidths identified in sample A (a) and sample B (b) from scans at the implantation depth. For sample B, that has comparatively few ^{14}NV centres at the implantation depth, we included three ^{14}NV centres found deeper in the diamond to enable a comparison between NVs formed from implanted versus native nitrogen. The distribution is represented as a cumulative distribution function (CDF, top), with the corresponding histogram shown below. The shaded region in the CDF indicates a 95% confidence interval calculated using Greenwood's formula. These data show that both diamonds supported narrow-linewidth NV centres, the majority of which originated from ^{14}NV s. While ^{15}NV do exhibit narrow lines, their median linewidth (M) is higher than for the ^{14}NV centres in both samples. We evaluate the probability that the observed linewidths for ^{14}NV centres and ^{15}NV centres are drawn from the same distribution with a Wilcoxon Rank Sum test, finding a p-value of 2.5×10^{-4} in sample A and 1.7×10^{-3} in sample B. (c-d) A magnification of the histograms shown in (a) and (b).

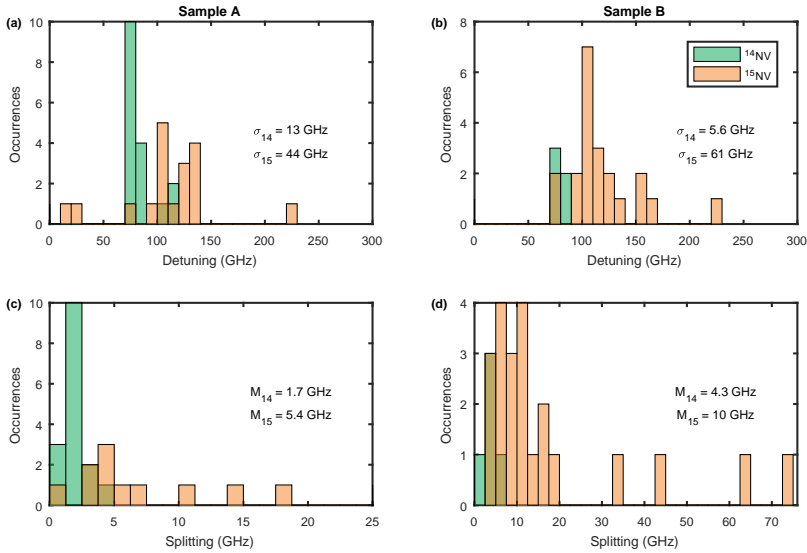


Figure 7.4: Strain analysis. (a–b) The distribution of axial strain (measured by average ZPL frequency detuning from 470.4 THz) in NVs acquired from analysis of sample A (a) and sample B (b). The ^{15}NV ZPLs exhibit a larger spread in axial strain (standard deviation, σ) than the ^{14}NV ZPLs. (c–d) The distribution of transverse strain (measured by half the splitting between E_x and E_y frequencies) in NV centres of sample A (c) and sample B (d). The ^{15}NV ZPLs show a greater median splitting (M) in both samples.

scribed above. The resulting distributions of optical linewidths for both N isotopes are shown in Fig. 7.3. Narrow optical linewidths in both samples can be attributed almost exclusively to NVs with a native ^{14}N host. In contrast, ^{15}NV centres exhibiting narrow optical linewidths are extremely rare, with a median linewidth for ^{15}NV centres of 3.1 GHz in sample A and 4.1 GHz in sample B.

Notably, in both datasets one NV centre with a ^{15}N host was found that showed narrow optical linewidths (< 100 MHz). Given their low occurrence and the non-zero natural abundance of ^{15}N , the creation mechanism of these narrow-linewidth ^{15}NV s cannot be conclusively determined. Nevertheless, their presence demonstrates that ^{15}NV centres can exhibit coherent optical transitions. Therefore, we conclude that the difference in distribution of optical linewidths between ^{14}NV s and ^{15}NV s is not due to an intrinsic effect related to the isotope itself, but due to differences in the local environment resulting from the implantation process.

7.5. LOCAL STRAIN FIELDS

Damage due to implantation may cause local strain fields. Axial strain results in an overall shift of the optical transition, while transverse strain will split the E_x and E_y transitions [54]. The distributions characterizing the strain for both NV isotopes are shown in Fig. 7.4. The spread of the distribution in ZPL detuning representing axial strain for

^{15}NVs (44 GHz for sample A, 60 GHz for sample B) is wider than for ^{14}NVs (13 GHz for sample A, 5.6 GHz for sample B). Further, we found that ^{15}NVs exhibit higher transverse strain, manifested by greater splitting with a median of 5.4 GHz (10 GHz) compared to 1.7 GHz (4.3 GHz) for ^{14}NVs in sample A (B). Assuming a similar strain susceptibility for both isotopes, these results indicate that local damage around the implanted ^{15}NVs creates a more strained environment, providing further evidence that implantation-induced local damage is responsible for the broadened ^{15}NV linewidth. In addition, in both samples we observed a shift of the average ZPL frequency for ^{15}NV compared to ^{14}NV ZPLs, possibly due to an intrinsic dependency of the energy levels on the isotope as observed in other color centres [56, 57].

The data show indications of an increase in ^{14}NV density in the implantation layer in both samples [46]. These ^{14}NV centres can be formed from naturally occurring nitrogen combining with vacancies created during implantation. Since they can be at greater distance from the main damage centre near the stopping point of the nitrogen, these NV centres can be coherent and may be useable for quantum information purposes. However, they have worse positioning accuracy as their spatial distribution is set by arbitrarily positioned naturally occurring nitrogen in combination with the diffusion length of the vacancies generated during implantation.

7.6. CONCLUSIONS

In summary, the implanted nitrogen atoms yield NV centres with predominantly broad optical lines (> 1 GHz) and substantially higher strain than NV centres formed from native nitrogen. These results indicate that implanted nitrogen atoms combined with an annealing process at high temperatures do not routinely produce NV centres with narrow optical linewidths. Vacancies produced in the implantation process may combine with existing nitrogen atoms to produce narrow NVs, but more work is needed for a statistically significant correlation. It is clear from this work that recipes for generating implanted NV centres should be re-investigated, addressing local lattice damage associated with implanted nitrogen. In addition, other approaches for precisely controlling the NV centres' positions while causing minimal local damage can be further explored, such as employing 2D nitrogen-doped diamond layers combined with electron irradiation or ion implantation for vacancy production [58, 59] or laser writing strategies for creating vacancies with 3D accuracy [60, 61].

ACKNOWLEDGEMENTS

The authors would like to thank L. Childress, Y. Chu, M. Loncar, P. Maletinsky, M. Markham, M. Trusheim, and J. Wrachtrup for helpful discussions, S. Meesala, and P. Latawiec for sample annealing at Harvard University, and S. Bogdanovic and M. Liddy for help with sample preparation. This work was supported in part by the AFOSR MURI for Optimal Measurements for Scalable Quantum Technologies (FA9550-14-1-0052) and by the AFOSR program FA9550-16-1-0391, supervised by Gernot Pomrenke. Further, we acknowledge support by the Netherlands Organization for Scientific Research (NWO) through a VICI grant, the European Research Council through a Consolidator Grant (QNETWORK) and a Synergy Grant (QC-LAB), and the Royal Netherlands Academy of Arts and Sciences

(KNAW) and Ammodo through an Ammodo science award. M.W. was supported in part by the STC Center for Integrated Quantum Materials (CIQM), NSF Grant No. DMR-1231319, in part by the Army Research Laboratory Center for Distributed Quantum Information (CDQI), and in part by Master Dynamic Limited. E.B. was supported by a NASA Space Technology Research Fellowship and the NSF Center for Ultracold Atoms (CUA). S.L.M. was supported in part by the NSF EFRI-ACQUIRE program Scalable Quantum Communications with Error-Corrected Semiconductor Qubits and in part by the AFOSR Quantum Memories MURI.

METHODS AND ADDITIONAL INFORMATION

7.6.1. SAMPLES AND PROCESSING

Sample B was prepared at Delft, with exception of an annealing procedure specified below. The dataset for sample B was acquired at Delft. As with sample A, we used a type IIa CVD grown diamond (Element Six), with a $\langle 100 \rangle$ crystal orientation. The nitrogen content is specified to be less than 5 ppb and is typically less than 1 ppb. The diamond contains a natural abundance of carbon isotopes. The diamond was cut, thinned and polished by Delaware Diamond Knives (DDK) into thin ($\sim 14 \mu\text{m}$) membranes, one of which is sample B. The membrane was implanted with $^{15}\text{N}^+$ at 400 keV (fluence of 10^8 N/cm^2) by Innovion Corporation. Subsequently, the sample underwent an acid clean in boiling sulfuric, nitric and perchloric acids [1:1:1] for one hour, and 15 minutes in a Piranha solution. Following cleaning, the sample was annealed at high temperatures [43] at Harvard University. During the annealing process the temperature was increased from room temperature to 400°C over a 4 hours period, and then the temperature was held constant for 8 hours. Subsequently, the temperature was increased to 800°C over a 12 hours period, and held constant for 8 hours. Finally, the temperature was increased to 1100°C and held constant for 2 hours. After annealing, the sample underwent the same acid treatments as before annealing. The sample was bonded to a fused silica substrate via Van der Waals forces [62]. The fused silica substrate contains integrated gold MW striplines for spin control as detailed in Ref. [62].

Sample A and the dataset for sample A were acquired and prepared at MIT. Sample A was prepared in a similar way to sample B; we highlight the differences. This sample is a bulk diamond, that was implanted with $^{15}\text{N}^+$ at 85 keV (fluence of 10^9 N/cm^2). During the annealing process the temperature was increased at a rate of $1^\circ\text{C}/\text{min}$ and held constant for 2 hours when temperatures reached 400°C , 800°C and 1200°C respectively.

7.6.2. ISOTOPE RECOGNITION

The NV isotope was determined by inspection of the multiplicity of the number of dips in the ODMR spectrum, and confirmed (for sample B) by the best goodness of fit out of fits with Gaussian dips with hyperfine splittings fixed to the ^{14}NV or ^{15}NV values. The isotope could not be reliably identified by inspection in 59 NV centres in sample A and 15 NV centres in sample B. We note that these contained both NV centres with broad ($> 500 \text{ MHz}$) and narrow ($< 500 \text{ MHz}$) linewidths.

Tables 7.1 and 7.2 shows a summary of the PLE and ODMR contrast for spots at the implantation depth and deeper in the diamond. In Figs. 7.5 and 7.6 a summary of the

	no ODMR contrast	no resolvable hyperfine	hyperfine resolved	failed	
PLE signal	59	14	36	1	110
no PLE signal	5	2	0	3	10
	64	16	36	4	120

Table 7.1: Table summarizing all data for sample A. This table has the numeric breakdown of all NVs reported. The bold numbers indicate a particular column or row summation. NVs that resulted in an error were either due to a hardware failure during the automated protocol or a peak that was detected in one scan but could not be found again (likely due to a false-positive originally).

	PLE signal	no PLE signal	
ODMR, isotope resolvable	35	0	35
ODMR, isotope unresolvable	16	1	17
no ODMR contrast	1	4	5
	51	5	57

Table 7.2: Table summarizing all data for sample B. This table has the numeric breakdown of all fluorescent spots reported, at the implantation depth (52 spots) and deeper in the diamond (5 NVs). Not included are two data-points for which spatial optimization was not successful, and 5 spots that contained more than one NV. The bold numbers indicate a particular column or row summation.

optical linewidths is shown, including the NVs with unknown isotopes. We find that the cumulative density function for the unknown isotopes and the combined ^{14}NV and ^{15}NV data overlap.

7.6.3. CHARACTERIZATION OF REPUMP LASER-INDUCED SPECTRAL DIFFUSION

On sample B we performed scans to isolate short timescale fluctuations from repump laser-induced spectral diffusion (see Fig. 7.2d).

For each NV centre we performed 30 consecutive scans, with a green repump laser pulse applied only in between the scans. The scans in which the NV centre did not ionize are selected. We fit a Lorentzian curve to the resonance in each scan and calculate the weighted average for each NV centre (see Eq. (6.2)). We also fit the sum of the scans with a Gaussian curve, extracting the FWHM including repump laser-induced spectral diffusion. When correlating the two analyses, as shown in Fig. 7.7, we find that the Lorentzian linewidths are mostly less than 200 MHz, while further broadening in the linewidth can be attributed to laser-induced spectral diffusion.

7.6.4. NV DENSITIES

In sample A (see confocal scans in Fig. 2a of the main text), the NV areal densities estimated from the verified isotopes at the implantation depth are at least $3.9 \times 10^{-2} \text{ }^{14}\text{NVs}/\mu\text{m}^2$ and $3.5 \times 10^{-2} \text{ }^{15}\text{NVs}/\mu\text{m}^2$. When assuming that the isotope distribution over the NVs with unknown isotope follows the same distribution as for the known NVs (this assumption is supported by the overlapping linewidth distributions in Fig. 7.5), the areal density

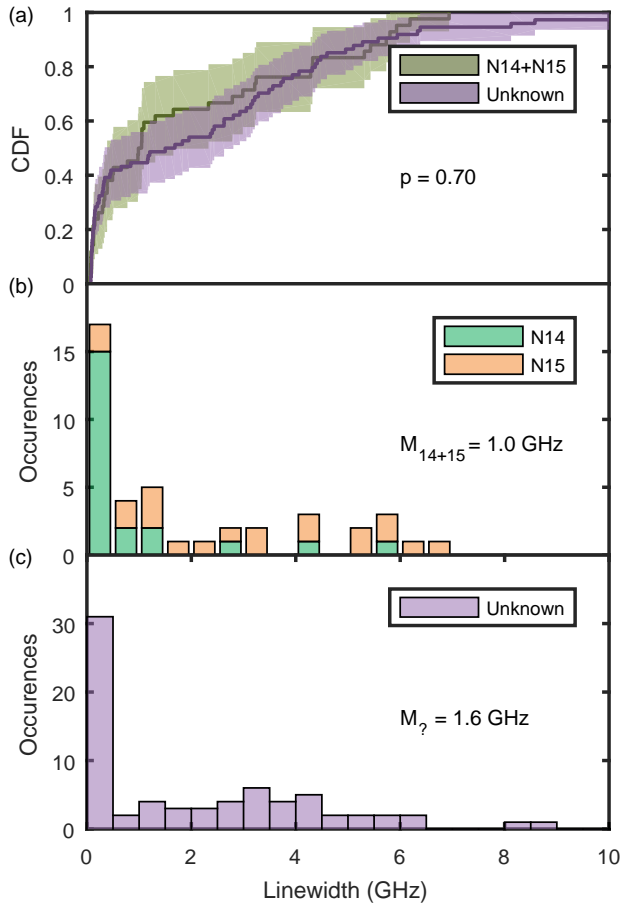


Figure 7.5: Summary of all data for sample A. (a) A CDF representing the distributions of unknown isotope to known isotope ZPL linewidths. A similar shape indicates that both sample sets are drawn from the same distribution indicating there is no inherent bias towards sampling ^{14}NV or ^{15}NV . The probability that the samples are drawn from the same distribution (p) is evaluated by a Wilcoxon rank-sum test. (b) A stacked histogram showing the all ^{14}NV and ^{15}NV ZPL linewidths. The median linewidth (M) is indicated. (c) A histogram showing the linewidths for the set of ZPLs with an unknown host isotope.

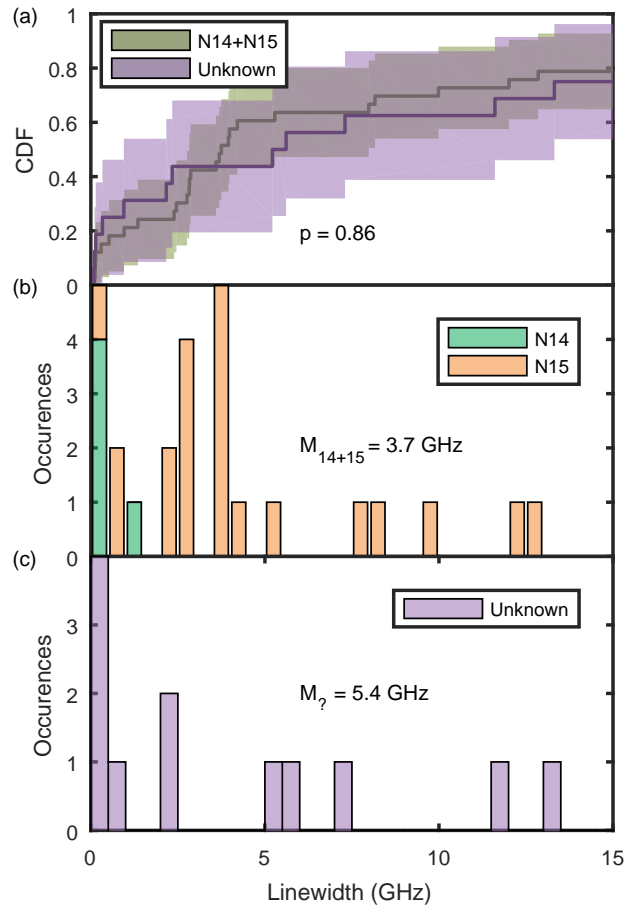


Figure 7.6: Summary of all data for sample B. (a) A CDF representing the distributions of unknown isotope to known isotope ZPL linewidths. A similar shape indicates that both sample sets are drawn from the same distribution indicating there is no inherent bias towards sampling ^{14}NV or ^{15}NV . The probability that the samples are drawn from the same distribution (p) is evaluated by a Wilcoxon rank-sum test. (b) A stacked histogram showing the all ^{14}NV and ^{15}NV ZPL linewidths. The median linewidth (M) is indicated. (c) A histogram showing the linewidths for the set of ZPLs with an unknown host isotope. The histograms in (c) and (d) do not show data for 7 ^{15}NV and 4 NVs with unknown isotope as they are out of the range ($> 15 \text{ GHz}$).

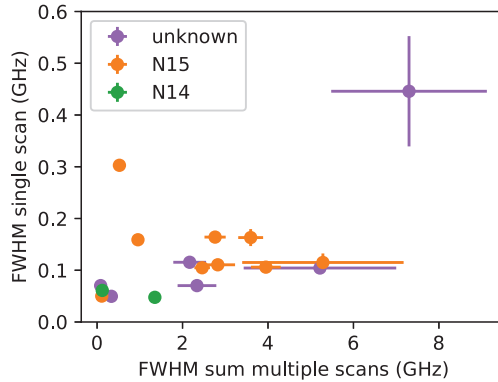


Figure 7.7: Optical linewidths from scans with red excitation only. Consecutive scans over a single resonance are performed as described in the text. The FWHM of the optical linewidth in individual scans (y -axis) is correlated to the FWHM of the summed scans including repump laser-induced spectral diffusion (x -axis). We conclude that the Lorentzian linewidths are mostly less than 200 MHz, while further broadening in the linewidth can be attributed to laser-induced spectral diffusion. This figure contains data for NV centres at the implantation depth with linewidths < 10 GHz.

estimates are $5.1 \times 10^{-2} \text{ }^{14}\text{NVs}/\mu\text{m}^2$ and $4.7 \times 10^{-2} \text{ }^{15}\text{NVs}/\mu\text{m}^2$.

At a scan deeper in the sample we found 3 NVs, that we assume to be ^{14}NV given their location in the diamond well below the implantation depth. The native areal density of ^{14}NVs that we estimate from this is $3 \times 10^{-2} \text{ }^{14}\text{NVs}/\mu\text{m}^2$.

Confocal scans of sample B are shown in Fig. 7.8, at the implantation depth and deeper into the sample to illustrate the change in NV density due to implantation.

The confocal scan at a depth of ~ 400 nm (see Fig. 7.8b) displays around ~ 180 fluorescent spots. We characterized 59 of these spots, identifying 57 NV centres (47 single NVs in a confocal spot and 5 spots with two NVs). We are able to determine the isotope for 37 NVs, 3 out of which are ^{14}NVs , and 34 are ^{15}NVs . From this, a lower-bound estimate of the ^{14}NV areal density after implantation is $4 \times 10^{-2} \text{ }^{14}\text{NVs}/\mu\text{m}^2$. We estimate the ^{15}NV areal density to be at least $5 \times 10^{-1} \text{ }^{15}\text{NVs}/\mu\text{m}^2$. When assuming that the unknown isotopes follow the distribution of isotopes for the known isotopes (as for sample A, this is supported by the overlapping linewidth distributions, see Fig. 7.6), the areal density estimates are $6 \times 10^{-2} \text{ }^{14}\text{NVs}/\mu\text{m}^2$ and $7 \times 10^{-1} \text{ }^{15}\text{NVs}/\mu\text{m}^2$.

We characterized 5 out of 6 bright fluorescent spots in the deep scan ($\approx 5 \mu\text{m}$ depth, Fig. 7.8b). All 5 spots were identified as NVs, and all displayed narrow linewidths in the red-green interleaved scan. The isotope were found to be ^{14}N for 3 out of 5 NVs, whereas the isotope could not be reliably determined from the ODMR measurement for 2 NVs (this is a comparable ratio of known versus undetermined isotopes as at the implantation depth). Because their location in the diamond was well below the implantation depth, these findings strongly suggest that these fluorescent spots are naturally occurring ^{14}NV . A best estimate of the ^{14}NV areal density before implantation is therefore $3 \times 10^{-2} \text{ }^{14}\text{NVs}/\mu\text{m}^2$.

Although the sample sizes are small, comparing the estimated ^{14}NV densities at the

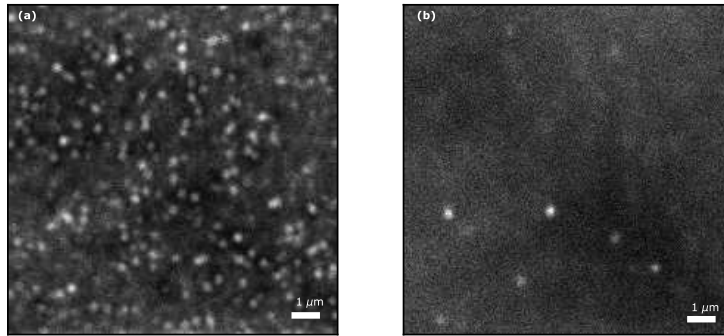


Figure 7.8: Confocal scans of sample B (a) at the implantation depth and (b) at $\approx 5 \mu\text{m}$ under the diamond surface.

implantation depth and deeper in the diamond we find indications that ^{14}NVs at the implantation depth are created during implantation in both sample A and B.

REFERENCES

- [1] van Dam, S. B. *et al.*, *Optical coherence of diamond nitrogen-vacancy centers formed by ion implantation and annealing*, arXiv:1812.11523 (2018).
- [2] Aharonovich, I., Englund, D. & Toth, M., *Solid-state single-photon emitters*, *Nat. Photonics* **10**, 631 (2016).
- [3] Awschalom, D. D., Hanson, R., Wrachtrup, J. & Zhou, B. B., *Quantum technologies with optically interfaced solid-state spins*, *Nat. Photonics* **12**, 516 (2018).
- [4] Lodahl, P., *Quantum-dot based photonic quantum networks*, *Quantum Sci. Technol.* **3**, 13001 (2018).
- [5] Wehner, S., Elkouss, D. & Hanson, R., *Quantum Internet: a vision for the road ahead*, *Science* **362**, 303 (2018).
- [6] Bar-Gill, N., Pham, L. M., Jarmola, A., Budker, D. & Walsworth, R. L., *Solid-state electronic spin coherence time approaching one second*, *Nat. Commun.* **4**, 1743 (2013).
- [7] Abobeih, M. H. *et al.*, *One-second coherence for a single electron spin coupled to a multi-qubit nuclear-spin environment*, *Nat. Commun.* **9**, 2552 (2018).
- [8] Kalb, N. *et al.*, *Entanglement Distillation between Solid-State Quantum Network Nodes*, *Science* **356**, 928 (2017).
- [9] Waldherr, G. *et al.*, *Quantum error correction in a solid-state hybrid spin register*, *Nature* **506**, 204 (2014).
- [10] Cramer, J. *et al.*, *Repeated quantum error correction on a continuously encoded qubit by real-time feedback*, *Nat. Commun.* **7**, 11526 (2016).

- [11] Lovchinsky, I. *et al.*, *Nuclear magnetic resonance detection and spectroscopy of single proteins using quantum logic*, *Science* **351**, 836 (2016).
- [12] Robledo, L. *et al.*, *High-fidelity projective read-out of a solid-state spin quantum register*, *Nature* **477**, 574 (2011).
- [13] Fu, K.-M. C. *et al.*, *Observation of the Dynamic Jahn-Teller Effect in the Excited States of Nitrogen-Vacancy Centers in Diamond*, *Phys. Rev. Lett.* **103**, 256404 (2009).
- [14] Tamarat, P. *et al.*, *Stark shift control of single optical centers in diamond*, *Phys. Rev. Lett.* **97**, 083002 (2006).
- [15] Batalov, A. *et al.*, *Temporal coherence of photons emitted by single nitrogen-vacancy defect centers in diamond using optical rabi-oscillations*, *Phys. Rev. Lett.* **100**, 077401 (2008).
- [16] Robledo, L., Bernien, H., Van Weperen, I. & Hanson, R., *Control and coherence of the optical transition of single nitrogen vacancy centers in diamond*, *Phys. Rev. Lett.* **105**, 177403 (2010).
- [17] Bernien, H. *et al.*, *Two-photon quantum interference from separate nitrogen vacancy centers in diamond*, *Phys. Rev. Lett.* **108**, 043604 (2012).
- [18] Sipahigil, A. *et al.*, *Quantum Interference of Single Photons from Remote Nitrogen-Vacancy Centers in Diamond*, *Phys. Rev. Lett.* **108**, 143601 (2012).
- [19] Bernien, H. *et al.*, *Heralded entanglement between solid-state qubits separated by three metres*. *Nature* **497**, 86 (2013).
- [20] Manson, N. B., Harrison, J. P. & Sellars, M. J., *Nitrogen-vacancy center in diamond: Model of the electronic structure and associated dynamics*, *Phys. Rev. B* **74**, 104303 (2006).
- [21] Fu, K.-M. C., Santori, C., Barclay, P. E. & Beausoleil, R. G., *Conversion of neutral nitrogen-vacancy centers to negatively charged nitrogen-vacancy centers through selective oxidation*, *Appl. Phys. Lett.* **96**, 121907 (2010).
- [22] Orwa, J. O. *et al.*, *Engineering of nitrogen-vacancy color centers in high purity diamond by ion implantation and annealing*, *J. Appl. Phys.* **109**, 083530 (2011).
- [23] Santori, C. *et al.*, *Nanophotonics for quantum optics using nitrogen-vacancy centers in diamond*, *Nanotechnology* **21**, 274008 (2010).
- [24] Faraon, A., Santori, C., Huang, Z., Acosta, V. M. & Beausoleil, R. G., *Coupling of nitrogen-vacancy centers to photonic crystal cavities in monocrystalline diamond*, *Phys. Rev. Lett.* **109**, 033604 (2012).
- [25] Siyushev, P. *et al.*, *Optically controlled switching of the charge state of a single nitrogen-vacancy center in diamond at cryogenic temperatures*, *Phys. Rev. Lett.* **110**, 167402 (2013).

- [26] Hensen, B. *et al.*, *Loophole-free bell inequality violation using electron spins separated by 1.3 kilometres*, *Nature* **526**, 682 (2015).
- [27] Pezzagna, S., Rogalla, D., Wildanger, D., Meijer, J. & Zaitsev, A., *Creation and nature of optical centres in diamond for single-photon emission-overview and critical remarks*, *New J. Phys.* **13**, 035024 (2011).
- [28] Mouradian, S. L. *et al.*, *Scalable integration of long-lived quantum memories into a photonic circuit*, *Phys. Rev. X* **5**, 1 (2015).
- [29] Schröder, T. *et al.*, *Review Article: Quantum Nanophotonics in Diamond*, *J. Opt. Soc. Am. B* **33**, 65 (2016).
- [30] Gaebel, T. *et al.*, *Room-temperature coherent coupling of single spins in diamond*, *Nat. Phys.* **2**, 408 (2006).
- [31] Dolde, F. *et al.*, *Room-temperature entanglement between single defect spins in diamond*, *Nat. Phys.* **9**, 139 (2013).
- [32] Yamamoto, T. *et al.*, *Strongly coupled diamond spin qubits by molecular nitrogen implantation*, *Phys. Rev. B* **88**, 201201 (2013).
- [33] Faraon, A., Barclay, P. E., Santori, C., Fu, K.-M. C. & Beausoleil, R. G., *Resonant enhancement of the zero-phonon emission from a colour centre in a diamond cavity*, *Nat. Photonics* **5**, 301 (2011).
- [34] Hausmann, B. J. M. *et al.*, *Coupling of NV centers to photonic crystal nanobeams in diamond*, *Nano Lett.* **13**, 5791 (2013).
- [35] Lee, J. C. *et al.*, *Deterministic coupling of delta-doped nitrogen vacancy centers to a nanobeam photonic crystal cavity*, *Appl. Phys. Lett.* **105**, 261101 (2014).
- [36] Li, L. *et al.*, *Coherent spin control of a nanocavity-enhanced qubit in diamond*. *Nat. Comm.* **6**, 6173 (2015).
- [37] Riedrich-Möller, J. *et al.*, *Nanoimplantation and Purcell enhancement of single nitrogen-vacancy centers in photonic crystal cavities in diamond*, *Appl. Phys. Lett.* **106**, 221103 (2015).
- [38] Riedel, D. *et al.*, *Deterministic enhancement of coherent photon generation from a nitrogen-vacancy center in ultrapure diamond*, *Phys. Rev. X* **7**, 031040 (2017).
- [39] Lea-Wilson, M. A., Lomer, J. N. & Van Wyk, J. A., *Electron spin resonance of the R4/W6 defect in irradiated diamond*, *Philos. Mag. B* **72**, 81 (1995).
- [40] Naydenov, B. *et al.*, *Increasing the coherence time of single electron spins in diamond by high temperature annealing*, *Appl. Phys. Lett.* **97**, 242511 (2010).
- [41] Yamamoto, T. *et al.*, *Extending spin coherence times of diamond qubits by high-temperature annealing*, *Phys. Rev. B* **88**, 075206 (2013).

- [42] Deák, P., Aradi, B., Kaviani, M., Frauenheim, T. & Gali, A., *Formation of NV centers in diamond: A theoretical study based on calculated transitions and migration of nitrogen and vacancy related defects*, Phys. Rev. B **89**, 075203 (2014).
- [43] Chu, Y. *et al.*, *Coherent optical transitions in implanted nitrogen vacancy centers*. Nano Lett. **14**, 1982 (2014).
- [44] Y. Chu, private communication.
- [45] Rabeau, J. R. *et al.*, *Implantation of labelled single nitrogen vacancy centers in diamond using ^{15}N* , Appl. Phys. Lett. **88**, 023113 (2006).
- [46] See Supplementary Information for additional derivations, data, and analysis.
- [47] De Oliveira, F. F. *et al.*, *Tailoring spin defects in diamond by lattice charging*, Nat. Commun. **8**, 15409 (2017).
- [48] Ziegler, J. F., Ziegler, M. & Biersack, J., *The Stopping and Range of Ions in Matter (SRIM-2013, <http://www.srim.org/>)*.
- [49] Davies, G., Lawson, S. C., Collins, A. T., Mainwood, A. & Sharp, S. J., *Vacancy-related centers in diamond*, Phys. Rev. B **46**, 13157 (1992).
- [50] Naydenov, B. *et al.*, *Enhanced generation of single optically active spins in diamond by ion implantation*, Appl. Phys. Lett. **96**, 163108 (2010).
- [51] Toyli, D. M., Weis, C. D., Fuchs, G. D., Schenkel, T. & Awschalom, D. D., *Chip-scale nanofabrication of single spins and spin arrays in diamond*. Nano Lett. **10**, 3168 (2010).
- [52] Ofori-Okai, B. K. *et al.*, *Spin properties of very shallow nitrogen vacancy defects in diamond*, Phys. Rev. B **86**, 1 (2012).
- [53] Yamamoto, T. *et al.*, *Isotopic identification of engineered nitrogen-vacancy spin qubits in ultrapure diamond*, Phys. Rev. B **90**, 081117 (2014).
- [54] Doherty, M. W. *et al.*, *The nitrogen-vacancy colour centre in diamond*, Phys. Rep. **528**, 1 (2013).
- [55] Tamarat, P. *et al.*, *Spin-flip and spin-conserving optical transitions of the nitrogen-vacancy centre in diamond*, New J. Phys. **10**, 045004 (2008).
- [56] Dietrich, A. *et al.*, *Isotopically varying spectral features of silicon-vacancy in diamond*, New J. Phys. **16**, 113019 (2014).
- [57] Ekimov, E. A. *et al.*, *Germanium–vacancy color center in isotopically enriched diamonds synthesized at high pressures*, JETP Lett. **102**, 701 (2015).
- [58] Ohno, K. *et al.*, *Engineering shallow spins in diamond with nitrogen delta-doping*, Appl. Phys. Lett. **101**, 82413 (2012).

- [59] Ohno, K. *et al.*, *Three-dimensional localization of spins in diamond using ^{12}C implantation*, *Appl. Phys. Lett.* **105**, 052406 (2014).
- [60] Chen, Y. C. *et al.*, *Laser writing of coherent colour centres in diamond*, *Nat. Photonics* **11**, 77 (2017).
- [61] Chen, Y.-C. *et al.*, *Laser writing of individual atomic defects in a crystal with near-unity yield*, arXiv:1807.04028 (2018).
- [62] Bogdanovic, S. *et al.*, *Robust nano-fabrication of an integrated platform for spin control in a tunable microcavity*, *APL photonics* **2**, 126101 (2017), arXiv:1708.07082 .

8

MEASUREMENT METHODS FOR FABRY-PÉROT MICROCAVITIES

This chapter describes measurement techniques for open Fabry-Pérot microcavities. In section 8.1 the techniques used to characterise open diamond-air cavities are presented. This includes measurements of cavity finesse, geometrical factors, and the cavity stability. In section 8.2 we describe the methods to detect the coupling of nitrogen vacancy centres to the cavity mode, and how this can be combined with controlled scanning of the cavity resonance frequency. These techniques form the basis for the experimental results presented in chapters 9 to 11.

8.1. CAVITY CHARACTERISATION

To assess the performance of the cavity, we subject it to characterisation measurements. We distinguish three cavity properties that together characterise the system. We list them here, emphasizing the parameters that we can measure to access these properties.

1. Cavity finesse

The cavity finesse is a measure for the losses in the cavity. It can be determined from measurements of the effective cavity length and *cavity linewidth* (Eq. (5.5)). The effective length is composite of the *diamond thickness* t_d , the *air gap width* t_a and the corresponding electric field distribution (Eq. (4.50)). If the effective cavity length is dominated by the diamond part ($n_d t_d \gg t_a, t_{pen}$, for a mirror penetration depth t_{pen}), it can be approximated by the optical length: $n_d L_{\text{eff}} \approx L_{\text{opt}} = n_d t_d + t_a$.

2. Geometrical factors

The cavity mode volume is a function of the effective cavity length and the *beam waist*. We note that to estimate the Purcell factor the beam waist plays the most important role (see section 5.3). We can calculate it from measurements of the *diamond thickness*, *air gap width*, and *radius of curvature (ROC)* of the fiber (Eq. (4.68)). We are further interested in the *effective dimple diameter* that enables us to calculate the expected clipping losses in the cavity.

3. Cavity Stability

Drift and vibrations affect the stability of a cavity system and can have a large impact on the average ZPL enhancement. We can find the *vibration amplitude* through measuring the broadened cavity linewidth, and we can reconstruct the *vibration frequency spectrum* by measuring the time-dependent cavity transmission.

In the rest of this section we describe the measurements of the parameters that give access to these elements. The setup with which these measurements are performed is schematically presented in Fig. 8.1.

8

8.1.1. CAVITY LENGTH MEASUREMENTS

For a bare cavity, the cavity length can be determined from the free spectral range (Eq. (4.9)). However, for a diamond-air cavity the diamond thickness and air gap width cannot easily be found from a single cavity spectrum measurement, due to the coupling between the diamond-like and air-like modes as described in section 4.3.3. Instead, we use a sequence of spectrum measurements for a varying air gap width. By fitting the obtained resonances to the resonance condition of a hybrid cavity, Eq. (4.45), the diamond thickness and air gap width can be inferred.

For these measurements a white light source is coupled into the cavity through the fiber port. The cavity transmission is collected via the free-space path into a single-mode fiber that is connected to a spectrometer. We then sweep the cavity length using the piezo controllers of the cryo-positioning stage. For every voltage step, we record the cavity spectrum on a spectrometer (Fig. 8.2).

To extract the cavity length from these measurements, first, the fundamental resonance peaks are identified in each spectrum. Next, we use the fixed separation in length

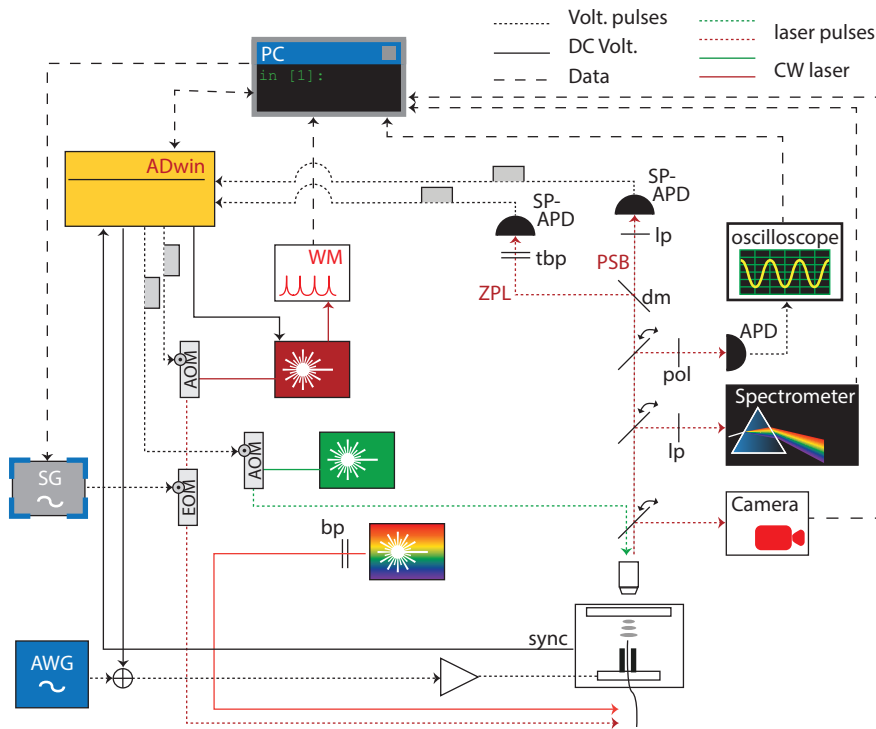


Figure 8.1: Schematic of the optical cavity setup. The cavity can be tuned spectrally and spatially using a high frequency positioner (*JPE CPS-HR*), with cryo linear actuators for large-range movement and piezo scanners for small range movement. The stage is mounted on a vibration isolation platform (*JPE CVIP-1*) to mitigate vibrations induced by the cryostation (*Montana Instruments C2*). Measurements of the cavity length are performed using a supercontinuum laser (*Fianium*) and spectrometer *Princeton Instruments SP-2500i* with CCD camera *Princeton Instruments PIXIS: 100*. Gratings of 300 g/mm and 1800 g/mm are used. Filters in the fianium source (*Thorlabs FELH 600 and FESH700*) and before the spectrometer (*Semrock FF01-593/LP-25*) are employed to minimize stray background in the spectrometer. For measurements of the cavity linewidth a red tunable laser *NewFocus Velocity TLB-6300-LN* (frequency monitored using a *HighFinesse WS/6* wavemeter) is modulated using a fiber-coupled electro-optical modulator (EOM, *Jenoptik PM635*) for which a signal is generated using a *Rohde & Schwarz SGS100A* signal generator. The cavity length is modulated by applying a signal to the positioners using a *Rigol DG1022* waveform generator that is combined with the DC signal generated using the *ADwin Pro II*. The transmitted light is collected on a *ThorLabs APD130A2*, and the signal is read on a *Yokogawa DLM 4038* oscilloscope. During NV measurement sequences a green laser (*Coherent Compass 315M-150*) is used for off-resonant excitation. The NV emission is collected on two single-photon avalanche photon detectors (SP-APD, *LaserComponents* and *PicoQuant*). The ZPL light is separated from the PSB using a dichroic mirror (PSB) using a dichroic mirror (*Semrock DI 02-R365*), and background is additionally filtered using two tunable bandpass filters (*Semrock TBP 01-700/13*) together filtering a region of ≈ 6 nm around the ZPL. A *Semrock LP02-647RU-25* filters additional background out of the PSB. For lifetime and autocorrelation measurements the SP-APD signals are registered by a *QuTools QuTAU* timetagger. The objective can be scanned using positioning stages (*PI P-625.2CL (X,Y)* and *PI P622.ZCL (Z)*). Figure adapted from [1].

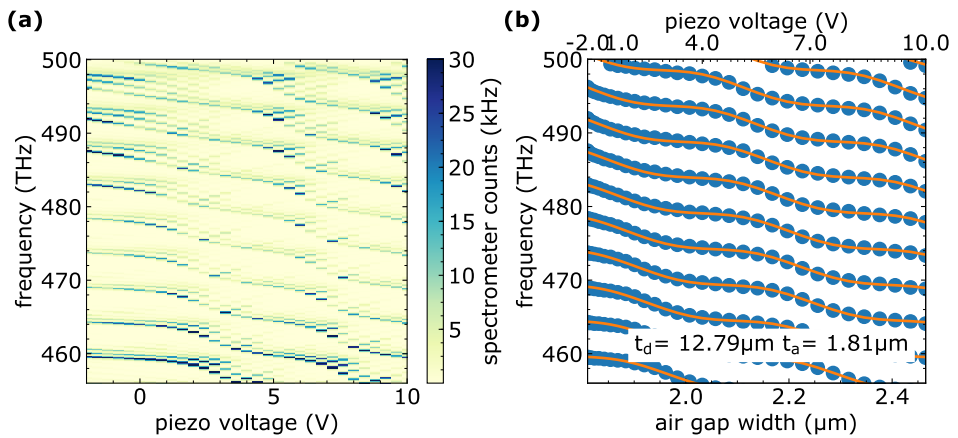


Figure 8.2: Measurement of the diamond thickness and air gap width. (a) The length-dependency of the cavity resonances is probed by recording a cavity spectrum at consecutive cavity lengths. The cavity is probed with a white light source while the transmitted light is imaged on a spectrometer that is (operated with a grating of 300 g/mm). The typical integration time is one second per point. The scan range corresponding to the full piezo voltage range (-2 to 10 V) is $\approx 2.5\ \mu\text{m}$ at room temperature, and reduces to $\approx 1\ \mu\text{m}$ at cryogenic temperatures (shown here). (b) With a peak finder the fundamental modes in the spectra are selected. Analytic solutions to the resonance frequencies (Eq. (4.45)) are fit to the data, to obtain the diamond thickness and air gap width.

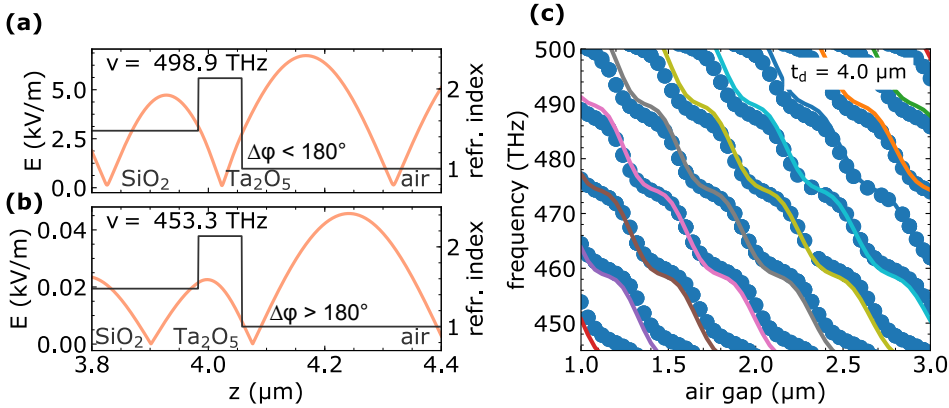


Figure 8.3: Resonance frequency shift for realistic mirrors. (a-b) The phase shift upon reflection deviates from 180° for frequencies away from the design frequency for a mirror with a finite stopband. As a result the location of the node of the cavity mode is shifted (a) into the mirror for higher frequencies, and (b) out of the mirror for lower frequencies, here depicted for operation on the edge of the stopband. The field density is low due to operation on the edge of the stopband. (c) The cavity resonance frequencies for a cavity with $t_d = 4.0 \mu\text{m}$ are obtained in two ways: analytically using Eq. (4.45), and numerically using the full transfer matrix model, including realistic mirrors. We find that for frequencies deviating from the design wavelength the two solutions deviate. In practice, this will lead to an overestimation of the air gap width when using the results from an analytic fit to the data. The mirrors in (a-c) are simulated with 21 alternating layers of SiO_2 and Ta_2O_5 , of $1 \times \lambda_0/(2n)$ and $3 \times \lambda_0/(2n)$ thickness respectively with $\lambda_0 = 637 \text{ nm}$ the design wavelength. The use of a $3 \times \lambda_0/(2n)$ thick Ta_2O_5 creates a mirror with a narrow stopband. It also causes a stronger frequency-dependency of the phase upon reflection.

between the fundamental modes ($\lambda/2$) to calibrate the piezo's voltage-to-length conversion up to a cubic term. Finally, the resonant conditions for a hybrid cavity are fit to the resonance peaks, by minimizing the root-mean-square distance between the fit and the peaks from the data.

The accuracy of the final fit is fundamentally limited by two effects. First, the cavity length can only be determined up to the unknown Gouy phase. Second, the phase upon reflection from the DBR mirrors is frequency-dependent. For the design frequency of the mirror the phase shift is 180° , but for higher (lower) frequencies the phase shift decreases (increases). As a result the antinode that is normally on the mirror interface moves into the mirror for higher resonance frequencies, and out of the mirror for lower frequencies (Fig. 8.3a,b). Since the model from which we derived the resonance conditions (Eq. (4.42)) assumes ideal mirrors, the model will not fit the data perfectly. We probe the deviation by finding the resonances for realistic mirrors using a numeric approach and comparing this with the resonances found in the analytic model for the same cavity parameters. Both results are shown in Fig. 8.3c. As expected we find that the realistic resonance spectrum (blue points) is more 'flat' than for ideal mirrors (lines). When using the analytic model to fit the data this may lead to an overestimation of the air gap width.

8.1.2. CAVITY LINEWIDTH MEASUREMENTS

An intuitive way to measure the cavity linewidth is by sweeping the laser frequency across the cavity resonance and measuring the linewidth of the transmitted (or reflected) signal. The laser frequency of a tunable laser can be finetuned by applying a voltage to a piezo that controls the grating. Therefore, a calibration from tuning voltage to frequency is needed to extract a cavity linewidth in frequency from this measurement. This calibration could be performed by measuring the laser frequency on a wavemeter for each voltage step. As the sweep speed influences the achieved scan range, such a calibration would have to be performed under realistic experimental conditions. However, achieving this is problematic: to probe the intrinsic cavity linewidth and exclude influence of vibrations, a scan has to be faster than the timescale of vibrations (> 1 kHz). At such high scanning speeds (the fine frequency tuning bandwidth of the laser is 2 kHz), the wavemeter is unable to record the frequency fast enough (as the wavemeter repetition rate is up to 400 Hz). Consequently, the voltage-to-frequency conversion cannot be calibrated for the required sweep speeds.

We therefore design a different method to perform the linewidth measurements, based on modulating the cavity length around the resonance. The red laser is coupled into the cavity via the fiber port, after which the transmitted light is collected on a fast photodiode (maximum bandwidth 50 MHz). The photodiode signal is visualised on an oscilloscope. The cavity length is then modulated around the resonance with a sinusoidal signal. To calibrate this length modulation to a frequency, we create sidepeaks on the laser frequency at a fixed distance to the fundamental mode using an electro-optic modulator (EOM).

The resulting signal that we record on the oscilloscope shows a repeating pattern of three Lorentzian-shaped peaks (Fig. 8.4). The linewidth in frequency is found by fitting three Lorentzian peaks to the signal, calibrating to the peak-to-peak distance set by the EOM driving frequency. We note that we here assume that the relation between length and frequency is linear. This is the case as long as the distance to the sidepeaks is small compared to the free spectral range, which holds for all cavity lengths that we consider in this thesis. To gain statistical confidence many single linewidth scans are averaged.

To get a Lorentzian signal from the cavity, the length sweep should be approximately linear around the resonance. The modulation amplitude should therefore be high enough to constrain the cavity resonance to the nearly linear part of the sinusoidal signal. The amplitude needed to achieve this is finesse-dependent: the lower the finesse of the cavity the larger length modulations are needed to sweep over the cavity resonance (compare to Eq. (5.23)). To ensure that the linewidth is probed at a timescale shorter than that of the most important vibrations, the amplitude and frequency of the length modulation should be large enough to sweep over the cavity resonance faster than the timescale set by the highest significant mechanical resonance frequency of the system.

In the case of strong vibrations at cryogenic temperatures, an effect of vibrations on the timescale of the signal may still be present. Vibrations on these timescales typically show a clear distortion of the signal, such as an asymmetry in the sidepeaks. These distortions are detected through the quality of the fitted Lorentzians (that are fixed to be symmetric around the centre peak), such that we can select the suitable data.

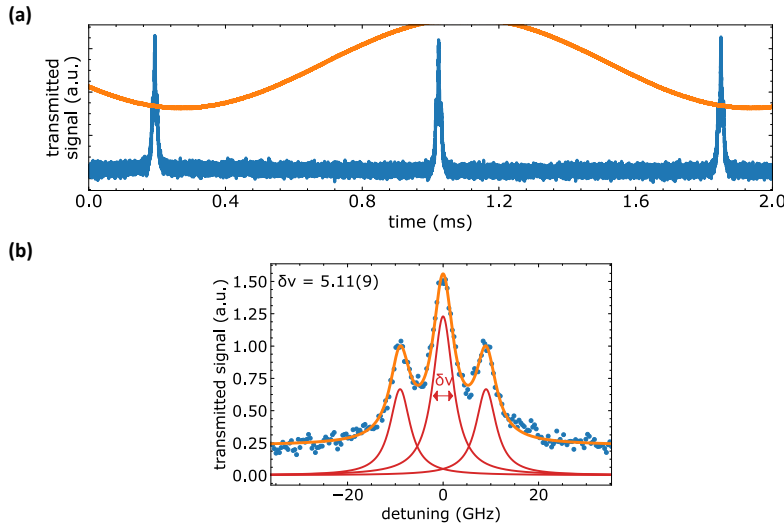


Figure 8.4: Measurement of the cavity linewidth. (a) The cavity length is modulated with a sinusoidal signal on the piezo positioners (orange). The cavity transmission (blue) shows peaks when the cavity is on resonance with the probing laser at a fixed frequency. The modulation and cavity signal are shifted with respect to each other due to delays. An equal spacing between all cavity peaks ensures that the sine can be approximated as linear at that point. (b) Sidepeaks generated on the probing laser serve as a frequency reference for the cavity linewidth. The sidepeaks are generated using a fiber-coupled EOM that we control with a signal-generator. To serve as a suitable reference the sidepeaks should be separated from the fundamental mode by more than the cavity linewidth, and there should be enough power in the sidepeaks to resolve them. Since the power in the sidepeaks decreases at higher driving frequency, in practice the maximum linewidth that can be measured using this method is ≈ 9 GHz. A fit of three Lorentzians (orange and red lines) gives the cavity linewidth (here the EOM frequency is 9 GHz and the extracted cavity linewidth is 5.11(9) GHz).

8.1.3. FIBER DIMPLE RADIUS OF CURVATURE AND EFFECTIVE DIAMETER

The radius of curvature (ROC) and diameter (D_d) of the fiber dimple can be determined from the profile of the fiber as measured using e.g. a white light interferometer during fabrication (Fig. 8.5). The expected fiber profile is Gaussian, which allows one to extract the ROC and D_d from a fit to the measured profile. The effective diameter D_d is then typically taken as the full width at $1/e$ of the Gaussian [2]. However, in some cases the fiber profile may deviate from a perfect Gaussian shape, such that from the fit it cannot be determined which ROC and diameter the cavity mode really experiences. In these cases we can use alternative measurements to find these parameters.

Radius of curvature The frequency separation of Hermite-Gauss modes in a plane-concave cavity are determined by the ROC, as described in section 4.3.2. Inverting the relationship in Eq. (4.41) for $ROC_x = ROC_y$ we find that the ROC is given by:

$$ROC = \frac{L_{cav}}{1 - \cos\left(\frac{2\pi L_{cav} \Delta\nu_{mn}}{(m+n)c}\right)^2}, \quad (8.1)$$

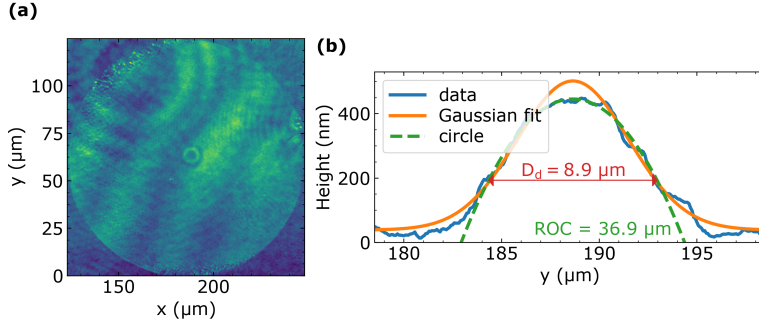


Figure 8.5: Parameters of a fiber dimple. (a) An image of a fiber dimple is created using a white light interferometer. In the middle of the fiber, the fiber core with the dimple are visible. (b) The dimple profile is extracted from the interference fringes of several images. For this fiber the profile deviates from a Gaussian fit (solid orange line), but a circle with a ROC of $36.9 \mu\text{m}$ as determined through independent measurements (Fig. 8.6) fits the shape well. The separately measured dimple diameter (Fig. 8.7) of $9.7 \mu\text{m}$ also provides a good fit to the profile. Figure created using data and analysis code by Thomas Fink.

where Δv_{mn} is the frequency separation between the Hermite-gaussian mode of order (m,n) and the corresponding fundamental mode.

From the cavity spectrum the locations of the fundamental and higher-order transverse modes can be determined, enabling the extraction of the cavity length and the ROC, as illustrated in Fig. 8.6.

Effective dimple diameter Clipping losses in the cavity arise when the beam width at the mirror exceeds the effective dimple diameter. The strength of the clipping losses in the cavity can be calculated from the beam width and the dimple diameter as described in Eq. (5.22). Conversely, the dimple diameter can thus be deduced from the clipping losses \mathcal{L}_{clip} as:

$$D_d = 2w_m \sqrt{\frac{-\ln(\mathcal{L}_{clip})}{2}}, \quad (8.2)$$

where the beam width on the fiber mirror can be found with Eq. (4.34):

$$w_m = w_0 \sqrt{1 + \left(\frac{L_{cav}\lambda_0}{\pi n w_0^2}\right)^2}, \quad (8.3)$$

in which w_0 is given by the cavity length and ROC through Eq. (4.39). Note that for a diamond-air cavity we can find w_m and w_0 by replacing $L_{cav} \rightarrow L' = t_a + t_d/n_d^2$ (see section 4.3.4).

If the cavity losses from other sources are very well characterised, a measurement of the cavity finesse ($\approx 2\pi/\mathcal{L}$) gives direct access to the clipping losses. Additionally, measuring the finesse as a function of the cavity length represents a more robust measurement that does not rely on knowing losses from all other sources. The effective fiber diameter can be extracted by fitting the length-dependency of the clipping losses, as shown in Fig. 8.7.

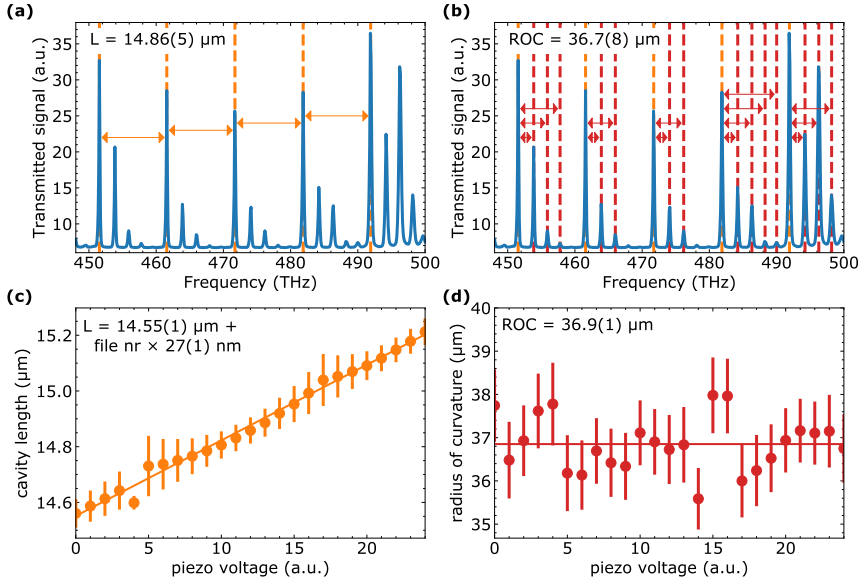


Figure 8.6: Characterisation of the bare cavity length and dimple radius of curvature. (a) The cavity spectrum is obtained by illuminating the cavity with a white light source and measuring the transmitted signal in the spectrometer. The cavity length is found from the free spectral range using Eq. (4.9). The free spectral range is found from the separation between the longitudinal modes. (b) The ROC is determined from the separation between the fundamental Gaussian mode and the higher order Hermite-Gaussian modes (Eq. (8.1)). (c) The cavity length is swept by changing the voltage on the piezo positioners. At every voltage the cavity length is determined from a spectrum as shown in (a). For the data shown here, the cavity length changes linearly with piezo voltage. (d) Changing the cavity length does not significantly influence the measured radius of curvature. The average radius of curvature is $ROC = 36.9(1) \mu\text{m}$.

We note that the effective diameter of the dimple can be reduced if the fiber tip is tilted. A geometric argument shows that for a tilt θ the new effective diameter D'_d relates to the old diameter D_d as:

$$D'_d = 2ROC (\arcsin(D_d/(2ROC)) - \theta/2) \quad (8.4)$$

$$\approx D_d - \theta ROC, \quad (8.5)$$

where the approximation holds in the limit of small arc angles, i.e. if $D_d/(2ROC) \ll 1$ (this is typically the case for laser-machined fiber tips [3]). The tip-tilt state used for the piezo-positioning in the setup described in Fig. 8.1 lateral positioning and fiber tilt are interdependent. Moving over the full lateral range induces a fiber tilt of 50 mrad. Since the value of the clipping losses is very sensitive to the dimple diameter, this effect may result in a significant change in cavity losses depending on the fiber tilt.

8.1.4. CAVITY DRIFT

We define cavity drift as a cavity length change over long timescales in a monotone direction. Cavity drift results mostly from piezo creep and temperature fluctuations.

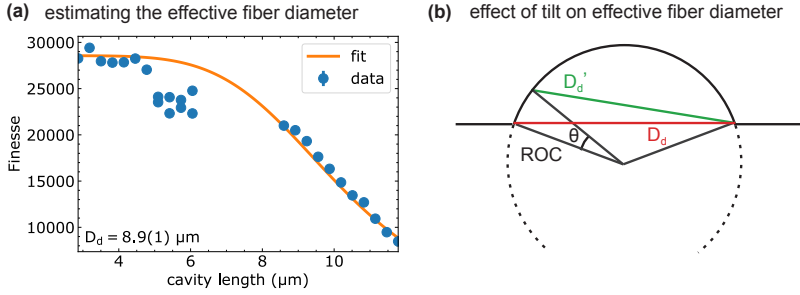


Figure 8.7: Characterisation of the fiber dimple diameter. (a) Measurements of the cavity finesse as a function of bare cavity length, for a mirror configuration with total losses of $\mathcal{L}_{\text{tot}} = 220$ ppm. The fiber dimple in this measurement is the same as used in Fig. 8.6, with a radius of curvature of $36.9(1) \mu\text{m}$. By fitting the clipping losses in the cavity given by Eq. (5.22) to the data, we extract the fiber diameter, that is $8.9 \mu\text{m}$. (b) The effective diameter depends on the tilt of the fiber. Through a geometrical argument depicted here we find that the relationship is given by: $\arcsin(D_d/(2ROC)) - \arcsin(D'_d/(2ROC)) = \theta/2$. We note that for the measurements in (a) the fiber tilt is not known. A tilt of 50 mrad (the maximum tilt induced by the tip-tilt stage) can change the effective diameter of that fiber by $1.8 \mu\text{m}$.

Piezo creep When a voltage step is applied to a piezoelectric material, the material continues to expand for some time after the step. It follows the following relation [4, 5]:

$$\delta L(t) = \delta L_0 \left(1 + \gamma \log \left(\frac{t}{0.1} \right) \right), \quad (8.6)$$

where $\delta L(t)$ is the change in length as a function of time, δL_0 is the length change at 0.1 seconds after the voltage step, and γ is a factor quantifying the amount of creep. In our system we measure a creep factor of $\gamma = 0.033 \pm 0.005$, by averaging over three measurements like the measurement presented in Fig. 8.8. Using the creep factor one can calculate how long the system needs to stabilize after a voltage step, when a stability of ν_{req} over a time t_{req} is needed:

$$t_{\text{stabilize}} = \frac{t_{\text{req}} \gamma \delta \nu_0}{\nu_{\text{req}} \ln(10)}, \quad (8.7)$$

with $\delta \nu_0$ the frequency step resulting from the voltage step. This can be a significant waiting time: for example after a frequency step of $\delta \nu_0 = 10$ THz it takes $t_{\text{stabilize}} = 70$ minutes waiting time for the system to stabilize to a level of $\nu_{\text{req}} = 1$ GHz over a $t_{\text{req}} = 30$ seconds time span.

Thermal drift At room temperature, the system is sensitive to environment temperature fluctuations that cause thermal expansion in the system and related drift. At low temperatures, the system is isolated from such fluctuations. In this case the dominant thermal drift is laser-induced. Absorption in the mirror coatings and diamond cause local heating, that result in thermal expansion of the mirror and fiber, changing the effective cavity length. Turning on and off the excitation laser, or moving the cavity on and

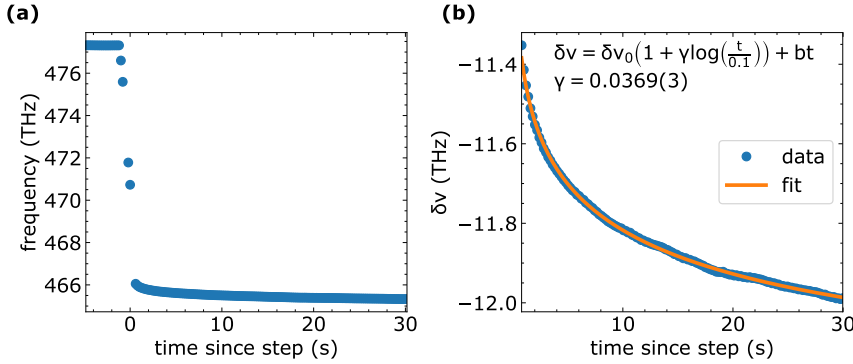


Figure 8.8: Measurements of the piezo creep. (a) The piezo creep is measured at cryogenic temperature by stepping the piezo voltage over 4 V while monitoring the cavity resonance frequency on the spectrometer. The step size in frequency in this measurement is $\delta\nu_0 = -11.017(4)$ THz. (b) Zooming in on the drift of the cavity resonance frequency, we can determine the creep factor. Eq. (8.6) is converted to frequency, using that δL and $\delta\nu$ are approximately linearly proportional. The creep factor determined is $\gamma = 0.0369(3)$. Additionally, a linear component of $b = 1.2(1)$ GHz/s is present, possibly resulting from thermal drift.

off-resonance with the red laser thus changes the cavity length. It should be noted that due to a sign-change of the thermal expansion coefficient of SiO_2 at low temperatures compared to room temperature the response of the cavity length to laser power is opposite to the reported changes at room temperature [6]. Indeed, we find that at cryogenic temperatures the cavity length increases with temperature applied laser power.

8.1.5. VIBRATIONS

While the amplitude of vibrations determines the impact on the cavity's performance for ZPL enhancement of the NV centre, the frequency of the vibrations gives us information about their origin, and a handle for mitigation with passive or active approaches. We are therefore interested in studying both. We describe two ways to measure vibrations: through the effective broadening of the linewidth, and by measuring the transmission of the cavity at the flank of the resonance. While the first only probes the amplitude of vibrations, with the second we can find both the amplitude and the spectrum.

Linewidth broadening To measure the effective linewidth including vibrations, in contrast to measurements of the intrinsic cavity linewidth, we aim to measure on a timescale slower than the vibrations. The longest characteristic timescale of the vibrations in our system is the period of the pulse tube cryostat, that is around ≈ 1 second. This sets the timescale of our sweep: at each datapoint we average the cavity signal for the full period of the pulse-tube. For these timescales a sweep of the laser frequency across the resonance is a suitable measurement method, since the laser frequency can be calibrated with the wavemeter for each frequency step during the measurement.

To measure the effective linewidth, the red laser is coupled into the fiber port of the cavity, and we detect the cavity transmission on the photodiode, that is read out with the ADwin. The ADwin reads the ADC out every 10 μs , and saves the averaged signal every 10

ms, such that in post-processing the signal can be binned. The start of the measurement is triggered by a synchronisation signal from the cryostat that is periodic with the pulse tube cycle. In this way the binned data can be related to a timing within the pulse tube cycle.

Due to the long measurement duration the recorded linewidth is sensitive to drift. To avoid piezo creep to influence the measurements, we wait for the system time to stabilize before starting the measurement. The thermal drift from the changing intra-cavity laser power for the on- and off- resonance cases also plays a role. In measurements where the cavity length is swept over the resonance this can result in narrower or wider line shapes depending on the sweep direction [2, 7]. In this case we however sweep the laser frequency over the resonance. As a result, the width of the lineshape does not change, but the response becomes asymmetric in frequency (as visible in chapter 10, fig 3b). Due to the sign-change of the thermal expansion coefficient of SiO_2 at low temperatures compared to room temperature the response of the cavity length to laser power in that figure is opposite to the reported changes at room temperature [6].

Vibration spectrum To obtain the vibration spectrum we record a time trace of the cavity transmission and use a Fourier transform to turn this into a spectrum. The transmission is probed at the flank of a resonance to achieve the largest sensitivity. For this measurement to be reliable, the amplitude of vibrations cannot be larger than approximately the cavity linewidth: otherwise the cavity can move across the resonance frequency which removes the one-to-one mapping of signal amplitude to vibration amplitude. This condition is more easily satisfied for a low-finesse cavity, since for a lower finesse the vibrations in frequency are smaller compared to the cavity linewidth (Eq. (5.24)). A cavity with low finesse can be made by using a laser with a wavelength far outside the cavity stopband, or by using a large cavity length such that the cavity experiences clipping losses section 5.3.2.

The vibration amplitude in length can also be found from this measurement, by calibrating the signal amplitude with the cavity linewidth, cavity length and resonance frequency. This requires assuming that the resonance frequency and cavity length have a linear relationship, which is true if the frequency deviations are small compared to the free spectral range.

8.2. NV-CAVITY COUPLING

An important step towards the observation of ZPL enhancement of an NV is to observe NV centres embedded in the cavity emitting into the cavity mode. In this section we describe the measurement techniques that enable this. First we describe how the cavity coupled emission can be observed in a spectrometer and in a single-photon APD. After that we describe a method for a controlled cavity length sweep, based on stabilization to a tunable laser. These controlled and stabilized measurement routines are the basis for more advanced protocols that may be used in the future, including resonant excitation or the stabilisation of the cavity resonance frequency during NV measurements.

8.2.1. DETECTION IN A SPECTROMETER

NV emission into the cavity mode can be detected in the spectrometer by sweeping the cavity across the resonance frequency. Simultaneously the NV is excited off-resonantly with a green laser. Since the excitation is off-resonant, it can be spectrally filtered from the NV emission.

The cavity length is not actively monitored or stabilised during this measurement, which has two consequences. Firstly, the cavity length has to be manually tuned to be near the ZPL frequency before the measurement. To that end, the cavity resonance can be observed in the spectrometer, visible through background fluorescence excited by the green laser, or - if this is not sufficiently visible - scanning the red laser to be on resonance. In the case the red laser is used, special care is taken to turn off the resonant laser during the measurement stage, since any background light at a resonant wavelength would lead to a false measurement result. Secondly, thermal drift during the measurement has to be minimized in order to scan over the desired range. To ensure this, the green laser used during the measurement is already turned on during the tuning of the cavity length before the measurement. If the resonant laser is used for that process, this should be done with the minimal power possible.

8.2.2. DETECTION WITH A SINGLE-PHOTON APD

Analogous to the measurement method described above, the NV emission can be detected in an APD instead of the spectrometer. The spectral selection of photons at the ZPL frequency is enabled by a narrow frequency filter in the detection path, created with two tunable band pass filters.

There are several advantages of detecting with an APD versus the spectrometer. It not only enables a higher sensitivity, but importantly also allows for the connection of a timetagger, enabling lifetime and auto-correlation measurements on the NV emission. Furthermore, in contrast to detection in the spectrometer, it is compatible with active control over the cavity length during the sweep, as will be outlined below.

8.2.3. CONTROLLED LENGTH-SWEEP

The measurement methods described above enable detection of the NV emission into the ZPL into the cavity, but lack active monitoring and feedback on the cavity length during the sweep across the resonance. In this section we describe how cavity length stabilisation can be included in the measurement procedure.

Stabilisation of the cavity length is performed by first stabilising the tunable red laser to a frequency setpoint, and next stabilising the cavity length to be on resonance with the laser frequency. When the cavity stabilisation is successful, the sequence enters a measure stage.

Laser frequency stabilisation The protocol starts with the stabilisation of the red laser frequency, using a proportional-integral (PI) feedback loop based on the difference between a wavemeter readout of the laser frequency and a setpoint that can be changed for each measurement step. The stabilisation is flagged successful if the difference between the setpoint and measured wavelength is less than a threshold value (set to 5 MHz).

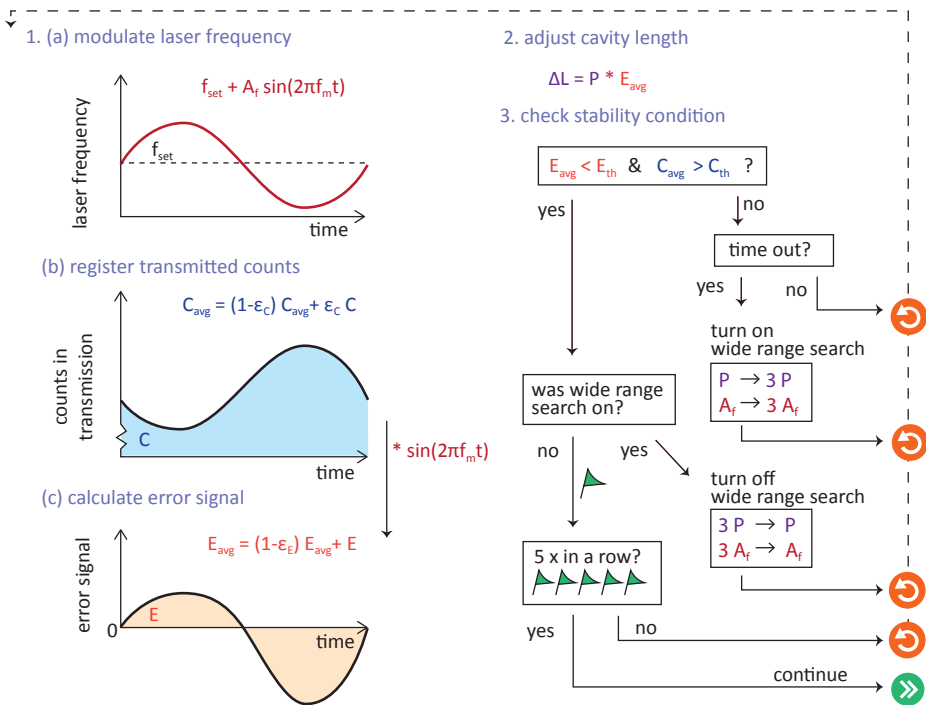


Figure 8.9: Cavity stabilisation procedure. The cavity is stabilised to a set laser frequency f_{set} . *Step 1. (a)* The laser frequency is modulated with a sinusoidal signal of frequency $f_m = 400$ Hz and amplitude ≈ 0.5 GHz in $n_b = 200$ steps per period while *(b)* the transmitted counts (C) are monitored. *(c)* The error signal E is $E = C \sin(2\pi f_m t)$. Average signals for transmitted counts and the laser frequency are calculated using a weighted running average with $\epsilon_C = 1/40$ and $\epsilon_E = 1/(50n_b)$. *Step 2.* The cavity length is adjusted with a proportionality factor P according to the obtained error signal. *Step 3.* Check whether the signal satisfy the stability criteria, and go to a wider-range scan with a larger modulation amplitude and larger proportional cavity length stepsize if the time out time of $t = 30$ s is reached.

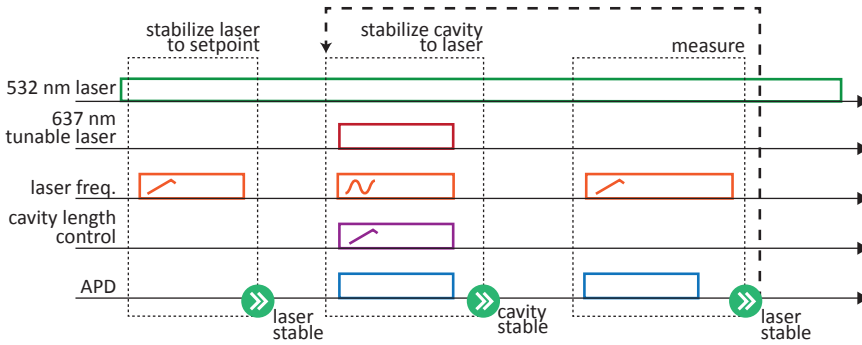


Figure 8.10: Measurement sequence for the detection of NVs in an optical cavity. The stabilize-and-measure sequence consists of three parts: laser stabilization, cavity stabilization and a measure stage. The green laser remains on during the full sequence to prevent thermal drift. The APD detects transmitted photons through the cavity during the cavity stabilisation stage, and resonantly emitted NV photons during the measurement stage. During the measure stage, the red tunable laser is off, but its frequency is already tuned to the next setpoint.

Cavity length stabilisation Next, the cavity length has to be adjusted such that the cavity is on-resonance with the red laser. The stabilisation protocol responsible for this is schematically outlined in Fig. 8.9. We measure how well on-resonance the cavity is with the red laser by monitoring the transmission through the cavity. The transmitted light is measured on an APD, so the red laser power is attenuated until only a few nW enter the fiber-port of the cavity. The counts on the APD are then well below saturation. By modulating the laser frequency around the setpoint frequency, the resulting modulation in resonance counts can be used to adjust the cavity length in the right direction. The detailed procedure by which the error signal is generated is outlined in Fig. 8.9a-c. The stabilisation is repeated until the cavity is successfully on resonance with the laser.

Success of the stabilisation is determined based on two thresholds: (1) The magnitude of the (normalised) error signal. The error signal is a running average over 50 modulation rounds. It has to be lower than an empirically determined threshold value ($0.1 \times$ the total counts in that round). (2) The average counts during stabilisation. The counts as a running average over the last 40 modulation rounds has to exceed $0.9 \times$ the pre-determined on-resonance counts. This criterion is required since the error signal far off-resonance is low: in that situation there is also no strong frequency-dependency of the detected counts. The selection on counts removes these cases from success.

Measure stage In the measure stage we use a high power green laser for off-resonant excitation. This significantly heats the system. If it would be turned on during the measurement stage only, it would induce thermal drift during the measurement stage compared to the stabilised length. It is therefore applied throughout the measurement sequence, including the laser and cavity stabilisation stages (Fig. 8.10). The NV ZPL emission that is induced by the green laser causes an unwanted background during the stabilisation stage. To ensure that this does not interfere with the cavity length stabilisation step, the measured count rate from the red laser should exceed the one from the ZPL. For the

measurement described in chapter 11 the count rates from the red laser on-resonance are fixed to ≈ 60 kHz.

REFERENCES

- [1] Pfaff, W., *Quantum Measurement and Entanglement of Spin Quantum Bits in Diamond*, Ph.D. thesis, Delft University of Technology (2013).
- [2] Hunger, D. *et al.*, *A fiber Fabry–Perot cavity with high finesse*, *New J. Phys.* **12**, 065038 (2010).
- [3] Hunger, D., Deutsch, C., Barbour, R. J., Warburton, R. J. & Reichel, J., *Laser micro-fabrication of concave, low-roughness features in silica*, *AIP Adv.* **2**, 012119 (2012).
- [4] Vieira, S., *The behavior and calibration of some piezoelectric ceramics used in the STM*, *IBM J. Res. Dev.* **30**, 553 (1986).
- [5] Jung, H. & Gweon, D. G., *Creep characteristics of piezoelectric actuators*, *Rev. Sci. Instrum.* **71**, 1896 (2000).
- [6] Farsi, A., Siciliani De Cumis, M., Marino, F. & Marin, E., *Photothermal and thermo-refractive effects in high reflectivity mirrors at room and cryogenic temperature*, *Journal Appl. Phys.* **111**, 043101 (2012).
- [7] Brachmann, J. F. S., Kaupp, H., Hänsch, T. W. & Hunger, D., *Photothermal effects in ultra-precisely stabilized tunable microcavities*, *Opt. Expr.* **24**, 21205 (2016).

9

ROBUST NANO-FABRICATION OF AN INTEGRATED PLATFORM FOR SPIN CONTROL IN A TUNABLE MICROCAVITY

**Stefan Bogdanović, Madelaine Liddy, Suzanne van Dam,
Lisanne Coenen, Thomas Fink, Marko Lončar, and Ronald
Hanson**

Coupling nitrogen-vacancy (NV) centers in diamond to optical cavities is a promising way to enhance the efficiency of diamond based quantum networks. An essential aspect of the full toolbox required for the operation of these networks is the ability to achieve microwave control of the electron spin associated with this defect within the cavity framework. Here, we report on the fabrication of an integrated platform for microwave control of an NV center electron spin in an open, tunable Fabry-Pérot microcavity. A critical aspect of the measurements of the cavity's finesse reveals that the presented fabrication process does not compromise its optical properties. We provide a method to incorporate a thin diamond slab into the cavity architecture and demonstrate control of the NV center spin. These results show the promise of this design for future cavity-enhanced NV center spin-photon entanglement experiments.

The results in this chapter have been published in *APL photonics* **2**, 126101 (2017) [1].

9.1. INTRODUCTION

Nitrogen-vacancy (NV) colour centers in diamond have emerged as attractive candidates for quantum photonic applications. Their electronic spin can be optically initialized, read out in a single shot [2], and coherently manipulated with the use of microwave signals [3]. This spin-photon interface provides a platform for distant entanglement generation [4], while additional coupling to nearby carbon-13 nuclear spins forms a multi-qubit quantum node [5–8]. These aspects make the NV center a good candidate for quantum network protocols [9–11]. The efficiency of entanglement generation between network nodes is currently limited by the NV center's low ($\approx 3\%$) emission rate of the resonant zero-phonon line (ZPL) photons. This problem can be addressed by coupling NV centers to optical microcavities [12–24], enhancing the ZPL emission rate and providing efficient photon extraction by means of the Purcell effect [25]. An appealing cavity design consists of an open, tunable Fabry-Pérot microcavity housing a large area diamond membrane [26–28] in which emitters retain their bulk-like properties [29]. The tunability of this design enables both spectral positioning of the cavity to be resonant with the emitter as well as selective lateral placement of the emitter within the center of the cavity mode. However, in order to use these emitters in quantum information protocols, microwave control must be integrated into the cavity architecture. Here, we present fabrication methods used to create a platform that integrates microwave control of an NV center spin within an optical cavity while maintaining the cavity's high finesse properties. While microwave addressing of a single NV center spin has already been realized in thin diamond slabs [30] and photonic crystal cavities [22], this is the first demonstration of NV center spin addressing within a framework tailored to the implementation of a tunable microcavity.

9.2. FIBER DIMPLE AND MIRROR COATINGS

The cavity consists of a laser ablated dimpled fiber tip [31, 32] and polished fused silica plate, both coated with a highly reflective dielectric mirror stack forming a Distributed Bragg Reflector (DBR) (Laseroptik).

The curved fiber profile was fabricated using a CO₂ laser ablation technique [31, 32]: A single 1 ms long circularly polarized laser pulse is focused onto the cleaved fiber facet. As a result of thermal evaporation and subsequent melting, a concave depression with low surface roughness of $\sigma_{\text{rms}} \lesssim 0.20 \pm 0.02$ nm is created. The depth and diameter of this depression can be controlled by varying a combination of the pulse power, duration, and beam waist. Due to the small fiber core diameter, care must be taken to center the depression onto the cleaved facet to ensure a good coupling efficiency to the cavity mode.

After laser ablation of the fiber tip the dimpled tip and a polished fused silica plate are both coated with a highly reflective dielectric mirror stack forming a Distributed Bragg Reflector (DBR) (Laseroptik). The residual transmission of this stack is measured to be 50 ppm at 637 nm wavelength. The observed fiber and specified fused silica surface roughness (0.2 nm and 0.5 nm RMS, respectively) correspond to scattering losses of 25 and 100 ppm [33]. Following coating, the planar mirror is annealed in vacuum at 300°C for 5 hours, which reduces the absorption losses of the stack from ≈ 50 ppm to ≤ 10 ppm

[34]. The total losses give an expected value of the cavity finesse of $F \approx 22\,000$.

9.3. FABRICATION OF STRIPLINES AND MARKER FIELD

In order to address the spin and index the location of the NV centers, parallel microwave striplines and a field of uniquely identifiable markers are fabricated on the planar mirror surface. For successful diamond bonding, the processed mirrors must possess a low profile for all patterned surface features. Therefore trenches of 65 nm depth are etched into the mirror plate, before evaporation of 5 nm titanium and 65 nm gold. The markers are deposited directly on the mirror by evaporation of 5 nm titanium and 5 nm gold.

Essential to the desired cavity architecture is the possibility to bond a several micrometer thin diamond membrane over the structures on the planar mirror. Irregular structures and frills on the edges of the fabricated striplines have been found to deter successful bonding. Furthermore, a microwave stripline that is fully recessed in the etched trench acts as a capillary channel for water used during the bonding process, preventing a good diamond-mirror bond. A uniform raised profile of a feature above the mirror surface by no more than 20 nm was found to allow for successful bonding.

9.4. CAVITY FINESSE

In order to preserve the optical performance of the cavity, mirror coatings must not be damaged or have surface residues left as a result of the processing. To verify that the presented fabrication procedure does not introduce additional losses to the planar mirror, the finesse of a cavity with a processed and unprocessed planar mirror is compared while keeping the fiber mirror unaltered. The finesse F is calculated from the cavity linewidth $\delta\nu$ and free spectral range (FSR) ν_{FSR} :

$$F = \frac{\nu_{FSR}}{\delta\nu} = \frac{c}{2 \cdot L_{cav} \cdot \delta\nu}, \quad (9.1)$$

where c is the speed of light and L_{cav} the cavity length.

The cavity linewidth is obtained by exciting the cavity with a 637 nm laser through the fiber port while modulating the planar mirror position with a 40 Hz sinusoidal signal scanning the cavity across the resonance. The measurement setup is presented in Fig. 9.1a. Before entering the cavity, the light passes through an electro-optic modulator (EOM) crating sidebands with a fixed frequency separation, used to convert the measured linewidth in length to frequency. The imperfect elliptical curvature in the fiber profile induces a polarization splitting of the cavity mode which is filtered using a polarizer in the detection path before the transmitted signal reaches the photodiode. An example of a measured linewidth for a cavity consisting of an unprocessed (processed) planar mirror is presented in Fig. 9.1b (Fig. 9.1c) for two different cavity lengths. The measured linewidth is an average over ten such single sweeps. It is to be noted that all cavity measurements were performed in the absence of a diamond slab, to compare only the processing effects on the mirror properties. For a study of the effects of a diamond slab incorporated into the cavity, see references [26, 27].

The FSR is obtained by coupling a broadband supercontinuum laser into the cavity and measuring the transmitted signal on a spectrometer. Fig. 9.1d (Fig. 9.1e) shows

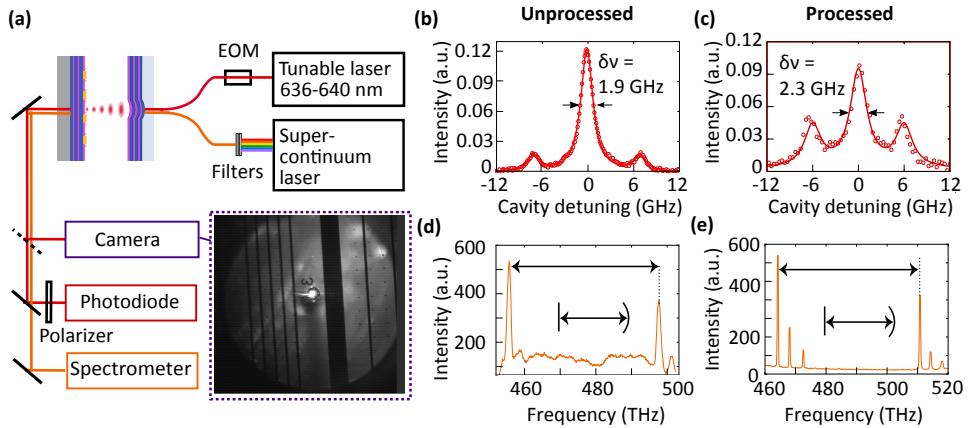


Figure 9.1: Measurement of the cavity finesse. (a) Schematic of the cavity finesse measurement setup. The cavity consists of the mirror coated ablated fiber tip (with fiber radius of curvature $ROC = 22.4 \mu\text{m}$) glued to a custom designed fiber mount and screwed into a Newport (462-XYZ-M) stage for coarse positioning, and a planar mirror glued onto a piezo stage (PI E509.X1) for fine spectral cavity tuning. The inset shows a camera image of the patterned planar mirror and fiber microcavity on resonance. (b) Linewidth measurements of the unprocessed and (c) processed cavity are performed by exciting the cavity with a 637 nm laser (Newfocus TLB-6304) while modulating the cavity length. An EOM (Jenoptik) induces sidebands in the laser profile with separation of 7 GHz in (b) and 6 GHz in (c) that enable measuring the linewidth in frequency units. The transmitted light is collected on a photodiode (Thorlabs APD130A2) and read out on an oscilloscope. (d) Unprocessed and (e) processed cavity transmission spectra measured by coupling a supercontinuum broadband laser (Fianium SC400) into the cavity and measuring transmitted light on the spectrometer (Princeton Instruments Acton SP2500). The distance between the fundamental modes determines the cavity length (Eq. (9.1)).

the results of the FSR measurement for a cavity with an unprocessed (processed) planar mirror. Fundamental cavity modes can be seen as well as higher order modes at higher frequencies, which are confirmed by their shape in a camera image (not shown). Using the measured linewidth and FSR, the finesse value of the unprocessed mirror cavity is calculated (Eq. (9.1)) to be $F = (23 \pm 3) \cdot 10^3$, while the finesse of the processed mirror is $F = (20 \pm 2) \cdot 10^3$. Measured finesse values are in good agreement with the finesse values calculated from the mirror transmission and losses. We conclude that our fabrication procedure preserves good optical properties of the mirrors.

9.5. DIAMOND MEMBRANE PREPARATION AND VAN DER WAALS BONDING

For integration into the cavity system the large-area diamond membranes must be bonded to the processed planar mirrors. Diamond membranes are obtained by slicing and mechanically polishing $2 \text{ mm} \times 2 \text{ mm} \times 0.5 \text{ mm}$ (100) bulk diamonds (Element Six), into $30 \mu\text{m}$ thick slabs (Delaware Diamond Knives). Leftover residue and surface damage from the mechanical polishing is removed by submerging the diamond in a boiling mixture of 1:1:1 (Perchloric : Nitric : Sulfuric) acid for 1 hour, followed by the removal of several μm on the top side of the polished diamond membrane using an Ar/Cl_2 based ICP

RIE (Methods). Chlorine based etching produces smooth diamond surfaces which is required to minimize scattering loss at the diamond interface within the cavity [35, 36]. The final diamond roughness, measured with Atomic Force Microscopy, was found to be 0.2 nm RMS. However, prolonged exposure to chlorine etch gas has been linked to degrading optical properties of the NV centers. Introducing an O₂ based plasma etching step has been found to resolve the surface chlorine contamination [28, 29].

In order to preserve optical properties of the cavity, the diamond must be fixed to the mirror without adhesives, constraining the type of bonding techniques permitted. First attempts to etch the diamond slab with the bottom surface coated with the dielectric mirror stack resulted in coating delamination, likely due to the difference in thermal expansion coefficients of the materials. Successful bonding of the diamond membrane to a processed planar mirror with an activated hydrophilic surface has been achieved via Van der Waals forces. Addition of a water droplet between the two interfaces promotes bonding via strong interfacial forces creating good optical contact between the diamond and the mirror, removing the need for adhesives [37, 38].

To prepare the processed mirror for bonding, it is placed in an Oxygen plasma environment at 0.4 mbar for 45 s with 100 W, altering the hydrophobicity of the surface (Fig. 9.2a-i). Water is pipetted onto the surface of the mirror (Fig. 9.2a-ii) followed by placing the diamond membrane on top of a patterned region. Using the light from an optical microscope objective, the water is evaporated while the bonding process is monitored simultaneously (Fig. 9.2a-iii). The quality of the bond can be evaluated with visual cues as well as with a profile measurement. Fig. 9.2a-iv and Fig. 9.2b show SEM and optical images respectively of the bonded diamond. A poor bond can be identified by the appearance of Newton rings, indicative of an uneven surface and the existence of an air gap between the mirror and diamond. In the optical image, a well bonded diamond is indicated by a uniform colouration. The "milky" colouration seen near the striplines highlights the slightly elevated areas. Profilometer measurements revealed an overall height variation of 100 nm over the diamond surface bonded on top of the patterned area.

9.6. ELECTRON SPIN RESONANCE

A scanning confocal microscope is used for fluorescence imaging of the NV centers under ambient conditions with off resonant laser excitation at 532 nm. The NV centers were located in close proximity to the marker field such that they can be easily indexed and located again (Fig. 9.2c). The embedded microwave stripline, seen on the left portion of the confocal scan in Fig. 9.2c, is used to identify and address the $m_s = 0 \rightarrow m_s = \pm 1$ NV center spin transitions [40, 41] in the presence of a static magnetic field $B_z \approx 10$ G. The optically detected electron spin resonance spectrum is shown in Fig. 9.2d. This demonstrates our ability to address NV center spin with microwaves when combining the stripline fabrication and diamond bonding technique.

9.7. CONCLUSIONS

In conclusion, we have presented the fabrication of an integrated platform for microwave control in an open, high finesse Fabry-Pérot microcavity enclosing a thin diamond mem-

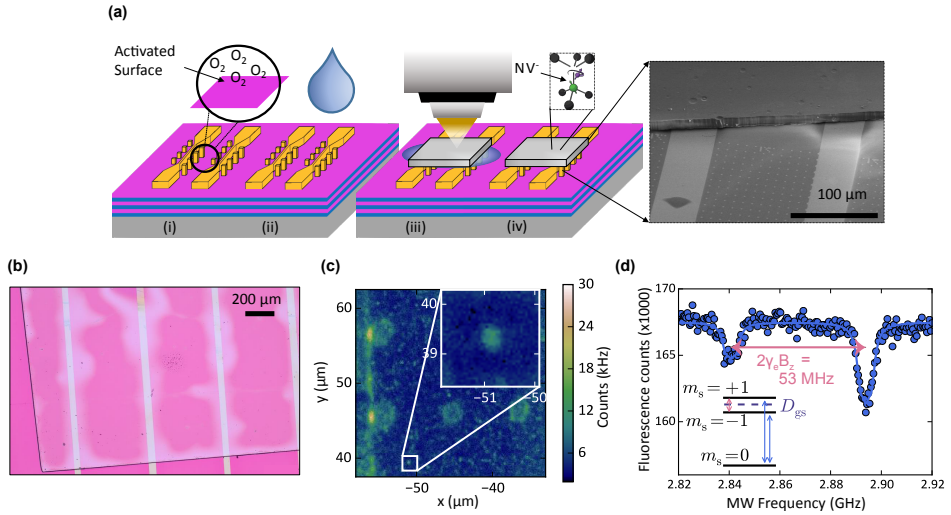


Figure 9.2: Diamond membrane bonding and NV center spin control. (a) Diamond bonding to the patterned mirror: (i) Surface activation of the processed mirror chip with an oxygen plasma at low vacuum. (ii) Water is pipetted onto the activated surface. (iii) The diamond membrane is placed onto the patterned surface followed by drying of the water using the light from the microscope objective. (iv) The diamond membrane containing NV centers is bonded to the mirror. Inset: A scanning electron microscope (SEM) image of a bonded diamond membrane atop a patterned planar mirror. (b) Optical image of an etched $2\text{ mm} \times 2\text{ mm} \times 8\text{ }\mu\text{m}$ diamond, bonded to the processed planar mirror with microwave striplines and marker array. (c) Scanning optical confocal image showing a single NV center (inset). The scans were performed at the depth of $\approx 1.5\text{ }\mu\text{m}$ below the surface of the diamond membrane. The $2\text{ }\mu\text{m} \times 2\text{ }\mu\text{m}$ spots correspond to the photoluminescence from the square gold markers. Part of the microwave stripline is visible on the left. (d) Optically detected electron spin resonance spectrum demonstrating NV spin addressing with the embedded microwave striplines. The spectrum exhibits two resonances associated with the $m_s = 0 \rightarrow m_s = \pm 1$ spin transitions (inset), centered at the zero field splitting $D_{gs} = 2.87\text{ GHz}$. Two resonances are separated by the Zeeman splitting $2\gamma_e B_z$ where γ_e is the NV electron spin gyromagnetic ratio and B_z is the static external magnetic field. Individual electron spin resonance dips are fitted using three Lorentzian profiles with a splitting of 2.16 MHz to account for the hyperfine splitting from the NV interaction with its host ^{14}N nuclear spin ($I_N = 1$) [39].

brane. Finesse measurements of the processed mirrors confirm that the fabrication procedure does not compromise their optical properties. We present a diamond bonding method that allows placing large area diamond membranes onto the cavity mirror while simultaneously enabling the microwave control of the NV center spin. The presented cavity architecture is well suited for enabling enhancement of the NV centers resonant emission along with the control of their spins.

ACKNOWLEDGEMENTS

The authors wish to thank P. Latawiec for helpful discussions. M.L. wishes to acknowledge the support of QuTech during his sabbatical stay. M.S.Z.L. acknowledges the Dutch Liberation Scholarship Programme. This work was supported by the Dutch Organiza-

tion for Fundamental Research on Matter (FOM), Dutch Technology Foundation (STW), the Netherlands Organization for Scientific Research (NWO) through a VICI grant, the EU S3NANO program and the European Research Council through a Starting Grant.

REFERENCES

- [1] Bogdanovic, S. *et al.*, *Robust nano-fabrication of an integrated platform for spin control in a tunable microcavity*, *APL photonics* **2**, 126101 (2017).
- [2] Robledo, L. *et al.*, *High-fidelity projective read-out of a solid-state spin quantum register*, *Nature* **477**, 574 (2011).
- [3] Jelezko, F., Gaebel, T., Popa, I., Gruber, A. & Wrachtrup, J., *Observation of coherent oscillations in a single electron spin*, *Phys. Rev. Lett.* **92**, 076401 (2004).
- [4] Bernien, H. *et al.*, *Heralded entanglement between solid-state qubits separated by three metres*, *Nature* **497**, 86 (2013).
- [5] Dutt, M. V. G. *et al.*, *Quantum register based on individual electronic and nuclear spin qubits in diamond*, *Science* **316**, 1312 (2007).
- [6] Neumann, P. *et al.*, *Single-shot readout of a single nuclear spin*, *Science* **329**, 542 (2010).
- [7] Taminiou, T. H. *et al.*, *Detection and control of individual nuclear spins using a weakly coupled electron spin*, *Phys. Rev. Lett.* **109**, 137602 (2012).
- [8] Reiserer, A. *et al.*, *Robust quantum-network memory using decoherence-protected subspaces of nuclear spins*, *Phys. Rev. X* **6**, 021040 (2016).
- [9] Kimble, H. J., *The quantum internet*, *Nature* **453**, 1023 (2008).
- [10] Kalb, N. *et al.*, *Entanglement distillation between solid-state quantum network nodes*, *Science* **356**, 928 (2017).
- [11] van Dam, S. B., Humphreys, P. C., Rozpędek, F., Wehner, S. & Hanson, R., *Multiplexed entanglement generation over quantum networks using multi-qubit nodes*, *Quantum Sci. Technol.* **2**, 034002 (2017).
- [12] Wolters, J. *et al.*, *Enhancement of the zero phonon line emission from a single nitrogen vacancy center in a nanodiamond via coupling to a photonic crystal cavity*, *Appl. Phys. Lett.* **97**, 141108 (2010).
- [13] Barclay, P. E., Fu, K. M. C., Santori, C., Faraon, A. & Beausoleil, R. G., *Hybrid nanocavity resonant enhancement of color center emission in diamond*, *Phys. Rev. X* **1**, 011007 (2011).
- [14] van der Sar, T. *et al.*, *Deterministic nanoassembly of a coupled quantum emitter–photonic crystal cavity system*, *Appl. Phys. Lett.* **98**, 193103 (2011).

- [15] Faraon, A., Santori, C., Huang, Z., Acosta, V. M. & Beausoleil, R. G., *Coupling of nitrogen-vacancy centers to photonic crystal cavities in monocrystalline diamond*, Phys. Rev. Lett. **109**, 033604 (2012).
- [16] Kaupp, H. *et al.*, *Scaling laws of the cavity enhancement for nitrogen-vacancy centers in diamond*, Phys. Rev. A **88**, 053812 (2013).
- [17] Albrecht, R., Bommer, A., Deutsch, C., Reichel, J. & Becher, C., *Coupling of a single nitrogen-vacancy center in diamond to a fiber-based microcavity*, Phys. Rev. Lett. **110**, 243602 (2013).
- [18] Hausmann, B. J. M. *et al.*, *Coupling of nv centers to photonic crystal nanobeams in diamond*, Nano Lett. **13**, 5791 (2013).
- [19] Lee, J. C. *et al.*, *Deterministic coupling of delta-doped nitrogen vacancy centers to a nanobeam photonic crystal cavity*, Appl. Phys. Lett. **105**, 261101 (2014).
- [20] Riedrich-Möller, J. *et al.*, *Nanoimplantation and purcell enhancement of single nitrogen-vacancy centers in photonic crystal cavities in diamond*, Appl. Phys. Lett. **106**, 221103 (2015).
- [21] Englund, D. *et al.*, *Deterministic coupling of a single nitrogen vacancy center to a photonic crystal cavity*, Nano Lett. **10**, 3922 (2010).
- [22] Li, L. *et al.*, *Coherent spin control of a nanocavity-enhanced qubit in diamond*, Nat. Commun. **6**, 6173 (2015).
- [23] Johnson, S. *et al.*, *Tunable cavity coupling of the zero phonon line of a nitrogen-vacancy defect in diamond*, New J. Phys. **17**, 122003 (2015).
- [24] Kaupp, H. *et al.*, *Purcell-enhanced single-photon emission from nitrogen-vacancy centers coupled to a tunable microcavity*, Phys. Rev. Applied **6**, 054010 (2016).
- [25] Purcell, E. M., Torrey, H. C. & Pound, R. V., *Resonance absorption by nuclear magnetic moments in a solid*, Phys. Rev. **69**, 37 (1946).
- [26] Janitz, E. *et al.*, *Fabry-Perot microcavity for diamond-based photonics*, Phys. Rev. A **92**, 043844 (2015).
- [27] Bogdanović, S. *et al.*, *Design and low-temperature characterization of a tunable microcavity for diamond-based quantum networks*, Appl. Phys. Lett. **110**, 171103 (2017).
- [28] Riedel, D. *et al.*, *Deterministic enhancement of coherent photon generation from a nitrogen-vacancy center in ultrapure diamond*, Phys. Rev. X **7**, 031040 (2017).
- [29] Chu, Y. *et al.*, *Coherent optical transitions in implanted nitrogen vacancy centers*, Nano Lett. **14**, 1982 (2014).
- [30] Hodges, J. S. *et al.*, *Long-lived NV^- spin coherence in high-purity diamond membranes*, New J. Phys. **14**, 093004 (2012).

- [31] Hunger, D. *et al.*, *A fiber fabry–perot cavity with high finesse*, *New J. Phys.* **12**, 065038 (2010).
- [32] Hunger, D., Deutsch, C., Barbour, R. J., Warburton, R. J. & Reichel, J., *Laser micro-fabrication of concave, low-roughness features in silica*, *AIP Adv.* **2**, 012119 (2012).
- [33] Klaassen, T., van Exter, M. P. & Woerdman, J. P., *Characterization of scattering in an optical Fabry–Perot resonator*, *Appl. Opt.* **46**, 5210 (2007).
- [34] *Laseroptik, internal communication.* .
- [35] Enlund, J. *et al.*, *Anisotropic dry etching of boron doped single crystal CVD diamond*, *Carbon* **43**, 1839 (2005).
- [36] Lee, C., Gu, E., Dawson, M., Friel, I. & Scarsbrook, G., *Etching and micro-optics fabrication in diamond using chlorine-based inductively-coupled plasma*, *Diamond Relat. Mater.* **17**, 1292 (2008).
- [37] Yablonovitch, E., Hwang, D. M., Gmitter, T. J., Florez, L. T. & Harbison, J. P., *Van der Waals bonding of GaAs epitaxial liftoff films onto arbitrary substrates*, *Appl. Phys. Lett.* **56**, 2419 (1990).
- [38] Latawiec, P. *et al.*, *On-chip diamond Raman laser*, *Optica* **2**, 924 (2015).
- [39] Neumann, P. *et al.*, *Excited-state spectroscopy of single NV defects in diamond using optically detected magnetic resonance*, *New J. Phys.* **11**, 013017 (2009).
- [40] Gruber, A. *et al.*, *Scanning confocal optical microscopy and magnetic resonance on single defect centers*, *Science* **276**, 2012 (1997).
- [41] Balasubramanian, G. *et al.*, *Nanoscale imaging magnetometry with diamond spins under ambient conditions*, *Nature* **455**, 648 (2008).



10

DESIGN AND LOW-TEMPERATURE CHARACTERIZATION OF A TUNABLE MICROCAVITY FOR DIAMOND-BASED QUANTUM NETWORKS

**Stefan Bogdanović, Suzanne van Dam, Cristian Bonato,
Lisanne Coenen, Anne-Marije Zwerver, Bas Hensen,
Madelaine Liddy, Thomas Fink, Andreas Reiserer, Marko
Lončar, and Ronald Hanson**

We report on the fabrication and characterization of a Fabry-Pérot microcavity enclosing a thin diamond membrane at cryogenic temperatures. The cavity is designed to enhance resonant emission of single nitrogen-vacancy centers by allowing spectral and spatial tuning while preserving the optical properties observed in bulk diamond. We demonstrate cavity finesse at cryogenic temperatures within the range of $F = 4,000 - 12,000$ and find a sub-nanometer cavity stability. Modeling shows that coupling nitrogen-vacancy centers to these cavities could lead to an increase of remote entanglement success rates by three orders of magnitude.

The results in this chapter have been published in Applied Physics Letters **110**, 171103 (2017) [1].

10.1. INTRODUCTION

Nitrogen-vacancy (NV) centers in diamond are promising building blocks for realizing quantum networks for computation, simulation and communication. The NV center electron spin and nearby nuclear spins form a robust multi-qubit quantum network node that is fully controlled by microwave and optical pulses [2, 3]. Separate network nodes can be entangled through spin-photon entanglement and subsequent two-photon interference and detection [4–6]. The success rate of such entangling protocols is limited by the low probability (few percent) of the NV center emitting into the resonant zero-phonon line (ZPL). Coupling of an NV center to an optical cavity can greatly increase the rate of generation and collection of ZPL photons through Purcell enhancement [7]. Purcell enhancement of the ZPL has been demonstrated in several cavity architectures such as diamond photonic crystal cavities [8–12], microring resonators [13] and hybrid structures with evanescently coupled nanodiamonds [14–17]. In recent years the open Fabry-Pérot microcavity [18] has emerged as a promising platform for diamond emitters [19–23]. Such a microcavity provides *in-situ* spatial and spectral tunability, while reaching strong field confinement due to its small mode volume V and high quality factor Q . Moreover, this architecture allows for the use of diamond slabs [24] in which the NV center can be relatively far removed from surfaces and thus exhibit bulk-like optical properties, as required for quantum network applications.

10.2. A FIBER FABRY-PÉROT CAVITY

Here we report on the realization of a high-finesse tunable microcavity enclosing a diamond membrane and its characterization under cryogenic conditions as relevant for quantum network applications. Our cavity employs a concave fiber tip fabricated using a CO₂ laser ablation technique [25] coated with a dielectric mirror stack, and a high reflectivity plane mirror onto which a thin diamond membrane is bonded (see Figure 1a). This cavity configuration is mounted inside a closed-cycle cryostation (Montana Instruments). To minimize scattering loss as required for a high finesse optical cavity, low surface roughness at the mirror-diamond and diamond-air interfaces is essential. We fabricate the diamond membrane (Figure 1b) by etching a polished 30 μm thick diamond sheet (ElementSix) down to $\approx 4 \mu\text{m}$ using Ar/Cl₂ inductively coupled plasma reactive ion etching. This etching process is known to preserve the surface smoothness of the diamond [26, 27]. Using AFM, we measure a final diamond roughness value of 0.35 nm RMS. Finally the membrane is bonded to the plane mirror by Van der Waals forces [28].

10.3. CAVITY MODE STRUCTURE

We first study the cavity modes by recording transmission spectra as a function of cavity length using broadband excitation from a supercontinuum laser (see Figure 1c). From these spectra we extract the frequency of the fundamental modes of the cavity. The fiber mirror can be moved laterally to obtain an empty cavity (spectrum in Figure 1d), or a cavity including a diamond membrane (Figure 1e). The notably different length dependency for the two cases is a direct consequence of the presence of the high refractive index ($n_d = 2.417$) diamond membrane within the optical cavity. The partially reflect-

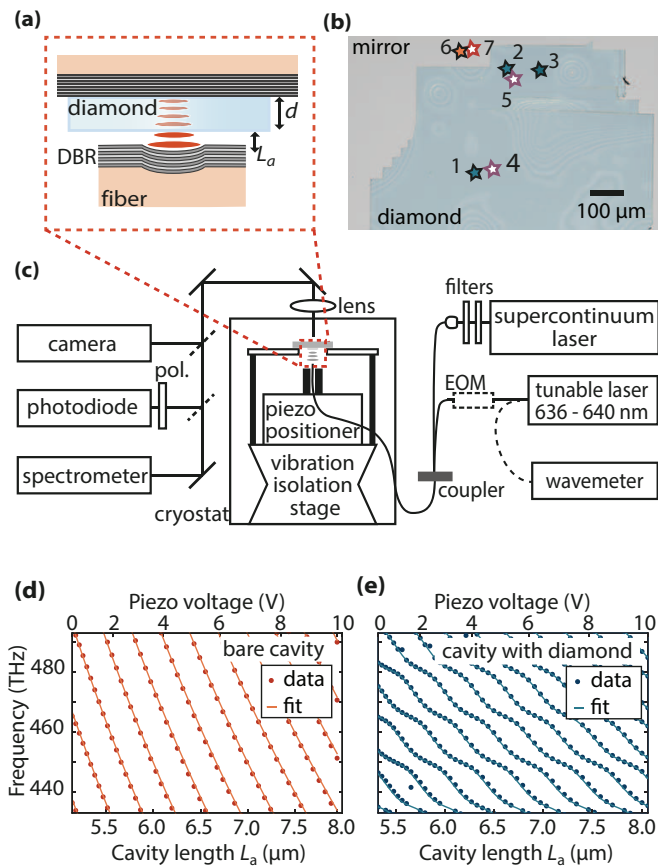


Figure 10.1: Design of the setup and the cavity transmission spectra. (a) Schematic of the cavity showing the concave fiber-tip and the plane mirror onto which a diamond membrane is bonded. The fiber-tip concavity (radius of curvature of $18.4\mu\text{m}$) is fabricated by CO_2 laser ablation and coated with a dielectric mirror (LASEROPTIK). The residual transmission of the fiber mirror is 50 ppm and losses are ≈ 70 ppm. The reflectivity of the plane mirror is $\approx 99.99\%$. From this follows an expected finesse of $F \approx 29,000$. (b) Microscope image of the $4\mu\text{m}$ -thick bonded diamond membrane. Positions at which cavity properties are measured at 300 K (11 K) are marked with filled (open) markers. (c) Overview of the experimental setup. Effects of mechanical noise sources such as the cryostat pulse tube operation are mitigated with a high-frequency resonance cryo-positioning stage and a low-frequency resonance passive vibration isolation stage (Janssen Precision Engineering CPSHR1-s and CVIP1). See Supplementary Material for low temperature mechanical noise spectrum. (d-e) The cavity fundamental modes dependency on the cavity length, for a bare cavity (position 6 in (b)) and a cavity containing diamond (position 1 in (b)). Higher order modes are removed to show only the fundamental mode which we fit with the resonant frequencies given by $\nu = cm/2L_a$ for (d) and by Eq. 1 for (e).

ing interface between diamond and air creates a configuration in which the cavity field can be localized in air-like modes, with a length dependency similar to Figure 1d, and in diamond-like modes, that are largely insensitive to changes in the cavity length. Due to the coupling between these modes, the behaviour of the fundamental modes in Figure 1e displays avoided crossings. The resulting resonant cavity frequencies ν are determined from a one-dimensional lossless cavity model [22, 29]:

$$\nu \approx \frac{c}{2\pi(L_a + n_d d)} \left\{ \pi m - (-1)^m \times \arcsin \left(\frac{n_d - 1}{n_d + 1} \sin \left(\frac{m\pi(L_a - n_d d)}{L_a + n_d d} \right) \right) \right\}, \quad (10.1)$$

and fit to the measured resonant frequencies to extract the diamond thickness d and the length of the air layer in the cavity L_a with an accuracy up to $\lambda/2$.

10.4. FINESSE MEASUREMENTS

The intrinsic cavity properties are described by the finesse that we calculate using the cavity length (as determined by the transmission spectra) and the cavity linewidth in frequency. To measure the latter we couple light with a frequency of 471.3 THz from a narrow-linewidth (< 1 MHz) diode laser into the cavity and detect the transmitted signal using a photodiode as we scan the cavity length across the resonance. Phase-modulation was used to create laser sidebands at a fixed 6 GHz separation to directly determine the cavity linewidth in frequency (Figure 2(a,b)). We obtain the finesse of the cavity for different cavity lengths. These measurements are repeated at different positions on the diamond membrane and at different temperatures (300 K and 11 K). The results are summarized in Figure 2c. For intermediate cavity lengths, high finesse values of approximately 10,000 are supported by our cavity architecture. For cavity lengths larger than $55 \times \frac{\lambda}{2}$, we observe a distinct drop in finesse which we attribute to clipping losses [18]. At short cavity lengths ($< 45 \times \frac{\lambda}{2}$, $L_{air} \approx 4 \mu\text{m}$) the finesse values show significant fluctuations. We note that similar scatter of finesse values at short microcavity lengths has been previously observed [18, 22]; potential causes are cavity misalignment and contact between the fiber and the plane mirror.

We further investigate the variation of the average finesse as a function of the character (air-like versus diamond-like) of the cavity mode. Cavities formed at the steepest part of a mode (Figure 1e) are assigned an ‘air-like character’ of 1, whereas the cavities at the flat part have air-like character of 0. Intermediate values are obtained from a linear interpolation by frequency. The bare cavity, that we approximate to have an air-like character of 1, has a finesse of $F \approx 28,000$ (Figure 2d), which is in agreement with the value expected from the mirrors’ parameters. Inserting the diamond membrane into the cavity reduces the finesse. We attribute this reduction to several effects. First, adding a diamond interface into the optical cavity introduces an additional loss mechanism due to scattering from the diamond surface. Given the measured surface roughness of the diamond membrane we expect a reduction in finesse due to scattering to $F \approx 21,000$ [30]. Second, the refractive index of the plane mirror coating is optimized for bare cavity applications. Inserting a diamond membrane (which has a higher refractive index than air) will lower its effective reflectivity, reducing the finesse threefold[22]. The influence

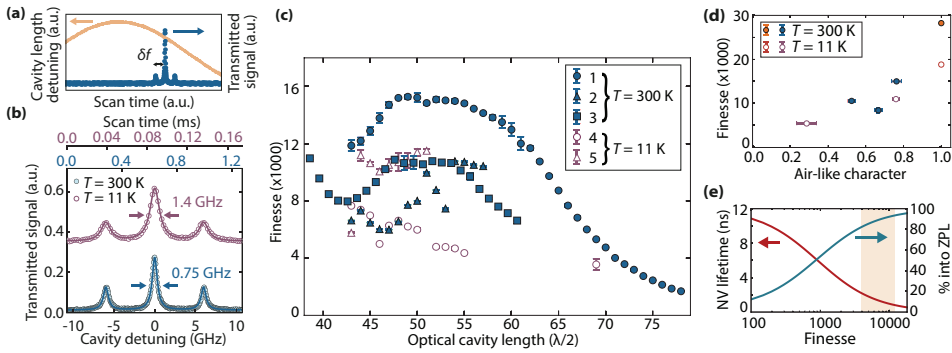


Figure 10.2: Measurements of intrinsic cavity properties. (a) Cavity linewidth measurements are performed by scanning the cavity length (orange) around the laser resonance and measuring the signal on the photodiode (blue). The laser frequency is modulated at $\delta f = 6$ GHz. (b) Two representative linewidth scans measured at $T = 300$ K and $T = 11$ K. A single polarization eigenmode is selected using a polarizer in the detection path. At cryogenic temperatures some scans show a deformation as a result of the system vibrations. To represent the intrinsic (vibration-independent) linewidth, we use only scans to which three Lorentzians could be reliably fitted. (c) Finesse dependence on cavity length measured at five different positions on the diamond membrane at $T = 300$ K (closed markers) and $T = 11$ K (open markers). Per cavity length 40-100 scans as in (b) are averaged to obtain the linewidth in frequency. (d) Finesse dependence on the air-like character of the cavity mode, averaged over $L = 47 \times \frac{\lambda}{2}$ to $L = 55 \times \frac{\lambda}{2}$. The data points with an air-like character of 1 represent measurements of the bare cavity finesse. (e) Simulations of the excited state lifetime and emission probability into the cavity mode via the ZPL for an NV center embedded in this optical cavity with $L = 45 \times \frac{\lambda}{2}$. The shaded region shows the finesse range 4,000 – 15,000 measured for cavities containing diamond.

of these mechanisms is strongly dependent on the character of the mode in the cavity. The modes with a diamond-like character have an antinode at the air-diamond interface, and therefore are most susceptible to scattering at the diamond surface. The trend in the data in Figure 2d is consistent with the above consideration, where modes with a more air-like character show a higher finesse.

We estimate the effect that the cavities realized here would have on an embedded NV center's excited state lifetime as well as the probability that emission occurs via the ZPL into the cavity mode (Figure 2e). We use the Purcell factor F for an ideally placed and oriented NV:

$$F = \frac{3}{4\pi^2} \left(\frac{c}{n_d v} \right)^3 \frac{Q}{V}, \quad (10.2)$$

and use bulk-like free-space values for the branching ratio into the ZPL (3%) and excited state lifetime (12 ns)[13]. A more complex model that explicitly takes dephasing, phonon side-band emission and other cavity modes into account [20, 31] yields quantitatively similar results (not shown). We find that the emission properties of the NV center would be greatly improved, with a probability of emission into the cavity mode via the ZPL above 80% for the current finesse values, compared to the $\approx 3\%$ probability into all modes for the uncoupled case. Thus, both the relative contribution of ZPL photons to the emission as well as the collection efficiency may be significantly enhanced using these cavities.

10.5. CAVITY STABILITY CHARACTERISATION

The linewidth measurements in Figure 2 probe the intrinsic cavity properties at time scales comparable to the scan time (0.1 ms at $T = 11$ K). Cooling the system to cryogenic temperatures introduces significant low-frequency (up to about 10 kHz) mechanical noise from the cryostation pulse tube, which results in cavity linewidth broadening when averaging over time scales longer than $(10 \text{ kHz})^{-1}$. We probe the effect of the low-frequency noise on the system by measuring the cavity transmission signal as a function of the laser frequency at a fixed cavity length ($50 \times \frac{\lambda}{2}$). The laser frequency is swept slowly compared to the pulse tube cycle time, ensuring that the full effect of pulse-tube-induced vibrations is visible in the data. The resulting signal is shown in the orange curve in Figure 3b. The broadened cavity linewidth is fitted with a Gaussian function, for which a full width half maximum (FWHM) of 22.2(7) GHz is found. This value is a direct measure of the cavity displacement from its resonance position of 0.80(3) nm.

Synchronization of our measurement to the 1-Hz cycle of the cryostation pulse tube gives further insight into the effect of the mechanical noise. In Figure 3c we present the dependence of the effective cavity linewidth on the measurement delay with respect to the cryostation sync signal (Figure 3a). We find that the vibrations of the system are strongly dependent on the timing within the cryostation cycle, with the cavity linewidth broadening varying from 14 GHz to 50 GHz. The open red datapoints in Figure 3b show the photodiode signal for the lowest vibration time-bin, 250-300 ms after the sync signal, for which the Gaussian fit gives a cavity length displacement of 0.48(3) nm. Cavity displacement can be further reduced by employing active cavity stabilization methods such as the Pound-Drever-Hall technique [32].

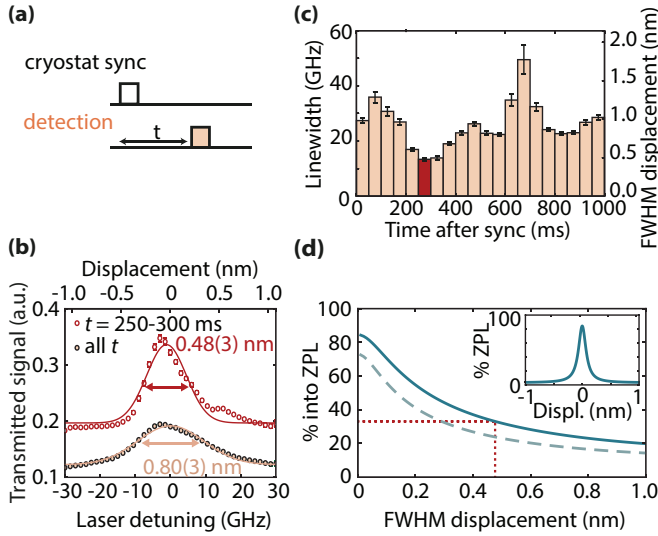


Figure 10.3: Vibration-sensitive measurements of the cavity linewidth. (a) Timing of the cavity linewidth detection with respect to the cryostation synchronization signal. (b) Measurement of the cavity transmitted signal, performed by sweeping the laser frequency over the cavity resonance during 41 cycles of the cryostat pulse tube. The center of 50 sweeps is overlapped and averaged, and fitted with a Gaussian curve, for data collected throughout the cryostation tube cycle (orange curve), and for data collected in the time bin 250-300 ms after the sync signal (red curve). (c) Cavity linewidth dependency on the measurement time with respect to the sync signal. (d) Simulation of the NV center emission via the ZPL for a cavity with length $45 \times \frac{\lambda}{2}$ subject to vibrations. The results include a perfectly oriented emitter in the cavity anti-node (solid line) and for an emitter with 30° dipole mismatch and $\frac{\lambda}{10}$ deviation of the emitter position from the cavity anti-node (dashed line). The inset shows the dependency of the NV center's emission into the ZPL on the cavity displacement from its resonance position.

Figure 3d shows the effect of the low-frequency vibrations on the expected fraction of the NV center's emission into the ZPL as calculated in Figure 2d. We use a Gaussian distribution of the displacements as found in the vibration-sensitive measurement of Figure 3b and a target cavity finesse of 5,000. For the measured vibration levels, we expect the resulting emission via the ZPL into the cavity mode to be 33% which still greatly surpasses the native NV center's emission. In the analysis, we assume the case of an ideally placed emitter within the cavity field (Figure 3d (solid line)). We additionally explore the effect of a non-ideal dipole orientation and emitter location, resulting in an emission probability of 26% (Figure 3d (dashed line)). In practice, close-to-ideal conditions could be achieved by utilizing a $\langle 111 \rangle$ -oriented diamond crystal and achieving a high NV-center concentration through nitrogen implantation [33] or nitrogen delta-doping growth [34]. Stable implanted NV centers with the desired linewidths have already been reported[33].

10.6. CONCLUSIONS

In conclusion, our tunable, high-finesse Fabry-Pérot microcavity with an embedded diamond membrane reaches high finesse values of $F \approx 12,000$ at cryogenic temperatures. The demonstrated 0.48 nm length stability under these conditions would enable an approximately 13 times increase in the NV ZPL photon emission. Additionally, these resonant photons are all fed into the well-defined spatial cavity mode that is well suited for collection, leading to an estimated 3 times enhanced collection efficiency. For demonstrated NV center remote entangling schemes that rely on two-photon interference[4, 6] the resulting boost in the generation and collection of resonant photons in the presented architecture would thus offer an $(3 \times 13)^2 \approx 10^3$ increase in success probability.

ACKNOWLEDGEMENTS

The authors wish to thank P. Latawiec, L. Childress and E. Janitz for helpful discussions. M.L. wishes to acknowledge the support of QuTech during his sabbatical stay. M.S.Z.L. acknowledges the Dutch Liberation Scholarship Programme. This work was supported by the Dutch Organization for Fundamental Research on Matter (FOM), Dutch Technology Foundation (STW), the Netherlands Organization for Scientific Research (NWO) through a VICI grant, the EU S3NANO program and the European Research Council through a Starting Grant.

10.7. METHODS

In order to determine the frequency spectrum of the mechanical noise of our cavity system operating at low temperature, we analyze the cavity transmission signal measured on the photodiode. By tuning the cavity on the fringe of a resonance and disconnecting the electronic elements of the piezo circuit, we are able to isolate and measure only the mechanical noise contribution. Using the Welch method [35] to analyze 100 ms long traces of the photodiode signal with $0.8 \mu\text{s}$ resolution, we obtain the noise power spectral density (Figure 1a) as well as cumulative noise power (Figure 1b). We attribute the

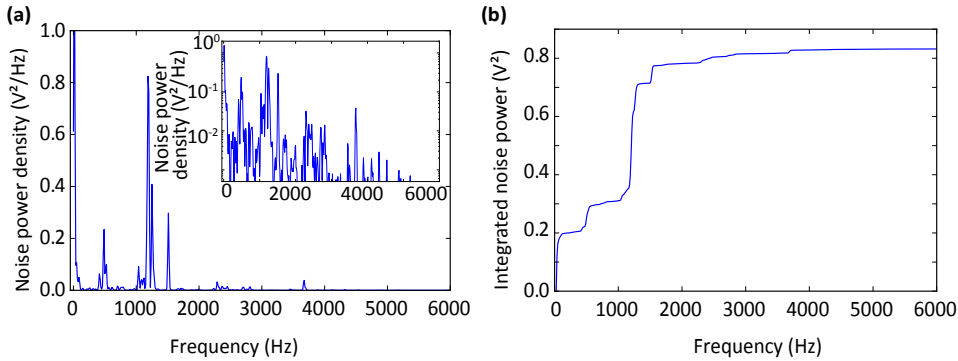


Figure 10.4: Measurement of the cavity mechanical noise spectral properties. (a) Noise power spectral density. The inset shows the plot on a logarithmic scale. (b) Cumulative noise power contribution.

frequency component at 1.2 kHz to the first natural resonant frequency of the cryo positioning stage [36].

REFERENCES

- [1] Bogdanović, S. *et al.*, *Design and low-temperature characterization of a tunable microcavity for diamond-based quantum networks*, *Appl. Phys. Lett.* **110**, 171103 (2017).
- [2] Dutt, M. V. G. *et al.*, *Quantum register based on individual electronic and nuclear spin qubits in diamond*, *Science* **316**, 1312 (2007).
- [3] Taminiou, T. H., Cramer, J., van der Sar, T., Dobrovitski, V. V. & Hanson, R., *Universal control and error correction in multi-qubit spin registers in diamond*, *Nat. Nanotech.* **9**, 171 (2014).
- [4] Barrett, S. D. & Kok, P., *Efficient high-fidelity quantum computation using matter qubits and linear optics*, *Phys. Rev. A* **71**, 060310 (2005).
- [5] Gao, W. B., Imamoglu, A., Bernien, H. & Hanson, R., *Coherent manipulation, measurement and entanglement of individual solid-state spins using optical fields*, *Nat. Photon.* **9**, 363 (2015).
- [6] Hensen, B. *et al.*, *Loophole-free bell inequality violation using electron spins separated by 1.3 kilometres*, *Nature* **526**, 682 (2015).
- [7] Purcell, E. M., Torrey, H. C. & Pound, R. V., *Resonance absorption by nuclear magnetic moments in a solid*, *Phys. Rev.* **69**, 37 (1946).
- [8] Faraon, A., Santori, C., Huang, Z., Acosta, V. M. & Beausoleil, R. G., *Coupling of nitrogen-vacancy centers to photonic crystal cavities in monocrystalline diamond*, *Phys. Rev. Lett.* **109**, 033604 (2012).

- [9] Hausmann, B. J. M. *et al.*, *Coupling of nv centers to photonic crystal nanobeams in diamond*, *Nano Lett.* **13**, 5791 (2013).
- [10] Lee, J. C. *et al.*, *Deterministic coupling of delta-doped nitrogen vacancy centers to a nanobeam photonic crystal cavity*, *Appl. Phys. Lett.* **105**, 261101 (2014).
- [11] Li, L. *et al.*, *Coherent spin control of a nanocavity-enhanced qubit in diamond*, *Nat. Commun.* **6**, 6173 (2015).
- [12] Riedrich-Möller, J. *et al.*, *Nanoimplantation and purcell enhancement of single nitrogen-vacancy centers in photonic crystal cavities in diamond*, *Appl. Phys. Lett.* **106**, 221103 (2015).
- [13] Faraon, A., Barclay, P. E., Santori, C., Fu, K.-M. C. & Beausoleil, R. G., *Resonant enhancement of the zero-phonon emission from a colour centre in a diamond cavity*, *Nat. Photon.* **5**, 301 (2011).
- [14] Englund, D. *et al.*, *Deterministic coupling of a single nitrogen vacancy center to a photonic crystal cavity*, *Nano Lett.* **10**, 3922 (2010).
- [15] Wolters, J. *et al.*, *Enhancement of the zero phonon line emission from a single nitrogen vacancy center in a nanodiamond via coupling to a photonic crystal cavity*, *Appl. Phys. Lett.* **97**, 141108 (2010).
- [16] Barclay, P. E., Fu, K. M. C., Santori, C., Faraon, A. & Beausoleil, R. G., *Hybrid nanocavity resonant enhancement of color center emission in diamond*, *Phys. Rev. X* **1**, 011007 (2011).
- [17] van der Sar, T. *et al.*, *Deterministic nanoassembly of a coupled quantum emitter–photonic crystal cavity system*, *Appl. Phys. Lett.* **98**, 193103 (2011).
- [18] Hunger, D. *et al.*, *A fiber Fabry–Perot cavity with high finesse*, *New J. Phys.* **12**, 065038 (2010).
- [19] Kaupp, H. *et al.*, *Purcell-enhanced single-photon emission from nitrogen-vacancy centers coupled to a tunable microcavity*, *Phys. Rev. A* **88**, 053812 (2013).
- [20] Albrecht, R., Bommer, A., Deutsch, C., Reichel, J. & Becher, C., *Coupling of a single nitrogen-vacancy center in diamond to a fiber-based microcavity*, *Phys. Rev. Lett.* **110**, 243602 (2013).
- [21] Johnson, S. *et al.*, *Tunable cavity coupling of the zero phonon line of a nitrogen-vacancy defect in diamond*, *New J. Phys.* **17**, 122003 (2015).
- [22] Janitz, E. *et al.*, *Fabry-Perot microcavity for diamond-based photonics*, *Phys. Rev. A* **92**, 043844 (2015).
- [23] Kaupp, H. *et al.*, *Scaling laws of the cavity enhancement for nitrogen-vacancy centers in diamond*, *Phys. Rev. Applied* **6**, 054010 (2016).

- [24] Magyar, A. P. *et al.*, *Deterministic coupling of delta-doped nitrogen vacancy centers to a nanobeam photonic crystal cavity*, Appl. Phys. Lett. **99**, 081913 (2011).
- [25] Hunger, D., Deutsch, C., Barbour, R. J., Warburton, R. J. & Reichel, J., *Laser micro-fabrication of concave, low-roughness features in silica*, AIP Adv. **2**, 012119 (2012).
- [26] Enlund, J. *et al.*, *Anisotropic dry etching of boron doped single crystal cvd diamond*, Carbon **43**, 1839 (2005).
- [27] Lee, C., Gu, E., Dawson, M., Friel, I. & Scarsbrook, G., *Etching and micro-optics fabrication in diamond using chlorine-based inductively-coupled plasma*, Diamond Relat. Mater. **17**, 1292 (2008).
- [28] Latawiec, P. *et al.*, *On-chip diamond Raman laser*, Optica **2**, 924 (2015).
- [29] Jayich, A. M. *et al.*, *Dispersive optomechanics: a membrane inside a cavity*, New J. Phys. **10**, 095008 (2008).
- [30] Klaassen, T., van Exter, M. P. & Woerdman, J. P., *Characterization of scattering in an optical Fabry–Perot resonator*, Appl. Opt. **46**, 5210 (2007).
- [31] Auffèves, A. *et al.*, *Controlling the dynamics of a coupled atom-cavity system by pure dephasing*, Phys. Rev. B **81**, 245419 (2010).
- [32] Black, E. D., *An introduction to pound–drever–hall laser frequency stabilization*, Am. J. Phys. **69**, 79 (2001).
- [33] Chu, Y. *et al.*, *Coherent optical transitions in implanted nitrogen vacancy centers*, Nano Lett. **14**, 1982 (2014).
- [34] Ohno, K. *et al.*, *Three-dimensional localization of spins in diamond using ^{12}C implantation*, Appl. Phys. Lett. **105**, 052406 (2014).
- [35] Welch, P., *The use of fast fourier transform for the estimation of power spectra: A method based on time averaging over short, modified periodograms*, IEEE Trans. Audio Electroacoust. **15**, 70 (1967).
- [36] *Janssen Precision Engineering CPSHR*, .



11

COUPLING NITROGEN-VACANCY CENTRES TO A MICROCAVITY

The realisation of a quantum network based on nitrogen-vacancy (NV) centres requires an efficient, coherent spin-photon interface. A high efficiency can be realised by placing the NV centre in an optical cavity, enhancing coherent emission through the Purcell effect. Crucial is that the NV centre environment has to be low in defects that induces optical decoherence or strong spectral diffusion. Embedding the NV centre in a diamond slab in a Fabry-Pérot microcavity is a promising approach: it allows the NV centres to be far removed from interfaces. With high energy electron irradiation we create optically coherent NV centres in a thin diamond membrane. We embed the membrane in a Fabry-Pérot microcavity and observe coupling of the emission of an NV ensemble into the cavity mode. Although a low cavity finesse hinders the observation of Purcell enhancement, these mark important steps towards Purcell enhancement of single emitters.

11.1. INTRODUCTION

The branching ratio of emission into the zero-phonon line (ZPL) of NV centres can be enhanced through the Purcell effect by coupling to an optical cavity [1]. Such enhancement has been established using optical cavities with several different designs, such as diamond microring resonators [2], diamond photonic crystal cavities [3–7], by evanescent coupling to optical cavities [8–12] or using Fabry-Pérot microcavities with embedded nanodiamonds [13–15] or diamond membranes [16]. However, so far, the optical properties of the NV centres in these optical cavities have not been suitable for applications in quantum networks.

The optical properties in such designs are mainly influenced by charge fluctuations in the neighbourhood of the NV centre through surface proximity [17]. A promising cavity design that avoids surface proximity embeds the NV centre in a diamond membrane in a Fabry-Pérot microcavity [16, 18, 19], where the NV can be far removed from the optical interface ($\gg 100$ nm). It has been shown that Purcell enhancement with such devices is possible [16]. But the NV centres employed in that demonstration had optical transitions that were strongly broadened (\approx GHz) compared to the lifetime limited linewidth (≈ 13 MHz) [16]. In Ref. [16], the NV linewidth broadening is observed after an etching step. This indicates that NV distance to the surface (≈ 65 nm) is not the limiting factor, but that optical decoherence and spectral diffusion are induced by a high concentration of damage in the lattice nearby the NV centre. Such high damage is described as a possible result of NV creation through implantation (see [20] and chapter 7 of this thesis) and etching processes [21].

Research aimed at embedding optically coherent NV centres in an optical cavity is thus still ongoing. We here show that it is possible to couple optically coherent NV centres to optical cavities. We embed a thin but unetched membrane with NV centres created by electron irradiation in a Fabry-Pérot microcavity (Fig. 11.1a). In this chapter we present observation of coupling of the emission of an NV ensemble into a cavity mode. A low cavity finesse hinders the observation of Purcell enhancement in the current cavity.

11.2. SAMPLE CHARACTERISATION

We create a diamond with a high density of NV centres by high-energy electron irradiation at a dose of $\approx 10^{14}$ e^-/cm^2 and subsequent annealing [22]. After this the diamond is sliced, thinned and polished (Diamond Delaware Knives) to a thickness of ≈ 13 μm . No further processing is performed. The diamond membrane is Van der Waals bonded to a plane mirror formed of a distributed Bragg reflector (DBR) deposited on a SiO_2 substrate using ion beam sputtering (LaserOptik). Microwave striplines are embedded in the mirror to provide spin addressing of the NV centre [23].

We characterise NV centres in this membrane in a confocal microscope at cryogenic temperatures. The high-dose electron irradiation creates a high density of NV centres, that we estimate to be ≈ 45 NVs/(25 μm^3) from confocal scans (Fig. 11.1b). There are many NV centres present in a confocal spot, but in measurements of the photoluminescence under resonant excitation the individual transitions can be spectrally distinguished (Fig. 11.1c-d). We characterise the intrinsic NV centre linewidth by sweeping the resonant excitation laser across a transition, while applying microwaves to prevent

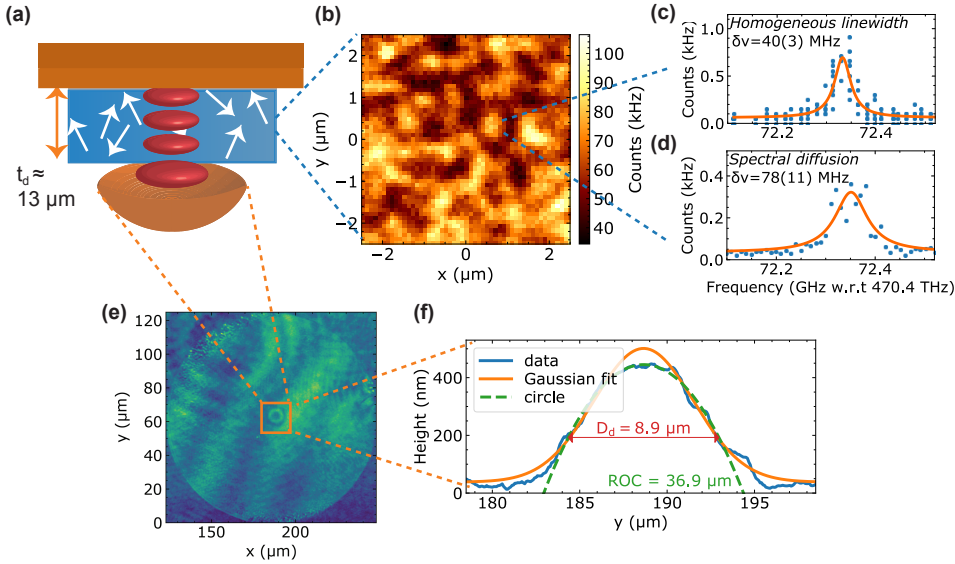


Figure 11.1: Fabry-Pérot microcavity with an electron-irradiated diamond membrane. (a) Schematic of a Fabry-Pérot microcavity. The diamond thickness is $\approx 13 \mu\text{m}$. The dimple and plane mirror are coated with a DBR stack of alternating layers of Ta_2O_5 and SiO_2 . (b) The diamond embedded in the cavity is a CVD-grown type IIa crystal (Element 6) that is electron irradiated at the Reactor Institute Delft with high-energy electrons at an energy of 2 MeV and a dose of $\approx 10^{14} e^-/\text{cm}^2$. This generates a high NV centre density as visible in a confocal scan under green excitation. (c-d) The many NV centres per confocal spot can be spectrally distinguished in a photoluminescence excitation measurement. The individual transitions show near-lifetime limited optical linewidths. Representative examples of (c) the homogeneous linewidth (a single scan over the linewidth) and (d) the linewidth under the influence of spectral diffusion (the sum of many scans over the linewidth interleaved with green excitation) of such a transition are shown. (e) The shape of the fiber dimple is determined from interferometric images. (f) We measured the dimple parameters to be: $\text{ROC} = 36.9 \mu\text{m}$, and $D_d = 9.7 \mu\text{m}$. These values fit well to the fiber shape measured by the white light source.

optical pumping into the dark state (for more measurement details see section 6.4 of this thesis). In these measurements we find linewidths of around 40 MHz, near the lifetime limited value of 13 MHz. To include the influence of spectral diffusion we repeat this scan many times, applying a green off-resonant laser pulse between each scan to induce spectral diffusion. The addition of many such scans gives a linewidth that is broadened to ≈ 80 MHz. This characterisation shows the suitability of these NV centres for applications in a quantum network: the narrow homogeneous linewidth enables high visibility two-photon quantum interference and entanglement [24–26] and the level of spectral diffusion is low enough to enable efficient spectral preselection [27].

11.3. BARE CAVITY CHARACTERISATION

To characterise the cavity parameters we first create a plane-concave Fabry-Pérot microcavity without diamond. The cavity consists of a plane mirror, and a fiber tip in which a concavity is created using laser ablation [19, 28]. A distributed Bragg reflector (DBR) stack is deposited on the dimple. The mirror parameters are measured as $T_1 = 2200$ ppm,

$T_2 = 50$ ppm, $S_{1(2)} + A_{1(2)} \approx 35$ (75) ppm, where subscripts 1 (2) corresponds to the plane (dimpled) mirror. The value of T_1 is the transmission as determined for termination on air. If the diamond is placed on it, the termination at the high diamond refractive index ($n_d = 2.41$) increases the transmission to 5280 ppm.

We first characterise the parameters of the fiber dimple (for details on measurement methods see section 8.1.3). A dimple radius of curvature of $ROC = 36.9 \pm 0.1$ μm is determined from measurements of the transversal mode frequency splitting [29]. We find the effective dimple diameter to be $D_d = 8.9 \pm 0.1$ μm from measurements probing clipping losses [28] by measuring the finesse versus the cavity length on a different cavity with the same dimple. Both these independently measured values fit the dimple shape as measured with white light interferometric imaging, shown in Fig. 11.1e-f.

We next measure the bare cavity finesse. We create a cavity with a length of 14.97 μm , and measure the cavity linewidth to be 5.41 ± 0.03 GHz, corresponding to a finesse of $F = 1851 \pm 10$. This corresponds to total round-trip cavity losses of $\mathcal{L}_{\text{tot}} = 3395 \pm 18$ ppm. Compared to the losses expected from the mirror properties alone ($\mathcal{L}_M = 2360$ ppm) we thus find additional losses at this cavity length of ≈ 1000 ppm. At the relatively large cavity length of ≈ 15 μm , these could result from clipping losses, that we estimate to be around 1650 ppm, for $D_d = 8.9$ μm . The finesse that we find is thus better than we would expect from clipping losses, which could be explained by variations of the effective fiber dimple diameter with the fiber tilt. From a geometrical argument we find that $D'_d = D_d - \theta ROC$, for an initial (resulting) effective diameter D_d (D'_d), and a fiber tilt θ (see section 8.1.3). An effective fiber diameter 9.3 μm consistent with 1000 ppm clipping losses would result from a reduction in fiber tilt of ≈ 10 mrad corresponding to the reference situation with $D_d = 8.9$ μm . These values of tilt are within the expected range for the employed setup.

11.4. DIAMOND-AIR CAVITY CHARACTERISATION

Having characterised the parameters of the bare cavity, we continue to assess the finesse of the diamond-air cavity. This can be found by measuring the diamond thickness (t_d), air gap width (t_a), and cavity linewidth ($\delta\nu$) (see for methods section 8.1). From these parameters we can calculate the corresponding finesse as:

$$F = \frac{c}{2L_{\text{eff}}\delta\nu}, \quad (11.1)$$

where we obtain the effective length L_{eff} of the cavity from the diamond thickness and air gap width as described in section 4.3.3.

The resulting finesse for several air gap widths in two cavities are plotted in Fig. 11.2a-b. The values fluctuate with cavity length but are mainly found around 750. This is significantly below the expected finesse of ≈ 1100 , that we determine from the bare mirror properties and the expected diamond surface roughness (0.4 nm RMS, estimated from AFM measurements on other polished samples). Due to the narrow air gap, the clipping losses are expected to be negligible. (An effective diameter of less than ≈ 7.5 μm , compared to the measured diameter $D_d = 8.9 \pm 0.1$ μm , would be needed for clipping losses above 200 ppm. The additional fiber tilt that would be needed to explain such a discrepancy (> 60 mrad) is more than expected for the employed setup.)

The discrepancy between the theoretical and measured value of effective losses is on average ≈ 2000 ppm. We note that for at least one position a finesse of $F = 1297(13)$ is measured, which surprisingly is higher than the expected finesse.

A possible cause of losses is mixing of the fundamental cavity mode with higher order Hermite-Gauss modes. Such mixing can result from deviations of the dimple from spherical [29], or from the deviation of the diamond surface from the beam curvature in the cavity [18]. We compare the cavity parameters to the regimes considered in Ref. [29]. For the cavities considered here the ratio of cavity length and ROC is $(t_a + t_d/n_d)/ROC \approx 0.1$, using $t_a + t_d/n_d$ as the equivalent bare cavity length (section 4.3.4). The beam waist on the dimpled mirror is $w_m \approx 1.7 \mu\text{m}$, such that $w_m/(D_d/2) \approx 0.35$. Figure 6 in Ref. [29] indicates that in this regime no mode mixing losses are expected for a Gaussian or parabolic shaped mirror. We note however that our mirror deviates from such an ideal shape, and that there may be influences from the specific fiber profile. Simulations based on Ref. [29] using the specific fiber profile however indicate that for the relevant cavity lengths no such effects are present (not shown) [30]. The effects from a flat diamond surface deviating from the beam curvature are small for the considered regime of cavity parameters [18]. We anticipate nevertheless that (smooth) deviations of the diamond surface from a flat plane may induce additional mode mixing. AFM measurements of the diamond surface could indicate whether such deviations are present.

We further investigate the increased cavity losses by studying the frequency dependency of the finesse in Fig. 11.2c-d. A frequency-dependency is expected for losses that are strongly bound to the diamond-like or air-like mode of the cavity as explored in-depth in section 5.2. For example, losses from scattering at the diamond-air interface have a strong effect on the diamond-like mode (green line in Fig. 11.2), while clipping losses that occur on the fiber mirror on the air-side of the cavity are expected to mainly affect the air-like mode (red line in Fig. 11.2). The effect of (high-frequency) vibrations that could artificially broaden the linewidth would be most strong in the air-mode. The measured finesse shows no clear dependency on the probe frequency, which indicates that none of these effects is dominant. The additional losses are thus either a combination of diamond-like and air-like losses, or they stem from a different type of losses that affects both types of modes, such as absorption in the diamond membrane.

11.5. NV-CAVITY COUPLING

We next look for signatures of NV centres emitting into the cavity mode. We apply off-resonant excitation at 532 nm, and look for the photoluminescence (PL) of the NV centre. Fig. 11.3a shows the PL spectrum in the spectrometer. At wavelengths above 650 nm, the phonon-sideband of the NV ensemble is visible, filtered by the cavity spectrum. The stopband of the plane cavity mirror through which this spectrum is detected extends to ≈ 680 nm. Beyond that the finesse of the cavity decreases, which shows up as the broadening of the peaks filtering the PSB. The PSB emission into the cavity mode is independent of the cavity length. However, the coupling of ZPL emission into the cavity mode does depend on the cavity length. When we zoom in on the ZPL emission frequency (Fig. 11.3b) we see that the number of photons emitted into the cavity mode peaks when the cavity is on resonance with the NV ZPL around 470.4 THz.

In the previous measurements we did not have active control over the cavity length

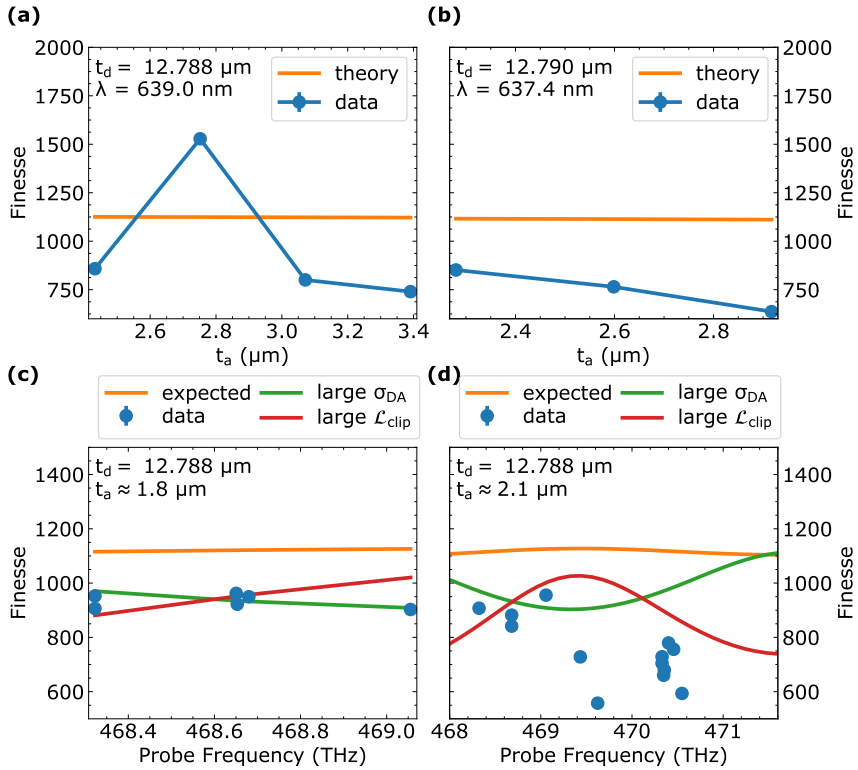


Figure 11.2: Characterisation of the diamond-air cavity. (a-b) The finesse is measured as a function of air gap width for two cavities formed at different locations on the diamond, and with a different diamond thickness. The expected finesse from the mirror properties, expected surface roughness ($\sigma_{\text{DA}} = 0.4 \text{ nm RMS}$) and effective diamond diameter ($D_d = 8.9 \mu\text{m}$) and clipping losses are indicated with an orange line. (c-d) The character of the losses can be examined by changing the probe frequency. If the losses are more ‘diamond-like’, such as losses from diamond surface roughness, the diamond-like mode is more sensitive to them, whereas the more air-like modes are more sensitive to ‘air-like losses’, such as clipping losses. This can be seen from the theoretical curves in which extreme cases are portrayed ($\sigma_{\text{DA}} = 1.2 \text{ nm RMS}$ and $D_d = 7.0 \mu\text{m}$ in the green and red curves respectively). The finesse for the case with large surface roughness (green line) is lowest for the diamond-like mode (around 469.4 THz) and highest for the air-like mode (around 471.6 THz). For the curve with large clipping losses the behaviour is opposite. The measured finesse shows no clear dependency on the probe frequency, indicating that either a combination of effects is responsible for the unknown loss source, or that they originate from a different type of loss source, such as absorption in the diamond.

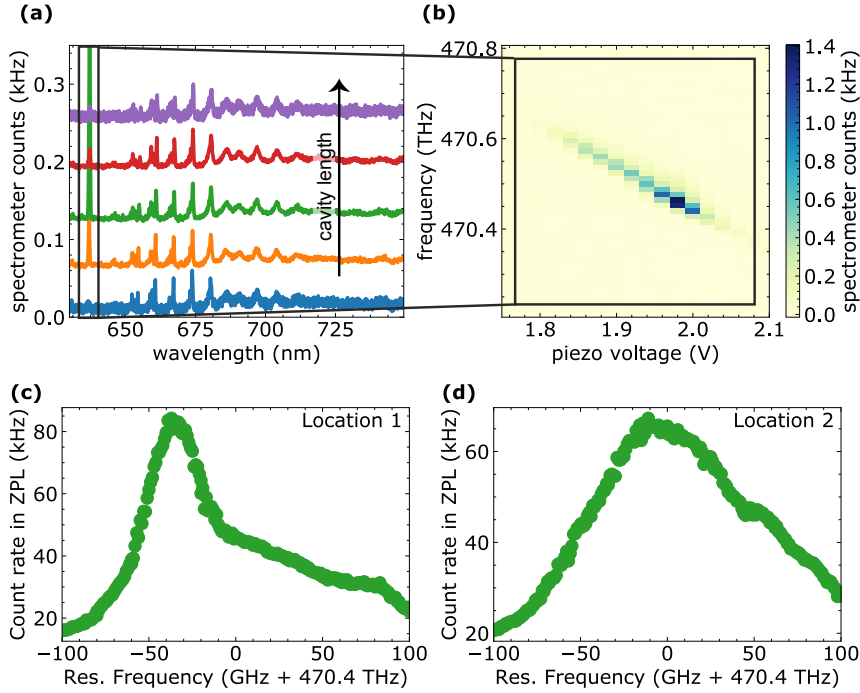


Figure 11.3: Coupling of NV emission into the cavity mode. (a) A spectrometer image of the emission from off-resonantly excited NV centres filtered by the microcavity. Consecutive scans at increasing cavity length are shown with an offset for clarity. Filtering of the PSB by the cavity is clearly visible, as well as a peak when the cavity becomes resonant with the ZPL. (b) Zoom-in on the peak around the ZPL frequency when the cavity length is scanned over the resonance. (c-d) The ZPL emission count rate of an ensemble of NV centres as measured in an APD in two cavities when controlledly scanning the cavity over the resonance. The broad signature indicates an axial strain distribution of NV optical transitions over ≈ 200 GHz.

while scanning. To enable such controlled scanning we design a stabilisation routine that stabilizes the cavity length to a laser frequency setpoint before taking the data for each datapoint. The details of the stabilisation procedure are described in section 8.2.3. The resulting count rate in the ZPL under green illumination is shown in Fig. 11.3c-d for two different cavities. The distribution of emission frequencies is ≈ 200 GHz, indicating that the inhomogeneous linewidth in the irradiated membrane is large. We emphasize here that the emission into the cavity originates from an ensemble of NV centres. Based on the density of NV centres observed in this membrane (Fig. 11.1c) we estimate the number of NV centres responsible for this signature to be around 40^1 .

¹This depends on the cavity mode volume in the diamond membrane. We estimate this using the beam waist ($w_0 \approx 1.5 \mu\text{m}$) giving a mode volume in diamond of $\approx \pi w_0^2/4 \times t_d \approx 20 \mu\text{m}^3$. Using an estimated NV density of $\approx 50 \text{ NVs}/(25 \mu\text{m}^3)$, we thus expect that there are around 40 NV centres in our cavity mode volume.

11.6. PROBING THE PURCELL EFFECT

We estimate whether we expect the NV ensemble ZPL transition rate to be enhanced by the Purcell effect [1]. We use the measured cavity parameters to estimate the Purcell factor, that is given by [31, 32]:

$$F_p = \xi^2 \frac{3c\lambda_0^2}{4\pi^2 n_d^3 V_0 \delta\nu}, \quad (11.2)$$

where $\xi^2 = |\vec{E} \cdot \hat{d}|^2 / |\vec{E}_{\max}|^2$ measures the overlap between the cavity mode electric field and the NV dipole. $\delta\nu$ is the measured linewidth, λ_0 is the free space wavelength of the ZPL and V_0 the cavity mode volume that we calculate using the electric field distribution over the diamond and air gap [33, 34]:

$$V_0 = \frac{\pi w_0^2}{2} \frac{\int_{cav} \epsilon(z) |E(z)|^2 dz}{\epsilon(z_0) |E(z_0)|^2}. \quad (11.3)$$

We use the finesse measurements presented in Fig. 11.2c-d to estimate that the Purcell factor is ≈ 3.2 for an optimally placed emitter ($\xi^2 = 1$) (Fig. 11.4a). For this an optimally placed emitter, the branching ratio into the ZPL would be $\approx 9\%$ (Fig. 11.4b), which is increases compared to the bulk branching ratio of 3%.

However, since we probe an NV ensemble we should consider the average overlap between the emitters and the cavity field. The arbitrary depth of the NVs, distributed over field nodes and -antinodes, decreases the average Purcell factor with a factor $|\vec{E}|^2 / |\vec{E}_{\max}|^2 = 1/2$. Furthermore, the dipole overlap is not perfect. The NV dipole orientations are confined to the plane perpendicular to the NV axis, leading to on-average a dipole overlap of 0.34 with the cavity field for NVs in a diamond with a $\langle 100 \rangle$ crystal orientation (see Methods section section 11.9 for more detail). The averaging over the ensemble of NV centres results in an average Purcell factor of $F_{p,avg} \approx 0.55$. We thus do not expect that the ZPL emission of the NV ensemble is Purcell enhanced.

Since we have a Purcell factor less than unity, we expect no change in average lifetime compared to the NV lifetime in bulk diamond (the change in lifetime is given by $\tau/\tau_0 = 1/(F_{p,avg}\beta_0 + 1)$, with $\beta_0 \approx 0.03$ the bulk branching ratio into the ZPL). We measure the lifetime of the NV centres using a pulsed laser an a time-tagger while sweeping across the resonance frequency (Fig. 11.4c-d). We record the lifetime of the NV centres in the ZPL and in the PSB paths, in both channels finding no change in lifetime between the on- and off resonance cases. A uniform increase in recorded lifetime in the ZPL path is the result of a significant contribution from the background resulting from a lower signal in the ZPL.

11.7. CONCLUSIONS

We have found optically coherent NV centres in a membrane of $\approx 13 \mu\text{m}$ thick, and embedded this membrane in a Fabry-Pérot microcavity. We observed the emission of an ensemble of NV centres filtered by the cavity mode and have developed measurement techniques to measure ZPL enhancement in such a cavity. However, a low cavity finesse hinders the observation of ZPL enhancement. The cavity finesse attains a lower

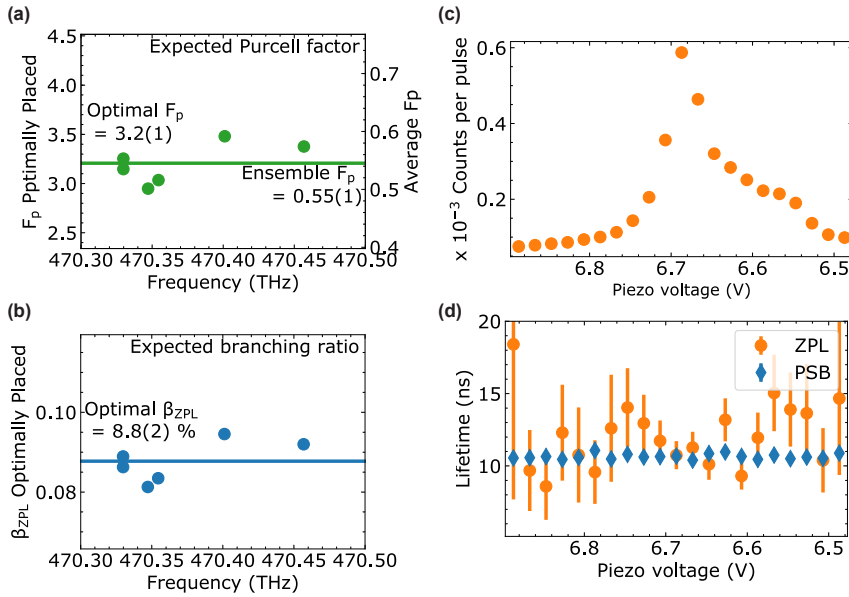


Figure 11.4: Probing the Purcell factor. (a) The measurements of the finesse for frequencies around the ZPL frequency for cavity 2 (Fig. 11.2c-d) are used to find the expected Purcell factor for a single NV optimally placed in the cavity. The average Purcell factor for the ensemble of NV centres has an on-average imperfect dipolar overlap with the cavity field, and is therefore a factor $\xi^2 = 0.17$ lower. This is less than unity so we do not expect Purcell enhancement for the ensemble. (b) The Purcell factor of 3.2 for the optimally placed emitter would lead to an increased branching ratio of emission into the ZPL. The expected lifetime for such an emitter would be altered by a factor 0.91. (c) The cavity length is swept across the NV ZPL resonance, while the NVs are excited with a pulsed green laser. The total number of photons detected after excitation in the zero phonon line shows that the cavity is on resonance at a piezo voltage around 6.7 V. (d) The lifetime of the NV emission is monitored in the ZPL and in the PSB during the sweep. No change in lifetime is detected during the sweep, as expected for the ensemble Purcell factor of 0.55. Due to a lower signal in the ZPL channel, the background fluorescence plays a larger role in the lifetime measurement, leading to a higher average recorded lifetime. This effect is stronger when off the resonance, than on-resonance around 6.7 V.

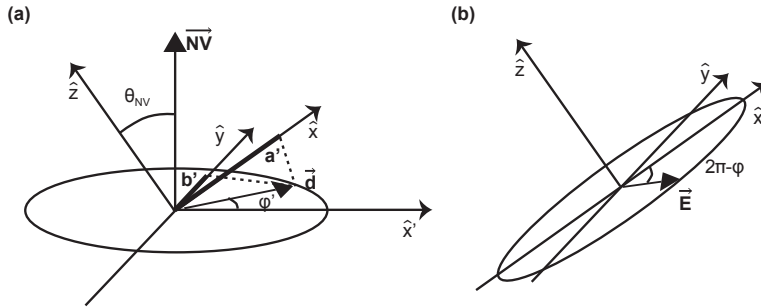


Figure 11.5: Geometrical overlap between an NV dipole and cavity field. We aim to find the average overlap between (a) the NV centre dipole \hat{d} that is bound to the plane perpendicular to the NV-axis (\overrightarrow{NV}) and (b) the cavity electric field polarisation \vec{E} that is bound the plane perpendicular to the cavity axis that coincides with the z -axis. In a diamond with a $\langle 100 \rangle$ crystal orientation the NV dipole and cavity axis are at a well-defined angle θ_{NV} .

value than expected from the bare mirror parameters and clipping losses, possibly resulting from mode-mixing or absorption in the diamond. To fully enable the capabilities of these cavities, more research is needed to find and address this source of cavity losses. Furthermore, higher reflectivity mirrors than employed here optimize the trade-off between Purcell enhancement and cavity vibrations (namely, with $T = 400$ ppm, see chapter 5), leading to a larger Purcell factor.

The high density in the current sample prevented observation of the emission of a single NV centre in the cavity. The ability to select an NV centre with a suitable position and dipole-orientation would enable a higher-than-average Purcell factor. Spectral selection through resonant excitation [35] or using a lower dose electron irradiation to create a lower NV density may lead to the coupling of a single NV centre to the cavity mode.

11.8. ACKNOWLEDGMENTS

We thank Maximilian Ruf and Airat Galiullin for stimulating discussions and sample fabrication and characterisation, Wouter Westerveld and Martin Eschen for building parts of the optical setup, and Thomas Fink for fabrication of the laser-ablated fiber tips.

11.9. METHODS

11.9.1. AVERAGE DIPOLE OVERLAP FOR AN ENSEMBLE OF NV CENTRES WITH WELL-DEFINED ORIENTATIONS

This section describes how to find the average dipole overlap between the cavity field and an NV centre in a diamond with a $\langle 100 \rangle$ crystal orientation. The geometrical problem is layed out in a convenient coordinate frame in Fig. 11.5.

Firstly, we express the NV dipole \hat{d} in terms of \hat{x} and \hat{y} , parametrising its location in

the plane with ϕ' Fig. 11.5a. We find that:

$$\hat{d} = a' \hat{x} + b' \hat{y}; \quad (11.4)$$

$$= \cos(\theta_{NV}) \cos(\phi') \hat{x} + \sin(\phi') \hat{y}, \quad (11.5)$$

where θ_{NV} is the angle that the NV makes with the cavity axis. Similarly we find the electric field polarisation $\hat{e} = \vec{E}/|E|$ in terms of \hat{x} and \hat{y} . From Fig. 11.5 we readily see it is given by:

$$\hat{e} = \cos(\phi) \hat{x} + \sin(\phi) \hat{y}. \quad (11.6)$$

The square overlap between these two can now easily be calculated as:

$$|\hat{e} \cdot \hat{d}|^2 = |\cos(\phi) \cos(\theta_{NV}) \cos(\phi') + \sin(\phi) \sin(\phi')|^2 \quad (11.7)$$

We remark that we can here see that for a *single* NV-centre it is always in principle possible to find or tune to get unity overlap with one of the NV dipoles and the cavity axis. In that case we require $\phi' = \pi/2, 3\pi/2$. To get the average dipole overlap (we call it ξ_{avg}^2), we now have to average over all dipole orientations ϕ' and over all field polarisations given by ϕ . We get this by integrating over ϕ and ϕ' , and normalising by $\int_0^{2\pi} d\phi = \int_0^{2\pi} d\phi' = 2\pi$ for both. We thus get:

$$\xi_{\text{avg}}^2 = \frac{\int_0^{2\pi} \int_0^{2\pi} |\cos(\phi) \cos(\theta_{NV}) \cos(\phi') + \sin(\phi) \sin(\phi')|^2 d\phi' d\phi}{\int_0^{2\pi} d\phi' \int_0^{2\pi} d\phi} \quad (11.8)$$

$$= \frac{1}{(2\pi)^2} \int_0^{2\pi} (\pi \cos^2(\phi) \cos^2(\theta_{NV}) + \pi \sin^2(\phi)) d\phi \quad (11.9)$$

$$= \frac{1}{(2\pi)^2} (\pi^2 \cos^2(\theta_{NV}) + \pi^2) \quad (11.10)$$

$$= \frac{1}{4} + \frac{1}{4} \cos^2(\theta_{NV}), \quad (11.11)$$

where we evaluate the integrals one by one. The crossterms in the first integral evaluate to zero.

The maximum average overlap (1/2) is obtained for NVs with axes parallel to the cavity axis. The minimum overlap 1/4 is for $\theta_{NV} = \pi/2$, when the NV axis is perpendicular to the cavity axis. For the case of diamond slabs with a $\langle 100 \rangle$ crystal orientation in a cavity, the NV centre axes are at an angle of 54 degrees to the cavity axis. In this case the average overlap of an *ensemble* of NV centres with a cavity mode is $\xi_{\text{avg}}^2 = 0.34$.

If the cavity polarisation modes are degenerate, the analysis can be extended to obtain $\xi_{\text{avg,2 pol.}}^2 = \frac{1}{2} + \frac{1}{2} \cos^2(\theta_{NV})$

REFERENCES

- [1] Purcell, E., *Spontaneous Emission Probabilities at Radio Frequencies*, in *Proc. Am. Physical Soc.*, Vol. 69 (1946).
- [2] Faraon, A., Barclay, P. E., Santori, C., Fu, K.-M. C. & Beausoleil, R. G., *Resonant enhancement of the zero-phonon emission from a colour centre in a diamond cavity*, *Nat. Photon.* 5, 301 (2011).

- [3] Faraon, A., Santori, C., Huang, Z., Acosta, V. M. & Beausoleil, R. G., *Coupling of nitrogen-vacancy centers to photonic crystal cavities in monocrystalline diamond*, Phys. Rev. Lett. **109**, 033604 (2012).
- [4] Hausmann, B. J. M. *et al.*, *Coupling of NV centers to photonic crystal nanobeams in diamond*, Nano Lett. **13**, 5791 (2013).
- [5] Lee, J. C. *et al.*, *Deterministic coupling of delta-doped nitrogen vacancy centers to a nanobeam photonic crystal cavity*, Appl. Phys. Lett. **105**, 2012 (2014).
- [6] Li, L. *et al.*, *Coherent spin control of a nanocavity-enhanced qubit in diamond*. Nature Comm. **6**, 6173 (2015).
- [7] Riedrich-Möller, J. *et al.*, *Nanoimplantation and Purcell enhancement of single nitrogen-vacancy centers in photonic crystal cavities in diamond*, Appl. Phys. Lett. **106**, 221103 (2015).
- [8] Englund, D. *et al.*, *Deterministic coupling of a single nitrogen vacancy center to a photonic crystal cavity*, Nano Lett. **10**, 3922 (2010).
- [9] Wolters, J. *et al.*, *Enhancement of the zero phonon line emission from a single nitrogen vacancy center in a nanodiamond via coupling to a photonic crystal cavity*, Appl. Phys. Lett. **97**, 141108 (2010).
- [10] van der Sar, T. *et al.*, *Deterministic nanoassembly of a coupled quantum emitter-photonic crystal cavity system*, Appl. Phys. Lett. **98**, 193103 (2011).
- [11] Barclay, P. E., Fu, K. M. C., Santori, C., Faraon, A. & Beausoleil, R. G., *Hybrid nanocavity resonant enhancement of color center emission in diamond*, Phys. Rev. X **1**, 011007 (2011).
- [12] Gould, M., Schmidgall, E. R., Dadgostar, S., Hatami, F. & Fu, K. M. C., *Efficient Extraction of Zero-Phonon-Line Photons from Single Nitrogen-Vacancy Centers in an Integrated GaP-on-Diamond Platform*, Phys. Rev. Appl. **6**, 011001 (2016).
- [13] Kaupp, H. *et al.*, *Scaling laws of the cavity enhancement for NV centers in diamond*, Phys. Rev. A **88**, 8 (2013).
- [14] Albrecht, R. *et al.*, *Narrow-band single photon emission at room temperature based on a single nitrogen-vacancy center coupled to an all-fiber-cavity*, Appl. Phys. Lett. **105**, 073113 (2014).
- [15] Johnson, S. *et al.*, *Tunable cavity coupling of the zero phonon line of a nitrogen-vacancy defect in diamond*, New J. Phys. **17**, 122003 (2015).
- [16] Riedel, D. *et al.*, *Deterministic enhancement of coherent photon generation from a nitrogen-vacancy center in ultrapure diamond*, Phys. Rev. X **7**, 031040 (2017).
- [17] Santori, C. *et al.*, *Nanophotonics for quantum optics using nitrogen-vacancy centers in diamond*, Nanotechnology **21**, 274008 (2010).

- [18] Janitz, E. *et al.*, *A Fabry-Perot microcavity for diamond-based photonics*, Phys. Rev. A **92**, 043844 (2015).
- [19] Bogdanović, S. *et al.*, *Design and low-temperature characterization of a tunable microcavity for diamond-based quantum networks*, Appl. Phys. Lett. **110**, 1 (2017).
- [20] Fu, K.-M. C., Santori, C., Barclay, P. E. & Beausoleil, R. G., *Conversion of neutral nitrogen-vacancy centers to negatively charged nitrogen-vacancy centers through selective oxidation*, Appl. Phys. Lett. **96**, 121907 (2010).
- [21] Cui, S., *Near-surface Nitrogen Vacancy Centers in Diamond*, Ph.D. thesis, Harvard University (2014).
- [22] Chu, Y. *et al.*, *Coherent optical transitions in implanted nitrogen vacancy centers*. Nano Lett. **14**, 1982 (2014).
- [23] Bogdanović, S. *et al.*, *Robust nano-fabrication of an integrated platform for spin control in a tunable microcavity*, APL Photonics **2**, 126101 (2017).
- [24] Bernien, H. *et al.*, *Two-photon quantum interference from separate nitrogen vacancy centers in diamond*, Phys. Rev. Lett. **108**, 043604 (2012).
- [25] Sipahigil, A. *et al.*, *Quantum Interference of Single Photons from Remote Nitrogen-Vacancy Centers in Diamond*, Phys. Rev. Lett. **108**, 143601 (2012).
- [26] Bernien, H. *et al.*, *Heralded entanglement between solid-state qubits separated by three metres*. Nature **497**, 86 (2013).
- [27] Robledo, L., Bernien, H., Van Weperen, I. & Hanson, R., *Control and coherence of the optical transition of single nitrogen vacancy centers in diamond*, Phys. Rev. Lett. **105**, 177403 (2010).
- [28] Hunger, D. *et al.*, *A fiber Fabry-Perot cavity with high finesse*, New J. Phys. **12**, 065038 (2010).
- [29] Benedikter, J. *et al.*, *Transverse-mode coupling and diffraction loss in tunable Fabry-Pérot microcavities*, New J. Phys. **17**, 053051 (2015).
- [30] Hermans, S., *Towards Purcell enhancement of the zero-phonon line of nitrogen-vacancy centres in diamond in an open Fabry-Pérot microcavity*, (2017), M.Sc. thesis.
- [31] Fox, M., *Quantum Optics* (Oxford University Press, 2016).
- [32] Haroche, S. & Raimond, J.-M., *Exploring the Quantum* (Oxford University Press, 2006).
- [33] Gérard, J.-M., *Solid-state cavity-quantum electrodynamics with self-assembled quantum dots*, in *Single Quantum Dots*, edited by Michler, P. (Springer, 2003) pp. 269–314.

-
- [34] Sauvan, C., Hugonin, J. P., Maksymov, I. S. & Lalanne, P., *Theory of the Spontaneous Optical Emission of Nanosize Photonic and Plasmon Resonators*, Phys. Rev. Lett. **110**, 237401 (2013).
- [35] Bersin, E. *et al.*, *Individual Control and Readout of Qubits in a Sub-Diffraction Volume*, arXiv:1805.06884 (2018).

12

MULTIPLEXED ENTANGLEMENT GENERATION OVER QUANTUM NETWORKS USING MULTI-QUBIT NODES

**Suzanne van Dam*, Peter Humphreys*, Filip Rozpędek*,
Stephanie Wehner, and Ronald Hanson**

Quantum networks distributed over distances greater than a few kilometers will be limited by the time required for information to propagate between nodes. We analyze protocols that are able to circumvent this bottleneck by employing multi-qubit nodes and multiplexing. For each protocol, we investigate the key network parameters that determine its performance. We model achievable entangling rates based on the anticipated near-term performance of nitrogen-vacancy centres and other promising network platforms. This analysis allows us to compare the potential of the proposed multiplexed protocols in different regimes. Moreover, by identifying the gains that may be achieved by improving particular network parameters, our analysis suggests the most promising avenues for research and development of prototype quantum networks.

Parts of this chapter have been published in *Quantum Science and Technology* **2**, 034002 (2017) [1].

*Equally contributing authors

12.1. INTRODUCTION

Recent progress in the generation, manipulation, and storage of distant entangled quantum states has opened up an avenue to the construction of a quantum network over metropolitan-scale distances in the near future [2, 3]. One of the key challenges in realizing such quantum networks will be to overcome the communications bottleneck induced by the long distances separating nodes. This occurs because probabilistic protocols require two-way communication and, for such distances, the entanglement generation rate becomes limited by the time required for quantum and classical signals to propagate.

It is unlikely that quantum networks will attain sufficient levels of complexity in the near future to support the transmission of complex multi-photon entangled states necessary to overcome this bottleneck through error correction [4, 5]. This motivates the development of alternative methods to circumventing this limited communication rate, of which the most promising near-term approach is through multiplexing entanglement generation [6–11].

Previous proposals have developed multiplexed entanglement-generation protocols for networks based on atomic-ensemble quantum memories and linear optics [7, 10, 12] and for networks in which each node consists of many optically accessible qubits that can be temporally, spectrally or spatially multiplexed [6, 8, 9, 11]. However, these proposals are not effective for promising multi-qubit hybrid network node architectures [13], in which one (or a few) optically accessible communication qubits in each node provide a communication bus to interface with multiple local memory qubits. Several platforms have demonstrated the key elements of such a system, including nitrogen-vacancy (NV) centres in diamond [14, 15], trapped ions [3], and quantum dots [15, 16].

Here we focus on the scenario of efficiently generating heralded remote entanglement between two hybrid multi-qubit nodes separated by tens of kilometers in a quantum network (Fig. 12.1). We propose two strategies for multiplexing entanglement generation using multi-qubit architectures, identifying the scaling of the entangling rates with the distance between nodes. We compare these strategies to an alternative protocol based on the distribution of entangled photon-pairs [17], modelling all three protocols analytically and with Monte Carlo simulations. This allows us to identify optimal protocols for different regimes of distance and node performance.

In order to be able to effectively assess the potential of these network protocols, it is vital to incorporate the known and anticipated limitations of potential platforms from the start. In this paper we therefore use network parameters representing the expected near-term performance of NV centre nodes. These centres are promising nodes for such a network, combining a robust and long-lived ^{13}C nuclear-spin quantum register [18, 19] with a photonic interface (Fig. 12.1). Our conclusions are nonetheless broadly applicable to other platforms with comparable system performances, particularly including trapped ions [3].

12.1.1. QUANTUM NETWORK PROTOCOLS

We begin by briefly introducing the three candidate protocols that we consider for a metropolitan-scale quantum network. For each network, we identify the scaling of the entanglement generation rate with the system transmission efficiency and the distance

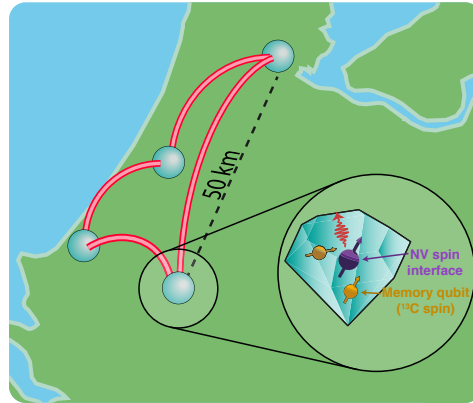


Figure 12.1: Quantum network. Quantum networks have the potential to reach metropolitan scales in the near term, opening up new challenges due to the time required to signal successful entanglement generation between nodes separated by many kilometers. Nitrogen-vacancy centres in diamond are promising candidates for the nodes of such a network, combining an electronic spin communication qubit interface for entanglement generation and local processing with long lived ^{13}C nuclear-spin memory qubits.

between nodes.

12.1.2. MULTIPLEXED BARRETT-KOK PROTOCOL

The first scheme is a multiplexed version of the Barrett-Kok (BK) protocol. In this scheme, entanglement is generated at both nodes locally between the spin state of the communication qubit and the modal occupation of a single photon (typically the photonic state is time-bin encoded for NVs). This procedure constitutes a single attempt to generate remote entanglement. The two photons are then transmitted to a remote beam splitter, where a probabilistic joint Bell state measurement (BSM) on the photons projects the two distant communication qubits into an entangled state upon measurement of the appropriate outcomes [20].

In this protocol each photon needs to be transmitted over a distance $d/2$ from the nodes to the central BSM station. This is followed by the transmission of classical information over the same $d/2$ distance heralding to the nodes the success or failure of the entangling attempt. Hence in the standard BK protocol, the entanglement attempt rate r_{BK} is limited by the combined quantum and classical communication time ($t_c = d/c$) required to establish whether the protocol succeeded: $r_{BK} \sim t_c^{-1}$. Even for modest distances, this time delay is sizable; e.g. for $d = 50$ km the delay is $t_c = 250$ μs , limiting the attempt rate to 4 kHz.

This rate limitation can be mitigated by using a multiplexed version of the BK protocol (Fig. 12.2), in which the spin state of the communication qubit is swapped to a memory qubit directly after spin-photon entanglement generation, freeing up the communication qubit for additional entanglement generation attempts. For the NV system, naturally occurring nearby ^{13}C nuclear spins provide robust memory qubits [19, 21]. The state is stored in this memory qubit until information about the success of the attempt

arrives. In the meantime, spin-photon entanglement generation and subsequent state swapping to other memories can continue until all of the memories are occupied. The multiplexed protocol allows N qubits per node to be utilised, where N includes both the communication qubit and the memory qubits.

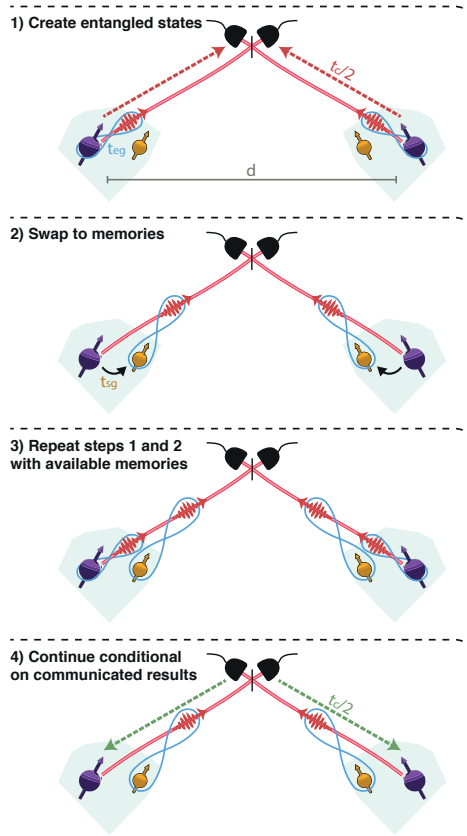


Figure 12.2: Multiplexing concept. The protocol starts with a creation of local entanglement between the communication qubits and single photons at both nodes (step 1). The state of the communication qubits is then immediately transferred to the memory qubits (step 2), which allows for a second entanglement attempt before the result of the first one is known (step 3). Once the signal heralding success or failure of the attempt is received at the nodes, the occupied memories can be reused for new attempts (step 4).

The maximum number of qubits per node that can be usefully employed in this protocol is given by $N_{\max} = \lceil t_c / t_{sg} \rceil$ ¹ where t_{sg} is the duration of the swap gate (typically much longer than the duration of entanglement generation attempts t_{eg}). The attempt rate of the multiplexed Barrett-Kok (mBK) protocol is therefore a factor N larger than for the standard BK scheme: $r_{\text{mBK}} \sim N / t_c$ for $N \leq N_{\max}$. This rate is upper bounded by $r_{\text{mBK}} \leq 1 / t_{sg}$.

¹ $\lceil x \rceil$ denotes $\text{ceil}(x)$

The success of each attempt of the BK scheme is conditioned on the detection of both the photons emitted by the communication qubits in the BSM. As a result, the system transmission efficiency η appears quadratically in the entanglement success rate R_{mBK} . Hence for $N \leq N_{\text{max}}$:

$$R_{\text{mBK}} \sim r_{\text{mBK}} \frac{\eta^2}{2} = \frac{1}{2} N \eta^2 / t_c. \quad (12.1)$$

The factor of half corresponds to the probability of a successful BSM at the beam splitter.

12.1.3. MULTIPLEXED EXTREME-PHOTON-LOSS PROTOCOL

In the case of high levels of photon loss ($\eta \ll 1$), a protocol based on entanglement distillation can be more effective than the BK protocol. In this protocol, instead of directly trying to generate a maximally entangled state $|\Psi\rangle = (1/\sqrt{2})(|01\rangle + |10\rangle)$, two weakly entangled states of the form $\rho \approx \frac{1}{2} |\Psi\rangle\langle\Psi| + \frac{1}{2} |00\rangle\langle 00|$ are efficiently generated conditional on the detection of only a single photon at the beam splitter station [13, 22]. Here $|0\rangle$ ($|1\rangle$) denotes the state of the communication qubit from which a photon is (is not) emitted. These weakly entangled states contain a contribution $|00\rangle\langle 00|$ from the case in which both communication qubits emitted a photon, but only one was detected. After the two states are successfully generated, an entanglement distillation procedure is performed using local operations and classical communication. This distillation produces a pure entangled state with a 1/8 probability. Since two raw states are consumed to generate a final entangled state, this extreme-photon-loss (EPL) protocol requires at least two qubits per node, as the first state has to be stored in a memory qubit until the second entangled state is generated.

The advantage of this scheme over the BK protocol is that it does not require the detection of coincident photons, instead allowing for multiple attempts to generate the second state. This results in a success probability that is proportional to η rather than η^2 and thus an entangling rate $R_{\text{EPL}} \sim \eta/(16t_c)$, where a factor 1/8 corresponds to the probability that the distillation operation succeeds, and a factor 1/2 reflects the need to generate two entangled states.

Analogously to the BK protocol, a multiplexed version of the scheme can be envisioned in which multiple entanglement generation attempts are performed within one communication cycle. Since, in the second stage of the protocol one memory is continuously occupied by the first entangled state, the maximum number of qubits that can be effectively utilised is one more than in the BK protocol: $N_{\text{max}} = \lceil t_c/t_{\text{sg}} \rceil + 1$. The resulting entanglement success rate R_{mEPL} for the multiplexed extreme-photon-loss protocol for $N \leq N_{\text{max}}$ is proportional to the inverse of the sum of the time spent in the first stage ($t_c/(\eta N)$) and second stage ($t_c/(\eta(N-1))$) of the protocol:

$$R_{\text{mEPL}} \sim \frac{N(N-1)}{2N-1} \frac{\eta}{8t_c}. \quad (12.2)$$

The entangled state fidelity in this protocol is sensitive to decoherence of the memories during entanglement attempts. In order to ensure a minimum fidelity, stored entangled states can be discarded after a set number of subsequent entanglement attempts, at the expense of decreasing the entanglement rate. Entanglement generated from a

single photon detection event is expected to succeed within at most a few hundred attempts (~ 100 attempts at 50 km, ~ 1000 attempts at 100 km) for the range of parameters considered here. For nitrogen-vacancy centre nodes, recent results indicate that ^{13}C nuclear-spin memories may effectively preserve quantum states over this number of attempts [19], and so this effect is not expected to significantly impact our conclusions.

12.1.4. MIDPOINT-SOURCE PROTOCOL

The final configuration that we consider is the midpoint source (MPS) protocol following Ref. [17]. In addition to the two nodes, this protocol requires an entangled-photon source (which emits pairs of photons with probability p_{em}) positioned midway between the nodes (Fig. 12.3). In this protocol, pairs of entangled photons generated by the photon source are split and one is sent to each of the two nodes. At each of the nodes, a BSM is performed between this photon and a photon generated by the local communication qubit. Entanglement swapping succeeds only if both BSMs succeed (requiring the detection of four photons in total).

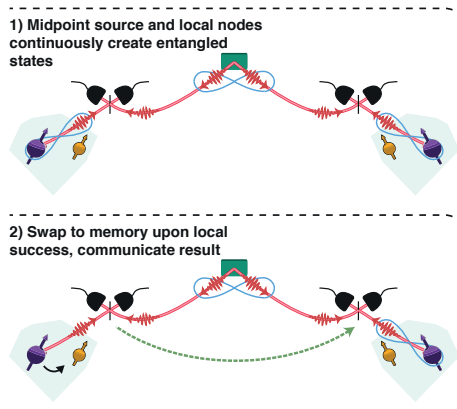


Figure 12.3: Midpoint-source (MPS) protocol. The photon source in the middle continuously generates pairs of entangled photons with probability p_{em} and transmits them to the two nodes (step 1). At the same time both nodes synchronously generate local entanglement between the communication qubit and emitted photons. Local beam splitter stations at each node perform BSM measurements between photons emitted from the source and the photons emitted from the local node. This gives the local node immediate knowledge of the local success or failure of each attempt. This information is also communicated to the other node, arriving d/c later.

Since the successes of the BSMs can be reported to their local nodes immediately, in the case of local failure the nodes can quickly proceed to a new entanglement generation attempt. In this way the entanglement attempt rate can be significantly increased. The attempt rate is upper bounded by $r_{MPS} \leq t_{eg}^{-1}$, where t_{eg} is the duration of the spin-photon entanglement generation.

This upper bound is saturated if the number of successful local BSMs per communication time t_c , $n = p_{BSM} t_c / t_{eg} \approx (1/2) p_{em} \eta t_c / t_{eg}$, satisfies $n \ll 1$. In this limit the protocol can be effectively run with a single qubit per node, and the rate is therefore

insensitive to the swap gate time t_{sg} . When operating the MPS protocol in this low n regime, the entanglement success rate is given by

$$R_{\text{MPS}} \sim p_{\text{em}} \eta^2 / (4t_{eg}), \quad (12.3)$$

where the factor of 1/4 arises because both BSs must succeed in the same round, and η includes the system losses for both the photon from the entangled photon source and the locally generated photon.

This scaling is different to that identified in Ref. 17 since, for the system parameters that we consider, t_{eg} is not small enough to ensure that the expected number of successes n per communication time t_c approaches unity. As shown in Fig. 12.5, for a shorter t_{eg} , the network could leave this low-success-probability regime. If the attempt rate is high enough to ensure that at least one attempt succeeds locally per t_c , the overall entanglement success rate will only primarily depend on whether there was a simultaneous success at the other node; the scaling is thus effectively proportional to η , which is the scaling described in Ref. 17. However, achieving this limit clearly requires a shorter t_{eg} as the loss $(1-\eta)$ increases.

For $n \sim 1$, the inclusion of additional memory qubits becomes beneficial to prevent idle time. In this case, after a local success, the communication qubit state is swapped to a memory qubit. This swapping operation therefore prevents the node from performing further entanglement generation attempts during a time t_{sg} , limiting the overall attempt rate.

12.2. MODELLING

We model each of the protocols described in the previous section with an approximate analytical approach as well as with Monte Carlo simulations. We use system parameters that are expected to be achievable for NVs and trapped ions in the near term (table 12.1). The outcoupling efficiency of the NV centre is assumed to benefit from coupling to an optical cavity (with outcoupling efficiency $p_{\text{out}} = 0.3$), and emitted photons are assumed to be frequency-converted to telecom-wavelength photons with efficiency $p_{\text{fc}} = 0.3$. Fiber losses are therefore limited to standard telecom values of $\alpha = 0.2$ dB/km. Hence the overall system transmission efficiency is given by $\eta = p_{\text{out}} p_{\text{fc}} 10^{-\alpha d/20}$ where the last term corresponds to the fiber losses over a distance of $d/2$.

It is as yet unclear how much progress will be made in the near term in overcoming the technical challenges necessary to demonstrate an entangled-photon-source with a high brightness and with spectral properties that are well-matched to the node emission. We therefore consider two possible values for p_{em} (0.1 and 0.01), taking 0.01 to be more technically feasible [23, 24].

12.2.1. SCALING WITH DISTANCE

The modelled dependency of the entangling rate on the node separation is shown in Fig. 12.4. As expected from section 12.1.1, the scaling with distance is most favorable for the mEPL protocol ($R_{\text{mEPL}} \sim 10^{-\alpha d/20} d^{-1}$), whereas the BK protocol scales worst ($R_{\text{mBK}} \sim 10^{-\alpha d/10} d^{-1}$). Even for an MPS protocol with an extremely efficient source ($p_{\text{em}} = 0.1$), the mEPL protocol outperforms it for distances greater than ~ 100 km since R_{MPS} scales less favourably with distance as $R_{\text{MPS}} \sim 10^{-\alpha d/10}$.

Table 12.1: Anticipated near-term parameters for a quantum network based on NV centers [14, 18, 25, 26]. These parameters are also anticipated to be achievable using trapped ions [3].

Variable	Description	Value
N	Total number of qubits at each node	2
p_{fc}	Frequency-conversion efficiency	0.3
p_{out}	NV-outcoupling efficiency	0.3
t_{eg}	Spin-photon entanglement generation time	1 μ s
t_{sg}	NV-carbon swap gate time	200 μ s
p_{em}	Midpoint-source photon-pair emission probability	0.01, 0.1

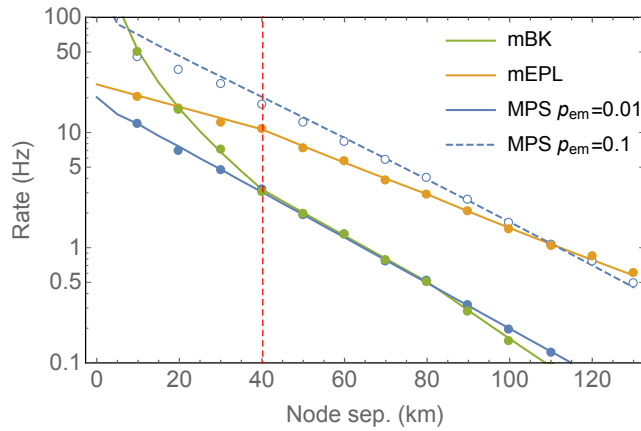


Figure 12.4: Scaling of entangling rate with distance. Modelled entanglement generation rates as a function of distance for the system parameters listed in table 12.1. Plotted lines give the results of our analytical model while the circles give equivalent Monte Carlo simulation data. Although two qubits are available to the system, the MPS protocol is always found to be in the low success probability regime ($n < 1$), in which only one qubit is required. For distances to the left of the red vertical dashed line the memory storage time t_{sg} is larger than the communication time t_c . In this regime it is optimal to use only one qubit for the mBK scheme. As the mEPL-scheme requires one memory qubit to store the first generated state in the second part of the protocol, for all distances both qubits are actively employed. The error bars associated with the Monte Carlo simulations are smaller than the plotted circles.

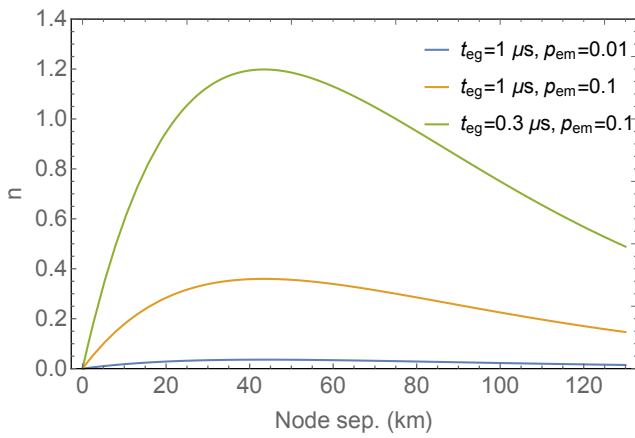


Figure 12.5: Successful local BSMs in the MPS protocol. Expected number of successful local BSMs n at each node per communication time t_c for the MPS protocol as a function of node separation. We see that for both values of p_{em} and for all distances $n < 1$, and hence a single qubit per node is sufficient.

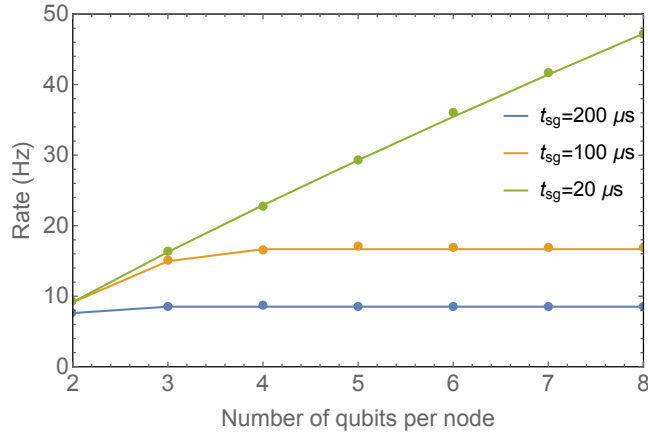


Figure 12.6: Entanglement-generation rate for the mEPL scheme. Modelled entanglement-generation rate for the mEPL scheme as a function of the number of qubits per node at $d = 50$ km. The three curves correspond to different values of the swap-gate time t_{sg} . An initial linear scaling of the rate with the total number of qubits is observed, as predicted by Eq. (12.2). The rate increases only up to $N_{\max} = \lceil t_c / t_{sg} \rceil + 1$, beyond which there is no further benefit. This rate saturation occurs over the addition of two qubits. This is because, while generating the second entangled state in the mEPL protocol, one memory qubit is always occupied by the first generated state. The addition of a further memory qubit beyond $N = \lceil t_c / t_{sg} \rceil$ therefore ensures that there are $\lceil t_c / t_{sg} \rceil$ qubits available for entanglement generation during both phases. However, this memory qubit is only used for the second state generation and so does not contribute as much as previous qubits. Error bars associated with the Monte Carlo simulations are smaller than the plotted circles.

In Fig. 12.5 we justify our claim that the MPS protocol will not benefit from more than a single qubit per node. We plot the expected number of successful BSMs n during the communication time as a function of distance, and observe that for our network parameters this stays well below one even for the case of a very efficient source ($p_{em} = 0.1$).

12.2.2. SCALING WITH NUMBER OF MEMORIES

Notably, for these near-term parameters, scaling up to a large number of qubits per node does not speed up the entanglement rate. As previously noted, the MPS protocol always operates in the low success probability regime in which only the communication qubit is actively used. For the mBK and mEPL protocols, the duration of the swap gate significantly limits the number of qubits per node that can be used over relevant node separations. We investigate the rate dependency of the mEPL protocol on the number of memory qubits in Fig. 12.6 for a fixed node separation of $d = 50$ km and a varying swap gate duration t_{sg} . For $t_{sg} \ll t_c$ the rate scales linearly with the number of qubits. However, as explained in section 12.1.1, once $N t_{sg} \approx t_c$ is reached, adding more memory qubits does not boost the entangling rate.

12.3. CONCLUSIONS

Our analysis highlights the potential of multiplexed distillation-based schemes to provide high rates of remote entanglement generation and the most favourable scaling with respect to losses. For such schemes, we have identified the swap gate time t_{sg} between the communication and the memory qubits as the key parameter in constraining the achievable entanglement generation rate, as this limits the number of quantum memories that can be used. This highlights the importance of developing methods to increase this storage rate while ensuring that memories remain robust to decoherence. One promising approach for nitrogen-vacancy centre nodes may be to use pairs of strongly coupled carbons to encode quantum memories in decoherence protected subspaces that combine rapid gates (due to their strong coupling) with long memory lifetimes [19].

We find that the midpoint-source protocol has a different dependence on the system parameters, with its performance only weakly constrained by the memory storage time. However, its increased sensitivity to losses hinders its performance over long distances. In addition, there is considerable uncertainty in the projected performance of entangled-pair sources in the near-term, particularly with regard to the source brightness. Until brightnesses on the order of 0.1 per attempt can be achieved, our analysis suggests that these schemes will not perform as effectively as the multiplexed distillation-based protocols.

12.4. ACKNOWLEDGMENTS

We acknowledge stimulating discussions with David Elkouss, Kenneth Goodenough, Norbert Kalb, Gláucia Murta, Tim Taminiau and Le P. Thinh. This work was supported by the Dutch Organization for Fundamental Research on Matter (FOM), Dutch Technology Foundation (STW), the Netherlands Organization for Scientific Research (NWO) through a VICI grant (RH), a VIDI grant (SW) and the European Research Council (ERC) through a Starting Grant (RH and SW).

REFERENCES

- [1] van Dam, S. B., Humphreys, P. C., Rozpędek, F., Wehner, S. & Hanson, R., *Multiplexed entanglement generation over quantum networks using multi-qubit nodes*, Quantum Science Technol. **2**, 034002 (2017), arXiv:1702.04885 .
- [2] Hensen, B. *et al.*, *Loophole-free bell inequality violation using electron spins separated by 1.3 kilometres*, Nature **526**, 682 (2015).
- [3] Hucul, D. *et al.*, *Modular entanglement of atomic qubits using photons and phonons*, Nature Physics **11**, 37 (2015).
- [4] Munro, W. J., Azuma, K., Tamaki, K. & Nemoto, K., *Inside quantum repeaters*, IEEE Journal of Selected Topics in Quantum Electronics **21**, 78 (2015).
- [5] Muralidharan, S. *et al.*, *Optimal architectures for long distance quantum communication*, Scientific Reports **6** (2016).

- [6] Collins, O. A., Jenkins, S. D., Kuzmich, A. & Kennedy, T. A. B., *Multiplexed Memory-Insensitive Quantum Repeaters*, Physical Review Letters **98**, 060502 (2007).
- [7] Simon, C. *et al.*, *Quantum repeaters with photon pair sources and multimode memories*, Physical Review Letters **98**, 190503 (2007), 0701239 .
- [8] Sangouard, N., Dubessy, R. & Simon, C., *Quantum repeaters based on single trapped ions*, Physical Review A **79**, 042340 (2009).
- [9] Munro, W. J., Harrison, K. A., Stephens, A. M., Devitt, S. J. & Nemoto, K., *From quantum multiplexing to high-performance quantum networking*, Nature Photonics **4**, 792 (2010), 0401076 .
- [10] Sinclair, N. *et al.*, *Spectral multiplexing for scalable quantum photonics using an atomic frequency comb quantum memory and feed-forward control*, Physical Review Letters **113**, 053603 (2014).
- [11] Vinay, S. E. & Kok, P., *Practical repeaters for ultralong-distance quantum communication*, Phys. Rev. A **95**, 052336 (2017).
- [12] Sangouard, N., Simon, C., de Riedmatten, H. & Gisin, N., *Quantum repeaters based on atomic ensembles and linear optics*, Reviews of Modern Physics **83**, 33 (2011).
- [13] Nickerson, N. H., Li, Y. & Benjamin, S. C., *Topological quantum computing with a very noisy network and local error rates approaching one percent*, Nature Communications **4**, 1756 (2013).
- [14] Bernien, H. *et al.*, *Heralded entanglement between solid-state qubits separated by three metres*. Nature **497**, 86 (2013).
- [15] Gao, W. B., Imamoglu, A., Bernien, H. & Hanson, R., *Coherent manipulation, measurement and entanglement of individual solid-state spins using optical fields*, Nature Photonics **9**, 363 (2015).
- [16] Delteil, A., Sun, Z., Gao, W. B., Togan, E. & Faelt, S., *Generation of heralded entanglement between distant hole spins*, Nature Physics **12**, 218 (2016).
- [17] Jones, C., Kim, D., Rakher, M. T., Kwiat, P. G. & Ladd, T. D., *Design and analysis of communication protocols for quantum repeater networks*, New Journal of Physics **18**, 083015 (2016).
- [18] Cramer, J. *et al.*, *Repeated quantum error correction on a continuously encoded qubit by real-time feedback*, Nature Communications **7**, 11526 (2016).
- [19] Reiserer, A. *et al.*, *Robust quantum-network memory using decoherence-protected subspaces of nuclear spins*, Physics Review X **6**, 021040 (2016).
- [20] Barrett, S. D. & Kok, P., *Efficient high-fidelity quantum computation using matter qubits and linear optics*, Physical Review A **71**, 060310 (2005).

- [21] Blok, M., Kalb, N., Reiserer, A., Taminiou, T. & Hanson, R., *Towards quantum networks of single spins: analysis of a quantum memory with an optical interface in diamond*, Faraday Discussions **184**, 173 (2015).
- [22] Campbell, E. T. & Benjamin, S. C., *Measurement-based entanglement under conditions of extreme photon loss*, Physical Review Letters **101**, 130502 (2008).
- [23] Clausen, C. *et al.*, *A source of polarization-entangled photon pairs interfacing quantum memories with telecom photons*, New Journal of Physics **16**, 093058 (2014).
- [24] Loredo, J. C. *et al.*, *Scalable performance in solid-state single-photon sources*, Optica **3**, 433 (2016).
- [25] Bogdanović, S. *et al.*, *Design and low-temperature characterization of a tunable microcavity for diamond-based quantum networks*, Appl. Phys. Lett. **110**, 171103 (2017).
- [26] Zaske, S. *et al.*, *Visible-to-telecom quantum frequency conversion of light from a single quantum emitter*, Physical Review Letters **109**, 147404 (2012).



13

CONCLUSIONS AND OUTLOOK

NV centres are promising building blocks for a diamond-based quantum network. The work presented in this thesis aims to enable extending these networks to multiple nodes and longer distances by addressing the entangling efficiency between nodes. We have taken steps towards an efficient NV photonic interface by developing optical cavities embedding coherent emitters, and have analyzed multiplexed protocols to overcome communication time delays in entangling rate. Here, we look ahead at the implementation of optical cavities in quantum networks, and the possible experiments and protocols that such an implementation enables.

13.1. SUMMARY

The work presented in this thesis can be summarised as follows:

- We implemented sequential three-qubit-parity measurements on nuclear spin surrounding the NV centre and used them for generation of multipartite entanglement and quantum contextuality tests. We developed a phase-echoed measurement technique that enables memory-efficient implementation of measurement sequences. This work highlights the versatility of the NV centre as a quantum network node.
- We created an analytical toolbox to describe and optimize the design of diamond-air cavities. We found that the focus for optimisation of diamond-air cavities should be: reducing vibration levels, reducing the mode volume through fiber shaping, and identifying or placing NV centres in a diamond-like mode.
- We found that nitrogen ion implantation and subsequent high-temperature annealing does not form optically stable NV centres from implanted nitrogen, contrary to the previous assumptions in the quantum engineering community. However, optically stable NVs may be formed from naturally occurring nitrogen atoms with lower position accuracy. Moreover, optically stable NVs are also created with high-energy electron irradiation and subsequent annealing.
- We devise a method for spin addressing in diamond membranes, and show characterisation of a Fabry-Pérot microcavity containing a thin diamond membrane at cryogenic temperatures. We find a diamond-air cavity finesse in the range 4,000-12,000, and vibrations < 0.5 nm RMS when selecting a quiet range in the one-second cryostat period. We observed cavity-coupled fluorescence from an NV ensemble in a Fabry-Pérot microcavity.
- We analyzed multiplexed quantum network protocols using local memories. Analytic and numeric modelling shows that multiplexed distillation-based schemes perform most effectively for near-term parameters.

In the remainder of this chapter we present an outlook towards diamond-based quantum networks with an efficient optical interface. First, in section 13.2 we describe next steps towards establishing an efficient optical interface in diamond beyond the work presented in this thesis. In section 13.3 we describe how conventional measurement sequences may need to be adapted for use with optical cavities. We provide a prospect for using the enhanced entangling efficiency with optical cavities for quantum repeaters in section 13.4. In the Introduction of this thesis we argued that progress in quantum foundational questions and quantum technology go hand-in-hand. In section 13.5 we first look ahead at foundational questions that may be addressed with NV centres in quantum networks in the future. We then discuss in detail the opportunities for device-independent quantum key distribution in section 13.6. For an extensive overview of the applications of a quantum internet we refer to Ref. [1].

13.2. TOWARDS AN EFFICIENT OPTICAL INTERFACE IN A QUANTUM NETWORK

The development of a diamond-air optical cavity for quantum networks requires several hurdles to be overcome, of which the main ones are NV optical coherence and cavity instability. Here we give an insight in how these can be overcome or circumvented.

13.2.1. EMITTERS WITH COHERENT OPTICAL TRANSITIONS

Diamond etching recipes that combine subsequent Ar/Cl₂ and O₂ steps have shown promising results in preserving the coherence of NV emission while creating smooth diamond surfaces [2–5]. Recent improvements in understanding of the etching dynamics in our lab (publication in preparation) led to a simplification of the recipe and enabled observation of narrow-linewidth NV centres in thin diamond membranes. These are encouraging results for the embedding of NV centres in optical cavities.

At the same time there are efforts to find alternative emitters with good optical properties, for applications in quantum networks. The NV centre is sensitive to electric fields due to its permanent electric dipole moment. Other defect centres, e.g. the negative silicon-vacancy (SiV⁻) in diamond, are inversion symmetric, thus having no permanent electric dipole moment. As a result, the optical transitions are less sensitive to electric fields, preventing spectral diffusion [6] and enabling incorporation in nanostructures such as photonic crystal nanocavities while retaining narrow optical linewidths [7]. Although the branching ratio into the ZPL for SiV⁻ is around 70% [8], incorporation in an optical cavity is still highly beneficial to overcome the centre's finite quantum efficiency (around 0.1 to 0.5 in nanostructures and bulk diamond respectively [9, 10]) and improve collection efficiency.

The described optical properties are promising, however the SiV⁻ coherence is not comparable to the NV spin coherence: at 4 K, spin coherence of the SiV is limited to ≈ 100 ns [11–13] due to phonon-induced relaxation within the ground state manifold [14]. Operation at millikelvin temperatures [15, 16] or in a high-strain environment [17, 18] is therefore required. Furthermore, research is needed to reduce readout times (currently 10 ms [15]) and to determine what limits the $T_2 = 13$ ms at millikelvin temperatures [15].

Next to the SiV⁻, other defect centres in diamond have been investigated for use in quantum network protocols, including the neutral silicon-vacancy [19, 20], the germanium-vacancy [21], tin-vacancy [22], and lead-vacancy [23], as well as defect centres in other materials such as the di-vacancy [24] and the silicon-vacancy in silicon-carbide [25], rare-earth ions in solids [26], and optically active donors in silicon [27]. Although some of these emitters have certain properties exceeding their NV counterpart, further research is needed to find their full suitability for quantum network applications. For an overview of recent progress with these emitters we refer to Ref. [28].

13.2.2. CAVITY STABILITY

The analytic descriptions of cavity parameters in chapter 5 guide the focus for optimising the microcavities described in this thesis. One of the conclusions is that although the current vibration levels suffice to in principle show substantial ($\approx 10^2$) speed-up in spin-photon entangling rate, further vibration reduction is highly desirable.

This can be achieved both passively and actively. A promising route for a passive solution is further decoupling of the cryostat's pulse tube from the cavity mounting [29–31]. Since these solutions typically introduce low-frequency drifts, they should be combined with active tracking for use in combination with free space optics.

Active stabilisation can be achieved through the Pound-Drever-Hall mechanism [32, 33]. This has been achieved at room temperatures for similar fiber Fabry-Pérot cavities [34], but an implementation at cryogenic temperatures in a pulse-tube cryostat is still missing. Challenges to overcome are the high number of mechanical resonances, and reproducibility of the resonance frequencies between cool-down runs.

We finally note that with improved understanding of local damage induced during NV creation and etching recipes (see section 13.2.1), it may become possible to create optically stable NV centres in nanostructured diamond near (≈ 100 nm) to the surface. In that case, photonic crystal cavities may become a viable design for NV centres in quantum networks. Cavity stability issue play a much less significant role for these cavities. However, the stability is connected with a loss of tunability, which presents a hurdle for these cavities.

13.3. QUANTUM NETWORK SEQUENCES IN OPTICAL CAVITIES

The embedding of the NV centre in an optical cavity has several consequences for the implementation of experimental sequences. We discuss three major anticipated adjustments to conventional sequences below.

13.3.1. SPIN READOUT

Readout of the spin-state is performed in current protocols using resonant spin-selective excitation, and detection of photons in the phonon side band (PSB) [35]. In a cavity setup, detection of the PSB is expected to be less efficient than in conventional setup. This is influenced by four system aspects.

(1) PSB photons are reflected by the cavity mirror. To circumvent this mostly, the cavity mirror can be designed with a narrow stopband¹, extending to 680 nm, to transmit ≈ 30 -50% of the PSB photons. (2) PSB photons, in contrast to ZPL photons not primarily emitted into the cavity mode, suffer from total internal reflection at the diamond surface. It is infeasible to place solid immersion lenses (SILs) around the NV centre as in conventional experiments [36], leading to a ≈ 10 times lower collection efficiency. (3) The relative emission into the ZPL is Purcell enhanced, at the expense of emission into the PSB. For optimal parameters in realistic conditions (see chapter 5), the emission into the PSB is reduced from 97% to $\approx 60\%$. (4) Outcoupling of the PSB through the mirror substrate (thickness ≈ 500 μm), requires using a longer working distance objective, with lower numerical aperture (NA). In the case that an NA of 0.5 is used (compared to a typical NA of 0.9), the collection efficiency is reduced by approximately a factor of 4.

Altogether, the collection efficiency of the PSB is expected to be around two orders of magnitude less than in conventional setups [37] prompting a new means for spin-

¹We note that the narrow stopband is created by using a thickness of $3\lambda/4$ instead of $\lambda/4$ for the high-refractive index DBR layer. This increases the penetration depth into this mirror approximately two times and thus increases the cavity mode volume.

readout. The increased branching ratio and efficient collection of the cavity mode makes detection of ZPL photons a promising alternative. This requires efficient suppression of the excitation light through polarisation or time filtering in combination with pulsed readout (see section 13.3.3), as well as the possibility to switch rapidly between local readout and long-distance entanglement generation.

13.3.2. COMBINING SPIN READOUT AND -INITIALISATION

NV electron spin initialisation and readout are performed optically. For readout, the cyclic and spin-conserving nature of the $m_s = 0$ optical transitions are used, while initialisation typically profits from the rapid spin flip in $m_s = \pm 1$ transitions. Depending on the strain in the sample and which transitions are used, these transitions may be at several GHz spacing. This is on the same order as the anticipated cavity linewidth. For spin initialisation in an optical cavity, efficient addressing of both transitions by rapid tuning, or an initialisation procedure using the $m_s = 0$ transition, e.g. combined with simultaneous microwave addressing, may need to be designed.

13.3.3. EXCITATION-LIGHT REJECTION

To generate spin-photon entanglement in a conventional entanglement scheme a spin-dependent optical transition (typically E_x or E_y) is resonantly excited, after which the resonantly emitted photon is detected. To do this effectively, excitation light and the emitted photon should be separated. The emitted photons cannot be spectrally filtered as they are at the same frequency as the excitation light. Instead, the emitted photons are filtered using polarisation and time filtering [38]. We here discuss the adjustments that these methods require in a microcavity setup.

Polarisation filtering Polarisation filtering uses orthogonality of the excitation and detection light. To employ this unaltered in a cavity setup, cavity modes with different polarization should be degenerate. However, in a fiber microcavity with a diamond membrane the polarization modes can be split in frequency (see section 4.3.6).

In the case of non-degenerate polarisation modes, using only one of the polarisation modes is not effective. We would require that mode to be partially overlapping in polarisation with both excitation and detection. However, when either the excitation or emitted light is coupled in the cavity, the polarisation is projected onto the cavity mode, hindering effective filtering.

Instead, if the degeneracy is lifted but the two cavity polarisation mode partially overlap in frequency, an alternative scheme can be used. The excitation and detection polarisations should be overlapped each with one of the cavity polarisation eigenmodes. The cavity eigenmode for detection should be on-resonance with the NV ZPL frequency to maximise Purcell enhancement. The excitation polarisation mode may be off-resonance, since we can compensate for inefficient excitation by using higher excitation power. The NV dipole needs to have partial overlap with both polarisation eigenmodes. This introduces a detection inefficiency, as the polarisation of the emitted photon evolves between the eigenmodes, resulting in a finite overlap with the excitation mode that is filtered [39]. However, the emitted light that is filtered can be free from excitation light.

In section 4.3.6 of this thesis we predicted that the source of polarisation non-degeneracy of the cavity modes is diamond birefringence and, to a less extent, fiber ellipticity. For a cavity with a diamond thickness of 4 μm and a dimple ellipticity within 5% we anticipate that the polarisation splitting is comparable in size to the cavity linewidth, such that $\approx 2\times$ more excitation power would have to be used compared to the degenerate case.

As a result of partial off-resonance and asymmetry of the cavity mirror design (see section 4.3.1) a significant part of the excitation light will be directly reflected off the cavity. The reflection can be in principle suppressed by polarisation- and time filtering. Moreover, to avoid having to suppress reflections it is possible to excite and detect from opposite sides of the cavity. This would require polarisation maintaining optics on both sides of the cavity. On the fiber-side this adds complexity: the cavity polarisation modes should be aligned with the optical axes of a polarisation maintaining fiber, requiring in-situ fiber rotation and low fiber ellipticity.

Time filtering A time-tagger can record the arrival time of photons to filter photons that arrived after the excitation pulse (NV emission only) from photons during the excitation pulse (including excitation light). Time filtering requires the excitation pulse to be short compared to the NV lifetime. Does the excitation pulse need to be reduced compared to current sequence as a result of the reduced the excited state lifetime from Purcell enhancement?

The expected lifetime for optimal parameters in realistic conditions is 5.2 ns (see chapter 5). Increasing the Purcell factor beyond this value has a relatively small effect on ZPL enhancement (Fig. 4.3), such that much shorter lifetimes are not expected for reasonable cavity designs. This is compatible with current sequences, as excitation pulses used in current entangling protocols have a duration of ≈ 2 ns [40], and can be in principle made shorter.

13.4. TOWARDS A QUANTUM REPEATER

For long distance photon losses eventually inhibit efficient entanglement generation between two nodes. A quantum repeater can overcome this, by using sequences of entanglement swapping between distant setups. In an envisioned quantum repeater based on NV centres, entanglement is generated between distant NVs and subsequently stored in a nuclear spin quantum memory, while entanglement generation is repeated between a next pair of NVs [41].

To efficiently implement a quantum repeater the entangling success probability should be higher than the inverse of the decay rate of the nuclear spin quantum memory. Dephasing times of the nuclear spin states are long (≈ 10 ms), however decoherence of the nuclear spin states is induced during entanglement generation through electron spin flips. The state-of-the-art nuclear spin memory preserves the nuclear spin during > 1000 NV entangling attempts [42]. For implementation of a quantum repeater, an entangling efficiency above 10^{-3} is thus needed. Embedding in an optical cavity is instrumental to achieve such entangling efficiencies.

For an optimal cavity design under realistic conditions (chapter 5) the expected photon emission efficiency into the preferred optical mode is $\approx 35\%$. The entangling effi-

ciency using the Barrett-Kok protocol [43], for nearby setups (distance \approx m), is then approximately $0.5 \times 0.35^2 = 6 \times 10^{-2}$, where the factor 0.5 is intrinsic to the protocol due to a probabilistic Bell state measurement. We assume a detection efficiency of order unity, as can be achieved with superconducting nanowire single-photon detectors [44]. For entanglement between truly distant setups (> 1 km), frequency conversion of the photons to telecom photons [45, 46] is needed. Assuming a frequency conversion efficiency of around 0.3 [45], the expected entangling efficiency is $\approx 6 \times 10^{-3}$.

In conclusion, both for nearby and distant setups the entangling efficiency would exceed the decay rate of the memories $(1000 \text{ attempts})^{-1}$. We thus expect that with NV centres embedded in optical cavities, memory coherence can be reliably preserved until a second round of entanglement is generated, opening up the possibility to realize quantum repeaters [47, 48].

13.5. FOUNDATIONAL QUESTIONS IN QUANTUM MECHANICS

An exciting prospect for the generation of quantum networks of larger entangled states is the possibility to perform foundational tests of quantum mechanics.

A particularly exciting idea is the implementation of a proposal described in Ref. [49] that finds that if the causal ‘influences’ between entangled subsystems in Bell tests are at a finite (superluminal) speed, they can be exploited for superluminal communication. While the experimental challenge for implementation is daunting, a future quantum network with high-fidelity links and local operations could support such a test.

Moreover, moving to larger entangled states and larger distances may turn out to show a boundary of the quantum world, via spontaneous localisation [50], or another, e.g. gravity-related mechanism [51, 52]. Together with experiments in quantum optomechanics [53, 54] and matter-wave interference [55] these network tests may reveal a solution to one of the most important outstanding problems in physics: the quantum measurement problem [56–58].

13.6. DEVICE-INDEPENDENT QUANTUM KEY DISTRIBUTION

This section is based on: G. Murta, S.B. van Dam, J. Rebeiro, R. Hanson, and S. Wehner, Towards a realization of a device-independent quantum key distribution, submitted for publication. arXiv:1811.07983 [59].

Quantum key distribution (QKD) [60, 61] is a remarkable example of the advantages that quantum systems bring to accomplishing classical tasks. In recent years, QKD has been pushed to long distances and out of the lab, to implementations over metropolitan connections [62–65] and in satellites [66, 67].

However, the security proofs of these implementations of QKD assume a good characterization of and trust in the experimental setup. Quantum properties allow us to overcome the need for this assumption: by exploiting the strong correlations that arise in quantum systems, one can prove security of quantum key distribution even in the very adversarial scenario where Alice and Bob, the communicating parties, have no knowledge of the internal working of their measurement devices or the underlying quantum system that they are measuring [68–73]. This is the *device-independent* (DI) model.

In this section we describe device-independent quantum key distribution (DIQKD),

and we analyze the possibility of an experimental implementation in several platforms. For details of the security analysis we refer to Ref. [59].

13.6.1. UNAVOIDABLE ASSUMPTIONS IN A DEVICE-INDEPENDENT MODEL

The DI scenario models the underlying system and measurement devices as black boxes: the only relevant information is the statistics of inputs and outputs. Therefore, no assumptions on the dimension of the quantum systems or the particular measurements performed by the devices are required.

However, in any implementation of a DI protocol four unavoidable assumptions remain: (1) *Isolated labs*: no information is leaked from or enters Alice's and Bob's labs, apart from the state distribution before the measurements and the public classical information dictated by the protocol. (2) *Isolated source*: the preparation of states is independent of the measurements. (3) *Trusted classical post-processing*: all public classical communication is performed using an authenticated channel and the local classical computations are trusted. (4) *Trusted Random Number Generators*: Alice and Bob possess independent and trusted random number generators.

Another assumption that can be used in security proofs is that the rounds of the experiment are independent and identically distributed (IID). This implies that the measurement devices are memory-less and the state shared by Alice and Bob is the same for every round of the protocol. Eavesdropper attacks corresponding to the IID scenario are *collective attacks*. Other attacks that we will consider are *coherent attacks*, where states shared between Alice and Bob can be arbitrarily correlated, and devices have memory and can operate according to results of previous rounds.

13.6.2. PROTOCOL AND PARAMETERS FOR DEVICE-INDEPENDENT QUANTUM KEY DISTRIBUTION

DIQKD relies on the violation of a Bell inequality to certify security of a generated key. The simplest DIQKD protocol uses the CHSH inequality [74] for a security test:

$$\beta = \langle xy \rangle_{0,0} + \langle xy \rangle_{0,1} + \langle xy \rangle_{1,0} - \langle xy \rangle_{1,1} \leq 2, \quad (13.1)$$

where $\langle xy \rangle_{a,b}$ represents the expectation value of the outputs x, y of Alice and Bob when they perform the measurement labeled by a, b respectively.

For DIQKD based on the CHSH inequality, we consider protocols where Alice possesses a device with two possible inputs $a \in \{0, 1\}$ and Bob has a device with three possible inputs $b \in \{0, 1, 2\}$. The inputs $a \in \{0, 1\}$ and $b \in \{0, 1\}$ are used to test for the CHSH inequality, and the inputs $a = 0$ and $b = 2$ are used for the other rounds, often called key generation rounds, where maximal correlation of the outputs is expected. An example of a honest implementation of this protocol on qubits, would link measurements along Z and X to Alice's device inputs $a = 0$ and $a = 1$ (with σ the two-qubit Pauli matrices). Bob's measurements would be along $(-Z + X)/\sqrt{2}$, $(-Z - X)/\sqrt{2}$, and Z for inputs $b = 0$, $b = 1$ and $b = 2$ respectively.

The relevant parameters for DIQKD are the Bell violation β achieved in the test rounds and the quantum bit error rate (QBER) Q in the key generation rounds. An implementation of the protocol is expected to have n rounds and a portion γn of these rounds is used

for testing of the CHSH condition. After generating a bit string, Alice and Bob perform classical error correction and privacy amplification.

13.6.3. EXPERIMENTAL IMPLEMENTATION OF DEVICE-INDEPENDENT QUANTUM KEY DISTRIBUTION

To certify security, the Bell test that DIQKD relies on should be free of loopholes that could be exploited by an adversary. While closing the detection loophole [75] is crucial for a DIQKD implementation, the spacelike separation required for loophole-free Bell tests can be relaxed. In a DIQKD experiment, no-communication between devices does not have to be guaranteed by space-like separation, since the assumption of isolated labs is already required. We are thus interested in considering Bell violations between distant - albeit not necessarily space-like separated - setups in which the detection-loophole is closed [37, 76–82]. The recent performance of fully loophole-free Bell tests [37, 80–82] mark the technological progress towards increasingly distant setups, needed for practically useful DIQKD.

Despite experimental progress described above, a DIQKD protocol has not yet been performed. A reason for this is that a Bell violation alone is not enough to guarantee security in a DIQKD protocol: the QBER also needs to be low. When the QBER is high, Alice and Bob leak a large amount of information during classical error correction. A larger Bell violation is then in turn needed to achieve a positive key rate. Moreover, security of the protocol demands a high number of minimal rounds to get a finite key rate, as a result of finite-size effects. Together, the requirements are to have a low QBER, high Bell violation and high entangling rates. We will quantify these requirements in light of different experimental platforms below.

13.6.4. PLATFORMS FOR DEVICE-INDEPENDENT QUANTUM KEY DISTRIBUTION

We distinguish two types of protocols for entanglement generation: (1) *All-photonic schemes*: Approaches in which the entangled state is encoded in a photonic state directly. Measurements of the photonic states on two remote setups enable their entanglement to be inferred. (2) *Heralded schemes*: In this case, the entangled state is typically created in a long-lived system and photons are used as a means of establishing, and heralding, the entanglement between two distant systems.

In the following, we discuss experimental platforms in which DIQKD may be implemented. We analyse Bell violations and the inferred QBER in previous Bell tests with distant setups and situate these parameters in a DIQKD security analysis. We evaluate the feasibility of DIQKD and the required numbers of minimal rounds for a positive key rate. A summary of these findings can be found in table 13.1 and Fig. 13.1.

DIQKD with all-photonic entanglement Since in all-photonic schemes the entanglement is carried by the photonic states, photon losses limit the entangled state fidelity and detection efficiency. Closing the detection loophole in a Bell test in photonic systems is thus a significant challenge: it requires highly efficient entangled-photon sources and photon detectors. Recently technological advances enabled all-photonic Bell tests

closing the detection-loophole [78, 79], later combined with space-like separation in loophole-free Bell tests [80, 81].

In photonic systems the detection efficiency also impacts the entangled state fidelity. We thus may expect that Bell violations are low in photonic systems. To avoid having to deal with undetected events, photonic Bell tests typically employ the CH-Eberhard inequality [83, 84]. The CHSH and CH-Eberhard inequalities are equivalent², such that we can estimate the CHSH violation achieved by photonic experiments. Table 13.1 illustrates the corresponding value for the CHSH inequality achieved in the experiments of Refs. [78–81]. One can note that the violations achieved are indeed low, ranging from $\beta = 2.00004$ to $\beta = 2.02$. Combined with a finite QBER ($> 2\%$), this poses a significant challenge for the implementation of a DIQKD protocol in photonic systems.

However, if these systems would enter the regime of positive key rates, the entanglement generation rate in photonic experiments can be very high ($\sim 10^5$ Hz [78–81]). In that case, asymptotic key rate values could thus be relatively easily reached.

DIQKD with heralded entanglement Due to the nature of heralded entangling schemes, photon losses do not influence the entangled state detection efficiency or fidelity. Heralded schemes have been used to entangle distant atomic ensembles [85, 86], trapped ions [87], atoms [88], NV centres [38], quantum dots [89], and mechanical oscillators [54]. So far, entangled state fidelities sufficient to violate Bell’s inequalities have only been reached with trapped ions [76, 77] and atoms [82, 88], and with NV centres [37, 90]. The observed Bell violations are in a range $\beta = 2.22$ to $\beta = 2.41$ (see table 13.1 for a full overview), with a QBER around 0.04 (estimated from detection efficiencies). Apart from the results reported in [77], these parameters are not in the region of positive key rate (see Fig. 13.1). However, all of them are in the proximity of this region, such that setup improvements may enable to reach it.

The challenge for these implementations is however their low entangling rate, induced by photon losses. Current rates range from (minutes)⁻¹ [76, 77, 82, 88] to (hours)⁻¹ [37, 90]. A significant speed-up in the entanglement generation rate is thus needed in order to achieve the minimum number of rounds required for DIQKD. Higher entangling rates in heralded schemes were recently achieved with trapped ions [91] and NV centres [40, 92], although with lower state fidelities, and no Bell violations are reported. Even though in ref. [40] the state fidelity is just high enough to be able to violate Bell inequalities, the expected Bell violation would be low. The enhancement in entangling rates with optical cavities as described in this thesis is thus instrumental to achieving an implementation of DIQKD.

In the next section we describe how the entangled state fidelity for NV centres could be improved to enter the region of positive key rate.

Nitrogen-vacancy centre-based networks In Refs. [37, 90] a CHSH violation $\beta = 2.38 \pm 0.14$ was observed between NV centres separated by 1.3 kilometers. Taking into account the entangled state fidelity and detection efficiency, we estimate that the corresponding

²One can see this by replacing non-detected events by the deterministic classical strategy “output 1” in a test of the CHSH inequality.

QBER would be $Q = 0.06 \pm 0.03$. Even though this Bell violation is considerably high, these parameters are not good enough to generate a secure key (see Fig. 13.1).

We suggest two setup improvements to enhance these parameters. First, the laser frequency stability used to excite NV centres during the entanglement protocols can be increased using an external cavity. This will increase photon indistinguishability leading to an expected improvement in two-photon quantum interference (TPQI) visibility from 0.88 to 0.90 [37, 90]. Second, both the CHSH violation β and the QBER Q are impacted by the NV electronic spin state readout. Improvements to the detection efficiency can be obtained by storing the electron spin state on the nearby nitrogen spin state, and performing repeated readout [93]. We estimate that the repeated readout can lead to an average readout fidelity of ≈ 0.985 compared to an initial 0.97 [94].

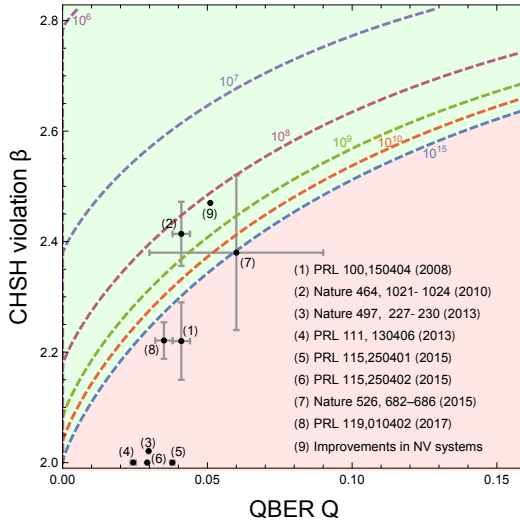
Taking into account these improvements, the expected DIQKD parameters are $\beta \approx 2.47$ and $Q \approx 0.051$. The security analysis described in Ref. [59] shows that this places the implementation in the regime of positive key rate.

The required minimum number of rounds however is on the order of 10^8 for general attacks, and about 5×10^6 for collective attacks (see Fig. 13.1). This is substantial, and with an entangling success probability of $\approx 10^{-8}$ (for setups at 1 km distance [37, 90]) and a repetition rate on the order of μs , it would take $\approx 10^3$ days to generate key even for the case of security against collective attacks. The availability of optical cavities with NV centres would make a significant difference to this. The estimated entangling success probability of 6×10^{-2} for nearby setups, or 6×10^{-3} for distant setups when including frequency conversion (section 13.4), would reduce the time to generate key assuming collective attacks to several hours, or less than a day respectively. This would bring a proof of principle demonstration of DIQKD with NV centres into the experimentally feasible regime.

	β	Q
(1) Matsukevich et al., PRL 100, 150404 (2008) [76]	2.22(7)	0.041(3)
(2) Pironio et al., Nature 464, 1021-1024 (2010) [77]	2.414(58)	0.041(3)
(3) Giustina et al., Nature 497, 227-230 (2013) [78]	2.02096(32)	0.0297(3)
(4) Christensen et al., PRL 111, 130406 (2013) [79]	2.00022(3)	0.0244(9)
(5) Giustina et al., PRL 115, 250401 (2015) [80]	2.000030(2)	0.0379(2)
(6) Shalm et al., PRL 115, 250402 (2015) [81]	2.00004(1)	0.0292(2)
(7) Hensen et al., Nature 526 682-686 (2015) [37]	2.38(14)	0.06(3)
(8) Rosenfeld et al., PRL 119, 010402 (2017) [82]	2.221(33)	0.035(3)
(9) Expected improvements for NV centres	2.47	0.051

Table 13.1: Summary of the estimated parameters for DIQKD, with experimentally realised Bell test. (1,2) are Bell tests with trapped ions, (3-5) are all-photonic experiments, (7) uses NV centres and (8) trapped atoms. In all experiments the detection loophole is closed; (5-8) additionally closed the locality loophole, in a Bell test free of all loopholes. The CHSH violations for neutral atoms (8), trapped ions (1,2) and NV centres (7) are as reported in the corresponding experiments. For (3), (4) and (5), in which the value of the CH-Eberhard inequality J is reported, we make use of the relation $\beta = 4J+2$ between the CHSH value and the CH-Eberhard value. This is found if in the CHSH inequality test one attributes "output 1" to the undetected events. For (6) the CHSH violation was estimated directly from the reported data. For the estimation of the QBER (Q), in (1),(2) and (8) we assume perfect classical correlation in the generated state and find a lower bound for the QBER from reported detection efficiencies (0.979 ± 0.002 [95] for (1) and (2), and 0.982 ± 0.002 [96] for (8)). For NV centres (7), we additionally account for imperfections in the entangled state based on the reported density matrix. For all-photonic systems (3-6), the QBER is estimated by taking into account the detection efficiency and using the reported estimated state and the measurements performed by Alice, optimizing over measurements for Bob.

(a) coherent attacks



(b) collective attacks

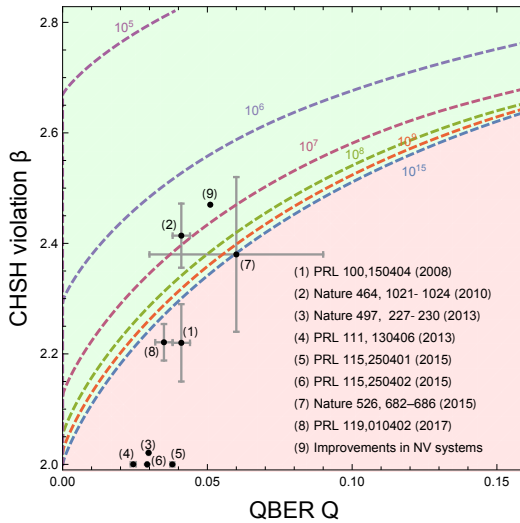


Figure 13.1: Regions of positive key rates for (a) coherent attacks and (b) collective attacks. The red area is the region of values of QBER (Q) and CHSH violation (β) for which a positive key rate cannot be reached with any number of rounds. In the green area, the dashed curves represents the minimum number of rounds required to get positive key rate. For parameters above each curve, a key rate can be extracted if the number of rounds is higher than specified in the curve. The points show the Bell violation and estimated QBER achieved by previous experiments (see table 13.1). They, however, do not reflect the corresponding entanglement generation rates. For the parameters expressing soundness and completeness [59] we take $\epsilon_{DIQKD}^c = 10^{-2}$ and $\epsilon_{DIQKD}^s = 10^{-5}$.

REFERENCES

- [1] Wehner, S., Elkouss, D. & Hanson, R., *Quantum Internet: a vision for the road ahead*, *Science* **362**, 303 (2018).
- [2] Cui, S., *Near-surface Nitrogen Vacancy Centers in Diamond*, Ph.D. thesis, Harvard University (2014).
- [3] Appel, P. *et al.*, *Fabrication of all diamond scanning probes for nanoscale magnetometry*, *Rev. Sci. Instrum.* **87**, 063703 (2016).
- [4] Johnson, S., Dolan, P. R. & Smith, J. M., *Diamond photonics for distributed quantum networks*, *Prog. Quantum Electron.* **55**, 129 (2017).
- [5] Challier, M. *et al.*, *Advanced fabrication of single-crystal diamond membranes for quantum technologies*, *Micromachines* **9**, 148 (2018).
- [6] Sipahigil, A. *et al.*, *Indistinguishable Photons from Separated Silicon-Vacancy Centers in Diamond*, *Phys. Rev. Lett.* **113**, 113602 (2014).
- [7] Evans, R. E., Sipahigil, A., Sukachev, D. D., Zibrov, A. S. & Lukin, M. D., *Narrow-Linewidth Homogeneous Optical Emitters in Diamond Nanostructures via Silicon Ion Implantation*, *Phys. Rev. Appl.* **5**, 1 (2016).
- [8] Neu, E. *et al.*, *Single photon emission from silicon-vacancy colour centres in chemical vapour deposition nano-diamonds on iridium*, *New J. Phys.* **13**, 025012 (2011).
- [9] Neu, E., Agio, M. & Becher, C., *Photophysics of single silicon vacancy centers in diamond: implications for single photon emission*, *Opt. Express* **20**, 3020 (2012).
- [10] Riedrich-Möller, J. *et al.*, *Deterministic Coupling of a Single Silicon-Vacancy Color Center to a Photonic Crystal Cavity in Diamond*, *Nano Lett.* **14**, 5281 (2014).
- [11] Pingault, B. *et al.*, *All-optical formation of coherent dark states of silicon-vacancy spins in diamond*, *Phys. Rev. Lett.* **113**, 263601 (2014).
- [12] Rogers, L. J. *et al.*, *All-optical initialization, readout, and coherent preparation of single silicon-vacancy spins in diamond*, *Phys. Rev. Lett.* **113**, 263602 (2014).
- [13] Pingault, B. *et al.*, *Coherent control of the silicon-vacancy spin in diamond*, *Nat. Commun.* **8**, 1 (2017).
- [14] Jahnke, K. D. *et al.*, *Electron-phonon processes of the silicon-vacancy centre in diamond*, *New J. Phys.* **17**, 43011 (2014).
- [15] Sukachev, D. D. *et al.*, *Silicon-Vacancy Spin Qubit in Diamond: A Quantum Memory Exceeding 10 ms with Single-Shot State Readout*, *Phys. Rev. Lett.* **119**, 223602 (2017).
- [16] Becker, J. N. *et al.*, *All-Optical Control of the Silicon-Vacancy Spin in Diamond at Millikelvin Temperatures*, *Phys. Rev. Lett.* **120**, 053603 (2018).

- [17] Sohn, Y. I. *et al.*, *Controlling the coherence of a diamond spin qubit through its strain environment*, Nat. Commun. **9**, 17 (2018).
- [18] Meesala, S. *et al.*, *Strain engineering of the silicon-vacancy center in diamond*, Phys. Rev. B **97**, 1 (2018).
- [19] Green, B. L. *et al.*, *Neutral Silicon-Vacancy Center in Diamond: Spin Polarization and Lifetimes*, Phys. Rev. Lett. **119**, 096402 (2017).
- [20] Rose, B. C. *et al.*, *Observation of an environmentally insensitive solid-state spin defect in diamond*, Science **361**, 60 (2018).
- [21] Siyushev, P. *et al.*, *Optical and microwave control of germanium-vacancy center spins in diamond*, Phys. Rev. B **96**, 081201 (2017).
- [22] Iwasaki, T. *et al.*, *Tin-Vacancy Quantum Emitters in Diamond*, Phys. Rev. Lett. **119**, 253601 (2017).
- [23] Trusheim, M. E. *et al.*, *Lead-Related Quantum Emitters in Diamond*, arXiv:1805.12202 (2018).
- [24] Christle, D. J. *et al.*, *Isolated spin qubits in SiC with a high-fidelity infrared spin-to-photon interface*, Phys. Rev. X **7**, 021046 (2017).
- [25] Nagy, R. *et al.*, *High-fidelity spin and optical control of single silicon vacancy centres in silicon carbide*, arXiv:1810.10296 (2018).
- [26] Zhong, T. *et al.*, *Optically addressing single rare-earth ions in a nanophotonic cavity*, Phys. Rev. Lett. **121**, 183603 (2018).
- [27] Morse, K. J. *et al.*, *A photonic platform for donor spin qubits in silicon*, Sci. Adv. **3**, 1 (2017).
- [28] Awschalom, D. D., Hanson, R., Wrachtrup, J. & Zhou, B. B., *Quantum technologies with optically interfaced solid-state spins*, Nat. Photonics **12**, 516 (2018).
- [29] Zhang, W. *et al.*, *Ultrastable Silicon Cavity in a Continuously Operating Closed-Cycle Cryostat at 4 K*, Phys. Rev. Lett. **119**, 1 (2017).
- [30] *Montana instruments hila*, .
- [31] *attocube attodry1000*, .
- [32] Drever, R. W. P. *et al.*, *Laser Phase and Frequency Stabilisation Using an Optical Resonator*, Appl. Phys. B **31**, 97 (1983).
- [33] Black, E. D., *An introduction to Pound-Drever-Hall laser frequency stabilization*, Am. J. Phys. **69**, 79 (2001).
- [34] Janitz, E., Ruf, M., Fontana, Y., Sankey, J. & Childress, L., *A High-Mechanical Bandwidth Fabry-Perot Fiber Cavity*, Opt. Express **25**, 20392 (2017).

- [35] Robledo, L. *et al.*, *High-fidelity projective read-out of a solid-state spin quantum register*, *Nature* **477**, 574 (2011).
- [36] Bernien, H. *et al.*, *Two-photon quantum interference from separate nitrogen vacancy centers in diamond*, *Phys. Rev. Lett.* **108**, 043604 (2012).
- [37] Hensen, B. *et al.*, *Loophole-free Bell inequality violation using electron spins separated by 1.3 kilometres*, *Nature* **526**, 682 (2015).
- [38] Bernien, H. *et al.*, *Heralded entanglement between solid-state qubits separated by three metres*, *Nature* **497**, 86 (2013).
- [39] Barrett, T. D., Barter, O., Stuart, D., Yuen, B. & Kuhn, A., *Atom-Photon Coupling in Birefringent Fabry-Perot Cavities*, arXiv:1807.07633 (2018).
- [40] Humphreys, P. C. *et al.*, *Deterministic delivery of remote entanglement on a quantum network*, *Nature* **558**, 268 (2018).
- [41] Childress, L., Taylor, J., Sørensen, A. & Lukin, M., *Fault-Tolerant Quantum Communication Based on Solid-State Photon Emitters*, *Phys. Rev. Lett.* **96**, 070504 (2006).
- [42] Kalb, N., Humphreys, P. C., Slim, J. J. & Hanson, R., *Dephasing mechanisms of diamond-based nuclear-spin memories for quantum networks*, *Phys. Rev. A* **97**, 062330 (2018).
- [43] Barrett, S. D. & Kok, P., *Efficient high-fidelity quantum computation using matter qubits and linear optics*, *Phys. Rev. A* **71**, 060310 (2005).
- [44] Marsili, F. *et al.*, *Detecting single infrared photons with 93 % system efficiency*, *Nat. Photonics* **7**, 210 (2013).
- [45] Bock, M. *et al.*, *High-fidelity entanglement between a trapped ion and a telecom photon via quantum frequency conversion*, *Nat. Commun.* **9**, 1 (2018).
- [46] Dréau, A., Tcheborateva, A., Mahdaoui, A. E., Bonato, C. & Hanson, R., *Quantum frequency conversion to telecom of single photons from a nitrogen-vacancy center in diamond*, *Phys. Rev. Appl.* **9**, 064031 (2018).
- [47] Rozpędek, F. *et al.*, *Parameter regimes for a single sequential quantum repeater*, *Quantum Sci. Technol.* **3**, 034002 (2018).
- [48] Rozpędek, F. *et al.*, *Near-term quantum repeater experiments with NV centers: overcoming the limitations of direct transmission*, arXiv:1809.00364 (2018).
- [49] Bancal, J.-D. *et al.*, *Quantum non-locality based on finite-speed causal influences leads to superluminal signalling*, *Nat. Phys.* **8**, 867 (2012).
- [50] Ghirardi, G. C., Rimini, A. & Weber, T., *Unified dynamics for microscopic and macroscopic systems*, *Phys. Rev. D* **34**, 470 (1986).

- [51] Diósi, L., *A universal master equation for the gravitational violation of quantum mechanics*, Phys. Lett. A **120**, 377 (1987).
- [52] Penrose, R., *On Gravity's Role in Quantum State Reduction*, Gen. Relativ. Gravit. , 581 (1996).
- [53] Marshall, W., Simon, C., Penrose, R. & Bouwmeester, D., *Towards quantum superpositions of a mirror*. Phys. Rev. Lett. **91**, 130401 (2003).
- [54] Riedinger, R. *et al.*, *Remote quantum entanglement between two micromechanical oscillators*, Nature **556**, 473 (2018), 1710.11147 .
- [55] Arndt, M. & Hornberger, K., *Testing the limits of quantum mechanical superpositions*, Nat. Phys. **10**, 271 (2014).
- [56] Bell, J., *Against 'measurement'*, Phys. World **3**, 33 (1990).
- [57] Schlosshauer, M., *Decoherence, the measurement problem, and interpretations of quantum mechanics*, Rev. Mod. Phys. **76**, 1267 (2003).
- [58] Gisin, N., *Collapse. What else?* arXiv:1701.08300 , 1 (2017).
- [59] Murta, G., van Dam, S. B., Ribeiro, J., R., H. & S., W., *Towards a realization of a device-independent quantum key distribution*, arXiv:1811.07983 .
- [60] Bennett, C. H. & Brassard, G., *Quantum cryptography: Public key distribution and coin tossing*, in *Proceedings of IEEE International Conference on Computers, Systems and Signal Processing* (1984) pp. 175 – 179.
- [61] Ekert, A. K., *Quantum cryptography based on Bell's theorem*, Phys. Rev. Lett. **67**, 661 (1991).
- [62] Peev, M. *et al.*, *The secoqc quantum key distribution network in vienna*, New J. Phys. **11**, 075001 (2009).
- [63] Sasaki, M. *et al.*, *Field test of quantum key distribution in the tokyo qkd network*, Opt. Express **19**, 10387 (2011).
- [64] Stucki, D. *et al.*, *Long-term performance of the SwissQuantum quantum key distribution network in a field environment*, New J. Phys. **13** (2011), 10.1088/1367-2630/13/12/123001.
- [65] Wang, S. *et al.*, *Field and long-term demonstration of a wide area quantum key distribution network*, Opt. Express **22**, 21739 (2014).
- [66] Vallone, G. *et al.*, *Experimental Satellite Quantum Communications*, Phys. Rev. Lett. **115**, 040502 (2015), arXiv:1406.4051 .
- [67] Liao, S. K. *et al.*, *Satellite-to-ground quantum key distribution*, Nature **549**, 43 (2017).

- [68] Pironio, S. *et al.*, *Device-independent quantum key distribution secure against collective attacks*, New J. Phys. **11**, 045021 (2009).
- [69] Acín, A., Gisin, N. & Masanes, L., *From Bell's theorem to secure quantum key distribution*, Phys. Rev. Lett. **97**, 120405 (2006).
- [70] Acín, A., Massar, S. & Pironio, S., *Efficient quantum key distribution secure against no-signalling eavesdroppers*, New J. Phys. **8**, 126 (2006).
- [71] Masanes, L., Pironio, S. & Acin, A., *Secure device-independent quantum key distribution with causally independent measurement devices*, Nat. Commun. **2**, 238 (2011).
- [72] Masanes, L., Renner, R., Christandl, M., Winter, A. & Barrett, J., *Full security of quantum key distribution from no-signaling constraints*, IEEE Transactions on Information Theory **60**, 4973 (2014).
- [73] Vazirani, U. & Vidick, T., *Fully device-independent quantum key distribution*, Phys. Rev. Lett. **113**, 140501 (2014).
- [74] Clauser, J. F., Horne, M. A., Shimony, A. & Holt, R. A., *Proposed Experiment to Test Local Hidden-Variable Theories*, Phys. Rev. Lett. **23**, 880 (1969).
- [75] Rowe, M. *et al.*, *Experimental violation of a Bell's inequality with efficient detection*, Nature **409**, 791 (2001).
- [76] Matsukevich, D. N., Maunz, P., Moehring, D. L., Olmschenk, S. & Monroe, C., *Bell inequality violation with two remote atomic qubits*, Phys. Rev. Lett. **100**, 150404 (2008).
- [77] Pironio, S. *et al.*, *Random numbers certified by Bell's theorem*, Nature **464**, 1021 (2010).
- [78] Giustina, M. *et al.*, *Bell violation using entangled photons without the fair-sampling assumption*, Nature **497**, 227 (2013).
- [79] Christensen, B. G. *et al.*, *Detection-loophole-free test of quantum nonlocality, and applications*, Phys. Rev. Lett. **111**, 130406 (2013).
- [80] Giustina, M. *et al.*, *Significant-loophole-free test of Bell's theorem with entangled photons*, Phys. Rev. Lett. **115**, 250401 (2015).
- [81] Shalm, L. K. *et al.*, *Strong loophole-free test of local realism*, Phys. Rev. Lett. **115**, 250402 (2015).
- [82] Rosenfeld, W. *et al.*, *Event-ready Bell test using entangled atoms simultaneously closing detection and locality loopholes*, Phys. Rev. Lett. **119**, 010402 (2017).
- [83] Clauser, J. F. & Horne, M. A., *Experimental consequences of objective local theories*, Phys. Rev. D **10**, 526 (1974).
- [84] Eberhard, P. H., *Background level and counter efficiencies required for a loophole-free einstein-podolsky-rosen experiment*, Phys. Rev. A **47**, R747 (1993).

- [85] Chou, C. W. *et al.*, *Measurement-induced entanglement for excitation stored in remote atomic ensembles*, *Nature* **438**, 828 (2005).
- [86] Usmani, I. *et al.*, *Heralded quantum entanglement between two crystals*, *Nat. Photon.* **6**, 234 (2012).
- [87] Moehring, D. L. *et al.*, *Entanglement of single-atom quantum bits at a distance*. *Nature* **449**, 68 (2007).
- [88] Hofmann, J. *et al.*, *Heralded entanglement between widely separated atoms*, *Science* **336**, 72 (2012).
- [89] Delteil, A., Sun, Z., Gao, W.-b., Togan, E. & Faelt, S., *Generation of heralded entanglement between distant hole spins*, *Nat. Phys.* **12**, 218 (2016).
- [90] Hensen, B. *et al.*, *Loophole-free Bell test using electron spins in diamond: second experiment and additional analysis*, *Scientific reports* **6**, 30289 (2016).
- [91] Hucul, D. *et al.*, *Modular entanglement of atomic qubits using photons and phonons*, *Nat. Phys.* **11**, 37 (2015).
- [92] Kalb, N. *et al.*, *Entanglement Distillation between Solid-State Quantum Network Nodes*, *Science* **356**, 928 (2017).
- [93] Jiang, L. *et al.*, *Repetitive Readout of a Single Electron Spin via Quantum Logic with Nuclear Spin Ancillae*, *Science* **326**, 267 (2009).
- [94] Pfaff, W. *et al.*, *Unconditional quantum teleportation between distant solid-state quantum bits*, *Science* **345**, 532 (2014).
- [95] Olmschenk, S. *et al.*, *Manipulation and detection of a trapped Yb^+ hyperfine qubit*, *Phys. Rev. A* **76**, 052314 (2007).
- [96] Henkel, F. *et al.*, *Highly efficient state-selective submicrosecond photoionization detection of single atoms*, *Phys. Rev. Lett.* **105**, 253001 (2010).



A

APPENDIX

This appendix describes the details of derivations supporting chapter 4 as well as details on optical characterisation measurements of NV centres. Appendix A.1 contains a full derivation of the resonance condition of a diamond-air cavity. The derivation of an analytic solution for the model describing Gaussian beams in a diamond-air cavity for a curved diamond surface can be found in appendix A.2. In appendix A.3 we describe samples with naturally occurring NVs in membranes as well as samples in which NVs are formed through high-energy electron irradiation and annealing.

A.1. RESONANCE CONDITION OF THE DIAMOND-AIR CAVITY

We here describe the derivation of the resonance condition of a diamond-air system as given section 4.3.3. We first determine the transmission ($T = |1/M_{1,1}|^2$) and assume ideal mirrors (lossless, and $r = 1$) to evaluate it:

$$\begin{aligned}
 T &= \frac{|(r_d - 1)t^2|^2}{|1 - e^{2ik(n_a t_a + n_d t_d)} + r_d(e^{-2ikn_a t_a} - e^{-2ikn_d t_d})|^2} \\
 &= \frac{(r_d - 1)^2 t^4}{(1 - e^{-2ik(n_a t_a + n_d t_d)} + r_d(e^{-2ikn_a t_a} - e^{-2ikn_d t_d}) \\
 &\quad \times (1 - e^{2ik(n_a t_a + n_d t_d)} + r_d(e^{2ikn_a t_a} - e^{2ikn_d t_d})))} \\
 &= \frac{(r_d - 1)^2 t^4}{2 - (e^{2ik(n_a t_a + n_d t_d)} + e^{-2ik(n_a t_a + n_d t_d)}) \\
 &\quad + 2r_d(e^{2ikt_a} + e^{-2ikn_a t_a} - e^{2ikn_d t_d} - e^{-2ikn_d t_d}) \\
 &\quad + r_d^2(2 + e^{2ik(n_d t_d - n_a t_a)} + e^{-2ik(n_d t_d - n_a t_a)})}
 \end{aligned} \tag{A.1}$$

where we use $k \equiv 2\pi\nu/c = k_a/n_a = k_d/n_d$.

We then use the trigonometric identities $e^{2i\phi} + e^{-2i\phi} = 2\cos(2\phi)$, $2 - 2\cos(2\phi) = 4\sin^2(\phi)$ and $\cos(u) - \cos(v) = -2\sin(\frac{u+v}{2})\sin(\frac{u-v}{2})$ to write this as:

$$\begin{aligned}
 T &= \frac{(r_d - 1)^2 t^4}{4\sin^2(k(n_a t_a + t_d)) + 4r_d^2 \sin^2(k(n_d t_d - n_a t_a)) \\
 &\quad + 8r_d(\sin(k(n_a t_a + t_d))\sin(k(t_d - n_a t_a)))} \\
 &= \frac{(r_d - 1)^2 t^4}{4(\sin(k(n_a t_a + n_d t_d)) - r_d \sin(k(n_a t_a - n_d t_d)))^2}.
 \end{aligned} \tag{A.2}$$

The condition that maximizes the transmission is:

$$\sin(k(n_a t_a + n_d t_d)) = r_d \sin(k(n_a t_a - n_d t_d)),$$

or equivalently:

$$(n_a + n_d) \sin\left(\frac{2\pi\nu}{c}(n_a t_a + n_d t_d)\right) = (n_a - n_d) \sin\left(\frac{2\pi\nu}{c}(n_a t_a - n_d t_d)\right) \tag{A.3}$$

We approximate ν by writing it as a deviation $\Delta\nu_{da}$ from the bare cavity resonance: $\nu = \frac{mc}{2(n_a t_a + n_d t_d)} + \delta\nu$, and neglect $\Delta\nu_{da}$ in the RHS of Eq. (A.3):

$$\begin{aligned}
 \sin\left(\pi m + \frac{2\pi\Delta\nu_{da}}{c}(n_a t_a + t_d n_d)\right) &= \frac{n_a - n_d}{n_a + n_d} \sin\left(\pi m \frac{n_a t_a - n_d t_d}{n_a t_a + n_d t_d}\right); \\
 (-1)^m \sin\left(\frac{2\pi\Delta\nu_{da}}{c}(n_a t_a + t_d n_d)\right) &= -\frac{n_d - n_a}{n_d + n_a} \sin\left(\pi m \frac{n_a t_a - n_d t_d}{n_a t_a + n_d t_d}\right); \\
 \frac{2\pi\Delta\nu_{da}}{c}(n_a t_a + t_d n_d) &= \arcsin\left(-(-1)^m \frac{n_d - n_a}{n_d + n_a} \sin\left(\pi m \frac{n_a t_a - n_d t_d}{n_a t_a + n_d t_d}\right)\right); \\
 \frac{2\pi\Delta\nu_{da}}{c}(n_a t_a + t_d n_d) &= -(-1)^m \arcsin\left(\frac{n_d - n_a}{n_d + n_a} \sin\left(\pi m \frac{n_a t_a - n_d t_d}{n_a t_a + n_d t_d}\right)\right); \\
 \Delta\nu_{da} &= \frac{c}{2\pi(n_a t_a + t_d n_d)} \left(-(-1)^m \arcsin\left(\frac{n_d - n_a}{n_d + n_a} \sin\left(\pi m \frac{n_a t_a - n_d t_d}{n_a t_a + n_d t_d}\right)\right)\right);
 \end{aligned}$$

so that we finally find the resonance condition of a diamond-air cavity:

$$\begin{aligned} \nu &= \frac{mc}{2(n_a t_a + n_d t_d)} + \Delta \nu_{da} \\ &= \frac{c}{2\pi(n_a t_a + t_d n_d)} \left(m\pi - (-1)^m \arcsin \left(\frac{n_d - n_a}{n_d + n_a} \sin \left(\pi m \frac{n_a t_a - n_d t_d}{n_a t_a + n_d t_d} \right) \right) \right) \end{aligned} \quad (\text{A.4})$$

We note that we can use Eq. (A.3) to find t_a that brings a cavity on resonance, given a diamond thickness t_d . We rewrite Eq. (A.3) in the following steps:

$$\begin{aligned} (n_a + n_d) &\left(\sin \left(\frac{2\pi}{\lambda_0} n_a t_a \right) \cos \left(\frac{2\pi}{\lambda_0} n_d t_d \right) + \cos \left(\frac{2\pi}{\lambda_0} n_a t_a \right) \sin \left(\frac{2\pi}{\lambda_0} n_d t_d \right) \right) \\ &= (n_a - n_d) \left(\sin \left(\frac{2\pi}{\lambda_0} n_a t_a \right) \cos \left(\frac{2\pi}{\lambda_0} n_d t_d \right) - \cos \left(\frac{2\pi}{\lambda_0} n_a t_a \right) \sin \left(\frac{2\pi}{\lambda_0} n_d t_d \right) \right) \\ 2n_d \sin \left(\frac{2\pi}{\lambda_0} n_a t_a \right) \cos \left(\frac{2\pi}{\lambda_0} n_d t_d \right) &= -2 \cos \left(\frac{2\pi}{\lambda_0} n_a t_a \right) \sin \left(\frac{2\pi}{\lambda_0} n_d t_d \right) \\ n_d \tan \left(\frac{2\pi}{\lambda_0} n_a t_a \right) &= -\tan \left(\frac{2\pi}{\lambda_0} n_d t_d \right) \\ t_a &= \frac{\lambda_0}{2\pi n_a} \arctan \left(-\frac{n_a}{n_d} \tan \left(\frac{2\pi n_d t_d}{\lambda_0} \right) \right) \end{aligned} \quad (\text{A.5})$$

A.2. ANALYTIC SOLUTION TO A COUPLED GAUSSIAN MODES MODEL FOR A CURVED DIAMOND SURFACE

We here derive the analytic solutions to the coupled Gaussian beams model if the diamond surface were curved, fixing the diamond surface radius of curvature to match the beam front curvature. The beam waist for curved surface is smaller than for a plane interface, as the results of a lensing effect.

The ABCD matrix for this situation is given by [1]:

$$\begin{pmatrix} A & B \\ C & D \end{pmatrix} = \begin{pmatrix} 1 & 0 \\ -\frac{(n_d - n_a)}{n_d R_{DA}} & n_a / n_d \end{pmatrix}, \quad (\text{A.6})$$

where R_{DA} is the radius of curvature of the diamond surface, that we assume to match the diamond and air Gaussian beam radius of curvature at that position: $R_a(t_d) = R_d(t_d) = -R_{DA}$. Following the ABCD-law for Gaussian beams [1], the complex beam parameters are related as:

$$q_d = \frac{Aq_a + B}{Cq_a + D} = \frac{q_a}{-\frac{(n_d - n_a)}{n_d R_{DA}} q_a - n_a / n_d}. \quad (\text{A.7})$$

The boundary conditions that this leads to are:

$$R_a(t_d) = R_d(t_d); \quad (\text{A.8})$$

$$W_a(t_d) = W_d(t_d), \quad (\text{A.9})$$

that can be solved analytically to give:

$$z_{0,a} = \frac{n_d n_a (1 + t_d^2 / z_{0,d}^2)}{n_d^2 + n_a^2 t_d^2 / z_{0,d}^2} z_{0,d} \approx \frac{n_a}{n_d} z_{0,d}, \quad (\rightarrow w_{0,a} \approx w_{0,d}). \quad (\text{A.10})$$

$$\Delta z_a = t_d \left(1 - \frac{n_d^2 (1 + t_d^2 / z_{0,d}^2)}{n_d^2 + n_a^2 t_d^2 / z_{0,d}^2} \right) \approx t_d (1 - n_a^2 n_d^2), \quad (\text{A.11})$$

where the approximation holds in the case $t_d \ll z_{0,d}$, which follows from $ROC \gg t_d$, as we describe below. We find that the ‘effective cavity length’ that determines the beam waist for the case with such a curved surface is $L'_{curv} \approx t_a + t_d / n_d^2$. This length is shorter than for a plane diamond surface, since the surface curvature creates a lensing effect, shifting the effective waist position of the Gaussian beam in air towards the diamond-air interface. The shorter effective length gives a narrower beam waist compared to the plane diamond.

Derivation of $t_d \ll z_{0,d}$ from $ROC \gg t_d$ In this paragraph we show that if we assume $ROC \gg t_d$, then it follows that $t_d \ll z_{0,d}$. First we assure ourselves that if $ROC \gg t_d$ holds, $R_{DA} \gg t_d$ also holds, where R_{DA} is the beam curvature at the diamond-air interface. We can deduce this by finding the conditions for which $R_{DA} = ROC$, and then deducing that $R_{DA} > ROC$ for at least all cavities with $2t_d + t_a < ROC$. We do this as follows: first we find the two solutions of $R_a(z) = ROC$:

$$z - \Delta z_a = \frac{ROC}{2} \pm \frac{\sqrt{ROC^2 - 4z_{0,a}^2}}{2}$$

If $R_{DA} = ROC$, one of these solutions must correspond to $z = t_d$, while the other should correspond to $z = t_a + t_d$. We thus conclude that $t_a = \sqrt{ROC^2 - 4z_{0,a}^2}$. If we use this in the solution for $z = t_d$ we find: $t_d - \Delta z_a = ROC/2 - t_a/2$. This is the limiting case: to have $R_{DA} < ROC$ we require $t_d + t_a/2 - \Delta z_a < ROC/2$, or at least $2t_d + t_a < ROC$. This condition is almost always satisfied for cavities with $t_d \ll ROC$ since in that case the condition reduces to $t_a \lesssim ROC$ which holds for all stable cavities.

We then use the constraint $t_d \ll R_{DA}$ to find constraints on $z_{0,d}$ and $z_{0,a}$. The curvature at the diamond air interface (R_{DA}) is given by $R_d(t_d)$ (Eq. (4.57)). This gives:

$$t_d \ll t_d \left(1 + \frac{z_{0,d}}{t_d} \right)^2; \quad (\text{A.12})$$

From this we find:

$$z_{0,d} \gg t_d; \quad (\text{A.13})$$

as required.

A.3. OPTICAL CHARACTERISATION OF NV CENTRES IN DIAMOND MEMBRANES

A.3.1. NATURALLY OCCURRING NV CENTRES

We characterised two samples with naturally occurring NVs:

- *N-1 (Harry)*¹
- *N-2 (Sophie)*;

An overview of these samples and the optical characterisation of NVs in them can be found in table A.1.

We first characterised *N-1* after it had been obtained from a bulk diamond through cutting, thinning, and polishing (we use *N-1A* to indicate the sample at this stage in the processing). In this sample, we found that the intrinsic linewidths were broadened, observing linewidths between 300-700 MHz. This can possibly be explained by a damaged layer after polishing. The NVs were located 2.4 - 5.4 μm away from the surface.

After thinning the sample down by 10 μm using an Ar/Cl₂ etch, no stable NVs were found (*N-1B* in table A.1). The photostability could not be recovered, neither after a first (*N-1C*) nor a second O₂ etch (*N-1D*). After these O₂ etches Cl contamination ($\approx 0.2\%$) was still found in an XPS measurement of this sample, indicating that the chlorine had not been fully removed.

In a separate sample (*N-2*) that was Ar/Cl₂ etched to 4 μm thickness, most NVs were not photostable. We nevertheless found one stable NV centre, whose ZPL we observed in the spectrometer under green illumination. We found linewidths of >100 GHz and extreme axial and transversal strain of ≈ 825 GHz (+470.4 THz) and ≈ 175 GHz.

From these measurements we conclude that an Ar/Cl₂ etch deteriorates NV properties, as described by Refs. [2–4]. An O₂ etch is reported to remove these effects, but special care has to be taken to remove all contamination from the etching chamber before performing these etches. The observed Cl contamination on *N-1*, even after the two O₂ etches, indicates that such contamination was present in the etching chamber during these steps.

¹In the tradition of our lab, all samples have names. We here index the samples with a letter (N for natural, Irr for irradiated) and a number for clarification, but also link the samples to their traditional name for completeness.

Table A.1: Overview of measured linewidths in samples with naturally occurring NVs.

sample	cut & polished	processing	thickness	substrate
<i>N-2</i>	DDK	Ar/Cl etch	3 μm	DBR
<i>N-1A</i>	DDK	-	20-30 μm	SiO ₂
<i>N-1B</i>	DDK	10-20 μm Ar/Cl etch	10 μm	SiO ₂
<i>N-1B</i>	DDK	10-20 μm Ar/Cl etch + 2 μm O ₂ etch	8 μm	SiO ₂
<i>N-1C</i>	DDK	10-20 μm Ar/Cl etch + 2 μm O ₂ etch + 2 μm O ₂ etch + triacid clean + O ₂ anneal	6 μm	SiO ₂

photo-stable?	size dataset	ξ_{\parallel} (GHz)	ξ_{\perp} (GHz)	$\delta\nu$ (MHz)	$\delta\nu_{\text{sd}}$ (MHz)	sample
some	1	≈ 750	≈ 150	-	≈ 150	<i>N-2</i>
yes	4	80-110	3.5-8	300-800	700-2000	<i>N-1A</i>
no	0	-	-	-	-	<i>N-1B</i>
no	0	-	-	-	-	<i>N-1B</i>
no	0	-	-	-	-	<i>N-1C</i>

A.3.2. NV CENTRES FORMED BY HIGH-ENERGY ELECTRON IRRADIATION

Two samples with NV centres formed by high-energy electron irradiation were studied:

- *Irr-1 (Sirius)*
- *Irr-2 (Giuseppe A)*

An overview of the results for these samples can be found in table A.2.

Both samples in which NV's were characterised show optical linewidths of < 100 MHz, both for the intrinsic linewidth and under the influence of spectral diffusion. For *Irr-2* the NV density was very high as the result of a high irradiation does, leading to the presence of many NV centres in a confocal spot (Fig. A.1).

These results establish the most consistently good results we have seen for NV centres in diamond membranes. We therefore believe high-energy electron irradiation is the most promising route for the creation of optically stable NV centres for optical cavities.

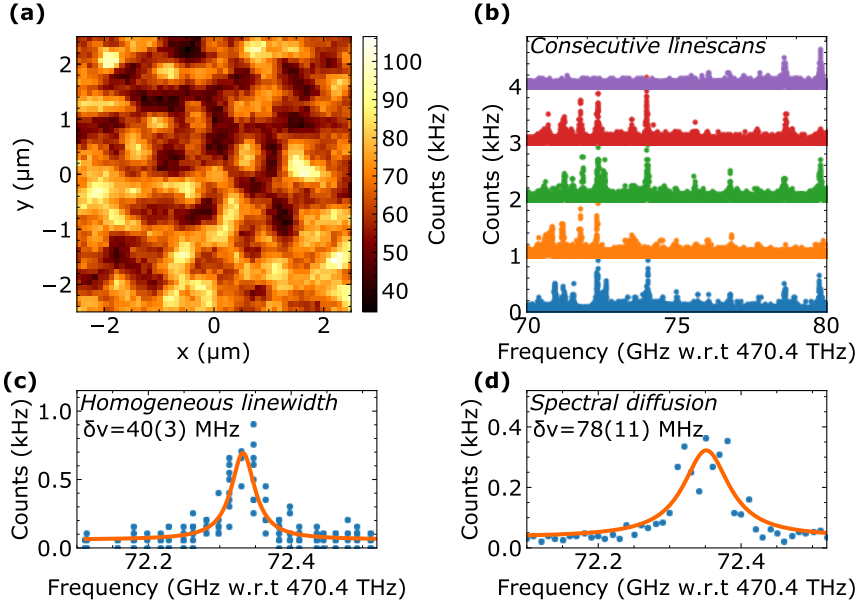


Figure A.1: Irradiated NVs (a) A fluorescence map of *Irr-2* shows a high density of NV centres. (b) Many optical transitions are visible in a single scan of the optical transitions, showing multiple NV centres in a single confocal spot. (c) The individual homogeneous linewidths are near lifetime limited, (c) and the influence of spectral diffusion is low.

Table A.2: Overview of measured linewidths in samples with irradiated NVs. After irradiation, all samples have been annealed in a three-step process based on [5], with a maximum temperature of 1100°C.

sample	irrad. dose (cm ⁻²)	cut & polished	processing	thickness (μm)
<i>Irr-1</i>	10 ¹⁴	?	Ar/Cl etch	12-18
<i>Irr-2</i>	5 · 10 ¹⁴ /10 ¹⁴	Almax	-	13

photo-stable?	size dataset	ξ_{\parallel} (GHz)	ξ_{\perp} (GHz)	$\delta\nu$ (MHz)	$\delta\nu_{sd}$ (MHz)	sample
yes	11	70-100	2-25	25-100	50-70	<i>Irr-1</i>
yes	?	?	?	37-48	≈ 80	<i>Irr-2</i>

ACKNOWLEDGEMENTS

We thank Airat Galiulin, Sophie Hermans, Lisanne Coenen, Steven de Rooij and Bas Hensen for their contributions to data acquisition, and Stefan Bogdanović, Maximilian Ruf, Erika Janitz, Srujan Meesala and Pawel Latawiec for sample fabrication.

REFERENCES

- [1] Saleh, B. & Teich, M., *Fundamentals of Photonics*, Wiley Series in Pure and Applied Optics (Wiley, 2007).
- [2] Cui, S., *Near-surface Nitrogen Vacancy Centers in Diamond*, Ph.D. thesis, Harvard University (2014).
- [3] Aharonovich, I. & Neu, E., *Diamond nanophotonics*, *Adv. Opt. Mater.* **2**, 911 (2014).
- [4] Appel, P. *et al.*, *Fabrication of all diamond scanning probes for nanoscale magnetometry*, *Rev. Sci. Instrum.* **87**, 063703 (2016).
- [5] Chu, Y. *et al.*, *Coherent optical transitions in implanted nitrogen vacancy centers*. *Nano Lett.* **14**, 1982 (2014).

SUMMARY

Quantum mechanics differs deeply from classical intuition and knowledge, sparking fundamental questions and radically new technology. Generating large entangled states between distant nodes of a quantum network will advance both domains. The nitrogen-vacancy (NV) centre in diamond is a promising building block for such a network. However, extending quantum networks to more nodes and larger distances relies upon improving the entangling efficiency of these defect centres. In this thesis we present experimental and theoretical work focused on addressing this challenge through embedding NV centres in an optical cavity, taking care to preserve coherence of the NV optical transition. We further analyze protocols for efficient quantum communication over an NV-based quantum network.

The NV centre in diamond has many features that are desirable for a quantum network node. It has a spin ground state that can be coherently controlled with microwave fields and optically read out in a single shot at cryogenic temperatures (≈ 4 K). Furthermore, the optical transitions can be coherent, allowing the spin-photon interface to be employed for the establishment of distant coherent links. Moreover, surrounding ^{13}C nuclear spins can be used as quantum memory or for quantum algorithms. We explore the use of such nuclear spins surrounding an NV centre for quantum foundational experiments and quantum information protocols in chapter 3. We realize a sequential non-destructive three-qubit parity measurement which enables the generation of genuine multipartite entanglement out of an initial mixed state. We further use these measurements for quantum contextuality experiments, probing the counter-intuitive nature of quantum mechanics. The developed techniques are directly applicable to quantum information protocols such as quantum error correction.

To establish distant links between NV centres, coherent optical transitions are key. For NV centres in bulk diamond, only 3% of the emitted photons correspond to such a decay via a coherent transition to the ground state. For entanglement generation these photons can be spectrally filtered from those resulting from incoherent transitions. However, this decreases the entangling efficiency. Additional photon losses result from a finite collection efficiency and fiber attenuation, limiting entangling rates to several Hz. A significant increase in efficiency can be obtained by embedding the NV centre in an optical cavity, benefiting from Purcell enhancement of the coherent transitions to increase both the emission- and collection efficiency of coherent photons. In this thesis we embed NV centres in a thin diamond membrane in an open Fabry-Pérot microcavity. We develop analytic models that provide an effective tool to find the optimal design parameters for such a cavity (chapter 5).

For incorporation in optical cavities it is highly desirable to create NV centres at pre-

cise locations in diamond membranes. However, the process of creating NV centres and fabricating thin membranes can introduce defects in the diamond. These defects can cause time-dependent electric field fluctuations around the NV centre, inducing instability of the NV optical transitions. In chapters 6 and 7 we experimentally explore the optical properties of NV centres in membranes, created with either high-energy electron irradiation or nitrogen-ion implantation, followed by high-temperature annealing. We find that NV centres created with electron irradiation can have coherent optical transitions, while, in contrast to previous assumptions in the quantum engineering community, NV centres formed from implanted nitrogen atoms do not routinely have narrow optical lines.

We report on the experimental realization of a Fabry-Pérot microcavity with embedded NV centres in chapters 9 to 11. We develop microwave striplines entrenched in a planar mirror that enable spin addressing of an NV centre in a cavity structure, without compromising cavity finesse. Further, we embed a thin diamond membrane in a microcavity at cryogenic temperatures. We find high finesse values within the range of $F = 4,000 - 12,000$ and a sub-nanometer cavity stability. For these parameters we estimate a potential increase in entangling rate of three orders of magnitude. We subsequently embed a membrane with optically coherent NV centres formed by electron irradiation in a microcavity. We observe the coupling of the emission an NV ensemble into the cavity mode. Although a low cavity finesse hinders the observation of Purcell enhancement, these mark important steps towards Purcell enhancement of single emitters.

In chapter 12 we look ahead to quantum networks distributed over distances greater than a few kilometers. We analyse protocols with multiplexing in multi-qubit quantum nodes to overcome limits on entangling rate imposed by classical communication time. We model achievable entangling rates based on anticipated performance of NV centres employing optical cavities. This analysis allows us to compare the potential of the proposed multiplexed protocols.

The optical cavities, coherent emitters, and protocols presented in this thesis advance the efficiency of quantum networks based on the NV centre in diamond. This reveals a path towards large-scale networks, enabling foundational tests and quantum technologies that rely on high entangling rates, such as device-independent quantum key distribution.

SAMENVATTING

Quantummechanica verschilt diepgaand van klassieke intuïtie en wetenschap waardoor het fundamentele vragen en radicaal nieuwe technologie genereert. Het maken van grote verstrengelde toestanden tussen knooppunten op afstand in een quantumnetwerk zal beide domeinen vooruit stuwten. Het stikstof-gatcentrum (NV-centrum) in diamant is een veelbelovende bouwsteen voor zo een netwerk. Maar, het uitbreiden van een quantumnetwerk naar meer knooppunten en grotere afstanden steunt op het verbeteren van de verstrengelingsefficiëntie van deze NV-centra. In dit proefschrift presenteren wij experimenteel en theoretisch werk toegeleid op het aanpakken van deze uitdaging door het inbedden van het NV-centrum in een optische trilholtte, daarbij zorg dragend voor het behouden van de coherentie van de optische transitie. Daarnaast analyseren we protocollen voor efficiënte quantumcommunicatie over een NV-gebaseerd quantumnetwerk.

Het NV-centrum in diamant is in veel aspecten geliefd als quantumnetwerkknooppunt. Het heeft een spin grondtoestand die coherent gecontroleerd kan worden met microgolfvelden en bij cryogene temperaturen (≈ 4 K) optisch uitgelezen kan worden in een enkele poging. Daarnaast kunnen de optische transitie coherent zijn, zodat ze gebruikt kunnen worden voor het totstandbrengen van coherent links over een afstand. Bovendien kunnen rondomliggende ^{13}C kernspins worden gebruikt als quantumgeheugen of voor quantumalgoritmes.

We onderzoeken het gebruik van zulke kernspins rondom een NV-centrum voor fundamentele experimenten en quantuminformatieprotocollen in hoofdstuk 3. We realiseren werkelijke verstrengeling van meerdere qubits vanuit een gemengde toestand met opeenvolgende niet-destructieve drie-qubitpariteitmetingen. Verder gebruiken we deze metingen voor een quantumcontextualiteit experiment, om de tegenintuïtieve natuur van quantummechanica te onderzoeken. De ontwikkelde technieken zijn direct toepasbaar op quantuminformatieprotocollen zoals quantumfoutencorrectie.

Om verafgelegen links tussen NV-centra te maken, zijn coherent optische transitie van groot belang. Voor NV-centra in bulk diamant is slechts 3% van de uitgezonden fotonen vervallen via zo een coherent transitie naar de grondtoestand. Om toch verstrengeling te kunnen maken kunnen deze fotonen spectraal gefilterd worden van de fotonen uitgezonden via incoherent transitie, maar dit gaat ten koste van de verstrengelingsefficiëntie. Daarbij komen fotonverliezen door een eindige collectie efficiëntie en verzwakking in glasvezelkabel, die de verstrengelingssnelheid limiteren tot enkele Hz. Een significante efficiëntievergroting kan worden verkregen door het NV-centrum in een optische trilholtte in te bedden, waarbij kan worden geprofiteerd van Purcell verbetering van de coherent transitie om zowel de uitzend- als collectieefficiëntie te vergroten. In dit proefschrift bedden we een NV centrum in een dun diamant membraan in in een

open Fabry-Pérot microtrilholte. We ontwikkelen analytische modellen die een effectief gereedschap leveren om de optimale ontwerpparameters te bepalen voor zo een trilholte (hoofdstuk 5).

Voor de incorporatie in optische trilholtes is het hoogstgewenst om NV-centra te creëren op precieze plekken in diamantmembranen. Maar het proces van NV creatie en de fabricage van dunne membranen kan defecten introduceren in de diamant. Deze defecten kunnen tijdsafhankelijke fluctuaties van het elektrisch veld veroorzaken, die zorgen voor instabiliteit van de NV optische transities. In hoofdstukken 6 en 7 verkennen we experimenteel de optische eigenschappen van NV-centra in membranen, gecreëerd met hoge-energie-electronenbestraling of door de implantatie van stikstof-ionen, gevolgd door uitgloeien bij hoge temperatuur. We vinden dat NV-centra die zijn gecreëerd door electronenbestraling coherente optische transities kunnen hebben terwijl, in contrast met eerdere aannames in de quantumtechnologiegemeenschap, NV-centra gevormd van geïmplanteerde stikstofatomen niet stelselmatig smalle optische lijnen hebben.

We rapporteren de experimentele realisatie van een Fabry-Pérot microtrilholte met ingebedde NV centre in hoofdstukken 9, 10 en 11. We ontwikkelen microgolfstriplijnen ingekaderd in een vlakke spiegel, die het mogelijk maken om de spin van het NV-centrum te adresseren, zonder de finesse van de trilholte aan te tasten. Daarnaast bedden we een dun diamantmembraan in in een microtrilholte bij cryogene temperaturen. We vinden een hoge finesse waarde in het bereik $F = 4,000 - 12,000$, en een subnanometer trilholtestabiliteit. Voor deze parameters schatten we een potentiële toename in verstrengelingssnelheid van drie orde groottes. Vervolgens plaatsen we een membraan met optisch coherente NV-centra, gevormd door elektronenbestraling, in een microtrilholte. We observeren de koppeling van de uitgezonden straling van een NV ensemble in de trilholtemodus. Hoewel een lage trilholtefinesse het observeren van Purcellverbetering verhindert, markeren dit belangrijke stappen naar Purcellverbetering van enkele uitzenders.

In hoofdstuk 12 kijken we vooruit naar quantumnetwerken gedistribueerd over afstanden meer dan enkele kilometers. We analyseren protocollen met multiplexing in quantumknooppunten met meerdere qubits om limieten aan de verstrengelingssnelheid die worden opgelegd door klassieke communicatietijd te overwinnen. We modelleren haalbare verstrengelingssnelheden gebaseerd op de verwachte prestatie van NV-centra als gebruik wordt gemaakt van optisch trilholtes. Deze analyse maakt het mogelijk om het potentieel van de voorgestelde multiplexing protocollen te vergelijken.

De optische trilholtes, coherente uitzenders en protocollen gepresenteerd in dit proefschrift bevorderen de efficiëntie van quantumnetwerken gebaseerd op het NV-centrum in diamant. Dit onthult een pad naar netwerken op grote schaal, met fundamentele tests en quantumtechnologie die uitgaat van hoge verstrengelingssnelheden zoals toestelafhankelijke quantumsluitedistributie.

ACKNOWLEDGEMENTS

I am thankful for having worked in the stimulating environment of QuTech for the last four years. Already during my MSc project I experienced the QT family feeling: Diamond dinners, the QT-uitje and even the werkbepreking contributed to that. Somewhere between the start of my master's project and the start of my PhD QT transformed to QuTech, but the exciting environment remained: werkbepreking, Diamond dinners and the QT-uitje became part of the QuTech family feeling. In the following I attempt to thank all the people that made such important contributions during the last four years.

Ronald, thank you for your scientific insight and your clear strategic ideas. Your capability to distill the important things from complex situations and focus on these not only inspire efficiency and relevance, but I believe are also the driving factor behind Team Diamond's success. Thank you for guiding me in my PhD process, and pointing me to situations where I could develop myself. And, thank you for the conversations while biking to The Hague after Diamond dinners!

Tim, thank you for your guidance in my first year, when we made initial plans for implantation in Delft, and started working on the contextuality project. That last one turned out to be the project making my PhD circular: it is also the project I am working on till the end of my PhD. Thank you for your eye for detail and your careful feedback and discussion.

The cavity project had already been running for a while when I joined you in it, Stefan. You had already arranged ablated fibers, and mirrors, built a setup and started sample fabrication from scratch. I think our compatible skills made a good team. Together, we could take the first data from the cavity setup, and I remember clearly how we were possessed with measurement fever - I don't think anyone ever enjoyed taking characterisation data as much as we did those days. I admire your sincere enthusiasm for science and the inclusiveness that you radiate. Cristian, I joined the cavity project when you were just leaving. Your crucial contributions in the early stage helped shape the project. Andreas, your experience with optical cavities was a valuable resource to us; thank you for all the advice on cavity measurements and stabilisation. Bas, I remember my excitement when you decided to join the cavity team for a few months after your PhD. I enjoyed working in the lab with you and learned a lot during that time. Marko, your presence in Delft was fantastic for the cavity team. Talking to you and your students about sample fabrication leveraged us forwards, and the excitement that you showed for tackling technical challenges was inspiring. I will never forget walking into the lab and finding you whistling excitedly, having found that it influenced the cavity stability. Madelaine, you are the most passionate person about fabrication I ever met. Your structured work helped the team forward, and your enthusiasm reached to all of team diamond. I still regret that our attempts to make you stay after your scholarship program were unsuccessful. Maarten, you joined the cavity project for a while when you started your PhD.

I enjoyed guiding you through these first months, and thank you for helping with the sample fabrication in that time. Later on we worked closely together on the implantation project; it was an interesting time, with late-evening calls with MIT and taking care that we had unbiased data. Wouter, switching fields after your PhD, you joined Team Diamond and the cavity project. You immediately got up to speed in the lab, building the optical setup for NV detection in the cavity. Unfortunately the adventure did not take too long; I am sure you will find a great place at IMEC! Max, you arrived with a bag of microcavity-experience, and picked up the sample fabrication. I admire your ability to involve people: for the sample fabrication and vibration stability of the setup you have gathered a lot of help from TNO, which I am sure will be crucial for the success of the cavity project. Matthew, we never worked in the lab together, but I have enjoyed our discussions on cavities. I think your experience with (unstable) cavities is of great value to the team. Martin, thank you for your all-round support, from building optical setups, to measuring vibration stability and building a full laser-ablation setup. Nick, Hans, and Jasper, thank you for the support in the cleanroom. To have robust sample fabrication is a critical element to the cavity project, and your contribution to that is essential.

During my PhD I got the opportunity to supervise students during their projects. Lisanne, I am impressed by how effectively you can get things done. I enjoyed working with you and learning from your efficient approach; and spending a weekend in a castle in Paris! Sophie, I was very excited when you decided to join as a master student. Thanks to your careful mapping of Harry, we could navigate around the sample (feeling like pirates). Airat, you showed yourself as a very hard worker, and a fun person to be around. Your correlations of optical and spin measurements on implanted NVs started off a whole new project. Steven, in your project we did the first measurements on NV centres in diamond membranes. Your good lab intuition and excitement for measuring made the measurements we did a lot of fun; despite the fact that we found that the NV centres were not as optically stable as we had assumed. Thom, as part of your double maths-physics bachelor you theoretically looked at NV centres in high strain regimes. With your independent attitude, I was curious each meeting to learn what new things you had been up to. Additionally, I want to thank all other MSc and Bsc students working on the cavity project that I did not directly supervise: Anne-Marije, Mark, Santi, Guus, and Jildou.

Being part of Team Diamond was a great experience that allowed me to learn a lot from many talented people. Wolfgang, thank you for guiding me during my master's project; working on teleportation was very exciting. Hannes, thank you for always being happy to share your excitement and lab skills whenever needed. Machiel, we shared an excitement for foundations of quantum mechanics, thank you for always bringing up the measurement problem! Anais, thanks for the discussions on science and chocolate! Norbert, we started at the same time and occasionally our scientific paths crossed. I am impressed by how much you managed to produce during your PhD in a short time. Mohamed, I was always keen to hear from you how many nuclear spins you have been controlling; keep me updated! Conor and Joe, good luck with the RF controlling and distant entanglement of carbons. Valeria, I wish you all the best for your PhD in Rome and hope our paths will cross again. Matteo, Sophie and Simon, I am sure you will entangle 3 nodes soon. Arian, you will make the distance! Anna, thank you for our chats on sci-

ence, and life. Dirk, thank you for always being open to discuss science. Erwin, Jaco and Sander, good luck with the demonstrator project.

Thank you, Stephanie, for initiating such a strong theory base in Delft, and for constructing the QINC discussion days that resulted in many common projects. Filip, Glauca, Kenneth and Jeremy, I have enjoyed our discussions and work together!

Dirk, Michael, Eric, and Sara, we set up a fruitful collaboration to scrutinize the coherence of implanted NV centres. Thank you for your sharp reasoning, and the many calls and discussions.

I wish to thank the support that I have received during the last four years. Remco, Mark, Nico, Siebe, Bram, Olaf en Jason, thank you for always being able to help with so many technical aspect of my PhD! Raymond, Raymond, and Marijn, thank you for helping out with any question on electronics. Hans, thank you for helping design new PCBs. Eugene, together we picked out an annealing oven; thank you for your help and expertise. Chantal and Marja, Yuki and Joanna, Judith, Jenny, and Heera thank you for all your help, and for always providing a warm environment when walking into your offices.

When I started my PhD I had the enormous office in F033 for myself. Although it was great for playing football and creating echoes, I was very glad when my first office mates started to arrive. Ali and Lily, thank you for sharing that first time with me. Olaf, Jason, and Nick, your presence brought a lot of life (and puzzles!) to the office. Thanks for shaking crucial parts out of cryostats, sharing bikerides home, and asking questions about quantum. Guoji, Martin, Roy, Lareine, Toivo, Udit, Amir and Diego, with you there the office grew to its full capacity. Lareine, thank you for the plant that you left with me, I moved it along with me to my new office. Diego, Mohamed, Jelmer, and Sophie, thank you for the fun office times there!

I also want to thank all the people that crossed my path outside of Team Diamond and QuTech. Adriaan, Jonas, James - my co-editors of the QuTech blog! Chris, thank you for your excitement about and many contributions to the blog. Anne-Marije, Guan, and Tim; good luck as new editors of Bits of Quantum. Julia, Jules, and Jacob, thanks for the fun times when organizing the best-QT-uitje-of-all-time. My PhD would not have been the same without all the QuTech running companions. David, Julia, Niels, thank you for immediately after my arrival in QT incorporating me in the Flying Qubits. Jelmer, thank you for organizing the Batavierenrace with me (my measurements are running too) - and all the enthusiastic QuTech runners for participating. Leo DC, it was great to be able to share running schemes, experiences and high-fives! Michiel, Alex, James, Norbert, Florian, we all arrived in QuTech just a few months apart - thanks for accompanying me during my full PhD. David, Shun, Joao and Martijn, thank you for the fun times TA'ing, making the grading of homework, minitests and exams a bit more fun! Anne-Marije, thanks for all the cups of tea we had.

Pieter, thank you for involving me and Alex in setting up the master's course on the Foundations of Quantum Mechanics. I have enjoyed the numerous discussions about interpretations and through them have been able to sharpen my mind on these topics. Miriam, thank you for the valuable conversations we have had during my PhD!

Thank you to all my doctoral committee members for taking the time and effort to read my thesis. It is an honour to have you in my doctoral defense.

My paranimfen: Julia and Sophie. Julia, we first met in the first week of our first year

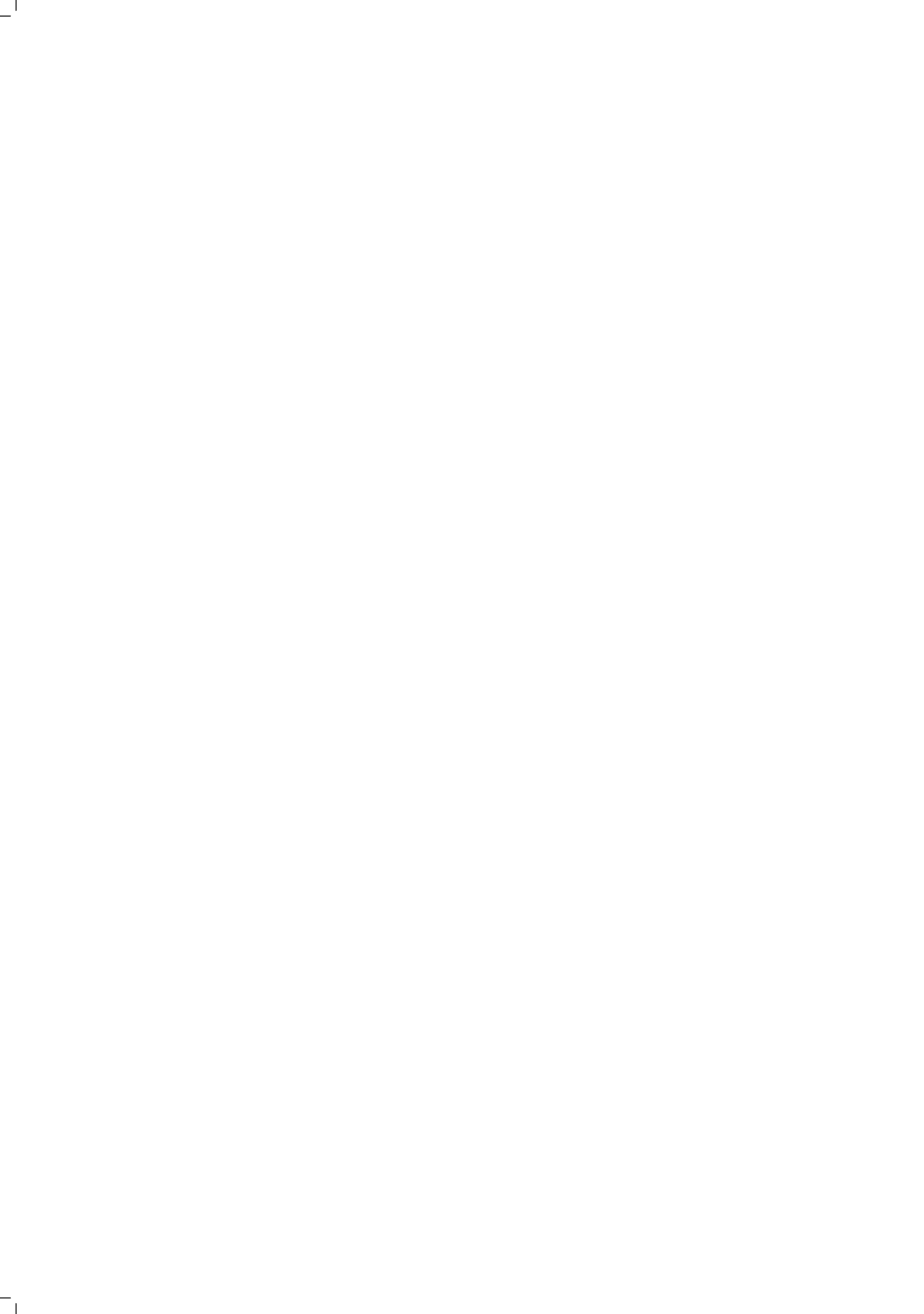
of physics. I had not imagined I would be filling fridges and controlling carbons with you seven years later. Having you so close during my PhD has been a great support. It is great to see you shine in your new role as communication scientist and science communicator. Sophie, I was a bit proud when you decided to stay in team diamond for your PhD after your master project. I think we have shown ourselves masters of analyzing situations with the help of graduate school courses and workshops.

Pappa en mamma, thank you for your promotion of curiosity, for invariably being available for deliberation, and always making me want to come home. Clara and Hans, it has been very special to be able to share a PhD and physics with you. Peter - your contribution to this thesis goes beyond explanation. I am looking forward to our future adventures!

LIST OF PUBLICATIONS

7. *Optical coherence of diamond NV centers formed by ion implantation and annealing.*
S. B. van Dam*, M. Walsh*, M. J. Degen, E. Bersin, S. Mouradian, A. Galiullin, M. Ruf, M. Ijspeert, T. H. Taminiau, R. Hanson, and D. R. Englund.
arXiv:1812.11523
6. *Towards a realization of device-independent quantum key distribution.*
G. Murta, **S. B. van Dam**, J. Ribeiro, R. Hanson, and S. Wehner.
arXiv:1811.07983
5. *Optimal design of diamond-air microcavities for quantum networks using an analytical approach.*
S. B. van Dam, M. Ruf, and R. Hanson.
New Journal of Physics **20**, 115004 (2018)
4. *Robust nano-fabrication of an integrated platform for spin control in a tunable microcavity.*
S. Bogdanović, M. S. Z. Liddy, **S. B. van Dam**, L. C. Coenen, T. Fink, M. Lončar, and R. Hanson.
APL photonics **2**, 126101 (2017)
3. *Multiplexed entanglement generation over quantum networks using multi-qubit nodes.*
S. B. van Dam*, P. Humphreys*, F. Rozpędek*, S. Wehner, and R. Hanson.
Quantum Science and Technology **2**, 034002 (2017)
2. *Design and low-temperature characterization of a tunable microcavity for diamond-based quantum networks*
S. Bogdanović, **S. B. van Dam**, C. Bonato, L. C. Coenen, A.-M.J. Zwerver, B. Hensen, M. S. Z. Liddy, T. Fink, A. Reiserer, M. Lončar, and R. Hanson.
Applied Physics Letters **110**, 171103 (2017)
1. *Unconditional quantum teleportation between distant solid-state quantum bits.*
W. Pfaff, B. J. Hensen, H. Bernien, **S. B. van Dam**, M. S. Blok, T. H. Taminiau, M. J. Tiggelman, R. N. Schouten, M. Markham, D. J. Twitchen, and R. Hanson.
Science **345**, 532 (2014)

*Equally contributing authors



CURRICULUM VITÆ

Suzanne Barbera VAN DAM

- 31-08-1989 Born in Rotterdam, The Netherlands.
- 2001–2007 Secondary School
Erasmiaans Gymnasium, Rotterdam, The Netherlands
- 2007–2011 Bachelor of Science in Applied Physics
Delft University of Technology, The Netherlands
Graduation research project in the Theoretical Physics group
Supervisor: Prof. dr. G. E. W. Bauer
- 2011–2012 Master of Advanced Study in Mathematics
University of Cambridge, United Kingdom
- 2012–2014 Master of Science in Applied Physics
Delft University of Technology, The Netherlands
Graduation research project in the Quantum Transport group
Supervisor: Prof. dr. ir. R. Hanson
- 2014 Technical Student Internship
European Organization for Nuclear Research (CERN), Switzerland
Research project in the CLIC Detector and Physics Study group
Supervisor: Dr. L. Linsen
- 2014 – 2019 Doctorate in Physics
Delft University of Technology, The Netherlands
QuTech and Kavli Institute of Nanoscience
Thesis: Optical cavities, coherent emitters, and protocols for
 diamond-based quantum networks
Promotor: Prof. dr. ir. R. Hanson

